Global Conservation Laws and Femtoscopy at RHIC

Dissertation

Presented in Partial Fulfillment of the Requirements for the Degree
Doctor of Philosophy in the Graduate School of The Ohio State University

By

Zbigniew Chajęcki

Graduate Program in Physics

The Ohio State University

2009

Dissertation Committee:

Dr. Michael A. Lisa, Advisor

Dr. Thomas J. Humanic

Dr. Yuri Kovchegov

Dr. Klaus Honscheid

ABSTRACT

It is increasingly important to understand, in details the space and momentum observables in elementary particle collisions (e.g. $p + p$ collisions), as they should serve as a reference to the same observables in heavy-ion collisions. Such a comparison is crucial to claim a discovery of new phenomena in the big system. However, in low-multiplicity systems, global conservation laws generate significant N-body correlations in addition to other physics effects. We discuss a formalism to analytically calculate these effects on single-particle distributions and multi-particle correlation functions.

Transverse mass distributions in relativistic heavy ion collisions provide valuable information about the dynamics of the system. The comparison of the spectra from big systems with analogous distribution from $p + p$ collisions led to a claims of discovery of strong collective flow dominating the low momentum part of the spectra in heavy ion collisions. However, we question such a comparison by pointing out the risk of ignoring conservation laws when comparing high- (e.g. $Au + Au$) and low-multiplicity (e.g. $p + p$) collisions. Then, we argue that a correct treatment of the effects due to energy and momentum conservation may account for most of the difference between spectra in small and big system. As a result, we show that after this effect is considered, $p + p$ collisions have similar amount of radial flow as $Au + Au$ collisions at RHIC.

The effect of phase-space constraints due to energy and momentum conservation project onto two-particle space in a non-trivial way, affecting the shape of the two-particle correlation functions, and therefore, complicating the femtoscopic analysis.

We also present results from $p + p$ collisions at $\sqrt{s}$=200 GeV, $d + Au$ collisions at $\sqrt{s_{NN}}$=200 GeV and $Au + Au$ collisions at $\sqrt{s_{NN}}$=19.6 GeV from the STAR Experiment at RHIC. The sizes of homogeneity regions are extracted through femtoscopic analysis of the pion correlations. In small system, we see a significant effect of phase-space constraints due to the energy and momentum conservations and we use our formalism to treat these non-femtoscopic correlations.

For the first time, we compare RHIC femtoscopic results from $Au + Au$ collisions at $\sqrt{s_{NN}}$=19.6 GeV with previously published results from SPS experiments at very similar energy of the collision. We put STAR results from small systems in the context of world data from femtoscopic studies in elementary particle collisions and observe trends seen in the data. We also directly compare STAR results from heavy-ion and $p + p$ collisions, under identical analysis, detector acceptance and performance. We identify that the multiplicity and the transverse mass dependence of femtoscopic radii in small systems is surprisingly similar to what is seen in heavy ion collisions.

Based on these similarities between spectra and femtoscopic results from small and big systems, we speculate that there is as strong radial flow in $p + p$ collisions as observed in $Au + Au$ collisions.

DEDICATION

Rodzicom

VITA

March 30, 1979	Born - Lomza, Poland
2003	M.S. Physics, Warsaw University of Technology, Warsaw, Poland
2007	M.S. Physics, The Ohio State University, Columbus, OH
2004-present	Graduate Research Assistant, Deprtment of Physics, The Ohio State University, Columbus, OH

Publications

[1] Zbigniew Chajęcki and Mike Lisa, Conservation laws and multiplicity evolution of spectra at energies available at the BNL Relativistic Heavy Ion Collider, Phys. Rev. C 79 (2009) 034908, e-Print: arXiv:0807.3569 [nucl-th]

[2] Zbigniew Chajęcki and Mike Lisa, Global Conservation Laws and Femtoscopy of Small Systems, Phys. Rev. C 78 (2008) 064903, e-Print: arXiv:0803.0022 [nucl-th]

[3] Z. Chajęcki, for the STAR Collaboration, Femtoscopy in p + p vs. heavy ion collisions in STAR, Eur.Phys.J.C49:81-86,2007.

[4] Z. Chajęcki, for the STAR Collaboration, Identical particle correlations in STAR, Nucl.Phys.A774:599-602,2006, e-Print: nucl-ex/0510014

[5] Zbigniew Chajęcki and Mike Lisa, Does Momentum Conservation Drive the Multiplicity Dependence of Spectra at RHIC?, Proc. 24th Winter Workshop on Nuclear Dynamics (2008) 339-344.

[6] Z. Chajęcki, Global Conservation Laws and Femtoscopy of Small Systems, Proc. 23rd Winter Workshop on Nuclear Dynamics (2007) 161-170.

[7] Z. Chajęcki, M. Lisa, Global conservation laws and femtoscopy of small systems, Braz.J.Phys.37:1057-1064,2007, e-Print: nucl-th/0612080

[8] S. Bekele *et al.*, Status and Promise of Particle Interferometry in Heavy-Ion Collisions, Braz.J.Phys.37:1057-1064,2007, e-Print: arXiv:0706.0537 [nucl-ex]

[9] Z. Chajęcki, for the STAR Collaboration, *Pion interferometry from p + p to Au + Au in STAR*, AIP Conf.Proc.828:566-571,2006, e-Print: nucl-ex/0511035

[10] B. Abelev et al. (the STAR Collaboration), Longitudinal double-spin asymmetry for inclusive jet production in $\vec{p} + \vec{p}$ collisions at $\sqrt{s}$=200 GeV, Phys. Rev. Lett. **100** (2008) 232003

[11] B. Abelev et al. (the STAR Collaboration), Spin alignment measurements of the K* and phi vector meson at RHIC, Phys. Rev. C **77** (2008) 61902

[12] B. Abelev et al. (the STAR Collaboration), Centrality dependence of charged hadron and strange hadron elliptic flow from $\sqrt{s_{NN}} = 200$ GeV Au+Au collisions, Phys. Rev. C **77** (2008) 54901

[13] B. Abelev et al. (the STAR Collaboration), Enhanced strange baryon production in Au+Au collisions compared to p+p at $\sqrt{s_{NN}} = 200$ GeV, Phys. Rev. C **77** (2008) 44908

[14] B. Abelev et al. (the STAR Collaboration), ρ^0 Photoproduction in Ultra-Peripheral Relativistic Heavy Ion Collisions with STAR, Phys. Rev. C **77** (2008) 34910

[15] B. Abelev et al. (the STAR Collaboration), Forward Lambda Production and Nuclear Stopping Power in d+Au Collisions at $\sqrt{s_{NN}} = 200$ GeV, Phys. Rev. C **76** (2007) 64904

[16] B. Abelev et al. (the STAR Collaboration), Rapidity and species dependence of particle production at large transverse momentum for d+Au collisions at $\sqrt{s_{NN}}$ = 200 GeV, Phys. Rev. C **76** (2007) 54903

[17] B. Abelev et al. (the STAR Collaboration), Energy dependence of pi, p and pbar transverse momentum spectra for Au+Au collisions at $\sqrt{s_{NN}} = 62.4$ and 200 GeV, Phys. Lett. B **655** (2007) 104

[18] B. Abelev et al. (the STAR Collaboration), Measurement of Transverse Single-Spin Asymmetries for Di-Jet Production in Proton-Proton Collisions at $\sqrt{s} = 200$ GeV, Phys. Rev. Lett. **99** (2007) 142003

[19] B. Abelev et al. (the STAR Collaboration), Partonic flow and phi-meson production in Au+Au collisions at $\sqrt{s} = 200$ GeV, Phys. Rev. Lett. **99** (2007) 112301

[20] B. Abelev et al. (the STAR Collaboration), Global polarization measurement in Au+Au collisions, Phys. Rev. C **76** (2007) 024915

[21] J. Adams et al. (the STAR Collaboration), Strangelet Search in AuAu collisions at 200 GeV, Phys. Rev. C **76** (2007) 011901

[22] B. Abelev et al. (the STAR Collaboration), Strange particle production in p+p collisions at $\sqrt{s}$ = 200 GeV, Phys. Rev. C **75** (2007) 64901

[23] B. Abelev et al. (the STAR Collaboration), Mass, quark-number, and $\sqrt{s_{NN}}$ dependence of the second and fourth flow harmonics in ultra-relativistic nucleus-nucleus collisions, Phys. Rev. C **75** (2007) 54906

[24] B. Abelev et al. (the STAR Collaboration), Transverse momentum and centrality dependence of high-p_T non-photonic electron suppression in Au+Au collisions at $\sqrt{s_{NN}}$ = 200 GeV, Phys. Rev. Lett. **98** (2007) 192301

[25] C. Adler et al. (the STAR Collaboration), Transverse momentum correlations and minijet dissipation in Au-Au collisions at $\sqrt{s_{NN}}$ = 130 GeV, J. Phys. G **34** (2007) 799

[26] J. Adams et al. (the STAR Collaboration), Delta-phi Delta-eta Correlations in Central Au+Au Collisions at $\sqrt{s_{NN}}$ = 200 GeV, Phys. Rev. C **75** (2007) 34901

[27] J. Adams et al. (the STAR Collaboration), Scaling properties of hyperon production in Au+Au collisions at $\sqrt{s_{NN}}$ = 200 GeV, Phys. Rev. Lett. **98** (2007) 62301

[28] J. Adams et al. (the STAR Collaboration), The energy dependence of p_t angular correlations inferred from mean-p_t fluctuation scale dependence in heavy ion collisions at the SPS and RHIC, J. Phys. G **34** (2007) 451

[29] B. Abelev et al. (the STAR Collaboration), Longitudinal Double-Spin Asymmetry and Cross Section for Inclusive Jet Production in Polarized Proton Collisions at $\sqrt{s}$ = 200 GeV, Phys. Rev. Lett. **97** (2006) 252001

[30] J. Adams et al. (the STAR Collaboration), Proton - lambda correlations in central Au+Au collisions at $\sqrt{s_{NN}}$ = 200 GeV, Phys. Rev. C **74** (2006) 64906

[31] B. Abelev et al. (the STAR Collaboration), Neutral Kaon Interferometry in Au+Au collisions at $\sqrt{s_{NN}}$ = 200 GeV, Phys. Rev. C **74** (2006) 54902

[32] J. Adams et al. (the STAR Collaboration), Direct observation of dijets in central Au+Au collisions at $\sqrt{s_{NN}}$ = 200 GeV, Phys. Rev. Lett. **97** (2006) 162301

[33] J. Adams et al. (the STAR Collaboration), Forward Neutral Pion Production in p+p and d+Au Collisions at $\sqrt{s_{NN}}$ =200 GeV, Phys. Rev. Lett. **97** (2006) 152302

[34] J. Adams et al. (the STAR Collaboration), Identified baryon and meson distributions at large transverse momenta from Au+Au collisions at $\sqrt{s_{NN}} = 200$ GeV, Phys. Rev. Lett. **97** (2006) 152301

[35] J. Adams et al. (the STAR Collaboration), Strange baryon resonance production in $\sqrt{s_{NN}} = 200$ GeV p+p and Au+Au collisions, Phys. Rev. Lett. **97** (2006) 132301

[36] J. Adams et al. (the STAR Collaboration), The multiplicity dependence of inclusive p_T spectra from p-p collisions at $\sqrt{s} = 200$ GeV, Phys. Rev. D **74** (2006) 32006

[37] C. Adler et al. (the STAR Collaboration), Minijet deformation and charge-independent angular correlations on momentum subspace (eta,phi) in Au-Au collisions at $\sqrt{s_{NN}}$= 130 GeV, Phys. Rev. C **73** (2006) 64907

[38] G. Van Buren et al., Correcting for distortions due to ionization in the STAR TPC , Nucl. Instrum. Meth. A **566** (2006) 22

[39] J. Adams et al. (the STAR Collaboration), Transverse-momentum p_T correlations on (eta,phi) from mean-p_T fluctuations in Au-Au collisions at $\sqrt{s_{NN}}$ =200 GeV, J. Phys. G **32** (2006) 0

[40] J. Adams et al. (the STAR Collaboration), Identified hadron spectra at large transverse momentum in p+p and d+Au collisions at $\sqrt{s_{NN}} = 200$ GeV, Phys. Lett. B **637** (2006) 161

[41] C. Adler et al. (the STAR Collaboration), Hadronization geometry and net-charge angular correlations on momentum subspace (eta,phi) in Au-Au collisions at $\sqrt{s_{NN}}$= 130 GeV, Phys. Lett. B **634** (2006) 347

[42] J. Adams et al. (the STAR Collaboration), Multiplicity and Pseudorapidity Distributions of Charged Particles and Photons at Forward Pseudorapidity in Au + Au Collisions at $\sqrt{s_{NN}} = 62.4$ GeV, Phys. Rev. C **73** (2006) 34906

[43] J. Adams et al. (the STAR Collaboration), Directed flow in Au+Au collisions at $\sqrt{s_{NN}} = 62$ GeV, Phys. Rev. C **73** (2006) 34903

[44] Ming Shao et al., Extensive particle identification with TPC and TOF at the STAR experiment, Nucl. Instrum. Meth. A **558** (2006) 419

[45] J. Adams et al. (the STAR Collaboration), Incident Energy Dependence of pt Correlations at RHIC, Phys. Rev. C **72** (2005) 044902

[46] J. Adams et al. (the STAR Collaboration), Distributions of Charged Hadrons Associated with High Transverse Momentum Particles in pp and Au+Au Collisions at $\sqrt{s_{NN}}$ = 200 GeV, Phys. Rev. Lett. **95** (2005) 152301

[47] J. Adams et al. (the STAR Collaboration), Multi-strange baryon elliptic flow in Au+Au collisions at $\sqrt{s_{NN}}$ = 200 GeV, Phys. Rev. Lett. **95** (2005) 122301

[48] J. Adams et al. (the STAR Collaboration), Multiplicity and Pseudorapidity Distributions of Photons in Au + Au Collisions at $\sqrt{s_{NN}}$ = 62.4 GeV, Phys. Rev. Lett. **95** (2005) 62301

[49] C. Adler et al. (the STAR Collaboration), Azimuthal Anisotropy in Au+Au Collisions at $\sqrt{s_{NN}}$ = 200 GeV, Phys. Rev. C **72** (2005) 14904

[50] C. Adler et al. (the STAR Collaboration), Event-wise mean-p_T fluctuations in Au-Au collisions at $\sqrt{s_{NN}}$ = 130 GeV, Phys. Rev. C **71** (2005) 64906

[51] J. Adams et al. (the STAR Collaboration), K(892)* Resonance Production in Au+Au and p+p Collisions at $\sqrt{s_{NN}}$ = 200 GeV at STAR, Phys. Rev. C **71** (2005) 64902

[52] J. Adams et al. (the STAR Collaboration), Experimental and Theoretical Challenges in the Search for the Quark Gluon Plasma: The STAR Collaboration's Critical Assessment of the Evidence from RHIC Collisions, Nucl. Phys. A **757** (2005) 102

[53] C. Adler et al. (the STAR Collaboration), Pion interferometry in Au+Au collisions at $\sqrt{s_{NN}}$ = 200 GeV, Phys. Rev. C **71** (2005) 44906

[54] C. Adler et al. (the STAR Collaboration), Pion, kaon, proton and anti-proton transverse momentum distributions from p+p and d+Au collisions at $\sqrt{s_{NN}}$ = 200 GeV, Phys. Lett. B **616** (2005) 8

[55] C. Adler et al. (the STAR Collaboration), Phi meson production in Au+Au and p+p collisions at $\sqrt{s_{NN}}$ =200 GeV, Phys. Lett. B **612** (2005) 181

[56] C. Adler et al. (the STAR Collaboration), Transverse-momentum dependent modification of dynamic texture in central Au+Au collisions at $\sqrt{s_{NN}}$= 200 GeV, Phys. Rev. C **71** (2005) 31901

[57] C. Adler et al. (the STAR Collaboration), Open charm yields in d+Au collisions at $\sqrt{s_{NN}}$ = 200 GeV, Phys. Rev. Lett. **94** (2005) 62301

[58] C. Adler et al. (the STAR Collaboration), Pseudorapidity Asymmetry and Centrality Dependence of Charged Hadron Spectra in d+Au Collisions at $\sqrt{s_{NN}}$ = 200 GeV, Phys. Rev. C **70** (2004) 64907

[59] C. Adler et al. (the STAR Collaboration), Azimuthal anisotropy and correlations at large transverse momenta in p+p and Au+Au collisions at $\sqrt{s_{NN}}$ = 200 GeV, Phys. Rev. Lett. **93** (2004) 252301

[60] C. Adler et al. (the STAR Collaboration), Measurements of transverse energy distributions in Au+Au collisions at $\sqrt{s_{NN}}$ = 200 GeV, Phys. Rev. C **70** (2004) 54907

[61] C. Adler et al. (the STAR Collaboration), Production of e+e- Pairs Accompanied by Nuclear Dissociation in Ultra-Peripheral Heavy Ion Collision, Phys. Rev. C **70** (2004) 031902(R)

Fields of Study

Major Field: Physics

TABLE OF CONTENTS

Chapters:

Appendices:

LIST OF TABLES

LIST OF FIGURES

xxv

xxxiii

CHAPTER 1

INTRODUCTION

1.1 Physics in soft sector [1] driven by flow

The motivation to study physics of heavy ion collisions is the desire to understand the equation of state of strongly interacting matter. It is expected that these collisions generate a bulk system that exhibits collective effects and that can be described in framework of thermodynamics. There are numerous claims in the literature that bulk matter is created at high energy heavy ion collisions at RHIC [1, 2, 3, 4] and that physics of the soft sector, low-p_T observables, is driven by a strong collective flow [5]. The flow is manifested in momentum observables like e.g. p_T spectra and azimuthal anisotropies in the distribution of emitted particles. The understanding of flow in heavy ion collisions usually involves hydrodynamic model calculations (e.g. [6]) or fits to the data using hydro-inspired parameterizations [7]. As an example, Figure 1.1 shows the distribution of $v_2(p_T)$ - a measure of the azimuthal anisotropy of emitted particles [6] - for pions and kaons plotted together with calculations from the hydrodynamic models. However, the momentum observables [1, 2, 3, 4] provide only

---

[1]Commonly used term "soft sector" refers to the physics of particles emitted with the transverse momentum smaller than approximately 2 GeV/c at mid-rapidity.
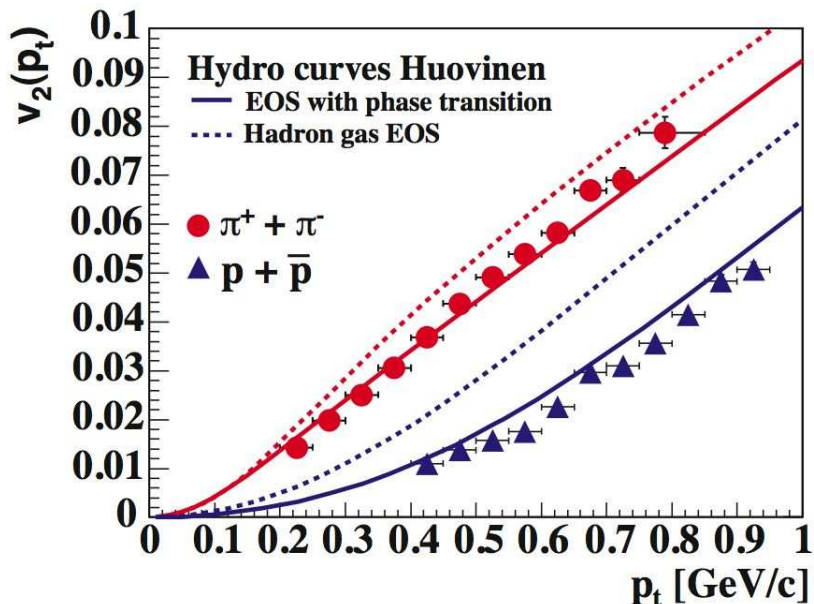
Figure 1.1: Comparison of pion and proton $v_2(p_T)$ dependence with hydrodynamic calculations for hadron gas and including the first order phase-transition [6]. Figure taken from [8].

indirect evidence of the flow (for the latest review of this topic see [8]) that is, in fact, a space-momentum correlation phenomena. The measurement that directly accesses both momentum and spatial scale is the femtoscopic study [9]. The decrease of the pion HBT radii with increasing transverse mass of the particles and the dependence of the homogeneity region of the particle type are direct evidence of the flow signal in heavy ion collisions [7].

1.2   Femtoscopy, homogeneity regions, and sensitivity to flow

The two-particle correlations represent a group of measurements that focus on various observables. In this thesis we use correlations of two particles at close relative velocities to study the size of the source. Since these sizes are of order of a

femtometer the two-particle interferometry technique is often called femtoscopy, the name introduced by Lednicky [10, 11].

In fact, the the two-particle correlations do not measure the size of the entire physical source but rather the size of the so-called homogeneity region that represent the scale over which pairs of particles with similar velocities are emitted [12].

The femtoscopic studies are sensitive to the evolution of the emission region. In particular, the collective effects like flow leave fingerprints on femtoscopic results. This issue is addressed and discussed in details in this thesis, in particular in chapters3 and 12.

1.3   "Know your reference" [2]

Usually, any kind of discovery in physics involves a comparison of a situation that the particular physics effect is present to the situation when it is not. Only a very careful study and understanding of such a comparison can lead to a claim of new discovery.

Similarly, the understanding of the physics behind the heavy ion collisions is crucial but any claims of new physics must involve the careful study of the system size dependence and should be based on a comparison to a system in which particular physics effects are not present. It is probably natural to consider $p + p$ collisions as a reference to heavy ion collisions. In fact such a comparison has been made at high-p_T physics at RHIC e.g. where it was demonstrated that the azimuthal correlations

---

[2]Phrase borrowed from Bill Zajc's talk given at Quark Matter 2009 Conference (http://www.phy.ornl.gov/QM09/).
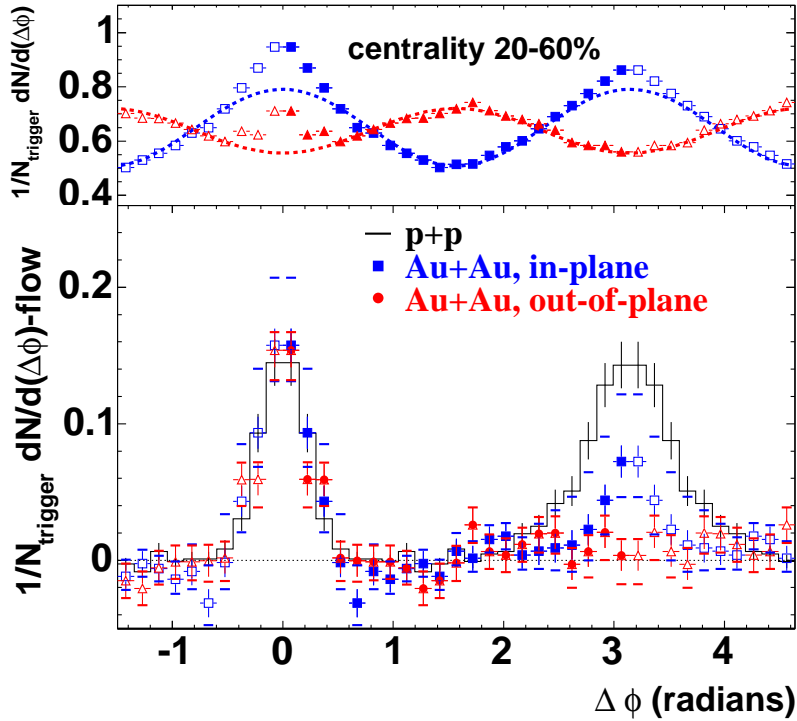
Figure 1.2: Azimuthal distributions of associated particles for trigger particles in-plane(squares) and out-of-plane (triangles) for $Au + Au$ collisions at centrality 20-60%. Open symbols are reflections of solid symbols around $\Delta\phi = 0$ and $\Delta\phi = \pi$. Elliptic flow contribution is shown by dashed lines. Lower panel: Distributions after subtracting elliptic flow, and the corresponding measurement in p+p collisions (histogram). Figure taken from [13].

of particles in $Au + Au$ collisions [14, 13] as well as the leading particle distribution [15, 16] are strongly suppressed relative to $p + p$ collisions that is an evidence of the medium effect. See Figs. 1.2 and 1.3.

So far, the assumption of using $p + p$ collisions as a reference system to heavy ion collisions have been widely accepted and not much questioned by heavy ion physicists.
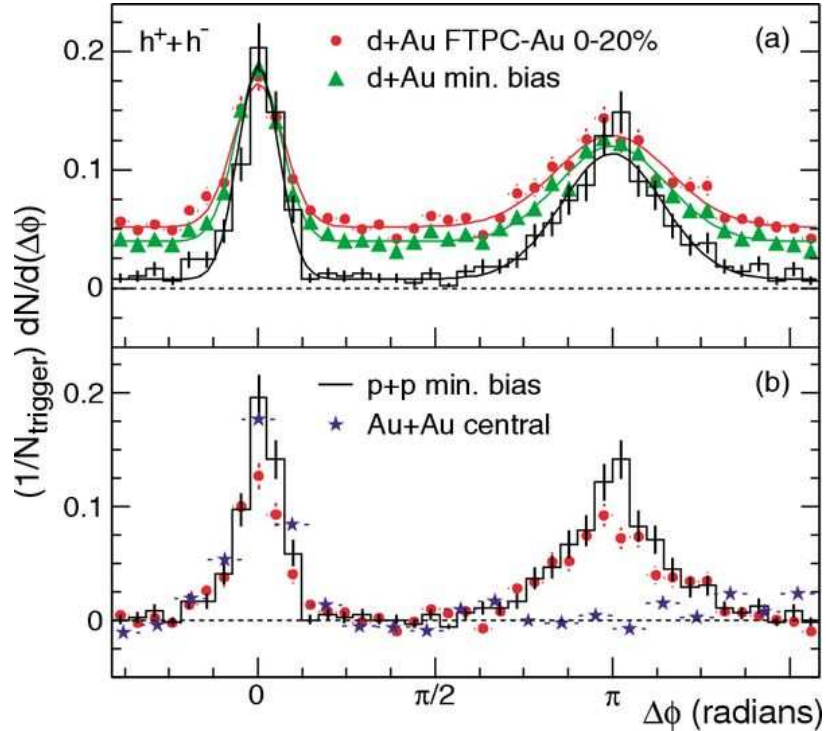
Figure 1.3: (a) Efficiency corrected two-particle azimuthal distributions for minimum-bias and central $d + Au$ collisions, and for $p + p$ collisions [14]. (b) Comparison of two-particle azimuthal distributions for central $d + Au$ collisions to those seen in $p + p$ and central $Au + Au$ collisions [14]. The respective pedestals have been subtracted. Figure taken from [17].

This assumption is based on a belief that $p + p$ collisions are a simple system much different than the bigger systems created in heavy ion collisions. Certainly the particle physicists do not share this point of view since we should not forget that even "simple" protons are made of many quarks and gluons. Thus, the physics behind elementary particle collisions may be far more complicated and thus can lead us to question the reference system ($p + p$ collisions). Especially, one may think about some physics effect like for example the phase-space constraints that affect small and big systems differently.

5

1.4 Why to study femtoscopy in $p + p$ collisions at RHIC?

Femtoscopic studies of mainly like-signed pions have a long tradition in elementary particle collisions (for review of the existing data see e.g. [18, 19, 20]). However the comparison of these results to a larger system, like $Au + Au$, was always problematic due to two main reasons. Firstly, different parameterizations of the Bose-Einstein correlations were used by various experiments, mostly within the particle physics community, what makes it impossible to perform an apple-to-apple comparisons with results from heavy ion collisions. Secondly, different analysis methods, the detector acceptance and the kinematic ranges of the particles of interest and even different definitions of quantities like the multiplicity made such a comparison very difficult if not feasible. The STAR experiment can overcome these difficulties since both $Au + Au$ and $p + p$ collisions can be studied at the same facility, using the same detector as well as the acceptance and even the same analysis technique and parameterizations of the femtoscopic correlations. All these advantages seriously reduce the systematic uncertainties when comparing small and big system.

1.5 In this thesis

In Chapter 3 we present brief overview of femtoscopy in heavy ion collisions, and we discuss the historical background and theoretical aspects of the two-particle intensity interferometry are discussed in Chapter 2. In Chapter 4 we present the formalism of the experimental correlation function and provide parameterizations of both femtoscopic and non-femtoscopic correlations. In the next chapter we present our new approach to study and present the 3D correlation function that is based on the spherical harmonic decomposition of the correlation function. In chapter 6

we present the formalism of how to account for the phase-space constraints due the the energy and momentum conservation in a single-particle distribution and multi-particle correlation function. We also demonstrate that most of the difference in the particle distribution between $p + p$ and $Au + Au$ collisions can be just due to the phase-space effect due to global conservation laws. We present the STAR detector in Chapter 7. As a part of this thesis, we performed original femtoscopic analysis for pions in $p + p$ and $d + Au$ collisions at $\sqrt{s_{NN}}$=200 GeV and $Au + Au$ collisions at $\sqrt{s_{NN}}$=19.6 GeV. Results of these studies are presented in Chapter 9. In the next chapter, we compare femtoscopic results from small systems with results from heavy ion collisions. Surprisingly, such a comparison reveals many similarities between small and big systems. In Chapter 11 we put the STAR results from $p + p$ collisions in the context of world systematics from elementary particle collisions. We present the study and the evidence of the radial flow in $p + p$ collisions in Chapter 12. Finally, we summarize in Chapter 13. This thesis includes material that has been already published in [21, 22, 20] and is the subject of future publications.

CHAPTER 2

THEORETICAL ASPECTS OF TWO-PARTICLE INTERFEROMETRY

2.1   Historical perspective

The enhancement of the probability of having two bosons close in phase-space is a consequence of Bose-Einstein symmetrization. In astronomy, this effect was first observed by Hunbary Brown and Twiss [23] who measured the angular size of stars using photon intensity interference.

The study of the intensity interferometry in particle physics started about 50 years ago when G. Goldhaber, S. Goldhaber, W. Lee and A. Pais studied angular distribution of pion pairs in reaction of the annihilation of proton-anti-proton [24]

$$\bar{p} + p \rightarrow \pi^+ + \pi^- + m\pi^0. \tag{2.1}$$

They showed that the probability of like-signed pions emitted at small relative angles were larger than for unlike-signed pions and it is due to Bose-Einstein effect. However, probably the most important breakthrough was done by Russian scientists Kopylov and Podgoretsky [25]. who introduced a new term *correlation function*, developed mathematical formalism and demonstrated that the symmetrization of the

wave function for identical pions provides information on the phase-space distribution of the emitted particles from the source. This issue is discussed in the next section.

2.2 Basics of Intensity Interferometry: Bose-Einstein statistics

Two identical pions are the most studied and understood system in two-particle interferometry. To show the nature of the Bose-Einstein effect we assume a system of two pions that are emitted from the source. Figure 2.1 shows a diagram of such situation. The first pion emitted from point $\mathbf{r_1}$ within the source Z has momentum
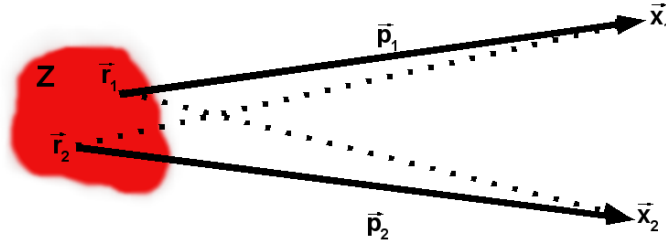
Figure 2.1: Diagram of two-particle correlations. Two particles are emitted from points $\mathbf{r_1}$ and $\mathbf{r_2}$ of the source Z with momentum $\mathbf{p_1}$ and $\mathbf{p_2}$.

$\mathbf{p_1}$. Analogously the second pion is emitted from $\mathbf{r_2}$ with $\mathbf{p_2}$. Then, the first pion is registered in point $\mathbf{x_1}$ and the second one in point $\mathbf{x_2}$. This case is represented by solid lines on Fig. 2.1. However, since it is not possible to distinguish these particles in detector it is possible that pion emitted with $\mathbf{p_1}$ is registered in point $\mathbf{x_2}$ and pion with $\mathbf{p_2}$ is registered in point $\mathbf{x_1}$. This case is shown by dotted lines on Fig. 2.1.

9

The amplitudes of these two cases add up, and the probability of observing two pions emitted from the source Z is proportional to the squared amplitude of the wave function of two pions

$$dP_{12} \sim \mid e^{i\mathbf{p_1}(\mathbf{x_1}-\mathbf{r_1})}e^{i\mathbf{p_2}(\mathbf{x_2}-\mathbf{r_2})} + e^{i\mathbf{p_1}(\mathbf{x_1}-\mathbf{r_2})}e^{i\mathbf{p_2}(\mathbf{x_2}-\mathbf{r_1})} \mid^2 dr_1 dr_2 \qquad (2.2)$$

Then, if we denote the source distribution of a single particle by $\rho(\mathbf{r})$ then the total probability can be expressed as

$$P_{12} \sim \int dP_{12}\rho(\mathbf{r_1})\rho(\mathbf{r_2}) = 1 + \mid \tilde{\rho}(\mathbf{q}) \mid^2, \qquad (2.3)$$

where $\mathbf{q} = \mathbf{p_1} - \mathbf{p_2}$ and $\tilde{\rho}(\mathbf{q})$ is the Fourier transformation of $\rho(\mathbf{r})$.

2.3 Theoretical correlation function

The probability expressed by Eq. 2.3 is called the correlation function denoted as C_2 (index 2 stands for the fact that we talk about two-particle correlations; the a three-particle correlation function is denoted C_3) in particle interferometry. The correlation function depends on $\mathbf{p_1}$ and $\mathbf{p_2}$ thus $\mathbf{q} = \mathbf{p_2} - \mathbf{p_1}$. If we decompose $\mathbf{q}$ into the relative three-momentum $\vec{q}$ and q_0 where $\vec{q} = \vec{p_2} - \vec{p_1}$ and $q_0 = |E_2 - E_1|$ then the equation on correlation function can be written as

$$C_2(\mathbf{p_1}, \mathbf{p_2}) = C_2(\mathbf{q}) = 1 + |\tilde{\rho}(\vec{q}, q_0)|^2. \qquad (2.4)$$

The interesting feature of this equation is that because the distribution $\rho(r)$ is normalized, $|\tilde{\rho}(\vec{q} = 0, q_0 = 0)|^2 = 1$, and the correlation function is equal to 2 when $q \to 0$.

From practical reasons [3] it is common to assume that the probability density of a single non-interacting particle has a Gaussian form and is given by

$$\rho(\vec{r}, t) = \frac{1}{\pi^2 R^3 \tau} e^{-\left(\frac{r}{R}\right)^2 - \left(\frac{t}{\tau}\right)^2},$$ (2.5)

where, $R(\tau)$ is the distribution of emission points. Then, if we put Eq. 2.5 into Eq. 2.4 we obtain the following formula for the correlation function

$$C_2(\vec{q}, q_0) = 1 + e^{-|\vec{q}|^2 R^2 - q_0^2 \tau^2}.$$ (2.6)

Figure 2.2 shows the correlation function expressed by Eq. 2.6 for two different values of R under assumption that $\tau = 0$.
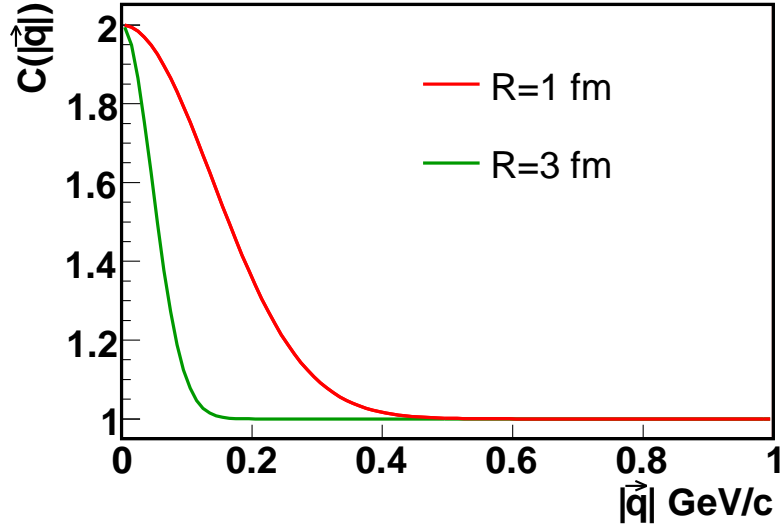
Figure 2.2: The correlation function (Eq. 2.6) for two values or $R = 1\ fm$ and $R = 3\ fm$ and $\tau = 0$.

---

[3]The correlation function is a Fourier transformation of the source distribution thus to get an analytical formula on the correlation function one needs to use the form of the source distribution that has an inverse Fourier transformation

CHAPTER 3

FEMTOSCOPY IN HEAVY ION COLLISIONS

As discussed in Chapter 1 the physics in heavy ion collisions at RHIC is believed to be driven by collective effect called flow. The hydrodynamic model calculations describe with a very good precision momentum observables in soft sector ($p_T < 2$ GeV/c) although they usually fail to reproduce the femtoscopic results as presented on Fig. 3.1. The failure of hydrodynamic models in describing the HBT results from heavy ion collisions is called the "HBT Puzzle" that has not been solved for a decade. Recently however, Pratt [27, 28] provided a possible explanation of this puzzle. In this chapter, we briefly review the femtoscopic results from heavy ion collisions focusing mainly on pion correlations and these results that we refer to further in this thesis. For detailed review of the femtoscopic program in heavy ion collisions see e.g. [26, 29, 30, 31, 32].

3.1 Transverse mass dependence

The negative correlation between the femtoscopic radii and the transverse mass of the particle pair is usually attributed to collective flow of a bulk system [9]. In a flow scenario, an approximately "universal" m_T dependence should apply to all particle types, not only pions. This is in fact observed in Figure 3.2, in which one-dimensional
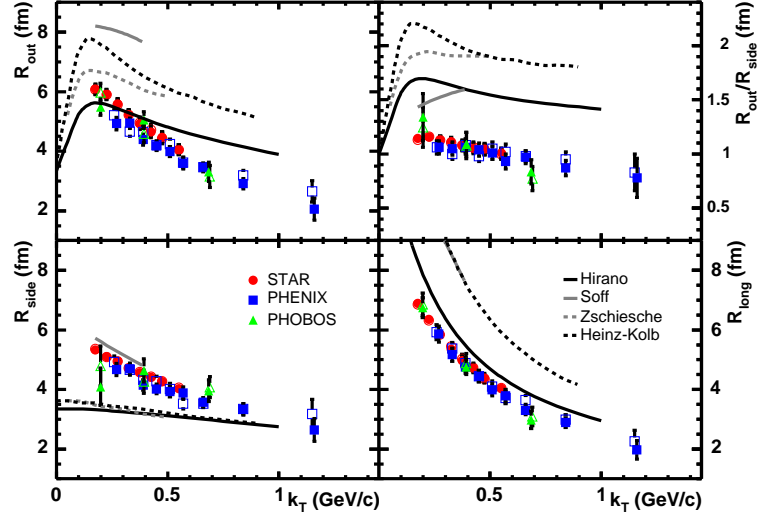
Figure 3.1: Hydrodynamic (Zschiesche, Hirano, Kolb) calculations in comparison to RHIC data from $Au + Au$ collisions at $\sqrt{s_{NN}}$=200 GeV. Open symbols represent data for (π^+, π^+) correlations and closed symbols for (π^-, π^-) correlations. Figure taken from [26].

radii from pion [34], charged kaon [34], neutral kaon [35], proton and anti-proton [36], and proton-Λ [37] correlations are plotted. Correlations between particles with very different masses also show characteristic signals of collective flow [38].

3.2   Multiplicity dependence

Figure 3.3 presents AGS/SPS/RHIC systematics of HBT radii dependence on $(dN_{ch}/d\eta)^{1/3}$ (N_{ch} - number of charged particles) for different colliding systems at different energies of the collisions. The main motivation for studying such a relation is its connection to the final state geometry through the particle density at freeze-out. As seen, all radii exhibit a scaling with $(dN_{ch}/d\eta)^{1/3}$. It is especially interesting that the radius parameters R_{side} and R_{long} follow the same curve for different collisions
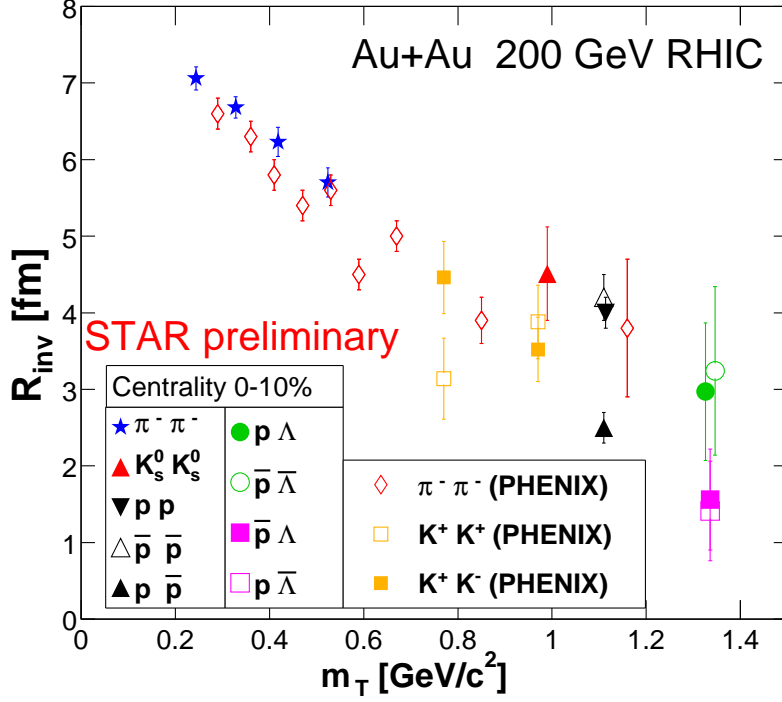
Figure 3.2: m_T dependence of R_{inv} for different particles. Figure taken from [33].

over a wide range of energies and given value of $< k_T >$. It is a clear signature that the multiplicity is a scaling variable that drives these geometrical radius parameters. R_{out} mixes space and time information. Therefore it is unclear whether to expect a simple scaling with the final state geometry.

3.3   Azimuthally sensitive HBT

With two particle intensity interferometry technique we can even measure the shape of the source at freeze-out by studying oscillations of the HBT radii with respect to the reaction plane. In a hydrodynamical picture these oscillations and in general the shape of the homogeneity region is driven by the elliptic flow [39, 30, 40].
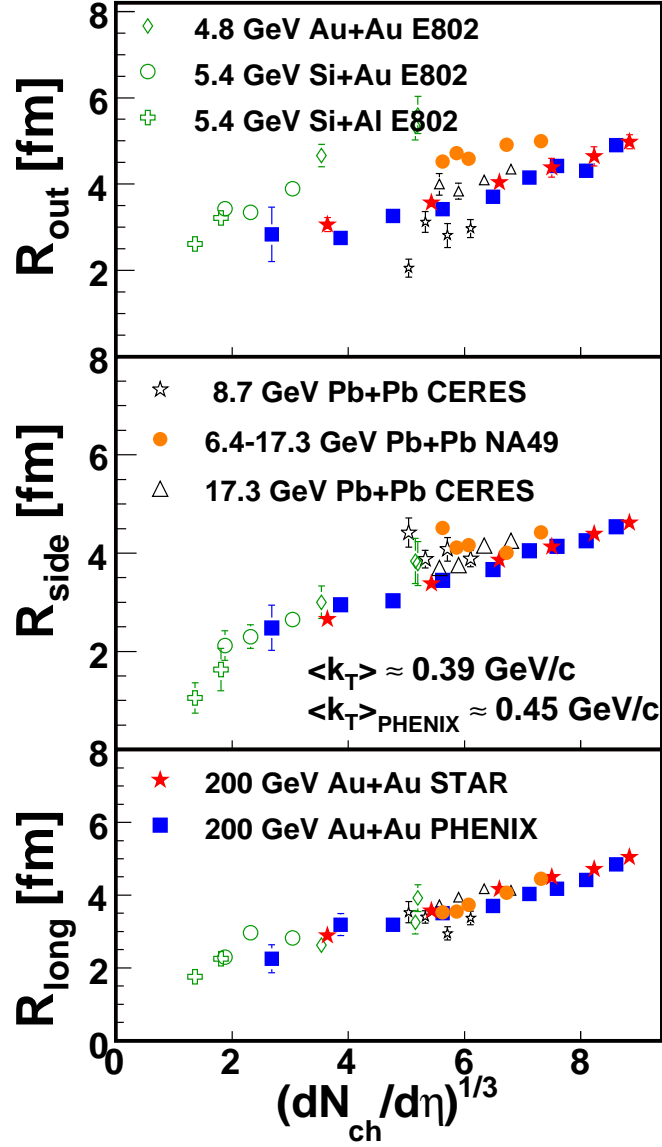
Figure 3.3: Femtoscopic radii dependence on the number of charged particle. Figure taken from [32].

Figure 3.4 shows the dependence of squared HBT radii on the reaction plane angle for three centrality classes from $Au + Au$ collisions at $\sqrt{s_{NN}}$=200 GeV at RHIC [42]. Clearly, the shape of the source depends on the reaction plane angle and the source is

15
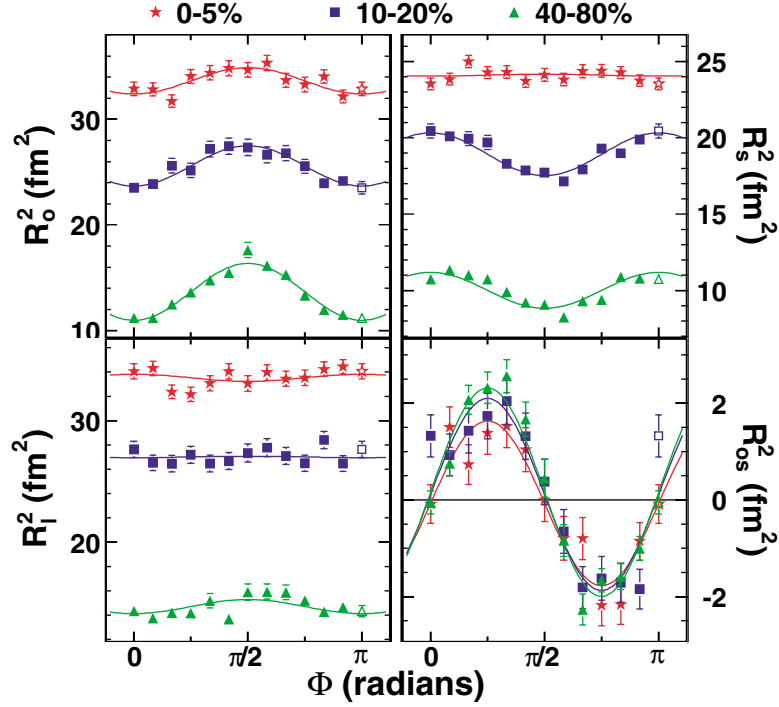
Figure 3.4: Squared HBT radii using radii relative to the reaction plane angle for three centrality classes from $Au + Au$ collisions at $\sqrt{s_{NN}}$=200 GeV. The solid lines show allowed [41] fits to the individual oscillations. Figure taken from [42].

out-of-plane extended. This result contradicts earlier predictions from hydrodynamical models that predicted the source at RHIC to be in-plane extended [43, 44, 45]. These results suggest that the time of the expansion is short enough so the expanding source does not recover from its initial out-plane geometry. For more information about azimuthally sensitive HBT see e.g. [26, 42] and references therein.

CHAPTER 4

EXPERIMENTAL CORRELATION FUNCTION

The correlation function is given by

$$C(p_1, p_2) = \frac{P(p_1, p_2)}{P(p_1)P(p_2)}, \tag{4.1}$$

where $P(p_1, p_2)$ is the probability of observing two particles with momenta p_1 and p_2, while $P(p_1)$ and $P(p_2)$ denote single-particle probabilities. Experimentally, the correlation function can be defined as

$$C(\vec{q}) = \frac{A(\vec{q})}{B(\vec{q})}, \tag{4.2}$$

where $\vec{q}$ is a difference between momenta of two particles. $A(\vec{q})$ represents a distribution of the pairs from the same event, and $B(\vec{q})$ is the reference (or "background") distribution. B represents all single-particle effects, including detector acceptance and efficiency, and is usually calculated with an event-mixing technique [46, 26].

In older or statistics-challenged experiments, the correlation function is sometimes constructed in the one-dimensional quantity $Q_{inv} \equiv \sqrt{(\vec{p_1} - \vec{p_2})^2 - (E_1 - E_2)^2}$. More commonly, it is constructed in three dimensions in the so-called the Pratt-Bertsch "out-side-long" coordinate system [9, 47]. In this system, the "out" direction is that of the pair transverse momentum, the "long" direction is parallel to the beam, and

17

the "side" direction is orthogonal to these two, as shown on Fig. 4.1. We will use the subscripts "o," "l" and "s" to indicate relative momentum or radius components in this system.
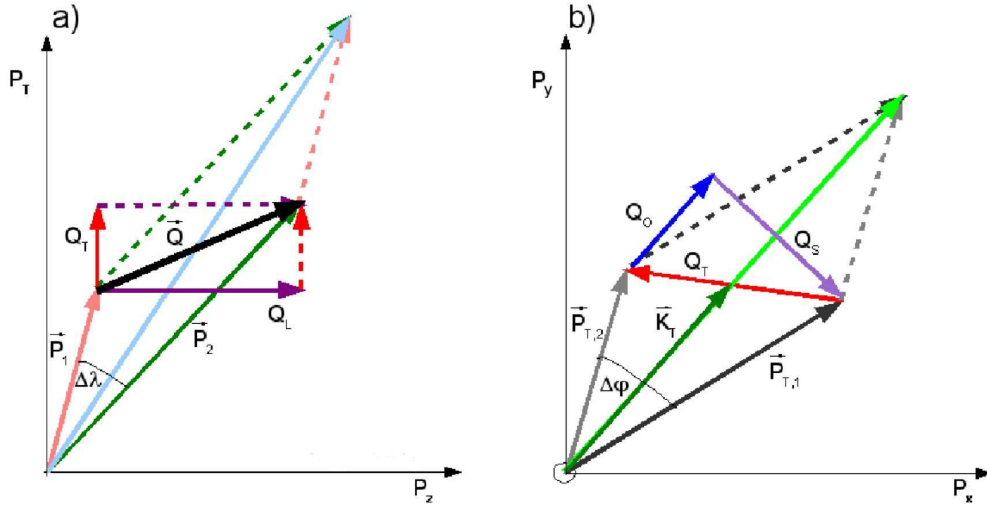
Figure 4.1: The decomposition of $\vec{q}$ in Pratt-Bertsch coordinates [9, 47].

It has been suggested by us and others [48, 49, 21] to construct the correlation function using spherical coordinates

$$q_o = |\vec{q}| \sin\theta \cos\phi, \qquad q_s = |\vec{q}| \sin\theta \sin\phi, \qquad q_l = |\vec{q}| \cos\theta. \qquad (4.3)$$

This aids in making a direct comparison to the spatial separation distribution through imaging techniques, and provides an efficient way to visualize the full three-dimensional structure of the correlations. Below, we will present data in the form of the Spherical Harmonic Decomposition coefficients, which depend explicitly on $|\vec{q}|$ as

$$A_{l,m}(Q) \equiv \frac{1}{\sqrt{4\pi}} \int d\phi \, d(\cos\theta) C\left(|\vec{q}|, \theta, \phi\right) Y_{l,m}\left(\theta, \phi\right). \qquad (4.4)$$

18

The spherical harmonic decomposition of the correlation function is discussed in more detail in Chapter 5 and Appendix F.

In heavy ion collisions, it is usually assumed that all of the correlations at low relative momentum are due to femtoscopic effects, i.e. quantum statistics and final-state interactions. At large $|\vec{q}|$ the femtoscopic effects have to vanish [26], so that, in the absence of other correlations, $C(\vec{q})$ must approach a constant value independent of the magnitude and direction of $\vec{q}$, and $A_{l,m}(|\vec{q}| \rightarrow \infty) = 0$ for $l \neq 0$.

However, it was experimentally observed [50, 51, 52, 53, 54, 20] that the correlation functions from elementary particle collisions have additional structure, clearly seen at large $\vec{q}$, that cannot be femtoscopic in origin. Usually this structure is parameterized in terms of a function $\Omega(\vec{q})$ that contributes in addition to the femtoscopic component $C_F(\vec{q})$.

$$C(\vec{q}) = C_F(\vec{q}) \cdot \Omega(\vec{q}). \tag{4.5}$$

Below, we discuss separately parameterizations of the femtoscopic and non-femtoscopic components.

4.1 Femtoscopic correlations

Femtoscopic correlations between identical pions are dominated by Bose-Einstein correlations and Coulomb final state effects.

In all parameterizations, the overall strength of the femtoscopic correlation is characterized by a parameter λ (e.g. [26]). Historically misnamed the "chaoticity" parameter, it generally accounts for particle identification efficiency, long-lived decays, and long-range tails in the separation distribution. We do not discuss it further.

In the simplest case, the Bose-Einstein correlations are often parameterized by a Gaussian,

$$C_F(Q_{inv}) = 1 + \lambda e^{-Q_{inv}^2 R_{inv}^2}, \tag{4.6}$$

where R_{inv} is a one dimensional "HBT radius."

Another historical parameterization uses the energy difference and the magnitude of the vector momentum difference in the laboratory frame:

$$C_F(q, q_0) = 1 + \lambda e^{-q^2 R_G^2 - q_0^2 \tau^2}, \tag{4.7}$$

where $q_0 = E_1 - E_2$ and $q = |p_1 - p_2|$. R_G and τ are the source size and lifetime.

Kopylov and Podgoretskii [25] introduced an alternative parameterization

$$C_F(q_T, q_0) = 1 + \lambda \left[\frac{2J_1(q_T R_B)}{q_T R_B} \right]^2 \left(1 + q_0^2 \tau^2 \right)^{-1}, \tag{4.8}$$

where q_T is the transverse component of $\vec{q} = \vec{p_1} - \vec{p_2}$ with respect to $\vec{p} = \vec{p_1} + \vec{p_2}$, $q_0 = E_1 - E_2$, R_B and τ are the size and decay constants of a spherical emitting source, and J_1 is the first order Bessel function.

Simple numerical studies show that R_G from Eq. 4.7 is approximately twice smaller than R_B obtained from Eq. 4.8 (e.g. [55, 56]).

The correlation function may be also analysed in 3D and then it can be constructed as a function of the three components of the pair relative momentum in the Pratt-Bertsch discussed above. If we choose the reference frame to be the longitudinally co-moving system (LCMS) of the pair, at midrapidity and integrating over the first and the second order reaction plane then the formula on the correlation function due to Bose-Einstein effect is

$$C_F(q_o, q_s, q_l) = 1 + \lambda e^{-q_o^2 R_o^2 - q_s^2 R_s^2 - q_l^2 R_l^2}, \tag{4.9}$$

20

where, $\vec{q} = (q_o, q_s, q_l)$ is defined in the longitudinally co-moving frame, q_l is the component parallel to the beam axis or trust axis (in $e^+ + e^-$), q_o is measured in transverse plane and points into the direction of outgoing pair and q_s is perpendicular to other two components. Analogously, the sizes of the source along these three directions are denoted as R_o, R_s and R_l.

Another femtoscopic effect that affects the correlation function at low $|\vec{q}|$ and should take into account is the Coulomb interaction. In this thesis, we will use Bowler-Sinyukov procedure [57, 58] to include Coulomb effect in the parameterization of the correlation function that has the following formula in 1D

$$C_F(Q_{inv}) = (1 + \lambda) + \lambda K_{coul}\left(Q_{inv}\right)\left(1 + e^{-Q_{inv}^2 R_{inv}^2}\right), \qquad (4.10)$$

and in 3D,

$$
\begin{aligned}
C_F(q_o, q_s, q_l) &= (1 - \lambda) + \lambda K_{coul}\left(Q_{inv}\right) \\
&\times \left(1 + e^{-q_o^2 R_o^2 - q_s^2 R_s^2 - q_l^2 R_l^2}\right).
\end{aligned} \qquad (4.11)
$$

4.2   Non-femtoscopic correlations

In the absence of non-femtoscopic correlations, one of the forms for $C_F(\vec{q})$ from Section 4.1 is fitted to the measured correlation function; i.e. $\Omega = 1$ in Equation 6.2. Such a "standard fit" works well in the high-multiplicity environment of heavy ion collisions [26]. In hadron-hadron or $e + e$ collisions, however, it does not describe the measured correlation function well, especially as $|q|$ increases. While this large-$|q|$ behavior is sometimes simply ignored, it is usually included in the fit either through ad-hoc [51] or physically-motivated [21] formula.

In this thesis, we will use three selected parameterizations of the non-femtoscopic correlations and study their effects on the femtoscopic parameters obtained from

the fit to experimental correlation functions. The first formula assumes that the nonfemtocopic correlations can be parameterized by the first order polynomial in q-components (used e.g. in [59, 60, 61, 62, 63]), so it has the following form in 1D

$$\Omega(q) = 1 + \delta q, \tag{4.12}$$

and in 3D

$$\Omega(\vec{q}) = \Omega(q_o, q_s, q_l) = 1 + \delta_o q_o + \delta_s q_s + \delta_l q_l. \tag{4.13}$$

For simplicity, we will use the name "$\delta - q$ fit" when the above formula was used in the fitting procedure.

Another form assumes that non-femtoscopic correlations contribute only to the two higher moments of the spherical harmonic decomposition of the correlation function [33] and their magnitude is independent of $\vec{q}$. Then, it can be expressed as

$$\Omega(|\vec{q}|, \cos\theta, \phi) = \Omega(\cos\theta, \phi) = 1 +$$
$$\beta\sqrt{\frac{5}{4}}(3\cos^2\theta - 1) + \zeta\sqrt{\frac{15}{2}}\sin^2\theta\cos 2\phi. \tag{4.14}$$

The fit that uses this formula to parameterize the non-femtoscopic correlations together with femtoscopic ones is called "$\zeta - \beta$ fit" further in this thesis.

These two forms (as well as few other ones that can be found in literature) [20] are motivated primarily by the shape of the measured correlation function. The dangers of such an ad-hoc approach have been discussed, and a physics-motivated form for the non-femtoscopic correlations has been formulated in [21]. This formula accounts for the restricted phase-space available to a system with a finite number of particles and constrained by energy and momentum conservation. This N-body correlation

22

must be present in any case, and is projected onto the two-particle space as

$$\Omega\left(p_1, p_2\right) = 1 - M_1 \cdot \overline{\{\vec{p}_{1,T} \cdot \vec{p}_{2,T}\}} - M_2 \cdot \overline{\{p_{1,z} \cdot p_{2,z}\}} \tag{4.15}$$
$$- M_3 \cdot \overline{\{E_1 \cdot E_2\}} + M_4 \cdot \overline{\{E_1 + E_2\}} - \frac{M_4^2}{M_3},$$

where

$$
\begin{aligned}
M_1 &\equiv \frac{2}{N\langle p_T^2 \rangle}, & M_2 &\equiv \frac{1}{N\langle p_z^2 \rangle} \\
M_3 &\equiv \frac{1}{N\left(\langle E^2 \rangle - \langle E \rangle^2\right)}, & M_4 &\equiv \frac{\langle E \rangle}{N\left(\langle E^2 \rangle - \langle E \rangle^2\right)}.
\end{aligned}
\tag{4.16}
$$

The notation $\overline{\{X\}}$ in Equation 4.15 is used to indicate that X is a two-particle quantity which depends on p_1 and p_2 (or $\vec{q}$, etc). In practice, this means generating histograms in addition to $A\left(\vec{q}\right)$ and $B\left(\vec{q}\right)$ (c.f. Equation 4.2) as pairs are formed. For example

$$\overline{\{\vec{p}_{1,T} \cdot \vec{p}_{2,T}\}}\left(\vec{q}\right) = \frac{\sum_{i,j} \vec{p}_{i,T} \cdot \vec{p}_{i,T}}{B\left(\vec{q}\right)}, \tag{4.17}$$

where the sum in the numerator runs over all pairs in all events.

There are four fit parameters in Eq. 4.15, $M_1 - M_4$ that are directly related to five physical quantities, (N - the number of particles, $\langle p_T^2 \rangle, \langle p_z^2 \rangle, \langle E^2 \rangle, \langle E \rangle$) through Eq. 4.16. If we assume that

$$\langle E^2 \rangle \approx \langle p_T^2 \rangle + \langle p_z^2 \rangle + m_*^2, \tag{4.18}$$

where m_* is the mass of a typical particle in the system (for our pion-dominated system, $m_* \approx m_\pi$), then we can express each physical parameters in terms of $M_1 - M_4$, e.g.

$$N \approx \frac{M_1^{-1} + M_2^{-1} - M_3^{-1}}{\left(\frac{M_4}{M_3}\right)^2 - m_*^2}. \tag{4.19}$$

23

In [21], the correlations leading to Equation 4.15 were called "EMCICs" (short for Energy and Momentum Conservation-Induced Correlations); we will refer to fits using this function with this acronym, in our figures.

The effect of using different non-femtoscopic formulas on the femtoscopic radii is presented in Sections 9.1 and 9.2.

4.3   Reference distribution

In Section 4 we defined the experimental correlation function and presented commonly used parameterizations that are being fit to extract the femtoscopic sizes. Here, we will discuss the methods of constructing the reference sample of the experimental correlation function ($B(Q)$ from Eq. 4.2).

4.3.1   Monte-Carlo Simulations

Some experiments used Monte-Carlo generated pairs to construct the background [54]. There are few difficulties when using this method. One requirement that is often hard to fulfill is that Monte-Carlo simulations should reproduce all physics effects seen in the data expect for femtoscopic correlations. That means that the at least single particle spectra, particle ratios and multiplicities produced by the event generator should be in a very good agreement in experimental results. Additionally, the experimental conditions like acceptance effects have to be imposed on the Monte-Carlo results. Only then it is justified to use Monte-Carlo simulations to construct the background of the correlation functions.

Another approach, also using Monte-Carlo simulations is to normalized the correlation function expressed by Eq. 4.2 with the ratio of the distributions for like- to unlike-signed pairs obtained from a Monte-Carlo [64].

4.3.2 Unlike-signed pairs

Another method is to use the distribution of unlike-signed pairs coming from the same events as the background [63]. The motivation behind this approach is that the distribution of non-identical pion pairs should include all physics effects as for identical pions expect for quantum interference. There is one major obstacle in this approach that is an effect of resonance production on non-identical pion correlations. While even if pions coming from resonance decays are misidentified as primary pions they do not change the strength of the correlation effect for identical pions only the chaoticity parameter (λ in Eqs.4.6) they can influence the shape of the correlation functions for non-identical pions in a non-trivial way [21]. The procedure of removing resonance peaks from the range of Q in a fit is not always simple and introduces an additional systematic error to the extracted results.

The above two methods are the most common in the field of elementary particle collisions and experiments often use both of them.

4.3.3 Swapping the momentum of one particle in a pair

Less common technique to form a background is to use the particles as to obtained the signal but when pairs are created the momentum of a one particle is flipped [65]. Such method can be used only by experiments having symmetric detectors and the main problem is that even in such cases the acceptance is not always fully symmetric because of common technical problems with detectors themselves when a part of the detector is either off or not functioning correctly. To be more specific, a non-symmetric hole in the acceptance will influence the real pair distribution and the background distribution obtained with this method in different way so its effect will not cancel

out while the correlation function should be insensitive to the acceptance effects since they should be identical in both distributions. Some experiments used this method or similar ones like swapping or reversing some of the momentum components [50, 63] in the background distribution.

CHAPTER 5

SPHERICAL HARMONIC DECOMPOSITION OF
CORRELATION FUNCTIONS

In this chapter, we will discuss a new method of representing the 3D correlation function and we will use the commonly used Pratt-Bertsch ("out-side-long") decomposition of the relative momentum $\vec{q}$ [66, 47], where q_l is parallel to the beam direction, q_o is parallel to the transverse total momentum of the pair, and q_s is perpendicular to those.

5.1 Motivation

Usually the 3-D correlation functions are presented as 1-D Cartesian projections along each axis (e.g. q_l) while the other q-components are kept small to keep the strength of the signal. Commonly, non-projected q-components are integrated approximately over the half width of the femtoscopic effect (e.g. the upper threshold is ≈ 0.03 GeV/c in $Au + Au$ collisions and ≈ 0.12 GeV/c in $p + p$). An example of such projections of the correlation function from $Au + Au$ collisions at $\sqrt{s_{NN}}$=200 GeV is shown on Fig. 5.1.

Such 1-D projections of the correlation function obtained from the GENBOD event generator (described in details in Sec. 6.1) are presented on Figure 5.2. As mentioned
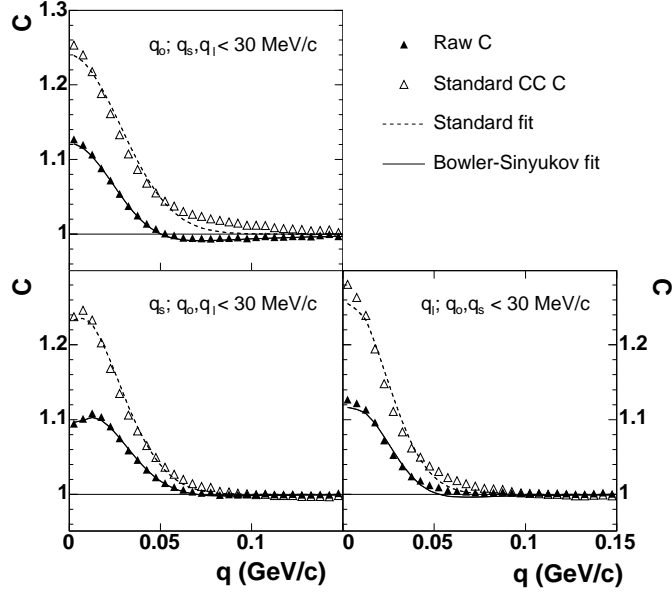
Figure 5.1: 1D projections of 3D correlation function from $[0\text{-}5]\%$ $Au + Au$ collisions at $\sqrt{s_{NN}}$=200 GeV. Figure taken from [67]

in Sec. 4.1, femtoscopic contributions to the the correlation function (those described by the Koonin-Pratt equation and discussed in [26]) must approach a constant value at asymptotically high relative momentum $|\vec{q}|$, usually normalized to unity, independent of the direction of $\vec{q}$. Naturally there are no femtoscopic correlations in our simulations. Thus, the correlations seen in Fig. 5.2 must be induced by the global conservation laws and are signaled by the non-unity value of the correlation function. As noticed, the correlation function does not only depend on the magnitude of $|\vec{q}|$ but also on the direction of $\vec{q}$.

However, one-dimensional projections represent only a part of the 3D correlation function. Thus, they are a poor tool for exploring its detailed and potentially important structure. In principle, to visualize the full structure of the correlation

28
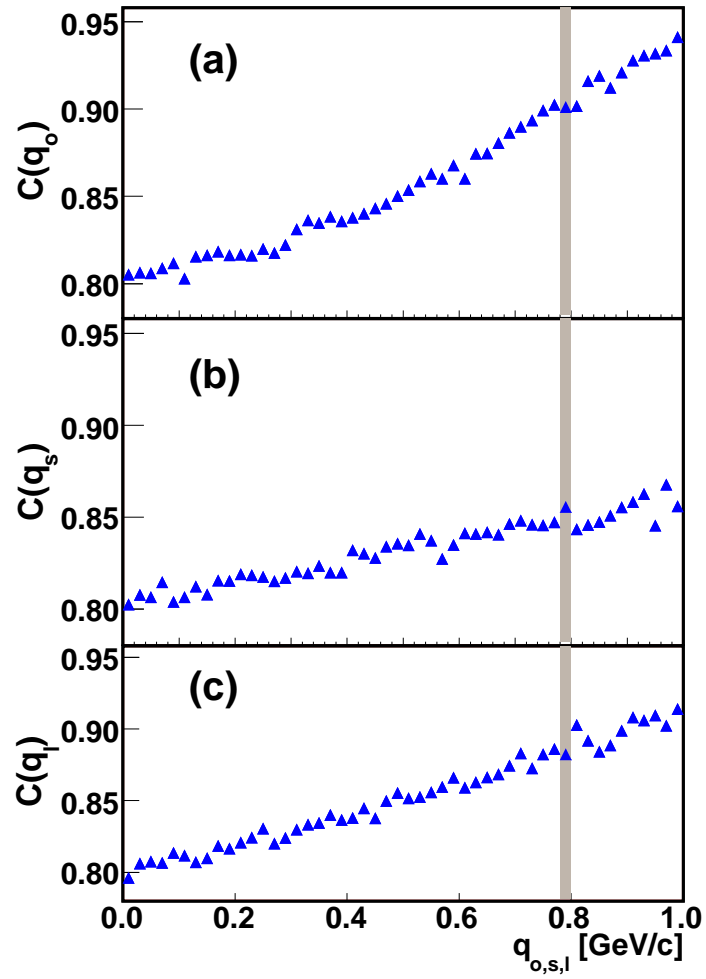
Figure 5.2: 1D projections of 3D correlation function calculated in LCMS frame for multiplicity-9 event calculated by GENBOD .

function one could plot a *series* of Cartesian projections in q_i over different ranges in $q_{j,k}$, where $i \neq j \neq k$. However, it would lead to a large number of figures, and the relevant patterns which cut across projections might not be well observed.

5.2 Formalism

By exploiting symmetries in $\vec{q}$-space, c.f. Appendix F, the spherical harmonic decomposition

(SHD) [4] [21] becomes a much more efficient representation which uses *all* of the data to show the shape of the correlation function. The spherical coordinates θ, ϕ, and $Q = |\vec{q}|$ relate to the Cartesian ones as

$$q_o = Q \sin\theta \cos\phi, \qquad q_s = Q \sin\theta \sin\phi, \qquad q_l = Q \cos\theta, \tag{5.1}$$

and we define harmonic moments $A_{l,m}$'s as

$$A_{l,m}(Q) \equiv \frac{1}{\sqrt{4\pi}} \int d\phi d(\cos\theta) C(Q,\theta,\phi) Y_{l,m}(\theta,\phi) \tag{5.2}$$

Naturally,

$$C(Q,\theta,\phi) \equiv \sqrt{4\pi} \left(\sum_{l=0}^{m} \sum_{m=-l}^{l} A_{l,m}(Q) Y_{l,m}^*(\theta,\phi) \right) \tag{5.3}$$

Since the experimental correlation functions are not continuous functions of Q, $\cos\theta$ and ϕ, but are constructed with bins of finite size, the Equation 5.2 needs some modification to account for finite-bin-size effects. In Appendix G we derive these corrections that have nice analytical forms only if we assume that the angular frequencies above Nyquist limit are negligible. Clearly it is not always an realistic assumption, however, numerical studies show that it works very well even if one takes into account the angular dependence of the correlation function. An alternative way of getting $A_{l,m}$'s components is simply to fit the correlation function using Eq. 5.3. This method is especially useful if the correlation function has some "empty" bins,

---

[4]Danielewicz and Pratt have studied a similar decomposition of the correlation function in terms of Cartesian Harmonics [48, 49].

e.g. due to the acceptance. Another method that calculates $A_{l,m}$ components directly from the correlation function has been proposed recently [68]. However, it requires much more computational power than the previous two methods and at the end gives almost identical results as e.g. the fit even in the presence of holes in the correlation function e.g. due to limited acceptance. From now on, we will assume these binning effects have been dealt with; i.e. we assume negligible bin size in $\cos\theta$ and ϕ.

5.3   Application of the method

In general, the correlation function may be decomposed into infinite number of $A_{l,m}$'s components. However, in reality symmetry constrains the number of relevant components. For femtoscopic analyses of identical particles at midrapidity which integrate over reaction-plane orientation (i.e. almost all analyses to date), only real parts of $A_{l,m}$'s with even values of l and m do not vanish. For the complete list of symmetries of $A_{l,m}$'s, see Appendix F. Further, it is natural to expect that the statistical relevance of high-l components is diminished.

As an example, Fig. 5.3 shows the calculated correlation function (the same as shown in Fig. 5.2) for one value of Q as a function of $\cos\theta$ and ϕ. Also shown are curves representing SHD with increasingly higher order components. In particular, the curves correspond to

$$
\begin{aligned}
C_{L,M}(Q,\theta,\phi) \;\equiv\; \sqrt{4\pi} \left(\sum_{l=0}^{L-2} \sum_{m=-l}^{l} A_{l,m}(Q) Y_{l,m}^{*}(\theta,\phi) \right. \\
\left. + \sum_{m=-M}^{M} A_{L,m}(Q) Y_{L,m}^{*}(\theta,\phi) \right).
\end{aligned}
\tag{5.4}
$$

For example, the curve labeled as "L=2 M=0" contains $A_{0,0}$ (the constant term) and $A_{2,0}$ components.

31
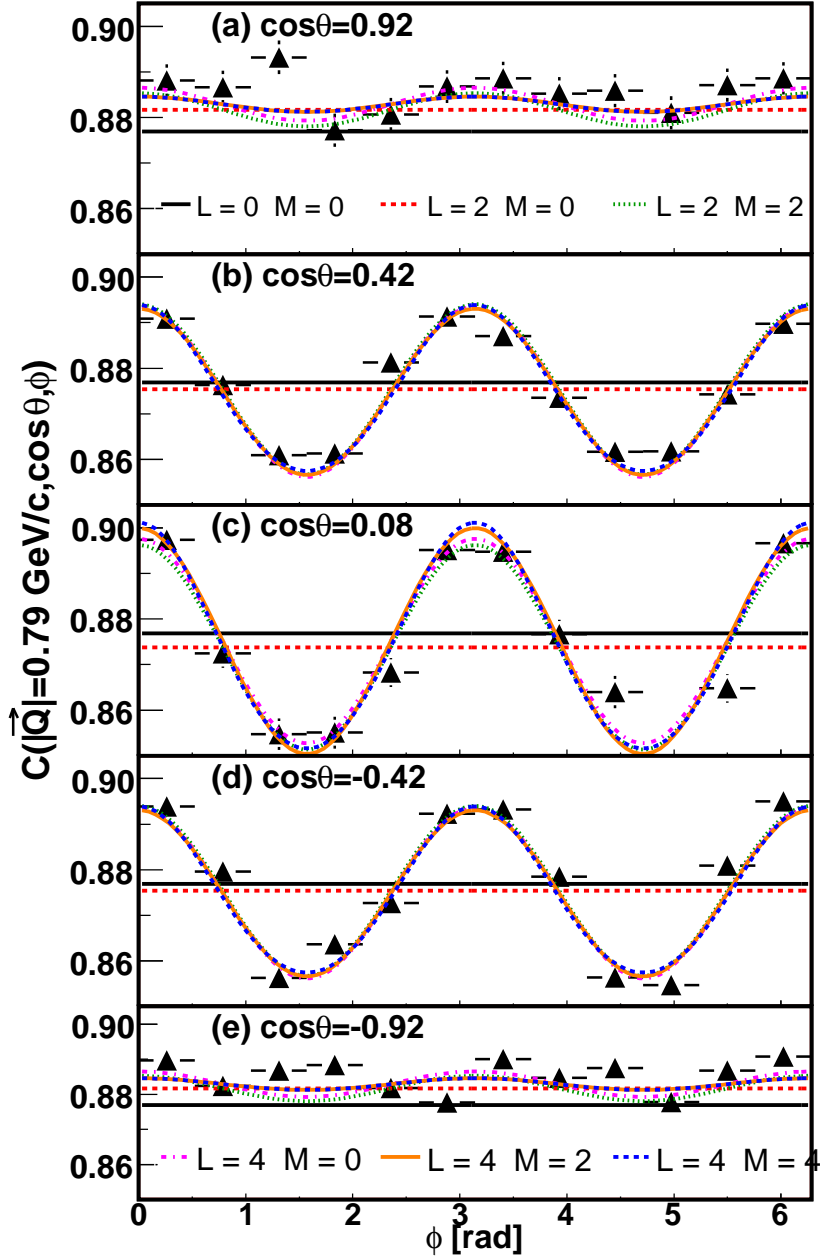
Figure 5.3: Correlation function for the same data presented in Fig. 5.2 is shown at a fixed value of $Q = 0.79 \; GeV/c$ (approximately indicated by the shaded region in Fig. 5.2) as a function of ϕ for five bins in $\cos(\theta)$. Curves represent the SHD components of various orders; see text for more details.
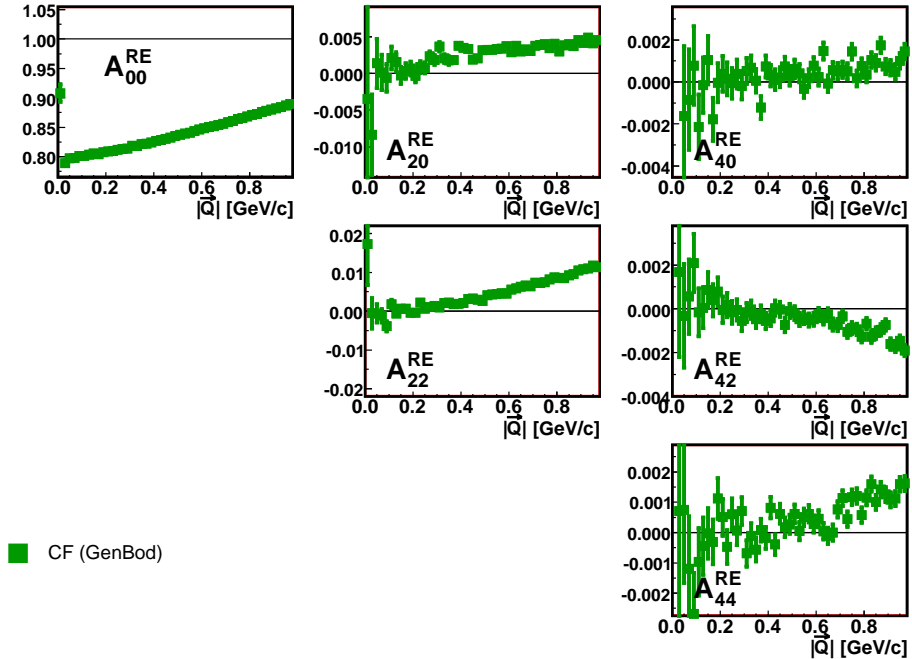
Figure 5.4: SHD coefficients for GENBOD -generated events consisting of 9 pions having average kinetic energy per particle $\bar{K} = 0.9$ GeV, as measured in the pair LCMS frame. No kinematic cuts were applied to data. Green squares are $A_{l,m}$'s from the GENBOD events.

Clearly, for this example, only the first few components are required to represent the structure of the correlation function. While a few higher-l terms may be required in some cases, the number of relevant $A_{l,m}$'s is generically expected to be small. This is from general considerations of smoothness and, for experimental data, statistical issues. Thus, by glancing at only a *few one-dimensional plots*, one views the *entire* correlation structure in three dimensions.

As an example, the first few $A_{l,m}$'s for the same GENBOD calculations presented in this section, are plotted as a function of Q in Fig. 5.4. The odd-l and -m moments (not shown) vanish as required by symmetry (c.f. Appendix F).

33

5.4 Simple study of the HBT signal in spherical harmonic representation

A good way to get more accustomed with the spherical harmonic representation of the correlation function is to perform some simple studies. Figure 5.5 shows the first six non-vanishing moments of the spherical harmonic decomposition of the correlation function in the presence of the Bose-Einstein effect. To do this study we constructed a correlation function according to the following equation

$$C(q_o, q_s, q_l) = 1 + \lambda e^{-q_o^2 R_o^2 - q_s^2 R_s^2 - q_l^2 R_l^2} \tag{5.5}$$

for a few values of R_o, R_s and R_l. Clearly, just by observing each $A_{l,m}(Q)$ distribution we can learn few things about the correlation function. For example, $A_{2,2}$ moment provides us information about the asymmetry between R_o and R_s. Then, if $R_o = R_s$ then $A_{2,2} = 0$, and if $R_o > R_s$ then $A_{2,2}$ is negative for low values of $|\vec{q}|$. Similarly, $A_{2,0}$ is sensitive to dependence between R_l and R_T.
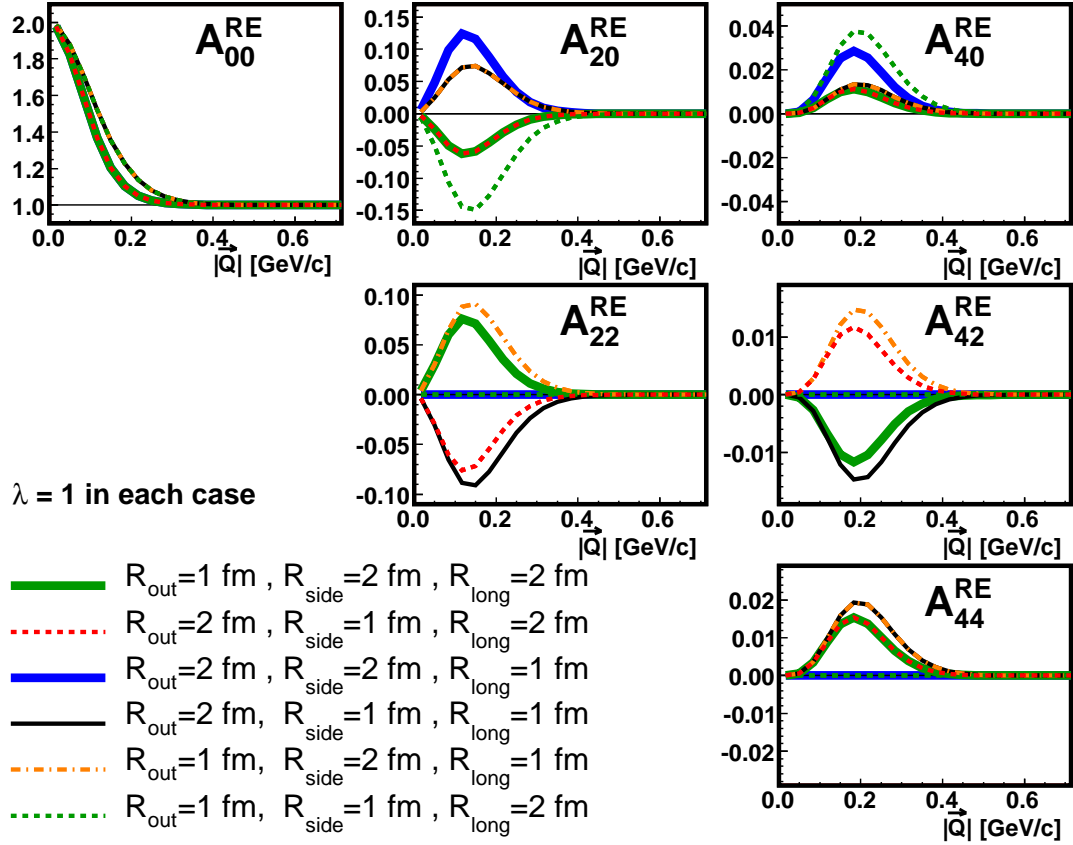
Figure 5.5: Spherical harmonic coefficients $A_{l,m}(Q)$ corresponding to a purely Gaussian correlation function with various HBT radii.

CHAPTER 6

PHASE-SPACE CONSTRAINTS DUE TO ENERGY AND MOMENTUM CONSERVATION

We present calculations of the effect of phase-space constraints due the energy and momentum conservation on k-particle distribution ($k = 1, 2, ...$) and m-particle correlation function ($m = 2, 3, ..$). We are going to use the acronym "EMCICs" when talking about this effect; it stands for the Energy and Momentum Conservation Induced Correlations/Corrections [5].

Most of the material presented in this chapter was published in [21, 22].

6.1 GENBOD - Monte-Carlo calculations of events with energy and momentum conservation

As a first step to understanding the role of conservation laws on various observables we would like to study events in which energy and momentum are conserved and there is no other physics involved. Luckily, the Monte-Carlo event generator called GENBOD (part of the CERN Library) has been developed over 40 years ago that meets our criteria. For a write-up on the physics and the method used to generate events see [69]. A user has to specify the number of particles per event (N), a list

---

[5] *corrections* when talking about a single particle distribution and *correlations* when talking about a multiparticle distribution or a correlation function

of their masses (m_i), and a total amount of energy (E_{tot}) to distribute among them as an input to the generator. As an output, GENBOD returns an event of random momenta (four-vectors p_j) isotropically distributed under only one condition that is the energy and momentum conservation. Additionally, it returns for each event a weight proportional to the probability that the event could appear in nature. This feature makes GENBOD different from other Monte-Carlo models like RQMD [70], UrQMD [71] and PYTHIA [72] in which each event returned is treated with equal probability.
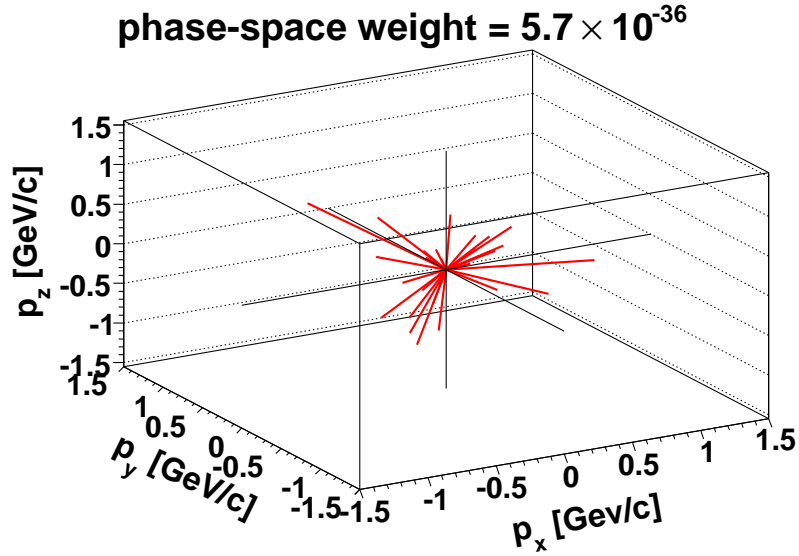
Figure 6.1: A high-probability multiplicity-30 event calculated by GENBOD . Lines correspond to particle momenta p_x, p_y, p_z.

This weight is based on the phase-space integral R_N [73]

$$R_N = \int^{4N} \delta^4 \left(P - \sum_{j=1}^{N} p_j \right) \prod_{i=1}^{N} \delta \left(p_i^2 - m_i^2 \right) d^4 p_i,$$

(6.1)

37

phase-space weight = 3.8×10^{-44}
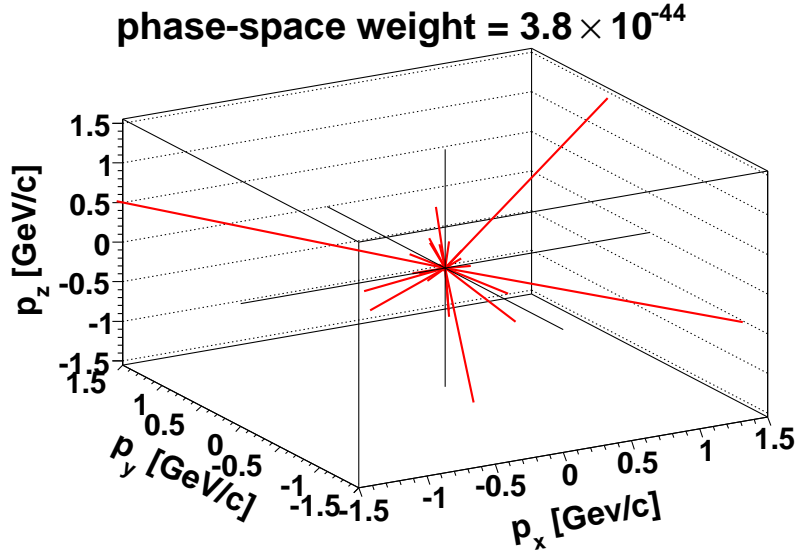
Figure 6.2: A low-probability multiplicity-30 event calculated by GENBOD . Lines correspond to particle momenta p_x, p_y, p_z.

where $P = \left(E_{\text{tot}}, \vec{0} \right)$ is the total momentum four-vector of the event. R_N figures dominantly in Fermi's statistical theory [74], in which the probability of having N particles in the final state is expressed by

$$P_N \sim \bar{S}_N \cdot R_N, \tag{6.2}$$

where, $\bar{S}_N$ is the phase-space-averaged S-function (or matrix element) associated with the process generating the final state and R_N is given by Eq. 6.1. Most of the time the goal is to study $\bar{S}_N$ since the phase-space effect is usually considered to be "trivial", however, we will demonstrate that it needs a lot of attention to be correctly taken into account.

In the calculations in this Chapter, we are going to assume that the momentum distribution is dominated by phase-space restrictions alone and the "dynamics" - $\bar{S}$ is a constant. This is the scenario simulated by GENBOD . Then, the spectrum

of a quantity α (say, an angle or transverse momentum) is given by the following formula [74, 73, 69]

$$f(\alpha) = \frac{d}{d\alpha} R_N. \tag{6.3}$$

For example, if α represents the ensemble of all momenta constituting a given event, Equation 6.3 gives the event phase-space weight. For more details on how to calculate R_N using a Monte-Carlo technique see [69].

In this thesis we mainly focus on pion-only events, mostly for simplicity. However, we have also studied events composed of several species of particles (e.g. kaons, protons), c.f. Section 6.6; in these cases the main conclusions of this thesis do not change. In the GENBOD calculations discussed further, we vary the event multiplicity (N) and the average kinetic energy per particle ($\bar{K}$), i.e. $E_{tot} = N(m_\pi + \bar{K})$.

In our studies, we select GENBOD events (according to the Monte-Carlo sampling of the distribution of event weights) and we analyze these events using the same software as we use to study experimental data, as presented e.g. in Sections 9.1 and 9.2. The huge advantage of this tool is its speed since we have to calculate large statistics of simulated events to perform different types of analysis. On average, we generated about 40 millions of events per analysis. We demand such a high statistics because the phase-space weights vary by large factors. Very extreme cases are presented on Figs. 6.1 and 6.2 that show a likely and unlikely event, respectively, for multiplicity $N = 30$. As one would expect, the "rounder" event is more likely, though one might be surprised by the fact that the first event (Fig. 6.1) is a hundred million times more likely than the second one (Fig. 6.2).

Figure 6.3 shows pion spectrum from GENBOD events having the same average energy per particle ($\langle E \rangle_c = 1\ GeV$) but different multiplicities. Clearly, the shape
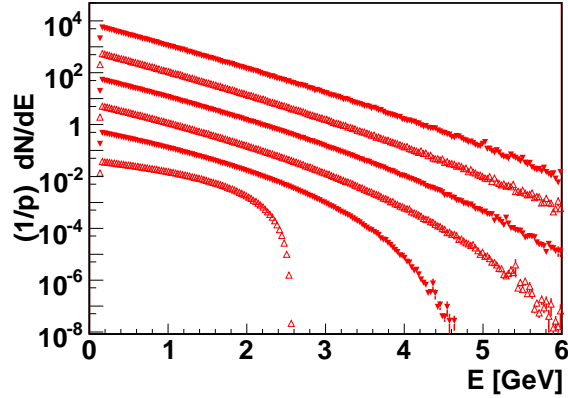
Figure 6.3: Pion spectrum obtained from GENBOD events run for the same average energy ($\langle E \rangle_c = 1 \ GeV$) but different multiplicities: $N = 5, 10, 15, 20, 30, 40$ pions.

of the spectra depends strongly on the total number of particles. In Section 6.5 we present simulations of EMCIC effect on two-particle correlations using GENBOD event generator.

6.2 Analytic calculation of EMCIC effects

We could potentially use GENBOD to generate EMCIC effects and "subtract" them from experimental data. However, there are several obstacles with this approach:

- there is a strong dependence of EMCIC effect on the total number of particles (see e.g. Fig. 6.3); thus to use GENBOD events to "correct" experimental data we should use the same number of particles as is emitted in real collisions. The problem is that we cannot measure all particles in a real experiment, like neutrinos and even less exotically, particles that are not registered by detectors due due to their finite acceptance

- there is strong sensitivity of EMCIC effects to the energy available for GEN-BOD events. It is far from obvious whether we should use the total energy of the collisions especially that usually not the entire energy is being used to produces particles (peripheral collisions)

- we never perfectly know the parent distribution and it is a crucial information when calculating any single-particle distributions using any type of models

- even though it is well known that the correlation functions are insensitive to the single-particle distributions, the correlations which they measure are, in fact, dependent of the phase-space to the physics effects. Since the EMCIC effects depend on the momentum of $\vec{p}_1$ and $\vec{p}_2$ of the particles entering the correlation function, the correlation functions themselves depend on the efficiency, acceptance and even kinematic cuts.

Therefore, we would like to use GENBOD simulations for qualitative studies of EMCICs but to estimate the effect of the phase-space distortion due to the energy and momentum conservations, we would like to use the experimental data itself. To do that, we want to calculate the EMCIC effect analytically and apply our formalism to data to estimate EMCIC effects. In this Section, we begin by following arguments similar to those in Refs [75, 76, 77] to obtain correction factors which implement EMCICs onto multi-particle distributions. In the course of the calculation, we make some simplifying approximations. The derived expressions are then tested for accuracy against the numerical GENBOD simulations. Finally, the expressions are used to calculate the EMCIC effect on the single-particle distribution and multi-particle correlation functions discussed later in this chapter.

41

6.2.1 Calculating corrections due to restricted phase-space

Danielewicz [75], and later Borghini, Dinh and Ollitrault [76], considered EMCIC-type effects on two-particle azimuthal correlations (quantified by v_2 and often used as a measure of elliptic flow [5]). They focused mostly on transverse momentum ($\vec{P}_T = \sum_i \vec{p}_{T,i}$) conservation only, but Borghini later [77] generalized to the case of an arbitrary number D of independent (orthogonal) spatial dimensions and recently considered momentum conservation effects on three-particle analyses of jet-like behavior [78].

As we shall see below, for correlation functions used in femtoscopy, the conservation of energy generates effects of similar magnitude as those due to conservation of (three-)momentum. We deal only with on-shell particles, for which energy can*not* be treated as independent of the momentum (as, say, p_x would be independent of p_y). Thus, unlike the above-mentioned works, we will explicitly begin with the more general multivariate central limit theorem.

We start with the case of interest– $D = 3$ spatial dimensions– and conserve 3-momentum $\vec{p}$. We implement energy conservation and on-shell constraints a bit later.

We define [6]

$$f\left(\vec{p}_i\right) \equiv \frac{d^3 N}{d\vec{p}_i^3} \tag{6.4}$$

as the single-particle momentum distribution *un*affected by EMCICs. This may be considered the unmeasured "parent" distribution. Then, the $k-$particle distribution

---

[6]Our use of symbols f and f_c follows the convention used in [76], which is significantly different than– if unfortunately similar-looking to– that used in [77] and [78].

(k less than the total multiplicity N) *including* EMCICs is

$$f_c\left(\vec{p}_1,...,\vec{p}_k\right) = \left(\prod_{i=1}^{k} f(\vec{p}_i)\right) \times$$
$$\frac{\int\left(\prod_{j=k+1}^{N} d^3\vec{p}_j f\left(\vec{p}_j\right)\right) \delta^3\left(\sum_{i=1}^{N}\vec{p}_i\right)}{\int\left(\prod_{j=1}^{N} d^3\vec{p}_j f\left(\vec{p}_j\right)\right) \delta^3\left(\sum_{i=1}^{N}\vec{p}_i\right)}. \tag{6.5}$$

Note the difference between numerator and denominator in the starting value of the index j on the product.

We implement total energy conservation $\sum E_i = \sqrt{s}$, by replacing $\delta^3\left(\sum_{i=1}^{N}\vec{p}_i\right) \rightarrow \delta^4\left(\sum_{i=1}^{N} p_i - P\right)$ in Equation 6.5. Here, $P = \left(\sqrt{s},\vec{0}\right)$ is the total energy-momentum of the event, and $p_{0,i} = E_i = \sqrt{\vec{p}_i^2 + m_i^2}$ is the energy of the on-shell particle.

We denote Lorentz-invariant distributions as

$$\tilde{f}(p_i) \equiv 2E_i\frac{d^3N}{d\vec{p}_i^3} = 2E_i f(p_i) \tag{6.6}$$

and rewrite Equation 6.5 as

$$\tilde{f}_c\left(p_1,...,p_k\right) = \left(\prod_{i=1}^{k}\tilde{f}(p_i)\right) \times$$
$$\frac{\int\left(\prod_{j=k+1}^{N}\frac{d^3\vec{p}_j}{E_j}\tilde{f}\left(\vec{p}_j\right)\right)\delta^4\left(\sum_{i=1}^{N}p_i - P\right)}{\int\left(\prod_{j=1}^{N}\frac{d^3\vec{p}_j}{E_j}\tilde{f}\left(\vec{p}_j\right)\right)\delta^4\left(\sum_{i=1}^{N}p_i - P\right)}$$
$$= \left(\prod_{i=1}^{k}\tilde{f}(p_i)\right) \times$$
$$\frac{\int\left(\prod_{j=k+1}^{N}d^4p_j\delta\left(p_j^2 - m_j^2\right)\tilde{f}\left(p_j\right)\right)\delta^4\left(\sum_{i=1}^{N}p_i - P\right)}{\int\left(\prod_{j=1}^{N}d^4p_j\delta\left(p_j^2 - m_j^2\right)\tilde{f}\left(p_j\right)\right)\delta^4\left(\sum_{i=1}^{N}p_i - P\right)}$$
$$= \left(\prod_{i=1}^{k}\tilde{f}(p_i)\right) \times$$
$$\frac{\int\left(\prod_{j=k+1}^{N}d^4p_j g\left(p_j\right)\right)\delta^4\left(\sum_{i=1}^{N}p_i - P\right)}{\int\left(\prod_{j=1}^{N}d^4p_j g\left(p_j\right)\right)\delta^4\left(\sum_{i=1}^{N}p_i - P\right)}. \tag{6.7}$$

Thus, we arrive at an integral over four independent variables, in which the integrand function $g(p)$ is "highly peaked" and with strong correlations in the 4-d $p-$space.

According to Equation 6.7, the k-body momentum distribution, including EM-CICs, is the k-body distribution *not* affected by EMCICs– i.e. just an uncorrelated product of single-particle distributions– multiplied by a "correction factor" which enforces the EMCIC. These correspond essentially to the terms and factorization of Eq. 6.2. The numerator of this factor counts the number of configurations in which the remaining $N - k$ on-shell particles conspire to conserve total energy and momentum, and the denominator normalizes the distribution.

6.2.2 Application of the Central Limit Theorem

To arrive at a useful result, we argue along lines similar to those of [75, 76, 77]. The distribution of a large number M of uncorrelated momenta $W = \sum_{i=1}^{M} p_i$ is, by the Central Limit Theorem, a multivariate normal distribution

$$
\begin{aligned}
F_M(W) &\equiv \int \left(\prod_{i=1}^{M} d^4 p_i g(p_i) \right) \delta^4 \left(\sum_{i=1}^{M} p_i - W \right) \qquad (6.8) \\
&= \sqrt{\frac{|B|}{(2\pi)^4}} \times \\
&\quad \exp\left(-\frac{1}{2} \left(W^\mu - \langle P^\mu \rangle \right) B_{\mu\nu} \left(W^\nu - \langle P^\nu \rangle \right) \right).
\end{aligned}
$$

Here, the average of the sum of 4-momenta is simply related to the single-particle average of the 4-momenta as

$$
\langle P^\mu \rangle = \sum_{i=1}^{M} \langle p_i^\mu \rangle = M \langle p_i^\mu \rangle, \qquad (6.9)
$$

44

where

$$\langle p_\mu^n \rangle \equiv \frac{\int d^4 p \, g(p) \cdot p_\mu^n}{\int d^4 p \, g(p)},$$

$$\langle p_\mu p_\nu \rangle \equiv \frac{\int d^4 p \, g(p) p_\mu p_\nu}{\int d^4 p \, g(p)}. \tag{6.10}$$

Finally, in Equation 6.8, $|B|$ denotes the determinant of the matrix B. Up to a factor of M, B is the inverse of the covariance matrix of the distribution $g(p)$:

$$B_{\mu\nu} = \frac{1}{M} b_{\mu\nu}, \tag{6.11}$$

$$\left(b^{-1} \right)_{\mu\nu} = \langle p_\mu p_\nu \rangle - \langle p_\mu \rangle \langle p_\nu \rangle. \tag{6.12}$$

We can now apply the CLT by recognizing the integral in the numerator in Equation 6.7 as the distribution of $N - k$ momenta $\sum_{j=k+1}^{N} p_j = P - \sum_{j=1}^{k} p_j$ so that for "large enough" $N - k$, we find

$$
\begin{aligned}
\tilde{f}_c(p_1, ..., p_k) &= \left(\prod_{i=1}^{k} \tilde{f}(p_i) \right) \frac{F_{N-k}\left(P - \sum_{i=1}^{k} p_i \right)}{F_N(P)} \\
&= \left(\prod_{i=1}^{k} \tilde{f}(p_i) \right) \cdot \left(\frac{N}{N-k} \right)^2 \times \\
&\exp\left[-\left(\sum_{i=1}^{k} (p_i^\mu - \langle p^\mu \rangle) \right) \frac{b_{\mu\nu}}{2(N-k)} \left(\sum_{i=1}^{k} (p_i^\nu - \langle p^\nu \rangle) \right) \right].
\end{aligned}
\tag{6.13}
$$

It is appropriate at this point to repeat the two approximations we have employed up to now. The first assumption, always important in using the CLT, is that $N - k$ is sufficiently large; recall that N is the total multiplicity and k is the order of the correlation being calculated ($k = 2$ for two-particle correlations). Secondly, we have implicitly assumed that all particles in the system are governed by the *same* single-particle distribution $g(p)$. Strictly speaking, then, the system must consist of particles

45

all of the same mass, and if there are several species with the same mass (say, π^- and π^+), they must furthermore have the same momentum distribution. This is at best an approximation for hadron or ion collisions, in which other particles contribute to the pion-dominated final state. In Sections 6.2.4 and 6.6, we discuss these approximations further.

6.2.3 Analytic proof that $B_{\mu\nu}$ diagonalizes and the correlation function

Even the single-particle momentum distribution is affected by EMCICs:

$$\tilde{f}_c(p_i) = \tilde{f}(p_i) \cdot \left(\frac{N}{N-1}\right)^2 \times$$
$$\exp\left[-\left(p^\mu - \langle p^\mu \rangle\right) \frac{b_{\mu\nu}}{2(N-k)} \left(p^\nu - \langle p^\nu \rangle\right)\right] \tag{6.14}$$

The product of such a single particle distribution forms the denominator of the k-particle correlation function

$$C(p_1, ..., p_k) \equiv \frac{\tilde{f}_c(p_1, ..., p_k)}{\tilde{f}_c(p_1) \cdots \tilde{f}_c(p_k)} = \frac{\left(\frac{N}{N-k}\right)^2}{\left(\frac{N}{N-1}\right)^{2k}} \times \tag{6.15}$$
$$\frac{\exp\left[\frac{-1}{2(N-k)} \sum_{i,j=1}^k \left(p_i^\mu - \langle p^\mu \rangle\right) b_{\mu\nu} \left(p_j^\nu - \langle p^\nu \rangle\right)\right]}{\exp\left[\frac{-1}{2(N-1)} \sum_{i=1}^k \left(p_i^\mu - \langle p^\mu \rangle\right) b_{\mu\nu} \left(p_i^\nu - \langle p^\nu \rangle\right)\right]}$$

In this thesis we concentrate on correlation functions in q_{out}, q_{side} and q_{long}, as is done in femtoscopic studies. However, the two-particle correlation function in relative azimuthal angle, which probes elliptic flow, may also contain EMCIC contributions through Equation 6.15. These effects turn out to be small and are discussed in Appendix E.

To first order in $1/N$, the two-particle correlation function becomes

$$C(p_1, p_2) = 1 - \frac{1}{N} \left(p_1^\mu - \langle p^\mu \rangle\right) b_{\mu\nu} \left(p_2^\nu - \langle p^\nu \rangle\right). \tag{6.16}$$

46

The multivariate CLT used in Section 6.2.2 accounts for correlations between vector components via the covariance matrix b^{-1} (Eq. 6.12) which has, in general, 10 non-vanishing elements. The average vector P (Eq. 6.9) has in general 4 non-vanishing elements. We now reduce these numbers significantly by considering the specific case of our interest.

Firstly, we choose to work in the global center-of-momentum frame, so that

$$\langle p^\mu \rangle = \delta_{\mu,0} \langle E \rangle \tag{6.17}$$

As for the correlations, we are interested in signals generated by EMCICs alone, not, for example, dynamical correlations due to flow. Neglecting elliptic flow (azimuthal anisotropies in the parent distribution [5, 79]) implies

$$\left(b^{-1}\right)_{1,2} = \langle p_x p_y \rangle = 0. \tag{6.18}$$

The same approach was adopted in earlier work [75, 76, 78]. Similarly, we assume no dynamical correlations due to directed flow [79], implying

$$\left(b^{-1}\right)_{1,3} = \left(b^{-1}\right)_{2,3} = 0. \tag{6.19}$$

The on-shell constraint generates an unavoidable dependence between energy and 3-momentum components. However, in the CLT limit, only the second moment (covariance) comes into play, and this vanishes. For $i \neq 0$,

$$\left(b^{-1}\right)_{0,i} = \langle E p_i \rangle - \langle E \rangle \langle p_i \rangle = \langle E p_i \rangle \tag{6.20}$$
$$= \frac{\int dE \int d^3\vec{p} \cdot E g\left(p\right) \cdot p_i}{\int dE \int d^3\vec{p} \cdot g\left(p\right)} = 0.$$

In the last step, we recognize that p_i is an odd function of momentum, whereas E and g are even. Equations 6.17- 6.20 are formal proof of what we showed numerically on Fig. 6.4 in Section 6.2.4.

47

In this scenario of interest, then, b is diagonal, and Equations 6.14 becomes

$$\tilde{f}_c\left(p_i\right) = \tilde{f}\left(p_i\right) \cdot \left(\frac{N}{N-1}\right)^2 \times \tag{6.21}$$

$$\exp\left[-\frac{1}{2(N-1)}\left(\frac{p_{i,x}^2}{\langle p_x^2 \rangle} + \frac{p_{i,y}^2}{\langle p_y^2 \rangle} + \frac{p_{i,z}^2}{\langle p_z^2 \rangle} + \frac{\left(E_i - \langle E \rangle\right)^2}{\langle E^2 \rangle - \langle E \rangle^2}\right)\right].$$

Similarly, Equation 6.15 becomes

$$C\left(p_1, ..., p_k\right) \equiv \frac{\tilde{f}_c\left(p_1, ..., p_k\right)}{\tilde{f}_c\left(p_1\right) \cdots \tilde{f}_c\left(p_k\right)} = \frac{\left(\frac{N}{N-k}\right)^2}{\left(\frac{N}{N-1}\right)^{2k}} \times \tag{6.22}$$

$$\frac{\exp\left[\frac{-1}{2(N-k)}\left\{\sum_{\mu=1}^{3}\left(\frac{\left(\sum_{i=1}^{k} p_{i,\mu}^2\right)^2}{\langle p_\mu^2 \rangle}\right) + \frac{\left(\sum_{1}^{k}(E_i - \langle E \rangle)\right)^2}{\langle E^2 \rangle - \langle E \rangle^2}\right\}\right]}{\exp\left[\frac{-1}{2(N-1)}\sum_{i=1}^{k}\left\{\sum_{\mu=1}^{3}\frac{p_{i,\mu}^2}{\langle p_\mu^2 \rangle} + \frac{(E_i - \langle E \rangle)^2}{\langle E^2 \rangle - \langle E \rangle^2}\right\}\right]}$$

and Equation 6.16 becomes

$$C(p_1, p_2) = 1- \tag{6.23}$$

$$\frac{1}{N}\left(2\frac{\vec{p}_{1,T} \cdot \vec{p}_{2,T}}{\langle p_T^2 \rangle} + \frac{p_{1,z} \cdot p_{2,z}}{\langle p_z^2 \rangle} + \frac{\left(E_1 - \langle E \rangle\right)\left(E_2 - \langle E \rangle\right)}{\langle E^2 \rangle - \langle E \rangle^2}\right),$$

where we have taken $\langle p_x^2 \rangle = \langle p_y^2 \rangle = \langle p_T^2 \rangle/2$ in the azimuthally-symmetric case of interest. In what follows and in Figures 6.16-6.21, we shall refer to the first, second, and third terms within the parentheses of Equation 6.23 as the "p_T" "p_z" and "E" components, respectively.

6.2.4 Numerical verification of the central limit theorem in 4-momentum space

The crucial step to find the analytical formula for a single particle distribution (Equation 6.7 for $k = 1$) and then to a two-particle correlation function (Equation 6.8) was to apply the central limit theorem in Eq. 6.13. However, it is not immediately obvious that this procedure is allowed in this case since in Eq. 6.8 there in an integral of a single particle distribution $g(p_i)$ over $\delta^4 p_i$ and this distribution is strongly

48
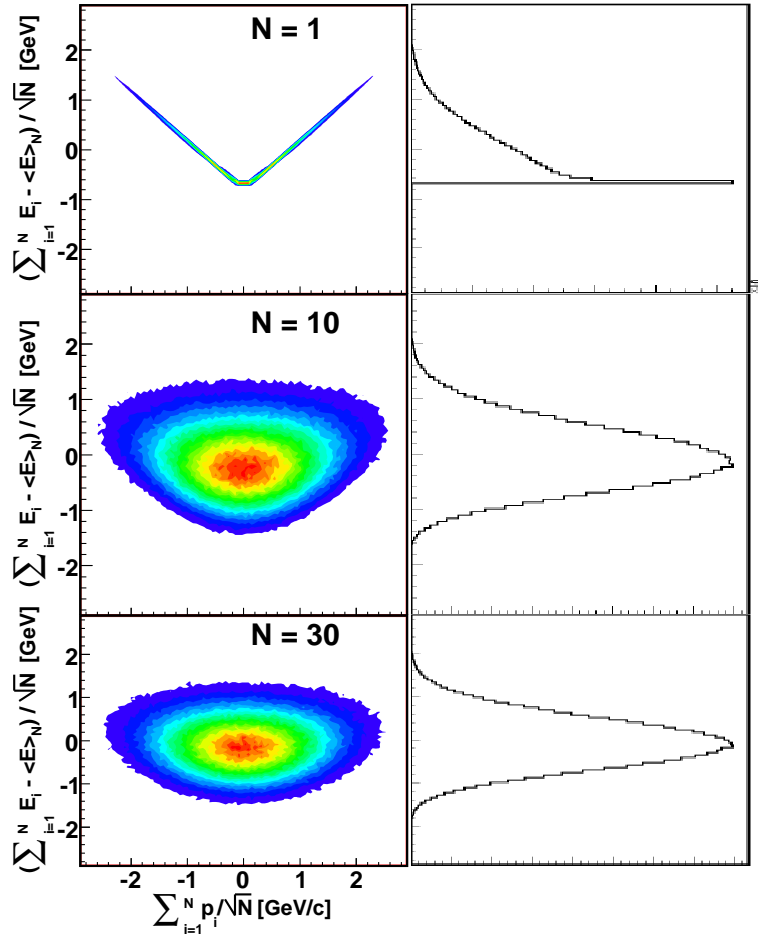
Figure 6.4: The distribution of the sum of the momentum vs the sum of energy (scaled and shifted as indicated by axis labels) for the system of N randomly-produced particles where the value of N is indicated on the plots.

correlated in 4D p-space due to on-shell requirement. In this section we verify numerically the range of application of the central limit theorem in 4-momentum space. To do that we study how important the correlation between energy and momentum distributions if the total number of particles in the system in increasing.

We generated the momenta of N particles from a Gaussian distribution using Monte-Carlo simulations and we calculated their energies assuming, for simplicity,

49

that all particles are pions. The results are presented on Figure 6.4 where the total energy (rescaled by $\sqrt{N}$ and centered at 0, for convenience) is plotted versus the (scaled) total momentum of the system of N randomly-selected particles.

The factorized CLT assumption is obviously broken for a single particle (top panel of Figure 6.4. In this simple example, particles are constrained to one dimension, so that there is a one-to-one relationship between the energy and the single momentum component.

The middle and bottom panels of Figure 6.4 show the same distributions for systems of $N = 10$ and $N = 100$ particles. The right panels of this figure represent the projections of the distributions from the left panels on the y axis. As seen, the correlations between the total energy and momentum of the system is getting weaker and the distribution of the total energy is becoming more Gaussian with increasing N. The results suggest that for $N \gtrsim 10$ we can neglect those correlations and apply CLT independently to both the energy and momentum distribution of the system.

In fact, the correlation between total energy and components of the total momentum breaks down even more rapidly if the momentum vector is allowed to have three components rather than one. For example, even for $N = 1$, the correlation between $\sum E$ and $\sum p_x$ would not be as severe as that in the top left panel of Figure 6.4.

6.3 Effects of energy and momentum conservation on single-particle spectra

6.3.1 A restricted phase space factor

Changing the size (central versus peripheral ion collisions, $e + e$ collisions, etc) and energy of a collision system will lead to different measured single-particle distributions, reflecting (1) possibly different physical processes driving the system and (2)

effects due to phase space restrictions. To focus on changes caused by the latter, we consider some Lorentz-invariant "parent" distribution $\tilde{f}(p) \equiv 2E \frac{d^3 N}{dp^3}$, driven by some unspecified physical process, but *un*affected by energy and momentum conservation. For simplicity, we assume that all particles obey the same parent distribution.

In the absence of other correlations, the measured single-particle distribution is related to the parent according to [75, 76, 77, 21]

$$\tilde{f}_c(p_1) = \tilde{f}(p_1) \times \tag{6.24}$$

$$\frac{\int \left(\prod_{j=2}^{N} d^4 p_j \delta \left(p_j^2 - m_j^2 \right) \tilde{f}(p_j) \right) \delta^4 \left(\sum_{i=1}^{N} p_i - P \right)}{\int \left(\prod_{j=1}^{N} d^4 p_j \delta \left(p_j^2 - m_j^2 \right) \tilde{f}(p_j) \right) \delta^4 \left(\sum_{i=1}^{N} p_i - P \right)},$$

where N is the event multiplicity. The integral in the numerator of Equation 6.24 represents the number of configurations in which the $N-1$ other particles counterbalance p_1 so as to conserve the total energy-momentum P of the event, and the denominator, integrating over all N particles, is a normalization.

For $N \gtrsim 10$ [21], one may use the central limit theorem to rewrite the factor in Equation 6.24 as [75, 76, 77, 21]

$$\tilde{f}_c(p_i) = \tilde{f}(p_i) \cdot \left(\frac{N}{N-1} \right)^2 \times \tag{6.25}$$

$$\exp \left[-\frac{1}{2(N-1)} \left(\frac{p_{i,x}^2}{\langle p_x^2 \rangle} + \frac{p_{i,y}^2}{\langle p_y^2 \rangle} + \frac{p_{i,z}^2}{\langle p_z^2 \rangle} + \frac{(E_i - \langle E \rangle)^2}{\langle E^2 \rangle - \langle E \rangle^2} \right) \right],$$

where

$$\langle p_\mu^n \rangle \equiv \int dp \tilde{f}(p) \cdot p_\mu^n \tag{6.26}$$

are average quantities and we have set the average three-momentum $\langle p_{(\mu=1,2,3)} \rangle = P_{\mu=1,2,3}/N = 0$. We stress that what appears in Equation 6.26 is the parent distribution $\tilde{f}$, not the measured one $\tilde{f}_c$. Hence, for finite multiplicity N, the averages $\langle p_\mu^n \rangle$

51

are not the measured ones, which we define as

$$\langle p_\mu^n \rangle_c \equiv \int dp \tilde{f}_c(p) \cdot p_\mu^n. \tag{6.27}$$

See also the discussion in Appendix C.

Since p_T distributions are commonly reported, we would like to estimate EM-CIC distortions to p_T distributions, integrated over azimuth and a finite rapidity bin centered at midrapidity. As discussed in Appendix D, for the approximately boost-invariant distributions at RHIC [80], the measured and parent p_T distributions are related by

$$\tilde{f}_c(p_T) = \tilde{f}(p_T) \cdot \left(\frac{N}{N-1} \right)^2 \times \tag{6.28}$$

$$\exp \left[-\frac{1}{2(N-1)} \left(\frac{2p_T^2}{\langle p_T^2 \rangle} + \frac{\overline{p_z^2}}{\langle p_z^2 \rangle} \right. \right.$$

$$\left. \left. + \frac{\overline{E^2}}{\langle E^2 \rangle - \langle E \rangle^2} - \frac{2\overline{E}\langle E \rangle}{\langle E^2 \rangle - \langle E \rangle^2} + \frac{\langle E \rangle^2}{\langle E^2 \rangle - \langle E \rangle^2} \right) \right].$$

The notation $\overline{X}$ indicates the average of a X over the rapidity interval used; see Appendix D for details. These averages depend, of course, on p_T and should not be confused with global averages $\langle X \rangle$ (Equation 6.26) which characterize the parent distribution.

We would also like to emphasize the fact that since Equation 6.28 depends on the energy of the particle (not just momentum) it is clear that the EMCIC effects are larger for heavier particles at the same p_T. Thus we should expect that the proton spectra will be more suppressed than pion spectra.

In what follows, we find that ignoring the $\overline{p_z^2}/\langle p_z^2 \rangle$ term does not affect our results, since the numerator is small for the narrow rapidity windows used here, and the

denominator is large. In discussions below, we set this term to zero. See Appendix H for more details.

6.3.2   Postulate of universal parent distribution

Equations 6.24-6.28 are reminiscent of Fermi's "Golden Rule" [74, 81], in which the probability for making a particular observation is given by the product of the squared matrix element and a quantity determined by available phase space. The first term represents the underlying physical process. In his original statistical model [74], Fermi originally assumed it to be a constant representing the volume in which emitted particles were produced; this is equivalent to setting $\tilde{f}(p)$ constant in Equation 6.24. While surprisingly successful in predicting cross sections and pion spectra(e.g. [82, 83]), the emission volume required to describe the data was considered unrealistically large [84]. Using the mean value theorem, Hagedorn [81] generalized the theory so that the "physics term" is the interaction matrix element, suitably averaged over all final states.

We wish to make no assumptions about the underlying physics (represented by $\tilde{f}$) driving the observed spectrum $\tilde{f}_c$. Rather, we wish to quantify the effect of changing the multiplicity N, which appears in the phase space term.

In particular, in the following Section, we compare measured single-particle spectra for different event classes.

We postulate that the parent distributions for, say classes 1 and 2, are the same ($\tilde{f}_1 = \tilde{f}_2$). By Equation 6.26, this implies $\langle p_\mu \rangle_1 = \langle p_\mu \rangle_2 \equiv \langle p_\mu \rangle$. In this case, the *only* reason that the observed spectra differ ($\tilde{f}_{c,1} \neq \tilde{f}_{c,2}$) is the difference in "multiplicity" $N_1 \neq N_2$; see Section 6.3.3 for a discussion of N_1.

To eliminate the (unknown) parent distribution itself, we will study the ratio of observed p_T distributions, which, by Equation 6.28 becomes

$$
\frac{\tilde{f}_{c,1}(p_T)}{\tilde{f}_{c,2}(p_T)} = K \times \left(\frac{(N_2 - 1) N_1}{(N_1 - 1) N_2} \right)^2 \times \tag{6.29}
$$
$$
\exp \left[\left(\frac{1}{2(N_2 - 1)} - \frac{1}{2(N_1 - 1)} \right) \left(\frac{2p_T^2}{\langle p_T^2 \rangle} + \right. \right.
$$
$$
\left. \left. + \frac{\overline{E^2}}{\langle E^2 \rangle - \langle E \rangle^2} - \frac{2\overline{E}\langle E \rangle}{\langle E^2 \rangle - \langle E \rangle^2} + \frac{\langle E \rangle^2}{\langle E^2 \rangle - \langle E \rangle^2} \right) \right],
$$

where the constant K is discussed at the end of Section 6.3.3. As mentioned at the end of Section 6.3.1, numerically unimportant terms in p_z have been dropped.

Naturally, our postulate cannot be expected to be entirely correct; one may reasonably expect the mix of physical processes in $p + p$ collisions to differ from those in $Au + Au$ collisions. Nevertheless, it is interesting to find the degree to which the change in single-particle spectra may be attributed *only* to finite-multiplicity effects. We will find that the postulate works surprisingly well in some regions, and fails in others. As we will discuss, both the success and failure raise interesting and surprising possibilities.

6.3.3 Testing the postulate

By our postulate, the phase space factor affecting a p_T distribution is driven by four quantities. Three, $\langle p_T^2 \rangle$, $\langle E^2 \rangle$ and $\langle E \rangle$, characterize the parent distribution, while N is the number of particles in the final state. In general, increasing any one parameter decreases the effect of phase space restrictions on the observed distributions. But what should we expect these values to be? They should characterize the relevant system in which a limited quantity of energy and momentum is shared. They are not,

54

however, directly measurable, and should only approximately scale with measured values, for at least five reasons discussed here.

Firstly, the energy and momentum is shared among measured and unmeasured (neutrals, neutrinos, etc.) particles alike so that N should roughly track the measured event multiplicity N_{meas}, but need not be identical to it. Secondly, emission of resonances smears the connection between N and N_{meas}; e.g. the emission of an omega meson which later decays into "secondary" particles ($\omega \to \pi\pi\pi$) increments N by unity, rather than three, as far as other particles are concerned. This latter consideration also affects the kinematic parameters $\langle p_T^2 \rangle$, $\langle E^2 \rangle$ and $\langle E \rangle$. While energy and momentum are, of course, conserved in resonance decay, the aforementioned quantities, themselves, are not. Thus, one need not expect perfect correspondence between the appropriate kinematic parameters in Equation 6.29, and the measured ones.

Thirdly, even restricting consideration to primary particles, it is unclear that all of them should be considered in the relevant ensemble of particles sharing some energy and momentum. In particular, for space-time extended systems in high-energy collisions, the momentum extent of characteristic physics processes (e.g. string breaking) and causality in an approximately boost-invariant scenario suggest that rapidity slices of roughly unit extent should be considered separate subsystems [78]. Of course, the total available energy in any event is shared among *all* such subsystems; i.e. the midrapidity subsystem in one event will not have exactly the same available energy as that in another event. However, such fluctuations are to be expected in any case– surely individual collisions will differ from one another to some extent. Thus, we

repeat our interpretation of the four parameters N, $\langle p_T^2 \rangle$, $\langle E^2 \rangle$ and $\langle E \rangle$: they characterize the scale, in energy and momentum, of the limited available phasespace to an N-particle subsystem.

Fourthly, Equations 6.24-6.29 are appropriate for fixed N, while we will be comparing to measured spectra selected by measured charged-particle multiplicity. Thus, N would inevitably fluctuate within an event class, even if we could ignore the above considerations. Naturally, high multiplicity events contribute to spectra more than low multiplicity events. Similarly, the average multiplicity in two-particle correlations is even more shifted to higher multiplicities.

Fifthly, as already mentioned in Section 6.3.1, the kinematic parameters $\langle p_T^2 \rangle$, $\langle E^2 \rangle$ and $\langle E \rangle$ correspond to the parent distribution, which will only correspond identically to the measured one in the limit of infinite multiplicity (i.e. no EMCIC distortions). See also the discussion in Appendix C.

For all of these reasons, we will treat N, $\langle p_T^2 \rangle$, $\langle E^2 \rangle$ and $\langle E \rangle$ as free parameters when testing our postulate against data. Our aim is not to actually measure these quantities by fitting the data with Equation 6.29; this is good, since our fits to the data only very roughly constrain our four parameters, as discussed in the next Section. Rather, our much less ambitious goal is to see whether "reasonable" values of these parameters can explain the multiplicity evolution of the spectra.

Finally, a word about normalization– the quantity K which appears in Equation 6.29. Not only energy and momentum, but also discrete quantum numbers like strangeness and baryon number are conserved event by event, affecting the overall yield of a given particle species. For example, the related phenomenon of "canonical suppression" affects the ratio of yields for strange versus non-strange particles, as

multiplicity varies [85, 86]. Since we restrict our attention to energy and momentum conservation and the effect on kinematic quantities, we are interested in the *shape* of the spectra ratio, as a function of particle momentum, and include a factor K in our Equation 6.29, which should be of order, but not necessarily identical to, unity. We do not discuss it further.
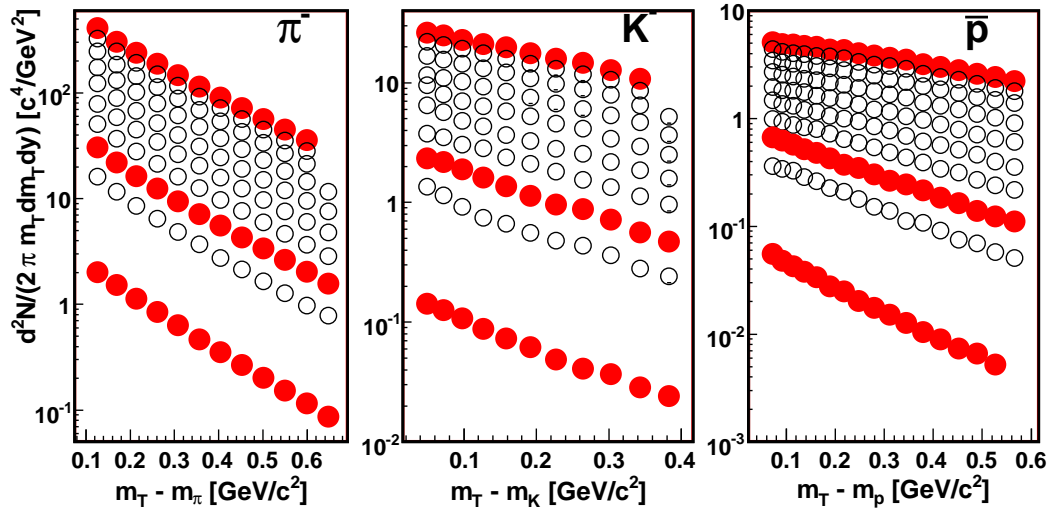
Figure 6.5: Transverse mass distributions for pions (left), kaons (center) and antiprotons (right) measured by the STAR Collaboration for $\sqrt{s_{NN}}$=200 GeV collisions [80]. The lowest datapoints represent minimum-bias $p + p$ collisions, while the others come from $Au + Au$ collisions of increasing multiplicity. Filled datapoints are for the top 5% and 60-70% highest-multiplicity $Au + Au$ collisions, and for the $p + p$ collisions. Figure taken from [22].

6.3.4   Comparing the postulate to data

We now explore the degree to which the postulate proposed above describes the multiplicity evolution of measured p_T spectra measured in $\sqrt{s_{NN}} = 200$ GeV collisions at RHIC. As is frequently done, we will separately discuss the "soft" ($p_T \lesssim 1$ GeV/c)
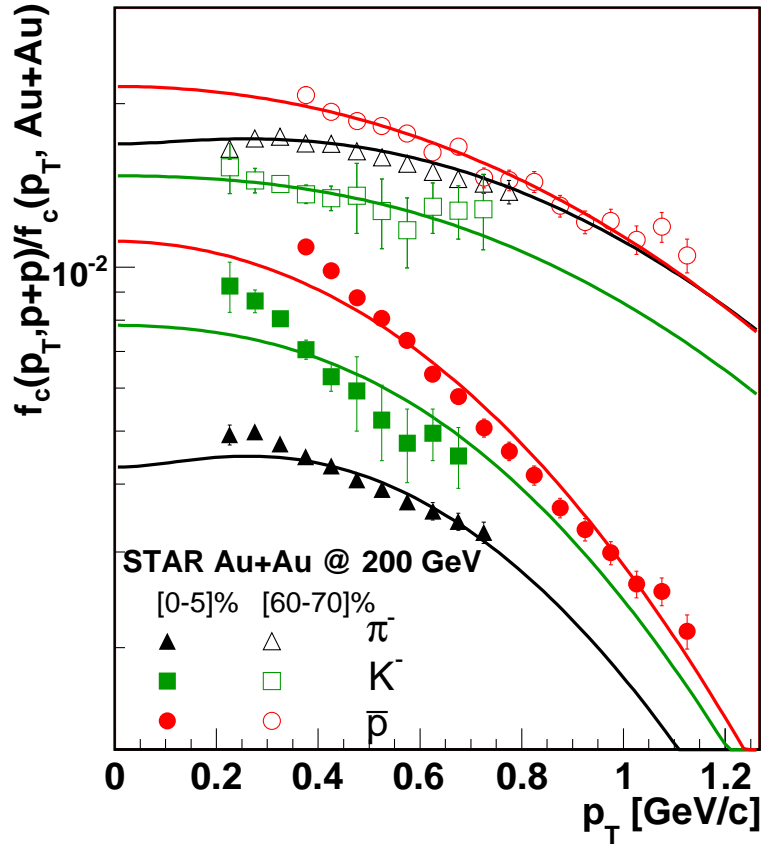
Figure 6.6: The ratio of the p_T distribution from minimum-bias $p + p$ collisions to the distribution from 0-5% (filled datapoints) and 60-70% (open datapoints) highest multiplicity $Au + Au$ collisions; c.f. Figure 6.5. The ratio of the kaon spectra from $p + p$ and 0-5% $Au + Au$ collisions (solid green squares) has been scaled by a factor 1.7 for clarity. Curves represent a calculation of this ratio (ratio of EMCIC factors) using Equation 6.29. Figure taken from [22].

and "hard" ($p_T \gtrsim 3$ GeV/c) portions of the spectra. This separation is not entirely arbitrary, as spectra in these two p_T ranges are thought to be dominated by quite different physics, and the multiplicity evolution in the two sectors is usually interpreted in terms of distinct physics messages.
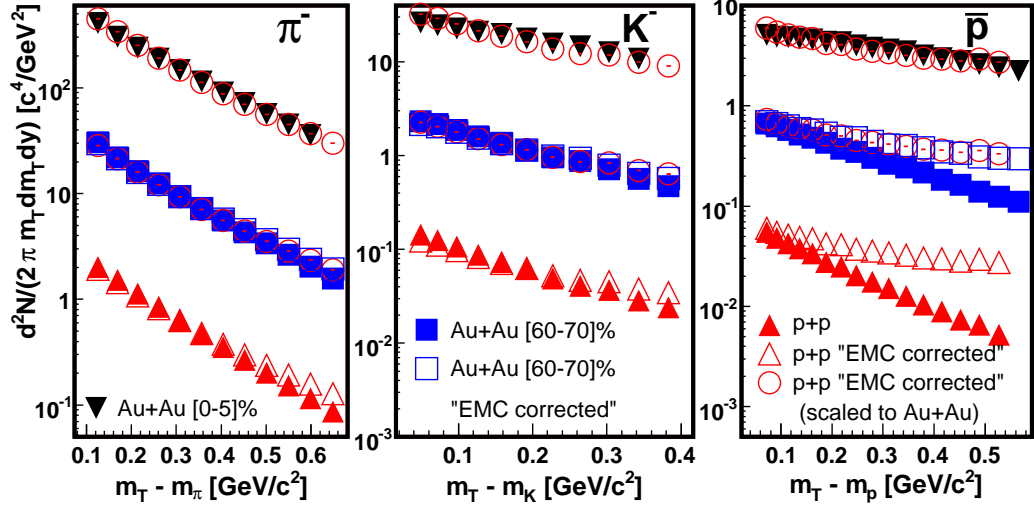
Figure 6.7: Transverse mass distributions of pions, kaons and antiprotons for minimum-bias $p + p$ collisions and 60-70% and 0-5% highest multiplicity $Au + Au$ collisions at $\sqrt{s_{NN}} = 200$ GeV. Filled datapoints are the same as in Figure 6.5. Open triangles represent the $p + p$ spectra divided by the lower curves shown in Figure 6.6. Open circles are the same spectra as the open triangles, except scaled up to compare to the spectra from the $Au + Au$ collisions. Open squares represent the spectra from 60-70% highest multiplicity $Au + Au$ events, divided by the ratio of upper and lower curves shown in Figure 6.6. See text for details. Figure taken from [22].

In the soft sector, the spectral shapes are often consistent with hydrodynamic calculations (e.g. [43, 87]), or fitted with blast-wave type models (e.g. [88, 7]), and show evidence of strong, explosive flow associated with a collective bulk medium. This is especially clear in the mass dependence of the spectra; the m_T (or p_T) spectrum of heavy particles like protons are significantly flatter than that for pions, in the presence of strong flow. The multiplicity evolution in this sector suggests that high-multiplicity collisions (say, central $Au + Au$ collisions) show much more collective flow than do low-multiplicity (say, $p + p$) collisions [80]. Such an interpretation initially sensible in a scenario in which flow is built up through multiple collisions among emitted

particles; the concept of a collective bulk medium in a very low-multiplicity collision is thus usually considered questionable.

Particle yields at high p_T, on the other hand, are generally discussed in the context of fragments from high-Q^2 parton scatterings in the initial stage of the collision. As the event multiplicity in $Au + Au$ collisions is increased, a suppression of high-p_T yields is observed, relative to a properly normalized minimum-bias spectrum from $p + p$ collisions. This suppression has been attributed to partonic energy loss in the bulk medium [1, 2, 3, 4].

The multiplicity evolution of the spectra in $p + p$ collisions, however, shows quite the reverse. Relative to the soft sector, the high-p_T yields increase as the multiplicity increases; one may also say that the p_T spectra become less steep as multiplicity increases [89]. This seems to reinforce the conclusion discussed above in relation to the soft sector, that $p + p$ collisions do not build up a bulk system capable of quenching jets.

Here, we reconsider these conclusions based on the multiplicity evolution of the spectra, in light of the phase space restrictions discussed above.

6.3.5 Soft sector: identified particles in $Au + Au$ versus $p + p$

Figure 6.5 shows m_T distributions for minimum-bias $p + p$ collisions and multiplicity-selected $Au + Au$ collisions, all at $\sqrt{s_{NN}} = 200$ GeV, reported by the STAR Collaboration at RHIC [80]. For the highest-multiplicity $Au + Au$ collisions (top-most filled datapoints), the spectrum for heavier emitted particles is less steep than the essentially exponential pion spectrum.

60

Event selection	N	$\langle p_T^2 \rangle$ $[(\mathrm{GeV/c})^2]$	$\langle E^2 \rangle$ $[\mathrm{GeV}^2]$	$\langle E \rangle$ $[\mathrm{GeV}]$
$p + p$ min-bias	10.3	0.12	0.43	0.61
$Au + Au$ 70-80%	15.2	"	"	"
$Au + Au$ 60-70%	18.3	"	"	"
$Au + Au$ 50-60%	27.3	"	"	"
$Au + Au$ 40-50%	38.7	"	"	"
$Au + Au$ 30-40%	67.6	"	"	"
$Au + Au$ 20-30%	219	"	"	"
$Au + Au$ 10-20%	> 300	"	"	"
$Au + Au$ 5-10%	> 300	"	"	"
$Au + Au$ 0-5%	> 300	"	"	"

Table 6.1: Multiplicity and parent-distribution kinematic parameters which give a reasonable description of the spectrum ratios for identified particles in the soft sector. See text for details. Note that the multiplicity changes with event class; the parent distribution is assumed identical.

Ratios of spectra from minimum-bias $p + p$ collisions to those from $Au + Au$ collisions are plotted in Figure 6.6. For the filled points, the denominator is the most central $Au + Au$ collisions, while the open points represent the ratio when the denominator is from peripheral (60-70% centrality) $Au + Au$ collisions. Pions, kaons, and protons are distinguished by different symbol shapes.

The curves show the function given in Equation 6.29, for the kinematic scales given in Table 6.1. Clear from the Table is that all curves in Figure 6.6 are generated with the same kinematic variables $\langle p_T^2 \rangle$, $\langle E^2 \rangle$ and $\langle E \rangle$; only the relevant multiplicity changes.

We do not quote uncertainties on the kinematic or multiplicity parameters, as the fitting space is complex, with large correlations between them. Furthermore, it is clear that the calculated curves do not perfectly reproduce the measured ratios. However, it is also clear that "reasonable" values of multiplicity and energy-momentum scales go

a long way towards explaining the multiplicity evolution of the spectra, even keeping physics ("parent distribution") fixed. Our postulate of Section 6.3.2 seems to contain a good deal of truth.

Another way to view the same results is useful. While the curves shown in Figure 6.6 only approximately describe the data shown there, one may approximately "correct" the measured m_T distributions, to account for EMCICs. This is shown in Figure 6.7, where the measured min-bias $p + p$ and central and mid-peripheral $Au + Au$ spectra have been copied from the full points of Figure 6.5 and are shown by full points. The open red triangles represent the min-bias $p + p$ spectra, divided by Equation 6.29, with the parameters from Table 6.1. This "EMCIC-corrected" spectrum is then scaled up to show comparison to the spectra from central $Au + Au$ (open red circles); the level of (dis)agreement is identical to that between the lower datapoints and curves in Figure 6.6.

Spectra from the mid-central $Au + Au$ collisions have been likewise "corrected." The open squares in Figure 6.7 may be compared to the open circles; again the level of (dis)agreement is equivalent to that between the upper datapoints and curves in Figure 6.6.

In summary, to the extent that the curves in Figure 6.6 describe the ratios shown there– which they do in sign, magnitude and mass dependence, but only approximately in shape– the data is consistent with a common parent distribution for spectra from all collisions. The residual deviation seen in Figure 6.6 is observed again in different forms in Figure 6.7. The upshot is that EMCICs may dominate the multiplicity evolution of the spectra in the soft sector at RHIC. Extracting physics messages

from the changing spectra, while ignoring kinematic effects of the same order as the observed changes themselves, seems unjustified.

6.3.6 Soft sector: unidentified particles in multiplicity-selected $p + p$ collisions

While minimum-bias $p + p$ collisions are the natural "reference" when studying $Au + Au$ collisions, the STAR experiment has also measured p_T spectra from multiplicity-selected $p + p$ collisions [89]. These are reproduced in Figure 6.8, in which the lowest-multiplicity collisions are shown on the bottom and the highest at the top. Numerical labels to the right of the spectra are included just for ease of reference here.

The solid curve is a power-law fit to the highest-multiplicity spectrum (#10), just for reference. This curve is scaled and replotted as dashed lines, to make clear the multiplicity evolution of the spectra. Concentrating on the soft sector for the moment, we perform the same exercise as above, to see to what extent this multiplicity evolution can be attributed to EMCICs.

In Figure 6.9 are shown three ratios of spectra, in which the second-highest-multiplicity spectrum (#9) is used as the denominator, to avoid statistical fluctuations associated with the highest multiplicity spectrum. Also shown are curves, using Equation 6.29 with the energy-momentum scales given in Table 6.2.

The spectra reported by STAR are for unidentified negative hadrons. In calculating these curves, we assumed that all particles were pions. This matters, since the energy terms in Equation 6.29 require the particle mass. We expect the energy-momentum scales listed in Table 6.2 to be affected by this simplistic assumption.
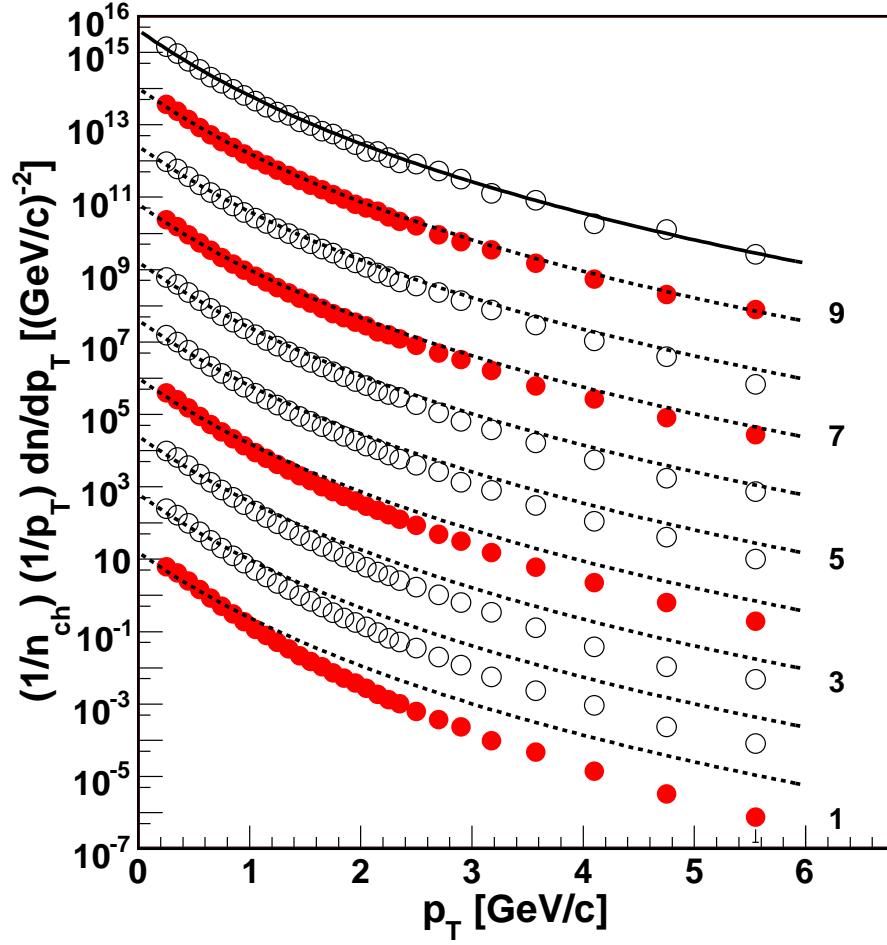
Figure 6.8: Transverse momentum spectra of unidentified negative hadrons from $p + p$ collisions at $\sqrt{s_{NN}} = 200$ GeV by the STAR Collaboration [89]. The lowest (highest) dataset corresponds to the lowest (highest) multiplicity collisions. The solid line is intended only to guide the eye and show the shape of the spectrum for the highest multiplicity selection. It is rescaled and redrawn as dashed lines below, to emphasize the multiplicity evolution of the spectrum shape. Figure taken from [22].

Particle-identified spectra from multiplicity-selected $p + p$ collisions would be required, to do better. Given this, and the only semi-quantitative agreement between the calculations and measured ratios shown in Figure 6.9, we conclude only that the

EMCIC contribution to the multiplicity evolution of low-p_T spectra in $p + p$ collisions is at least of the same order as the observed effect itself.

6.3.7   From the soft to the hard sector

Figure 6.6 shows the central result of this thesis: namely, that the multiplicity evolution of the mass and p_T dependence of single particle spectra in the soft sector may be understood almost entirely in terms of phase-space restriction with decreasing event multiplicity.

Plotted in that figure is the ratio of spectra from low-multiplicity events over spectra from high-multiplicity events. Experimental studies sometimes show this ratio's inverse, often called R_{AA} [90]. While of course the same information is shown in both representations, we choose that of Figure 6.6 for two reasons. The first is to emphasize the effects of EMCICs, the topic of this thesis; these are, generically, to suppress the particle yield at high energy and momentum, particularly for low-N final states. (In multiparticle distributions, they also generate measurable correlations [21].)

The second reason is to stress that we have been discussing spectra in the soft sector, whereas the ratio R_{AA} is generally studied at high p_T. At large p_T, we expect

Multiplicity cut	N	$\langle p_T^2 \rangle$ [(GeV/c)^2]	$\langle E^2 \rangle$ [GeV^2]	$\langle E \rangle$ [GeV]
# 1	6.7	0.31	0.90	0.84
# 4	11.1	"	"	"
# 7	24.2	"	"	"
# 9	35.1	"	"	"

Table 6.2:   Multiplicity and parent-distribution kinematic parameters which give a reasonable description of the spectrum ratios for unidentified particles in the soft sector from multiplicity-selected $p + p$ collisions. See text for details. Note that the multiplicity changes with event class; the parent distribution is assumed identical.
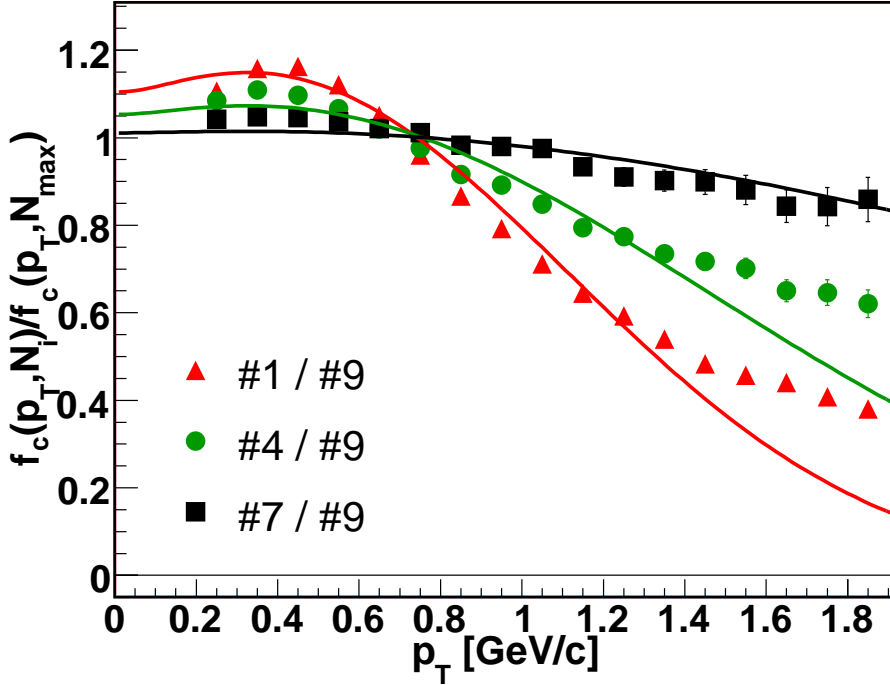
Figure 6.9: Ratio of the p_T spectra shown by full points in Figure 6.8. Spectra for the lowest-multiplicity (red triangles), fifth-lowest (green triangles) and seventh-lowest (squares) multiplicity collisions are divided by the spectrum for the second-highest multiplicity collisions. Curves represent a calculation of this ratio (ratio of EMCIC factors) using Equation 6.29; see text for details. Figure taken from [22].

that a purely EMCIC-based explanation of the multiplicity evolution of the spectra might break down, for two reasons. Firstly, even if particles of all momenta shared phase-space statistically, our approximation of Equation 6.25 is expected to break down for energies much above the average energy, as discussed in Appendix C. Secondly, it is believed that the high-p_T yield has a large pre-equilibrium component; thus, high-p_T particles might participate less in the statistical sharing of phase-space, as discussed in Section 6.3.3.

As we discuss in the next Section, EMCICs surely do *not* dominate the multiplicity evolution of the hard sector in heavy ion collisions. For interpreting high-p_T spectra from multiplicity-selected $p + p$ collisions, accounting for EMCICs may or may not be important. In order to make the connection to Figure 6.6, we will plot spectra from low-multiplicity collisions over those from high-multiplicity, as well as the inverse, to make the connection to R_{AA}.

6.3.8 Spectra in the hard sector

The generic effect of EMCICs is to suppress particle yields at energy-momentum far from the average value. The effect is stronger for lower multiplicity N. It is clear, then, that EMCICs cannot account for the multiplicity evolution of the spectra at high p_T in $Au + Au$ collisions, since high-multiplicity collisions are observed to have *more* suppression at high p_T than do low-multiplicity collisions [90]. Thus, we conclude that our postulate fails for $Au + Au$ collisions at high p_T; the "parent distribution" describing the underlying physics in this region does, indeed, change with multiplicity.

But in $p + p$ collisions, the multiplicity evolution in the hard sector is opposite to that in $Au + Au$ collisions. In particular, in $p + p$ collisions, the yield at high p_T (relative to lower p_T) is *inc*reased as multiplicity increases, as is clear from Figure 6.8; similar results have been observed in $\overline{p} + p$ collisions at the Tevatron [91], ISR [92], and $Sp\overline{p}S$ [93]. A "hardening" of the spectrum with increasing multiplicity goes in the same direction as would EMCIC effects. To what extent can EMCICs account for the multiplicity evolution of spectra from $p + p$ collisions, in the hard sector?

67
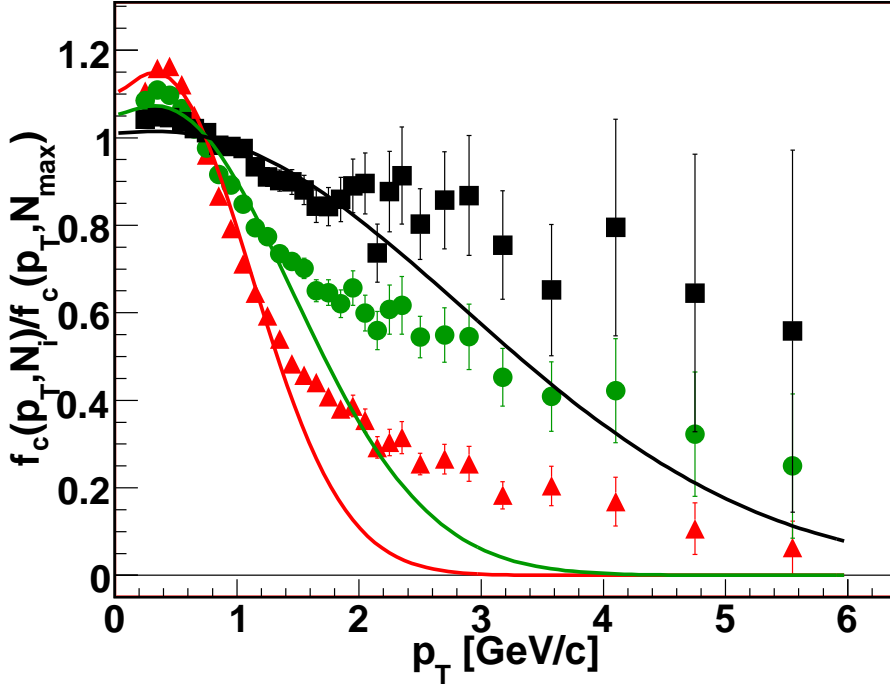
Figure 6.10: The same data and curves as shown in Figure 6.9, but plotted over the entire measured p_T range. Figure taken from [22].

Some insight on this question may be gained from Figure 6.10, in which the data and curves shown in Figure 6.9 are plotted out to $p_T = 6$ GeV/c. Clearly, the calculated suppression function (Equation 6.29) fails dramatically at high p_T.

We recall that Equations 6.25 and 6.29 are based on the central limit theorem (CLT), which naturally leads to Gaussian distributions. As discussed in Appendix C, one expects the breakdown of the CLT approximation in the far tails of the distribution– e.g. when $p_T^2 \gg \langle p_T^2 \rangle$. Thus, any inferences we make about EMCIC effects in the hard sector remain qualitative. Nevertheless, the level of disagreement between the calculations and measurements leads us to conclude that EMCICs do *not*

fully explain the multiplicity evolution of p_T spectra in $p + p$ collisions in the hard sector.

However, this, in itself, raises a fascinating possibility. Figure 6.10 shows that, relative to high-multiplicity $p + p$ collisions, the suppression of high-p_T yields from low-multiplicity collisions is not as strong as one expects from our simple postulate. Said another way, the high-p_T "enhancement" in high-multiplicity collisions may not be as large as one expects from phasespace considerations alone. This is emphasized in Figure 6.11, in which is plotted "R_{pp}", the ratio of the spectrum from high-multiplicity to lower-multiplicity collisions; R_{pp} is the analog of R_{CP} from heavy ion collisions [90].

The motivation for studying quantities like R_{AA} and R_{CP} (and now R_{pp}) is to identify important differences between one class of collisions and another. Presumably, one is interested in physics effects (jet quenching, etc.), above and beyond "trivial" energy and momentum conservation. Thus, it makes sense to attempt to "correct" for EMCICs by dividing them out as we did in Section 6.3.5, keeping in mind the caveats just discussed.

The result of this exercise is shown in Figure 6.12, in which the datapoints from Figure 6.11 are divided by the curves from the same Figure, to form a new quantity, R'_{pp}. Explicitly, the green circles on Figure 6.12, which compare multiplicity selections #9 and #4 are given by

$$R_{pp}^{\prime(\#9,\#4)}(p_T) \equiv \frac{\left. \frac{dn}{dp_T} \right|_{\#9}}{\left. \frac{dn}{dp_T} \right|_{\#4}} \times \tag{6.30}$$

$$\exp\left[\left(\frac{1}{2\,(N_{\#9} - 1)} - \frac{1}{2\,(N_{\#4} - 1)} \right) \left(\frac{2p_T^2}{\langle p_T^2 \rangle} + \frac{(E - \langle E \rangle)^2}{\langle E^2 \rangle - \langle E \rangle^2} \right) \right],$$

where the relevant quantities from Table 6.2 are used. Again, all particles are assumed to have pion mass. Qualitative though it is, Figure 6.12 raises the possibility that,
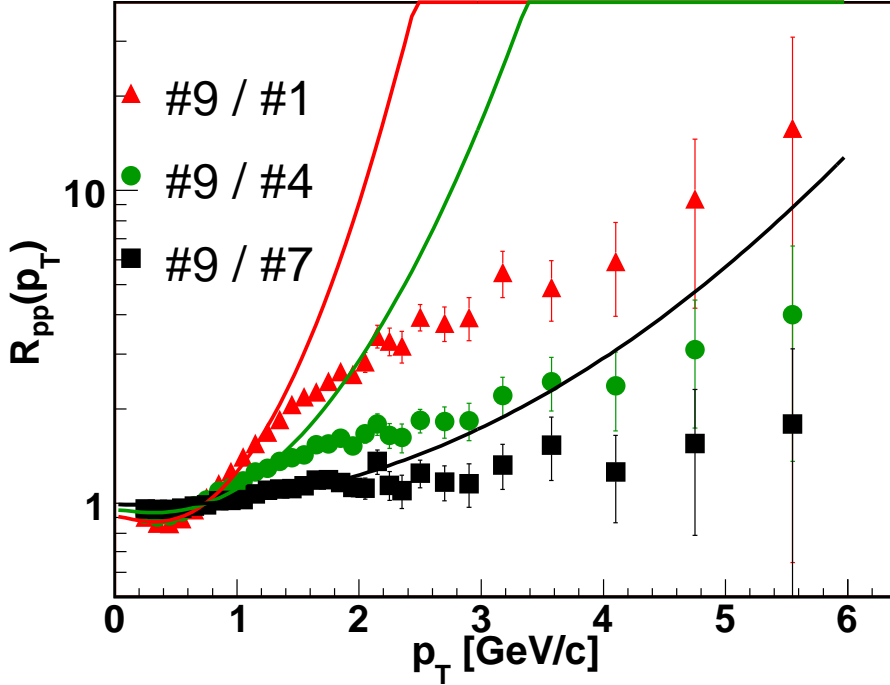
Figure 6.11: "R_{pp}," the analogue of "R_{CP}" used in heavy ion collisions. The spectrum from the highest-multiplicity $p + p$ collisions are divided by spectra from lower-multiplicity collisions (see filled datapoints in Figure 6.8). The data and curves are simply the inverse of those shown in Figure 6.10. Figure taken from [22].

when "trivial" EMCICs are accounted for, the high-p_T yield from high-multiplicity $p + p$ collisions is *suppressed* relative to low-multiplicity collisions, a trend in the same direction as that observed in $Au + Au$ collisions.

In the hard sector, our estimates are mathematically and conceptually too simplistic to decide whether this implies "jet quenching" in high-multiplicity $p + p$ collisions. However, it is quite clear that conservation-induced phasespace restrictions might be sufficiently large in the hard sector, so that a high-p_T "enhancement" in high-multiplicity $p + p$ collisions turns into a "suppression," when these effects are accounted for. Extracting physics messages (e.g. about mini-jet production or jet

quenching) from the multiplicity evolution of $p + p$ spectra is a non-trivial task, in light of this potentially huge background effect. At the very least, EMCICs should not be ignored, as they usually are, when extracting physics messages.
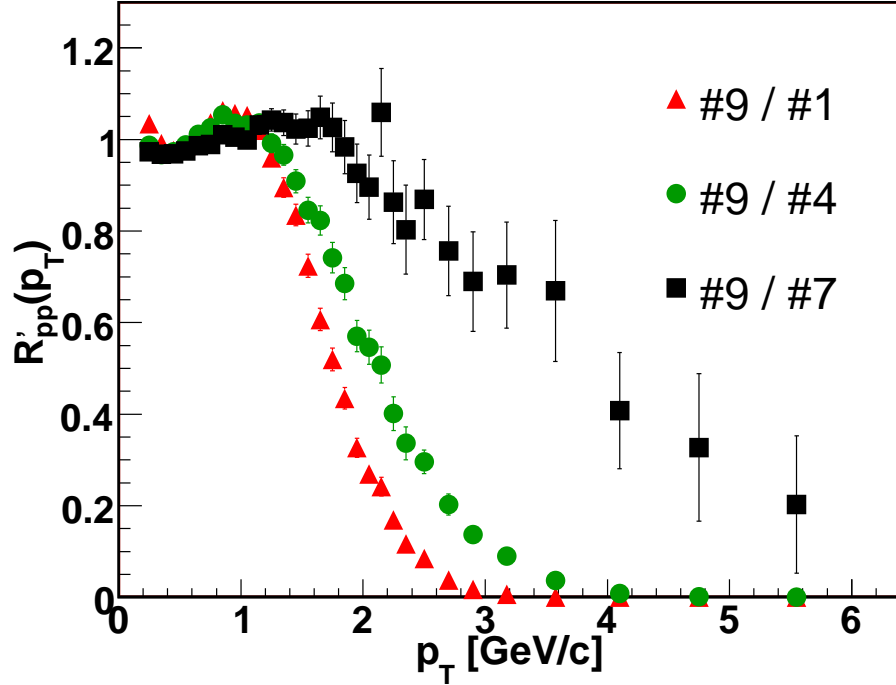
Figure 6.12: R_{pp} (c.f. Figure 6.11) divided by the EMCIC contribution to R_{pp}, as calculated by Equation 6.30. Figure taken from [22].

6.4 Effect of EMCICs on particle ratio and $\langle p_T \rangle$.

The dependences on the colliding system of $\langle p_T \rangle$ and particle rations are frequently measured in heavy ion collisions. They are usually considered to reflect the evolution of collectivity and chemistry, respectively, with energy density, size, etc. Figure 6.13 shows the distribution of $\langle p_T \rangle$, K^-/π^- and $\bar{p}/\pi^-$ as a function of $dN_{ch}/d\eta$ from the $p + p$ and $Au + Au$ collisions at $\sqrt{s_{NN}}$=200 GeV from the STAR Experiment [80].
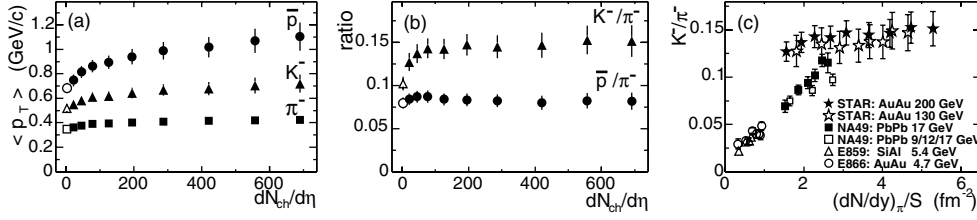
Figure 6.13: a) $\langle p_T \rangle$, K^-/π^- and $\bar{p}/\pi^-$ as a function of $dN_{ch}/d\eta$. c) Midrapidity K^-/π as a function of $\frac{dN/dy)_\pi}{S}$. Figure taken from [80].

In this section we would like to briefly discuss the EMCIC effect on these two observables in the absence of any other physics that can affect them.

Equation 6.28 provides us formula on the EMCIC effect on the single particle distribution. However, to make any calculation involving integrated spectra (Eq. 6.28) we have to make an assumption about the parent distribution ($\tilde{f}(p_T)$). Here, we are going to use the thermal distribution $\tilde{f}(p_T) \sim e^{-m_T/T}$. We also use the following EMCIC parameters in Eq. 6.28: $\langle p_T^2 \rangle = 0.17$ (GeV/c)^2, $\langle p_z^2 \rangle = 0.32$ (GeV/c)^2, $\langle E^2 \rangle = 0.51$ GeV^2 and $\langle E \rangle = 0.68$ GeV. At the end, we use the following values of the parameter T in the thermal distribution: $T = 100$ MeV for pions and $T = 200$ MeV for protons.

Now, we are ready to calculate the ratio of integrated spectra for pions and protons for different multiplicities. For the sake of the argument we assume that this ratio is equal to 1 in the absence of EMCIC effect. Results are presented in Fig. 6.14

Similarly, we can calculate the effect of EMCIC on the average momentum. Figure 6.15 shows the average momentum for pions and protons plotted versus the multiplicity. In our calculations we assumed that $\langle p_T \rangle = 0.3$ GeV/c for pions and $\langle p_T \rangle = 0.6$ GeV/c for proton, independence on the multiplicity. Thus, we would expect flat lines
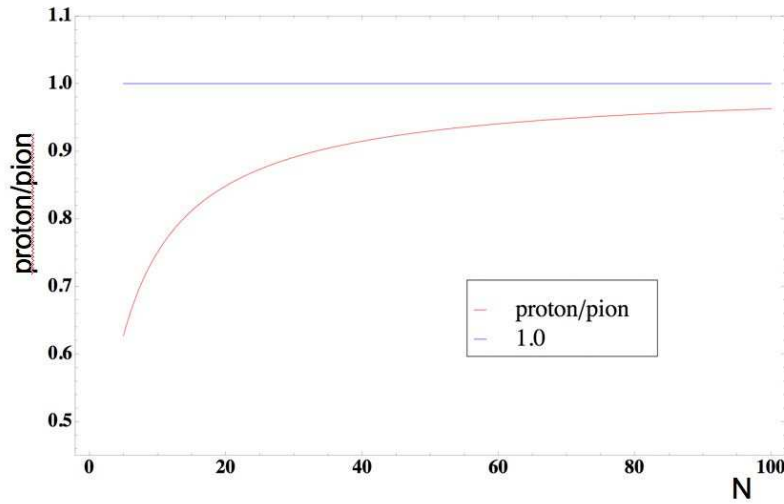
Figure 6.14: The EMCIC effect on the pion to proton ratio (y-axis) plotted versus the event multiplicity (x-axis).

on Fig. 6.15 in the absence of the conservation laws. However, it is clear that these distributions have strong dependence on the multiplicity at lower multiplicity range and the effect is stronger for heavier particles.

We showed that the phase-space effect due to energy and momentum conservation laws has a strong effect on average momentum and the particle ratios. Thus, one must account for this effect before speculating on other physics effects that can cause a difference in these two quantities in small systems like $p + p$ and big systems like $Au + Au$ collisions.
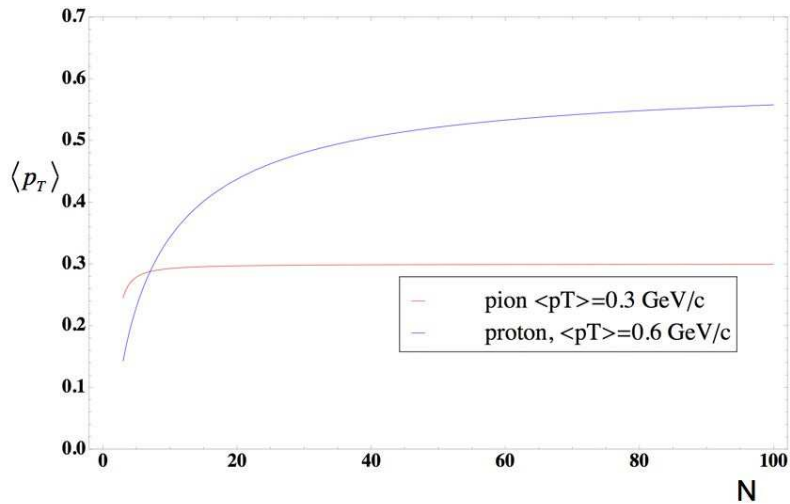
Figure 6.15: The EMCIC effect on the average p_T

6.5 EMCICs in two-particle correlations

6.5.1 EMCICS from GENBOD

In this Section, we briefly discuss factors which affect the $A_{l,m}$ moments, using Figures 6.16-6.21. For the present, we focus only on the green squares, labeled "CF (GenBod)," in those Figures.

Figures 6.16, 6.17 and 6.18 show the $A_{l,m}$'s calculated in LCMS frame [26] from GENBOD events that have the same average kinetic energy per particle ($\bar{K} = 0.9$ GeV) but different multiplicity. As expected, the strength of the EMCICs decreases with event multiplicity. Similarly, for a given event multiplicity, one expects larger EMCICs when there is less available energy. As shown in Figures 6.17 and 6.19 for multiplicity-18 events, this is indeed the case.

Since the definition of the "out," "side" and "long" directions– and thus the angles θ and ϕ– depend on the frame of measurement, one expects the spherical harmonic

74
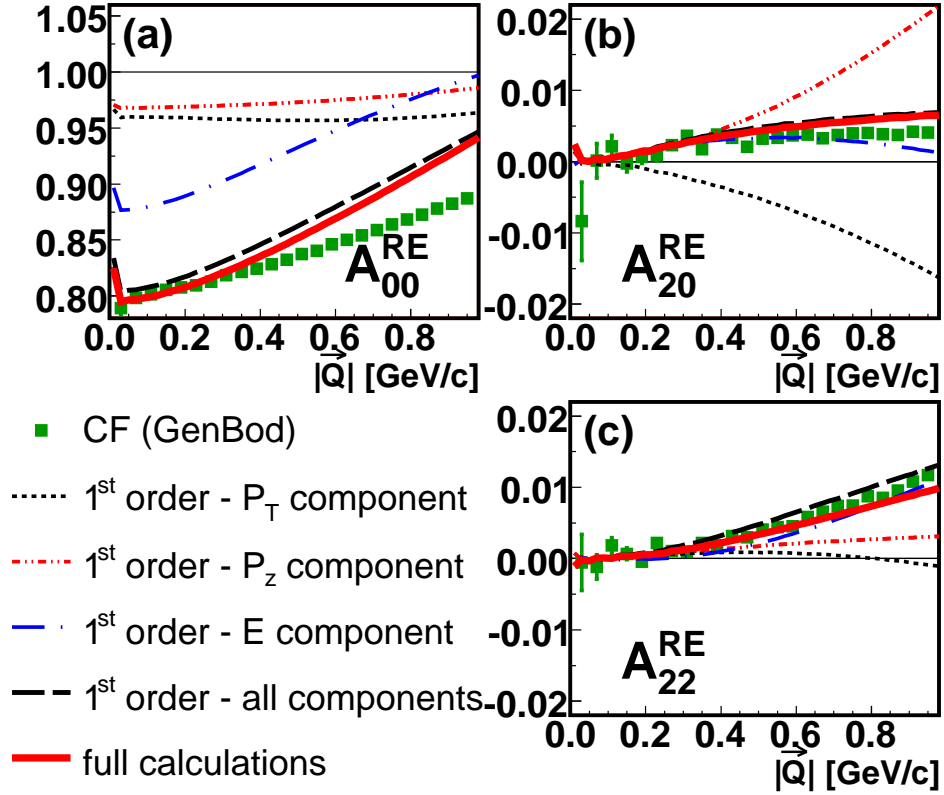
Figure 6.16: SHD coefficients for GENBOD -generated events consisting of 9 pions having average kinetic energy per particle $\bar{K} = 0.9$ GeV, as measured in the pair LCMS frame. No kinematic cuts were applied to data. Green squares are $A_{l,m}$'s from the GENBOD events. Red solid lines are the SHD coefficients of Equation 6.22 for k=2. Black dotted, red dot-dash-dotted and blue dash-dotted lines are SHD coefficients of the first, second and third terms, respectively, of the right side of Equation 6.23. Black dashed lines are SHD coefficients of the right side of Equation 6.23.

coefficients $A_{l,m}$ to depend on reference frame. This is shown in Figures 6.17 and 6.20

for correlations measured in LCMS and pair CMS frames.
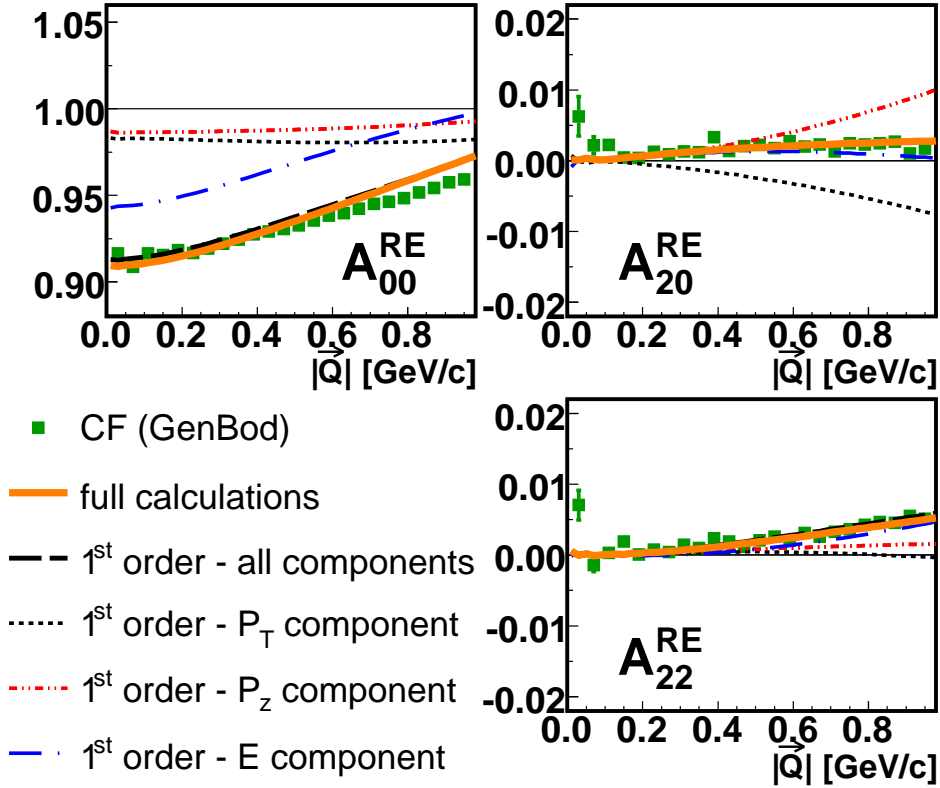
Figure 6.17: SHD coefficients for GENBOD -generated events consisting of 18 pions having average kinetic energy per particle $\bar{K} = 0.9$ GeV, as measured in the pair LCMS frame. No kinematic cuts were applied to data. Green squares are $A_{l,m}$'s from the GENBOD events. Orange solid lines are the SHD coefficients of Equation 6.22 for k=2. Black dotted, red dot-dash-dotted and blue dash-dotted lines are SHD coefficients of the first, second and third terms, respectively, of the right side of Equation 6.23. Black dashed lines are SHD coefficients of the right side of Equation 6.23.

6.5.2 Kinematic cut dependence

Less intuitive is the observation that the correlation strength depends also on kinematic cuts. Figures 6.20 and 6.21 show the $A_{l,m}$'s calculated by GENBOD for 18-pion events without and with a selection of $|\eta| < 0.5$, respectively. (Note that this cut applies to the pions which are used in the analysis, *not* to the set of particles for which

76
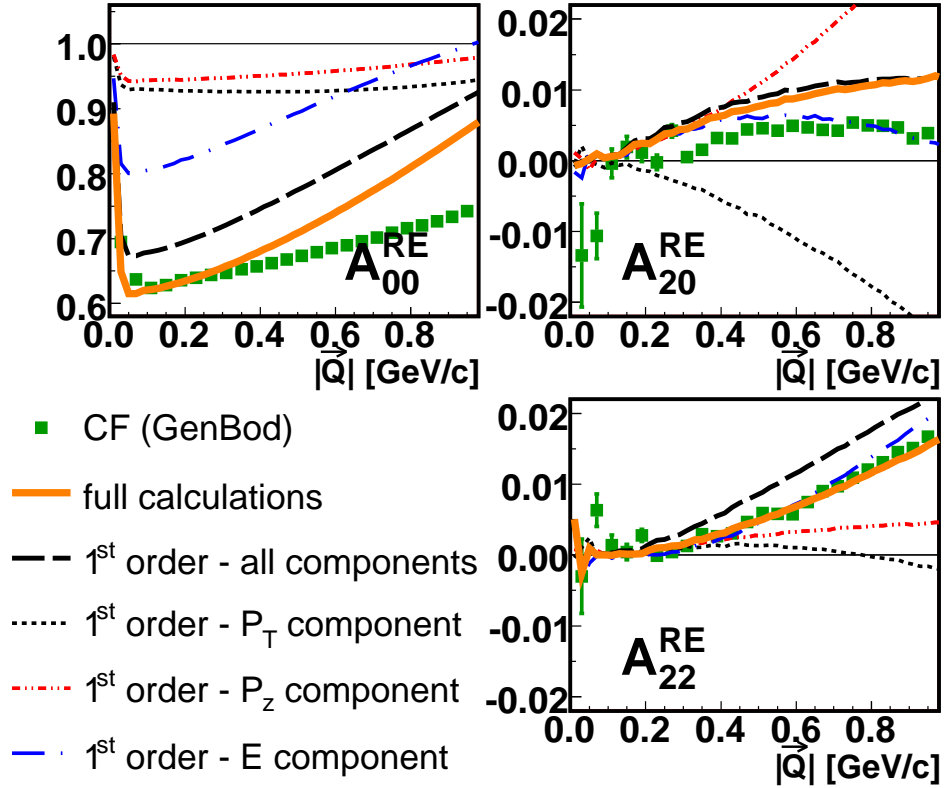
Figure 6.18: SHD coefficients for GENBOD -generated events consisting of 6 pions having average kinetic energy per particle $\bar{K} = 0.9$ GeV, as measured in the pair LCMS frame. No kinematic cuts were applied to data. Green squares are $A_{l,m}$'s from the GENBOD events. Orange solid lines are the SHD coefficients of Equation 6.22 for k=2. Black dotted, red dot-dash-dotted and blue dash-dotted lines are SHD coefficients of the first, second and third terms, respectively, of the right side of Equation 6.23. Black dashed lines are SHD coefficients of the right side of Equation 6.23.

energy and momentum is conserved; energy and momentum is always conserved for the full event.)

Finally, we note two important and generic effects. Firstly, EMCICs are present at all values of $|\vec{Q}|$, reminding us that we cannot (responsibly) ignore these effects in a femtoscopic analysis. Secondly, in Figures 6.20 and 6.21, we have included $A_{l,m}$ components up to $l = 4$. Typically, $|A_{l+2,m}/A_{l,m}| \sim 0.1$, another reminder that
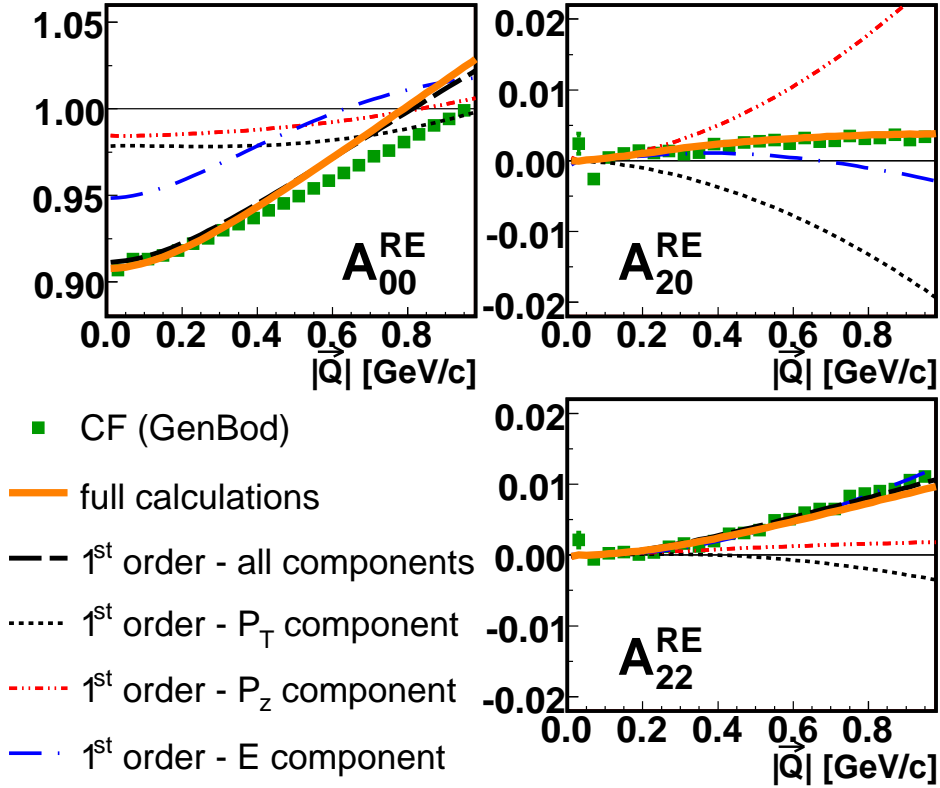
Figure 6.19: SHD coefficients for GENBOD -generated events consisting of 18 pions having average kinetic energy per particle $\bar{K} = 0.5$ GeV, as measured in the pair LCMS frame. No kinematic cuts were applied to data. Green squares are $A_{l,m}$'s from the GENBOD events. Orange solid lines are the SHD coefficients of Equation 6.22 for k=2. Black dotted, red dot-dash-dotted and blue dash-dotted lines are SHD coefficients of the first, second and third terms, respectively, of the right side of Equation 6.23. Black dashed lines are SHD coefficients of the right side of Equation 6.23.

characterization of the 3-dimensional correlation function requires only a few harmonic components.

6.5.3 Calculating EMCICs from GENBOD

In Section 6.2.3 we derived the formula for EMCIC effect on two-particle correlation function. If we somehow know N, $\langle p_T^2 \rangle$, $\langle p_z^2 \rangle$, $\langle E^2 \rangle$ and $\langle E \rangle$, we can calculate
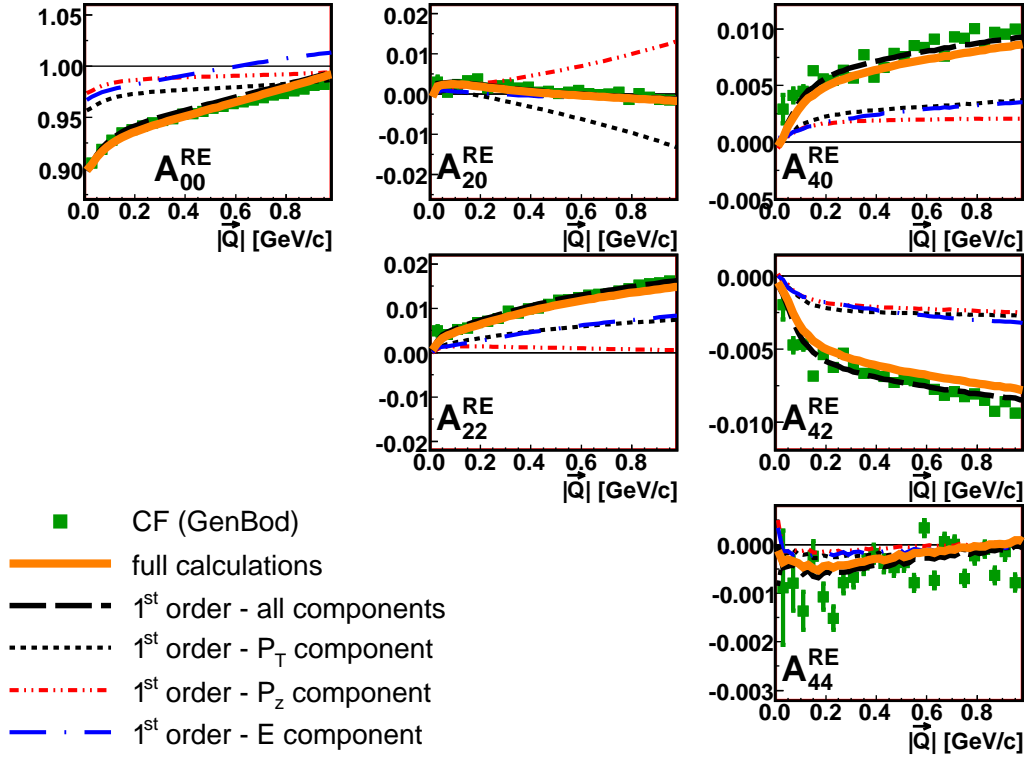
Figure 6.20: SHD coefficients for GENBOD -generated events consisting of 18 pions having average kinetic energy per particle $\bar{K} = 0.9$ GeV, as measured in the pair CMS frame. No kinematic cuts were applied to data. Green squares are $A_{l,m}$'s from the GENBOD events. Orange solid lines are the SHD coefficients of Equation 6.22 for k=2. Black dotted, red dot-dash-dotted and blue dash-dotted lines are SHD coefficients of the first, second and third terms, respectively, of the right side of Equation 6.23. Black dashed lines are SHD coefficients of the right side of Equation 6.23.

EMCICs using Equation 6.22. (See, however, the discussion at the start of the next Section.) Better yet, if N is large enough, then we can use Equation 6.23. This is what is done in Figures 6.16-6.21. The open circles and orange inverted triangles represent the results of Equation 6.22 and Equation 6.23, respectively. The black circles, blue stars, and red triangles show the individual components of Equation 6.23; this decomposition will be relevant when we discuss the "experimentalist's formula" in the next Section.
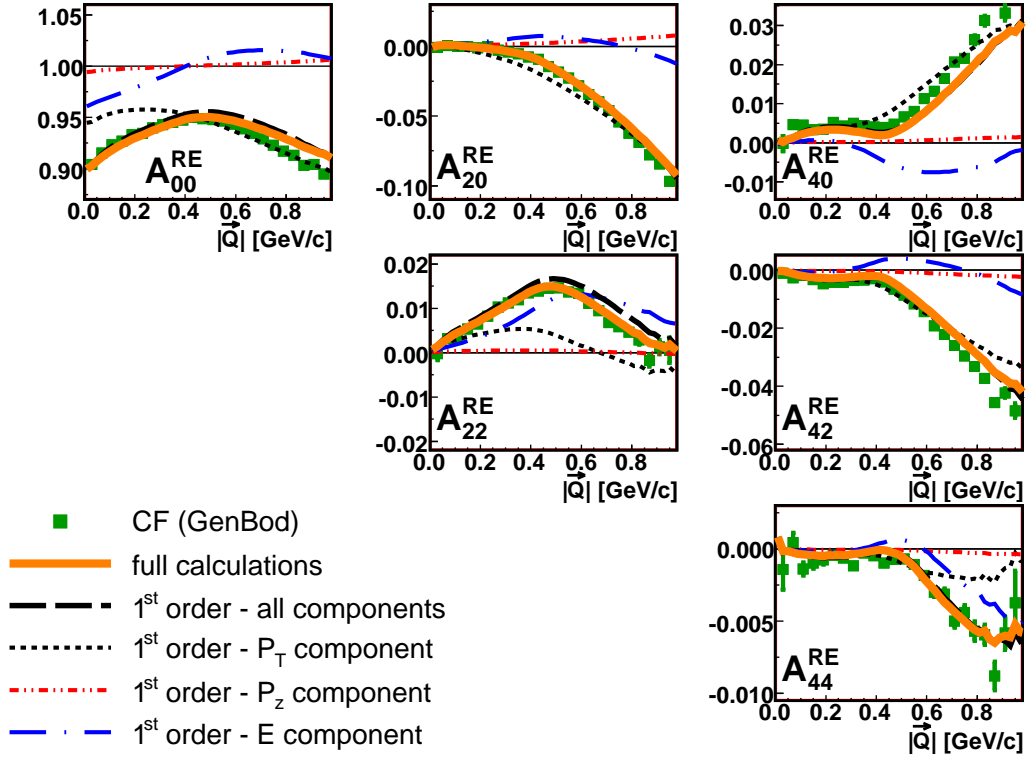
Figure 6.21: SHD coefficients for GENBOD -generated events consisting of 18 pions having average kinetic energy per particle $\bar{K} = 0.9$ GeV, as measured in the pair CMS frame. Only particles with $|\eta| < 0.5$ used in the correlation function. Green squares are $A_{l,m}$'s from the GENBOD events. Orange solid lines are the SHD coefficients of Equation 6.22 for k=2. Black dotted, red dot-dash-dotted and blue dash-dotted lines are SHD coefficients of the first, second and third terms, respectively, of the right side of Equation 6.23. Black dashed lines are SHD coefficients of the right side of Equation 6.23.

Figures 6.16-6.21 make clear that each of the three terms in Equation 6.23 produces non-trivial behavior of the $A_{l,m}$'s. Also clear is the importance of not neglecting the energy term. We find also that the p_z term affects $A_{2,2}$; this may be surprising since $A_{2,2}$ quantifies the behavior of the correlation function in the "out-side" plane, while $\hat{z}$ is the "long" direction in the Pratt-Bertsch system. Clearly, EMCICs projected onto a 2-particle space are non-trivial objects.

The first-order expansion (Equation 6.23) agrees well with the full expression (Equation 6.22) for $N \gtrsim 10$. Such multiplicities are relevant for $p + p$ measurements at RHIC (recalling that N includes all particles, even unmeasured ones). We see also that the analytic calculations (open circles and inverted triangles) approximate the results of the GENBOD simulation (green squares), especially as the multiplicity and total energy of the event increases; increasing agreement for large N and E_{tot} is expected, given the approximations leading to our analytic expressions. We observe also that the analytically-calculated expressions respond identically to the kinematic cuts as does the simulation (c.f. Figures 6.20 and 6.21).

Finally, the analytic calculations never reproduce *exactly* the simulations; we discuss this further in the next Section.

6.5.4 An experimentalist's formula

Even for large N and energy, the calculations do not exactly reproduce the EMCIC effects in the simulation. One reason for this may be found, in fact, in the definition of the average values (e.g. $\langle p_z^2 \rangle$) themselves. In Equation 6.10, average quantities are calculated using the distribution $\tilde{f}(p)$, which is not affected by EMCICs. Naturally, the only measurable distribution available to the experimentalist (even when GENBOD simulations serve as the "experiment") is $\tilde{f}_c(p)$.

Thus, it appears the experimentalist cannot plug her data into the equations 6.10 and 6.23 to fully calculate EMCICs. However, such an ambition would have been hopeless anyhow. After all, even the total multiplicity N (again, including photons etc) is rarely fully measured, and in principle N is a number of "primary" particles, a murky concept in itself.

To the practicing femtoscopist, there is a natural solution. Having at hand (1) educated guesses for the quantities N, $\langle E^2 \rangle$ etc, and (2) a physically-motivated functional form which connects these quantities to the correlations, one may perform a fit. Let us rewrite Equation 6.23 as

$$C\left(p_1, p_2\right) = 1 - M_1 \cdot \overline{\{\vec{p}_{1,T} \cdot \vec{p}_{2,T}\}} - M_2 \cdot \overline{\{p_{1,z} \cdot p_{2,z}\}} \tag{6.31}$$
$$-M_3 \cdot \overline{\{E_1 \cdot E_2\}} + M_4 \cdot \overline{\{E_1 + E_2\}} - \frac{M_4^2}{M_3},$$

where

$$M_1 \equiv \frac{2}{N\langle p_T^2 \rangle} \quad , \quad M_2 \equiv \frac{1}{N\langle p_z^2 \rangle}$$
$$M_3 \equiv \frac{1}{N\left(\langle E^2 \rangle - \langle E \rangle^2\right)} \quad , \quad M_4 \equiv \frac{\langle E \rangle}{N\left(\langle E^2 \rangle - \langle E \rangle^2\right)}. \tag{6.32}$$

The notation $\overline{\{X\}}$ in Equation 6.31 highlights the fact that X is a two-particle quantity which depends on p_1 and p_2 (or $\vec{q}$, etc). From a practical point of view, X will be averaged over the same $\vec{q}$ bins as used for the correlation function. For infinitesimally narrow q-bins, $\overline{\{X\}} = X$. The binned functions $\overline{\{X\}}$ then automatically reflect the same event and particle selection as the correlation function. This involves nothing more than adding four more histograms to the several already being constructed by the experimentalist as she processes pairs in the data.

Here, we should emphasize that, in Equation 6.31, $\vec{p_1}$, E_1, $\vec{p_2}$, and E_2 should be calculated in the collision center-of-momentum (CCM) frame. The reason is that Equation 6.7 (hence Eqs. 6.8-6.32) assumes some fixed total energy and momentum to be conserved. The event's total energy and momentum (hence $\langle E \rangle$, $\langle \vec{p} \rangle$, etc appearing in Eqs. 6.8-6.32) are fixed quantities in any given frame. In a *pair*-dependent frame (e.g. LCMS), the total energy and momentum of the event will fluctuate, pair-by-pair. Thus, while the correlation function may be *binned* in whatever frame one

chooses, the momenta p_i^μ on the right side of Eqs. 6.7-6.32 must be calculated in a pair-independent frame. In fact, starting with Equation 6.17, we have chosen the CCM, for simplicity.

The parameters M_i defined in Equation 6.32, on the other hand, are global and independent of p_1 and p_2. It is these which we will use as fit parameters. The task is then fast and straightforward; the EMCIC part of the correlation function $C(\vec{q})$ is simply a weighted sum of four functions. Indeed, one may calculate coefficients as in Equation 4.4 for the four new functions. For example

$$A_{l,m}^{pz}(Q) \equiv \sum_{\text{bins } i} \overline{\{p_{1,z} \cdot p_{2,z}\}}(Q, \cos\theta_i, \phi_i) \cdot Y_{l,m}(\cos\theta_i, \phi_i), \tag{6.33}$$

etc. Then, thanks to the linearity of Equation 6.31 and the orthonormality of $Y_{l,m}$'s, the measured $A_{l,m}$'s themselves are similarly just weighted sums of harmonics

$$A_{l,m}(Q) = \delta_{l,0} \cdot \left(1 - M_4^2/M_3\right) - M_1 \cdot A_{l,m}^{pr}(Q) \tag{6.34}$$

$$-M_2 \cdot A_{l,m}^{pz}(Q) - M_3 \cdot A_{l,m}^{(E \cdot E)}(Q) + M_4 \cdot A_{l,m}^{(E+E)}(Q).$$

Treating Equation 6.34 as a fit, we have a few (say six, for $l \leq 4$) *one*-dimensional functions to fit with four adjustable weights. The number of degrees of freedom in this four-parameter fit remains high: ~ 300, for six $A_{l,m}$'s, each with 50 bins in $|Q|$.

An example is shown in Figure 6.22, where GENBOD -calculated correlation functions are fitted with the form of Equation 6.34. Not surprisingly, the minimization procedure returned fit parameters M_i very close to the values calculated via Equation 6.32. However, exact agreement between the "best" parameter values returned by the fit, and those from Equation 6.32 is not expected. This is because the large-N approximation is only approximately valid and due to the fact that $\tilde{f}(p) \neq \tilde{f}_c(p)$, as

83
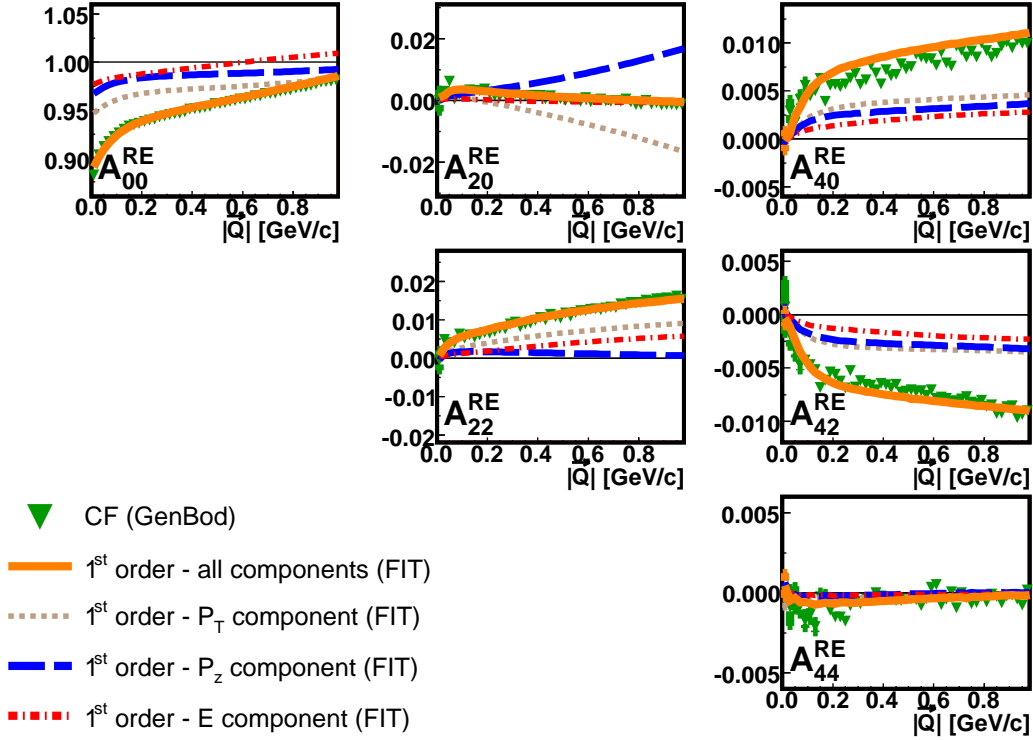
Figure 6.22: Green inverted triangles show the $\pi^- - \pi^-$ correlation function, in the pair rest frame, from 18-pion GENBOD -generated events. The black curve is a result of a fit with the "experimentalist's formula" from Equation 6.34. Other curves represent the three component terms of the fit: $M_1 \cdot A^{p_T}_{l,m}(Q)$ in the brown dotted line; $M_2 \cdot A^{p_z}_{l,m}(Q)$ in the blue dashed line; $M_3 \cdot A^{E \cdot E}_{l,m}(Q) + M_4 \cdot A^{E+E}_{l,m}(Q)$ in the red dash-dot line. See text for details.

discussed previously. Treating the M_i as adjustable parameters leads to a slightly different weighting of the terms, and a slightly better fit to the data.

Our original goal was not to understand EMCICs *per se*, but to extract the femtoscopic information from measured two-particle correlations. Assuming that the only non-femtoscopic correlations are EMCICs, one may simply add the femtoscopic terms $\Phi_{\text{femto}}(p_1, p_2)$ to the fitting function in Equation 6.31 or 6.34.

$$C\left(p_1, p_2\right) = \Phi_{\text{femto}}(p_1, p_2) \times \tag{6.35}$$

$$\left(\ 1 - M_1 \cdot \overline{\{\vec{p}_{1,T} \cdot \vec{p}_{2,T}\}} - M_2 \cdot \overline{\{p_{1,z} \cdot p_{2,z}\}}\right.$$
$$\left.-\ M_3 \cdot \overline{\{E_1 \cdot E_2\}} + M_4 \cdot \overline{\{E_1 + E_2\}} - \frac{M_4^2}{M_3}\right).$$

Common femtoscopic fitting functions (e.g. Gaussian in the out-side-long space) usually contain ~ 5 parameters (e.g. N, λ, R_i, $i = o, s, l$). In the imaging technique [94], one assumes the separation distribution is described by a sum of splines, rather than a Gaussian; here, too, there are usually 4-5 fit parameters (spline weights). So, by including EMCIC effects, we have roughly doubled the number of fit parameters, relative to a "traditional" fit which ignores them. This is a non-trivial increase in analysis complexity. However, we keep in mind two points.

Firstly, the increased effort is simply necessary. EMCICs (and possibly other important non-femtoscopic correlations) are present and increasingly relevant at low multiplicity. One option is to ignore them, as has sometimes been done in early high-energy experiments. However, with the new high-quality data and desire for detailed understanding at RHIC, ignoring obvious features such as those presented in [95] is clearly unacceptable. Perhaps a slightly better option is to invent an ad-hoc functional form [51] without a strong real physical basis. We hope that the results here present a relatively painless and more reasonable, third option.

Secondly, while the non-femtoscopic EMCICs are not confined to the large-Q region (an important point!), the femtoscopic correlations are confined to the small-Q region. Therefore, one hopes that the addition of four new parameters to the fit of the correlation function will not render the fit overly unwieldy. While we cannot

expect complete block-diagonalization of the fit covariance matrix, one hopes that the M_i are determined well enough at high Q that the femtoscopic fit parameters can be extracted at low Q.

6.6   Non-identical particle correlations

For at least two reasons, it is important to turn attention to correlations between non-identical particles.

First, it is natural to ask whether one can use other particle combinations to "correct" for effects of EMCICs in, say, identical-pion correlation functions. After all, EMCICs are induced by global constraints on the entire event, not a specific particle species. For example, various experiments have explored using (π^+, π^-) correlations to account for EMCICs in (π^+, π^+) correlation functions [50, 52, 96].

Second, it is also important to know whether EMCICs could cloud the interpretation of correlations between non-identical particles. It is increasingly common to study asymmetries in the correlation functions of, say $\pi - K$ pairs [38], interpreting such as a "shift" in the average point of emission between the two particles [97]. In the spherical harmonic decomposition, such shifts appear in the $l = 1$ moments (c.f. Appendix F). We will find that EMCICs can indeed generate an asymmetry which might naively be considered proof of a femtoscopic shift.

Here we discuss two effects– one immediately obvious and one more subtle– which are relevant for the above issues. The discussion is broken into three parts. Neglecting EMCICs and any other source of correlation at first, we briefly show the effects of two common resonances on correlations between oppositely-charged pions in a toy model. Thus calibrated, we use the more realistic and complex PYTHIA model to illustrate

a non-trivial interplay between EMCICs and the resonances, which can mock up a femtoscopic asymmetry signal. Finally, we return to a toy model– now with non-identical particles and EMCICs, but without resonances or the several other sources of correlation present in PYTHIA – to make clear the mechanism behind the special effects EMCICs have on non-identical particle correlations.

6.6.1 Effect of resonances

First we consider the effect of resonances. To focus on effects other than global EMCICs we use a toy model in which only ten identical resonances per event are generated and no other particles. The momentum of each resonance is generated from a thermal distribution; energy and momentum are conserved for each decay separately, but not globally for the whole event.

Figure 6.23 shows the spherical harmonic moments of (π^+, π^-) correlation functions for events including ω (blue squares) and ρ resonances (orange triangles). As seen, even without considering EMCICs, the correlations among particles coming from resonance decays produce non-trivial structure. In this case, one cannot simply divide (π^+, π^+) correlation function by (π^+, π^-) to "remove" EMCICs.

6.6.2 Entrance channel asymmetries

In addition to the correlation between daughters of resonance decays (c.f. Fig. 6.23), there is a more subtle effect to consider. This happens when the two particles have different inclusive momentum distributions *and* energy and momentum are globally conserved. Under these conditions non-identical particle correlations exhibit structure absent in identical particle correlations.
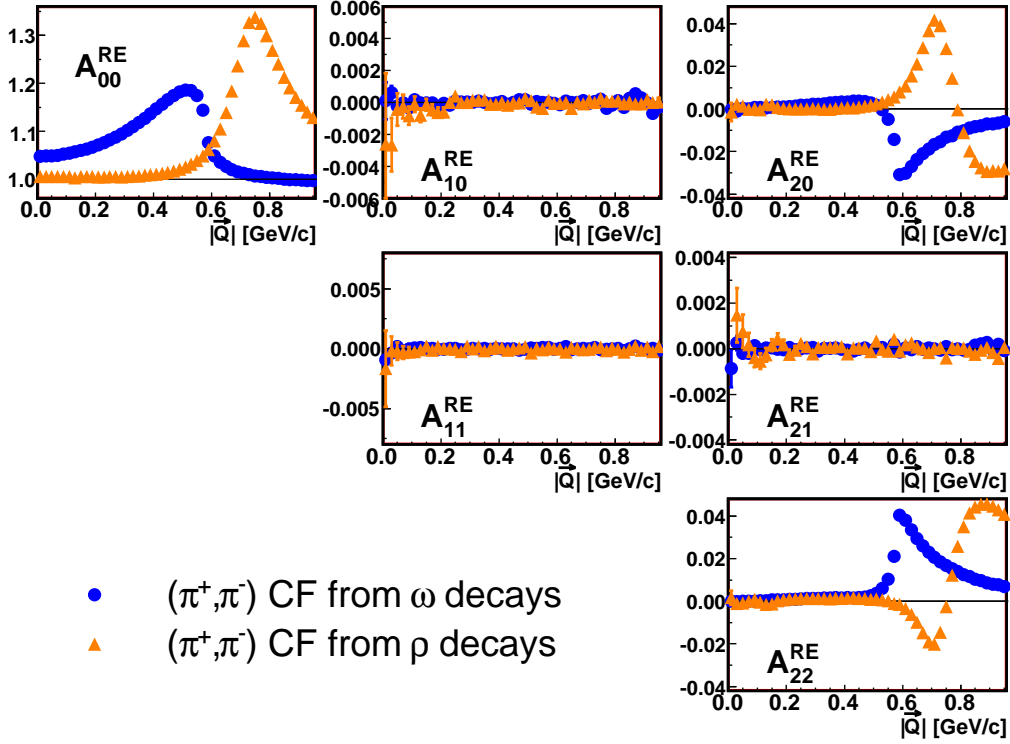
Figure 6.23: (π^+, π^-) correlation functions calculated in the LCMS frame for events including ω (blue squares) and ρ (orange triangles) resonances .

Figure 6.25 shows PYTHIA [72] calculations of (π^+, π^-) correlations for $p + p$ and $p + \bar{p}$ collisions at 200 GeV. In addition to obvious correlations between daughters of resonance decays (K_s^0, ω, ρ), we see additional structure. We focus on the structure in the $l = 1$ moments. In general, such moments need not vanish for correlations of non-identical particles, as discussed in Appendix F.

Correlations between sibling daughters of ρ and ω resonance decay do not generate $l = 1$ moments, as seen in Section 6.6.1. However, pions which are daughters of these decays will in general have a different single-particle momentum distribution than pions from other sources in the event. If the fraction of pions from resonance decay, as a function of pion momentum, is different for π^+ and π^-, then the single-particle
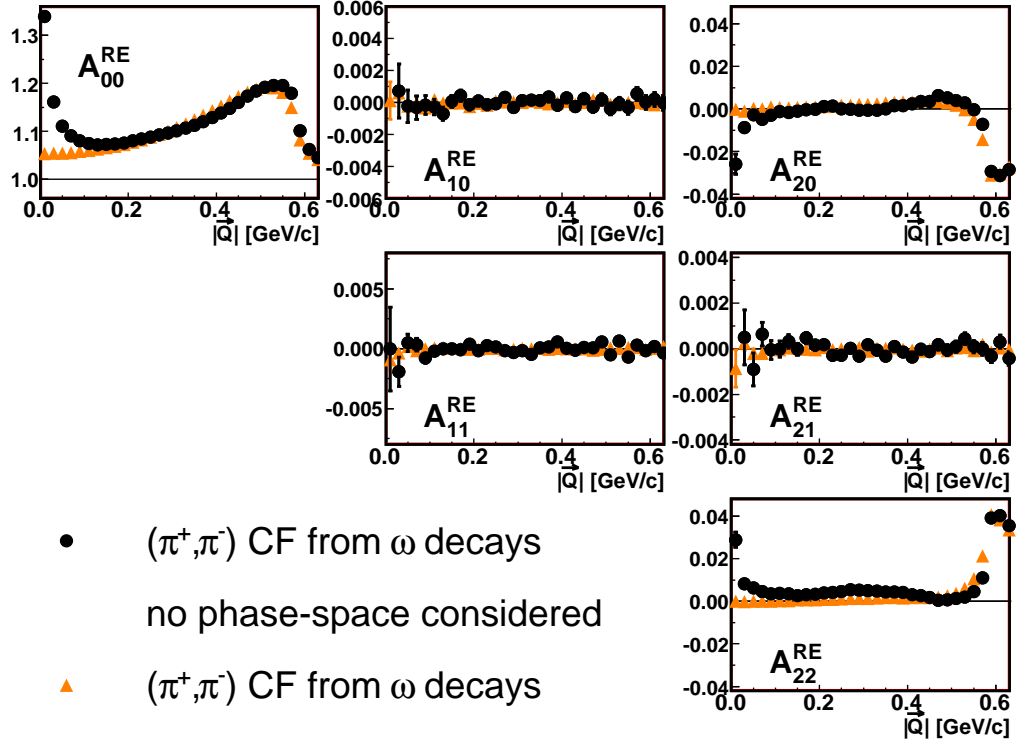
Figure 6.24: (π^+, π^-) correlation functions calculated in the LCMS frame for events including ω resonances. Orange triangles represent the same data as plotted on Fig. 6.23. Black circles represent results from similar simulations but without taking into account the phase-space of ω decays.

distributions of positive and negative pions will be different. We argue below that it is this difference in single-particle distributions which is the key to the non-vanishing $l = 1$ moments; that this difference may arise from resonances in the case at hand is irrelevant.

In the $p + \bar{p}$ collisions, the fraction of π^+ coming from any given source (e.g. ρ-decay) must be identical to that of π^-, for a given value of p_T. Thus the p_T distribution of π^- must be identical to that of π^+. However, the rapidity distributions will be mirror images of each other. Thus, any asymmetry in $\pi^- - \pi^+$ correlations from $p + \bar{p}$ collisions will be associated with q_{long}, and will appear in $A_{1,0}$, as seen in Figure 6.25.
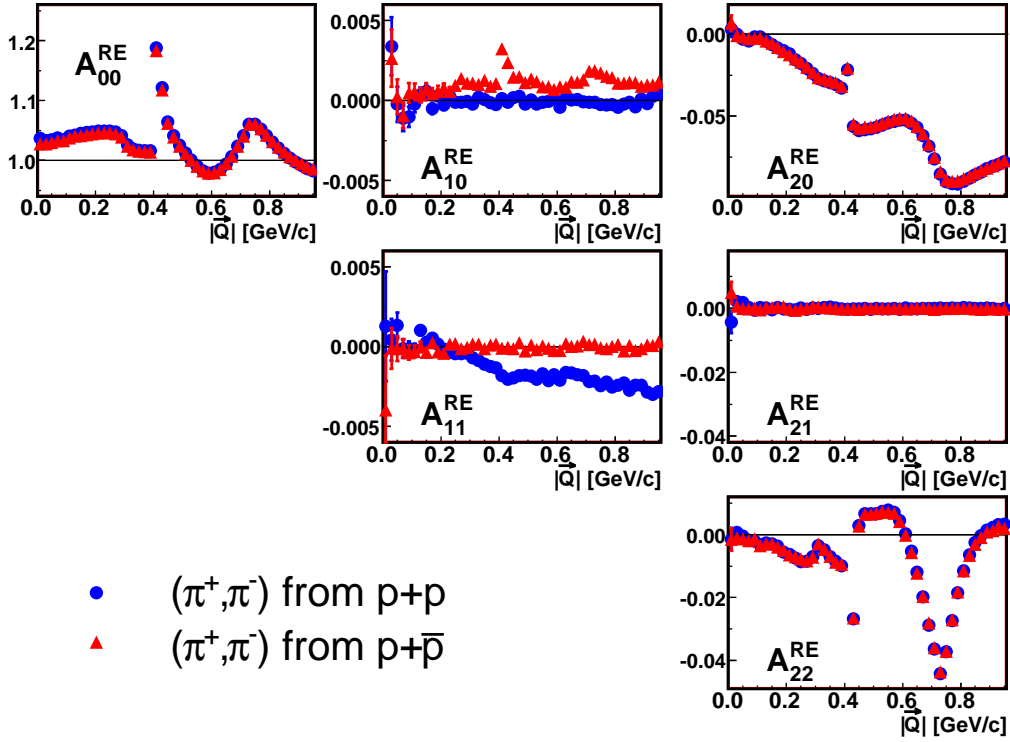
Figure 6.25: SHD moments of (π^+, π^-) correlation function from $p + p$ and $p + \bar{p}$ collisions at 200 GeV calculated from PYTHIA events.

Similarly, the vanishing (non-vanishing) moment $A_{1,0}$ $(A_{1,1})$ for $p+p$ collisions reflects the fact the single-particle distributions will show no asymmetry in rapidity, but may differ as a function of p_T.

Since single-particle distributions divide out of a correlation function, a difference between π^+ and π^- momentum distributions, by itself, cannot generate a signal in $A_{l,m}$'s. Rather, a global correlation, coupled with this difference, generates the signal. We discuss this further below.

6.6.3 A simpler case

In Section 6.6.2, we argued that the small difference in single-particle momentum distributions between positive and negative pions produced by PYTHIA , coupled with global conservation laws, generated non-trivial EMCICs in the non-identical particle correlations. However, PYTHIA contains many non-EMCIC sources of correlations, related to string fragmentation and other processes, which might be flavor/isospin-dependent. To make clearer our argument, we here show a simple GENBOD simulation, containing both pions and protons, but no explicit correlations between them such as a Δ resonance. Due at least to their different masses, $\tilde{f}_{\text{proton}} \neq \tilde{f}_{\text{pion}}$ is guaranteed.

Figures 6.26 shows the $\pi - p$ correlation function. Since the underlying single-particle proton and pion distributions are isotropic, $A_{1,0}$ (sensitive to shape elongation in $C(\vec{q})$ in q_l relative to transverse components) is expected to vanish. $A_{1,1}$ is finite, however, due to differences in p_T distributions. Since there is no other source of correlation in the simulation, this obviously is an EMCIC.

From Figure 6.26 it is also clear that neither Equation 6.22 nor its first-order expansion 6.23 fully describes the correlation function. This is due to the fact that our formalism is built on the assumption that all particles in the system follow the same parent distribution, as pointed out after Equation 6.10.

6.7 The System

All formulas that describe the effect of the phase-space constraints on momentum observables (e.g. Eqs. 6.28 and 6.35) depend on five parameters N, $\langle p_T^2 \rangle$, $\langle p_z^2 \rangle$, $\langle E \rangle$ and $\langle E^2 \rangle$.
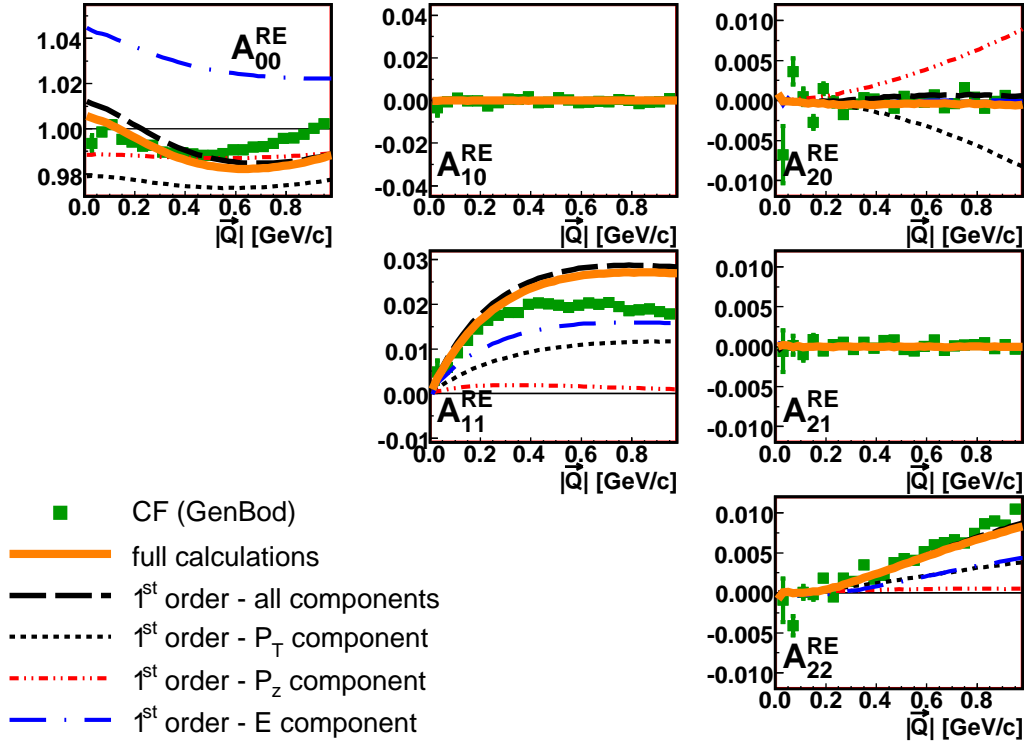
Figure 6.26: Green squares show the $\pi - p$ correlation function, in the pair rest frame, from GENBOD -generated events. Orange solid lines are the SHD coefficients of Equation 6.22 for k=2. Black dotted, red dot-dash-dotted and blue dash-dotted lines are SHD coefficients of the first, second and third terms, respectively, of the right side of Equation 6.23. Black dashed lines are SHD coefficients of the right side of Equation 6.23.

Clearly, we do not know and even cannot know the values of these parameters a priori. However, we expect that they should track measured quantities but not be identical to them. For example, the multiplicity N carries information of all primary particles while we can never measure all particles experimentally. Probably it is fine to assume that secondary decays should not count in N. It rather become clear that the these parameters should describe the characteristic scales of the relevant system

in which limited energy-momentum is shared and not the entire system (e.g. all particles emitted in $p + p$ collisions).

In this chapter, we will try to give a rough estimate on what the values of these parameters we should expect based on analytical and Monte-Carlo calculations.

6.7.1 PYTHIA

η_{max}	$\langle N \rangle$	$\langle p_T^2 \rangle_c$	$\langle p_z^2 \rangle_c$	$\langle E^2 \rangle_c$	$\langle E \rangle_c$
1.0	7.5	0.58	0.41	1.45	0.98
2.0	13.4	0.59	2.81	3.89	1.57
3.0	17.9	0.59	12.95	14.01	2.65
4.0	21.5	0.59	82.45	83.55	5.13
5.0	23.4	0.59	262.88	265.03	8.29
∞	23.6	0.59	275.23	276.4	8.48

Table 6.3: For a given selection on pseudorapidity $|\eta| < \eta_{max}$, the number and kinematic variables for primary particles from a PYTHIA simulation of $p + p$ collisions at $\sqrt{s_{NN}} = 200$ GeV are given. Units are GeV/c or $(GeV/c)^2$, as appropriate. 100k events were used and all decays were switched off in simulations.

η_{max}	$\langle N \rangle$	$\langle p_T^2 \rangle_c$	$\langle p_z^2 \rangle_c$	$\langle E^2 \rangle_c$	$\langle E \rangle_c$	$\langle p_T \rangle_c$
1.0	16	0.20	0.11	0.40	0.44	0.32
2.0	29	0.21	0.76	1.05	0.68	0.32
3.0	39	0.21	3.5	3.8	1.2	0.32
4.0	47	0.21	24	25	2.2	0.33
5.0	51	0.22	88	89	3.7	0.33

Table 6.4: For a given selection on pseudorapidity $|\eta| < \eta_{max}$, the number and kinematic variables for final state particles from a PYTHIA simulation of $p + p$ collisions at $\sqrt{s_{NN}} = 200$ GeV are given. 100k events were generated and default PYTHIA parameters were used in simulations. Units are GeV/c or $(GeV/c)^2$, as appropriate.

To get a feeling for these values, we look at $p + p$ collisions at $\sqrt{s_{NN}}$=200 GeV, simulated by the PYTHIA event generator (v6.319) [72]. In the model, we can identify primary particles, thus avoiding some of the issues discussed above. However, the fact that PYTHIA conserves momentum means that we access $\langle p_\mu^n \rangle_c$ as defined by Equation 6.27, not the parameters of the parent distribution. Nevertheless, a scale for our expectations may be set. Table 6.3 summarizes the result for primary particles satisfying a varying cut on pseudorapidity where all particle decays where switched off in PYTHIA simulations. The results from simulations when resonance decays were included in simulations are presented in Table 6.4. These two tables gives us rough estimates of ranges of the total multiplicity and kinematic variables that one may expect.

Additionally, we list the average number of particles per event for different particle species in Tables 6.5 and 6.6.

particle	η_{max}						
	0.5	1.0	2.0	3.0	4.0	5.0	∞
π^+	0.300	0.596	1.139	1.570	1.875	2.054	2.100
π^-	0.284	0.565	1.076	1.464	1.719	1.822	1.849
π^0	0.298	0.585	1.130	1.534	1.825	1.968	1.992
K^+	0.072	0.141	0.270	0.363	0.418	0.444	0.447
K^-	0.063	0.126	0.239	0.316	0.362	0.376	0.374
K^0	0.068	0.133	0.253	0.337	0.384	0.394	0.401
K^0_*	0.093	0.179	0.318	0.457	0.515	0.524	0.527
K^+_*	0.095	0.189	0.366	0.497	0.568	0.593	0.590
K^-_*	0.085	0.167	0.320	0.430	0.489	0.496	0.499
ρ^0	0.266	0.523	1.016	1.389	1.643	1.738	1.744
ρ^+	0.270	0.537	1.037	1.425	1.705	1.838	1.852
ρ^-	0.258	0.502	0.976	1.331	1.542	1.609	1.611
ω	0.266	0.527	1.013	1.386	1.633	1.737	1.752
η	0.153	0.300	0.579	0.786	0.925	0.982	0.989
$\eta(958)$	0.054	0.107	0.206	0.280	0.326	0.346	0.349
p	0.060	0.116	0.224	0.319	0.542	0.819	0.830
$\bar{p}$	0.053	0.103	0.199	0.268	0.298	0.298	0.301
n	0.054	0.109	0.207	0.295	0.496	0.760	0.772
e^-	0.001	0.002	0.004	0.005	0.005	0.006	0.006
γ	~ 0	~ 0	~ 0	~ 0	~ 0	~ 0	~ 0

Table 6.5: The total number of primary particles per event for a given selection on pseudorapidity $|\eta| < \eta_{max}$ from a PYTHIA simulation of $p + p$ collisions at $\sqrt{s_{NN}} = 200$ GeV is given. 100k events were used and all decays were switched off in simulations.

6.7.2 Maxwell-Boltzmann distribution

The bulk component of single-particle spectra is often estimated with Maxwell-Boltzmann distributions, with inverse slope parameters in the range $T \sim 0.15 \div 0.35 \, GeV$. Again, simply for rough guidance, we list Maxwell-Boltzmann expectations for our kinematic parameters in Table 6.7, assuming pion-dominated system.

particle	η_{max}	
	1.0	∞
π^+	2.946	10.200
π^-	2.878	9.503
π^0	~ 0	~ 0
K^+	0.351	1.068
K^-	0.320	0.939
K^0	~ 0	~ 0
K^0_*	~ 0	~ 0
K^+_*	~ 0	~ 0
K^-_*	~ 0	~ 0
ω	~ 0	~ 0
η	~ 0	~ 0
$\eta(958)$	~ 0	~ 0
p	0.244	1.808
$\bar{p}$	0.225	0.612
n	0.231	1.437
e^-	6.794	23.230
γ	0.042	0.142

Table 6.6: The total number of final state particles per event for a given selection on pseudorapidity $|\eta| < \eta_{max}$ from a PYTHIA simulation of $p + p$ collisions at $\sqrt{s_{NN}} = 200$ GeV is given. 100k events were generated and default PYTHIA parameters were used in simulations.

	non-rel. limit	ultra-rel. limit	if $T = 0.15 \div 0.35 GeV$
$\langle p_T^2 \rangle$	$2mT$	$8T^2$	$0.045 \div 0.98 \ (GeV/c)^2$
$\langle E^2 \rangle$	$\frac{15}{4}T^2 + m^2$	$12T^2$	$0.10 \div 1.50 \ GeV^2$
$\langle E \rangle$	$\frac{3}{2}T + m$	$3T$	$0.36 \div 1.00 \ GeV$

Table 6.7: The average kinematic variables obtained from the Maxwell-Boltzmann distribution $f(p) = \frac{dN}{dp^3} \sim e^{-E/T}$ using non-relativistic and ultra-relativistic limit. A pion gas is assumed.

6.7.3 Blast-wave model

We also used the Blast-wave model [7] to estimate the kinematic scales of the system. In our calculations we assumed that the radial velocity $\beta = 0.52c$ and temperature $T = 100 MeV$. As a results we got the following numbers for pions

$$
\begin{aligned}
\langle p_T \rangle &= 0.405 \ [\text{GeV/c}] \\
\langle p_T^2 \rangle &= 0.240 \ [(\text{GeV/c})^2] \\
\langle m_T \rangle &= 0.435 \ [\text{GeV}] \\
\langle m_T^2 \rangle &= 0.259 \ [\text{GeV}^2]
\end{aligned}
\tag{6.36}
$$

More details and applications of this model can be found in chapter 9.3.

CHAPTER 7

THE STAR EXPERIMENT

The STAR Experiment is one of the four experiments at RHIC. In this chapter, we describe the STAR detector focusing on the most important sub-detectors that were crucial for the analysis presented in this thesis.
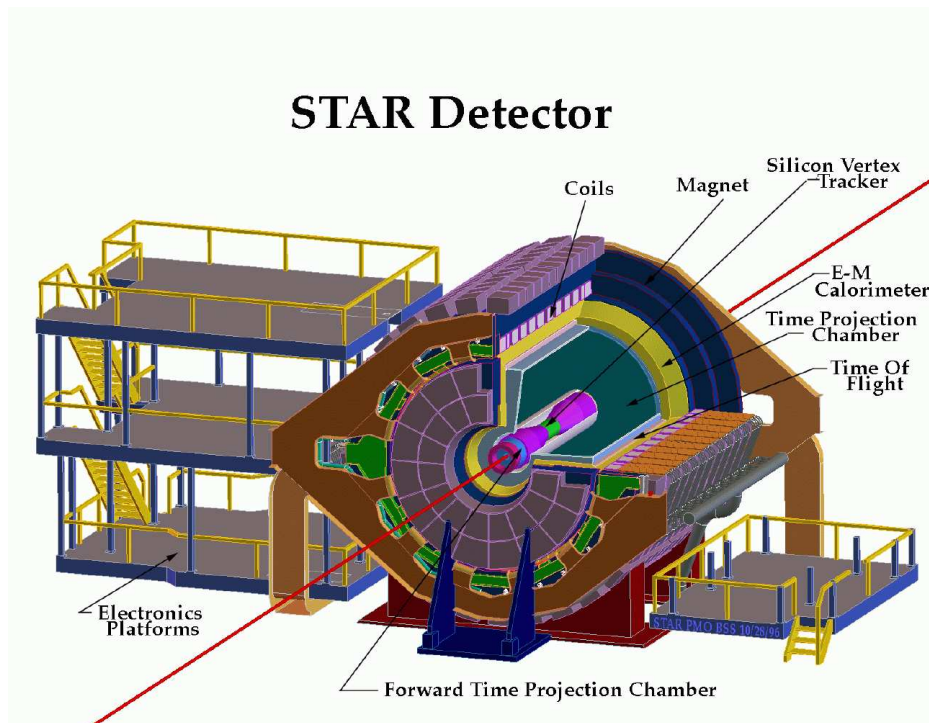
Figure 7.1: The STAR Detector.

7.1 The Relativistic Heavy Ion Collider

The Relativistic Heavy Ion Collider (RHIC) is located at Brookhaven National Laboratory (BNL) on Long Island, New York. The circumference of the RHIC ring is about 3.8 km and there are six interaction points at which two beams can collide. The design luminosity for gold-gold collisions is of order $10^{26}cm^{-2}s^{-2}$ and for proton-proton collisions it is $10^{32}cm^{-2}s^{-2}$. The maximum polarization of the proton beam is $\approx 70\%$.

There were four experiments developed at RHIC. One of them PHOBOS [98] that was designed to study heavy-ion collisions finished taking data in 2005. Two biggest experiments are PHENIX [99] and STAR [100] and BRAHMS [101] is the fourth one. The last three experiments can also study transversely polarized proton+proton collisions and additionally PHENIX and STAR can also study longitudinally polarized protons.

The diagram of the RHIC facility is presented in Figure 7.2. For a complete overview see [102, 103].

7.2 $p + p$ collisions. Proton structure

The proton, together with neutron and electron, is one of the basic building blocks of atomic matter. Although it was discovered more than 80 years ago and its complexity has been studied extensively for decades, its composition is still not completely understood. It is known that the proton consists of *partons*, including *quarks* and particles carrying the force that binds them, called *gluons*. Additionally, quarks can be categorized as *valence* or *sea* (quarks). In the simplest model, the proton consists of three valence quarks (uud) and each one carries one third of proton's linear
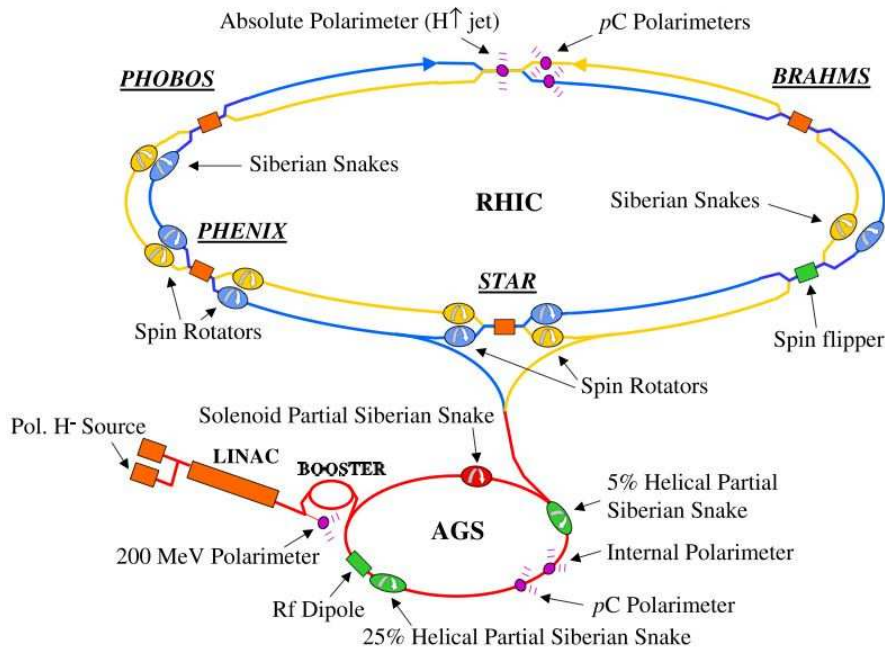
Figure 7.2: The RHIC-AGS complex.

momentum. However, measurements showed that also gluons and sea $q - \bar{q}$ pairs are present and even though each of them carries a small fraction of the proton's momentum their summed momentum is significant.

The Relativistic Heavy Ion Collider (RHIC) at Brookhaven National Laboratory is capable of colliding heavy ions up to the energy of $\sqrt{s_{NN}} = 200$ GeV and polarized protons up to 500 GeV. It can also operate with different species in the two beams as e.g. $d + Au$ collisions. Due to its versatility it can cover a wide range of physics interests.

For the first few years of taking data, the main focus was on the heavy ion program whose main goal is the investigation of the properties of nuclear matter at extremely high temperatures and energy densities. It allows to verify whether a new form of

matter called quark-gluon plasma (QGP) [104] has been formed and to study its properties. The other interest of the experiments at RHIC is the polarized proton program whose goal is a better understanding of the spin structure of the proton and eventually to solve the "proton spin crisis". The advantage of exploring the proton structure using hadronic collisions, rather than to the electromagnetic probes which do not couple to the electromagnetically neutral gluons, is that the observation of gluon-scattering processes can be made directly. The other advantage of RHIC is that it can provide collisions at very high energies in the center of the mass frame that are much higher than can be achieved in the fixed-target experiments. In such conditions the hard processes can be studied using the perturbative quantum chromodynamics (pQCD).

7.3   The Solenoidal Tracker At RHIC (STAR) detector
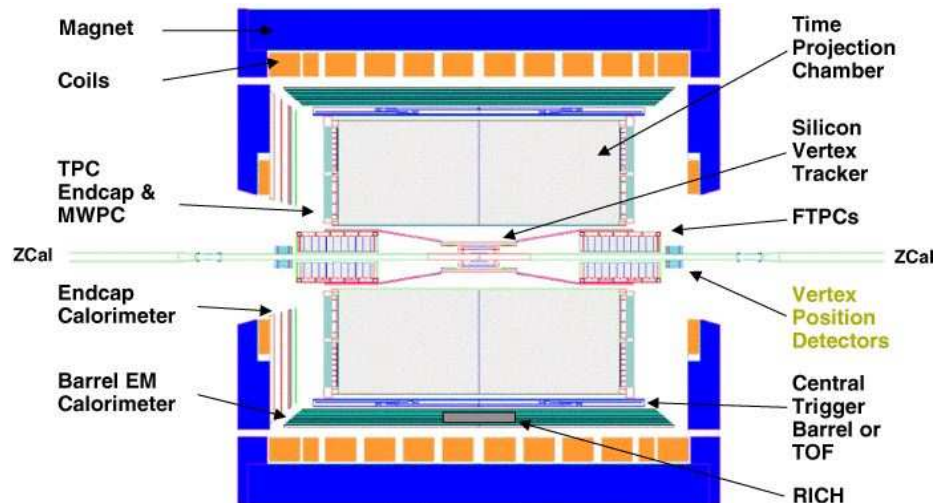
Figure 7.3: The STAR Detector.

The main tracking device of the STAR experiment (The Solenoidal Tracker at RHIC) - and also the largest one (see Fig.7.3) is the Time Projection Chamber (TPC) [105] that covers the pseudorapidity range $-1.2 < \eta < 1.2$ and has a full acceptance in the azimuthal angle. Also the Forward Time Projection Chamber (FTPC) [106] is used to reconstruct charged particles emitted in at the forward rapidity ($2.8 < |\eta| < 3.8$).

Beam Beam Counters (BBC) are scintillator detectors surrounding the beam pipe and serve are the minimum bias trigger as well as an device to measure absolute and relative luminosity. Additionally BBC coincidences are used to suppress a beam gas background. These detectors cover the pseudorapidity range $3.3 < |\eta| < 5.0$. Forward Pion Detector (FPD) consists of eight calorimeters of lead glass cells and serves as a trigger and reconstruction device of neutral pions produced with $3.3 < \eta < 4.2$. The other two STAR calorimeters are Barrel Electromagnetic Calorimeter (BEMC) [107] and Endcap Electromagnetic Calorimeter (EEMC) [108].

CHAPTER 8

DATA ANALYSIS

8.1 Event selection

The primary sub-detector used to reconstruct particles in the analysis of the data from $p + p$ and $d + Au$ and $Au + Au$ collisions is the Time Projection Chamber (TPC) [105]. Due to the size and acceptance of the TPC detector we use only events that come from collisions that appeared close to the center of the TPC detector. Thus, we require the z-component (along the beam axis) of the primary vertex to be within 30 cm from the center of the detector for $p + p$ collisions at $\sqrt{s}$=200 GeV and 50 cm for $d + Au$ collisions at $\sqrt{s_{NN}}$=200 GeV and 40 cm for $Au + Au$ collisions at $\sqrt{s_{NN}}$=19.6 GeV.

Additionally, since we are interested in studying same charged pion correlations we require each event to have at least two like-sign pions at midrapidity, $|y| \leq 0.5$.

Figure 8.1 presents the distribution of the number of the charged particles registered per unit of rapidity in the STAR TPC detector. Particles that go into this number must have a reconstructed vertex within 1 cm from the reconstructed collision vertex, $p_T < 3$ GeV and $|\eta| \leq 0.5$. With the current data statistics from
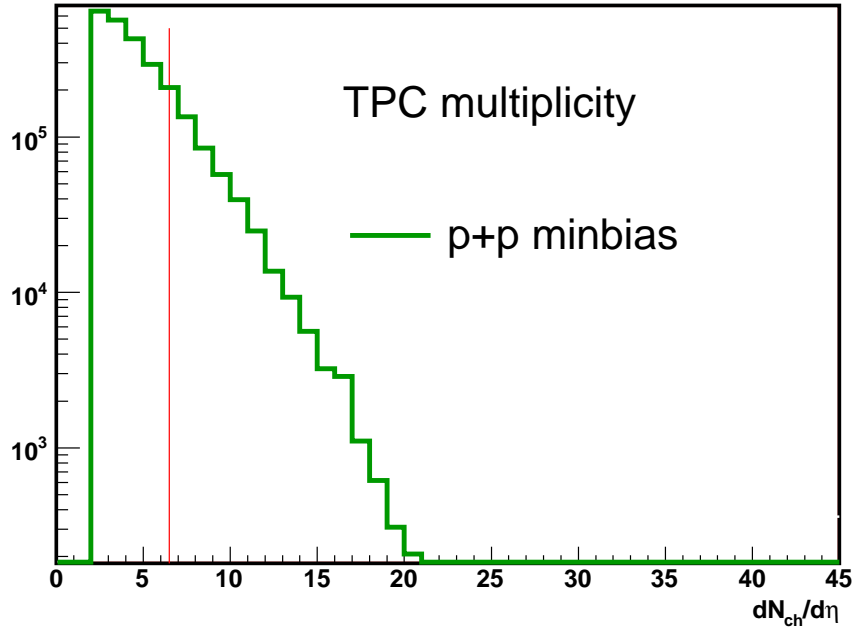
Figure 8.1: The multiplicity distribution from $p + p$ collisions at $\sqrt{s}$=200 GeV measured using information from the TPC detector. (STAR Preliminary results).
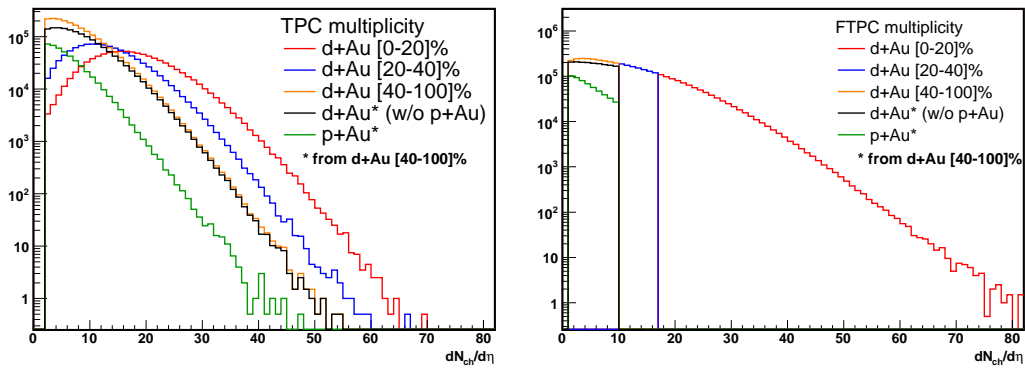
Figure 8.2: The multiplicity distribution from $d + Au$ collisions at $\sqrt{s}$=200 GeV for different centralities and the distribution from $p + Au$ and $d + Au$ collisions extracted from the peripheral $d + Au$ collisions measured using information from the TPC detector (left panel) and the FTPC detector (right panel).

104
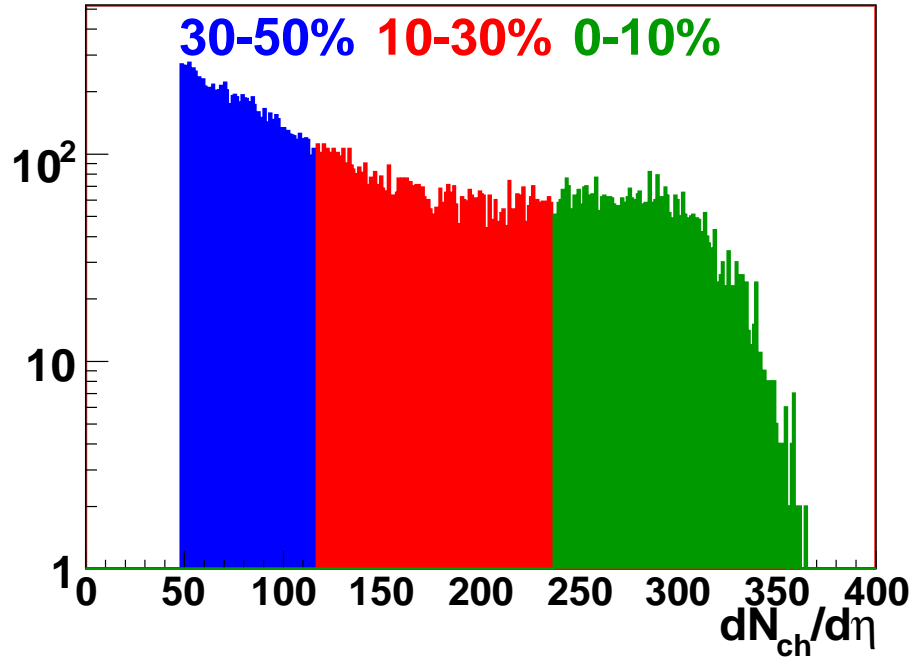
Figure 8.3: The multiplicity distribution from $Au + Au$ collisions at $\sqrt{s}$=19.6 GeV for different centralities.

$p + p$ collisions we were able to divide the data sample into two multiplicity bins: $dN_{ch}/d\eta = [2, 6]$ and $dN_{ch}/d\eta = [7, \infty)$. Red line on Fig. 8.1 shows this separation.

A large data statistics in $d + Au$ collisions allows to perform an analysis for three centralities. This selection is based on the number of charged particles within $-3.8 < \eta < -2.8$ measured by the Forward Time Projection Chamber (FTPC) [106]. The distribution of the number of charged particles measured in both TPC and FTPC detectors is presented on Fig. 8.2. Additionally, by using the Zero Degree Calorimeter (ZDC) detector we are able to separate $p + Au$ from $d + Au$ collisions by selecting events with a single neutron tagged in ZDC in the deuteron beam director.

E

system	$\langle dN_{ch}/d\eta \rangle$
$d + Au\ [0-20]\%$	17.20
$d + Au\ [20-40]\%$	12.41
$d + Au\ [40-100]\%$	7.38
$d + Au\ (w/o\ p+Au)$	7.40
$p + Au$	4.90
$p + p\ min-bias$	4.26
$p + p\ [2,6]$	3.47
$p + p\ [7,100]$	8.75

Table 8.1: Average number of charged particles per unit of rapidity in different systems at the same energy of the collision; $\sqrt{s_{NN}}$=200 GeV after the requierement that there have to be at least 2 identical pions in the event.

Table 8.1 list the average number of the charged particles per unit of rapidity obtained for different systems and centralities. After cuts, about 5 million minimum bias events from $p + p$ collisions at $\sqrt{s}$=200 GeV and 8 million minimum bias events from $d + Au$ collisions at $\sqrt{s_{NN}}$=200 GeV were used.
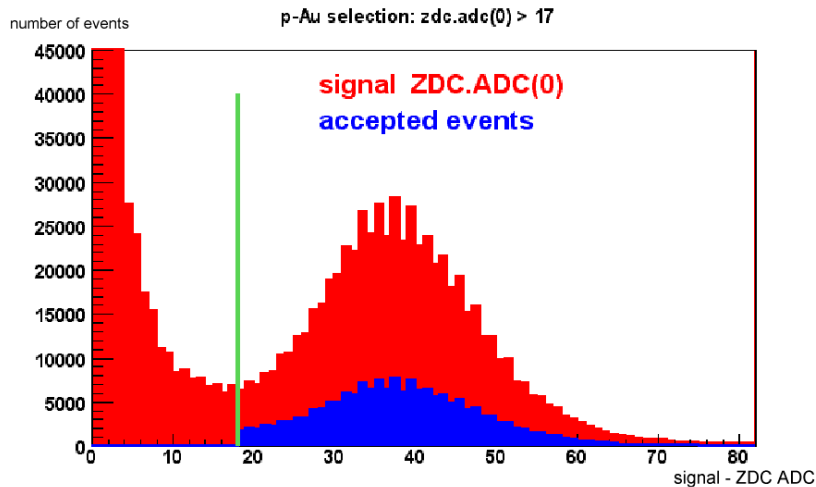
Figure 8.4: Signal (ZDC ADC) registered in the center of the ZDC detector used to identified a single-neutron tagged events - $p + Au$ collisions (events on the right side of the vertical line plotted on this figure.

The low energy $Au + Au$ run was very short and we have only about 44 thousands events. However, even with such a low data statistics, we were able to do HBT analysis in the most central $Au + Au$ collisions at $\sqrt{s_{NN}}$=19.6 GeV using about 20 thousands events. The average multiplicity in this [0-10%] centrality bin is 114.

8.2   Particle selection
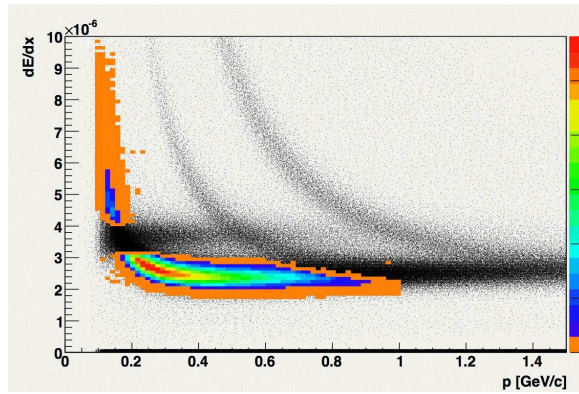
Figure 8.5: The distribution of the ionization energy loss of particle in the gas of the TPC detector versus its transverse momentum in $d + Au$ collisions at $\sqrt{s_{NN}}$=200 GeV. Color band represent particles reconstructed as pions. See text for more details.

Particle identification (PID) was achieved by measuring the correlation between the momentum and specific ionization losses of charged particles in the gas of TPC (d/dx technique). A particle was considered to be a pion if its dE/dx value for a given momentum was within two sigma around the pion Bethe-Bloch band and more than two sigma of the electron, kaon and proton bands. The contamination due to electrons and kaons is found to be small and impacts mostly the value of λ obtained from the fit white it was only a 1% effect of the femtoscopic radii. The PID technique used in this analysis allows to reconstruct particle momentum of about 800
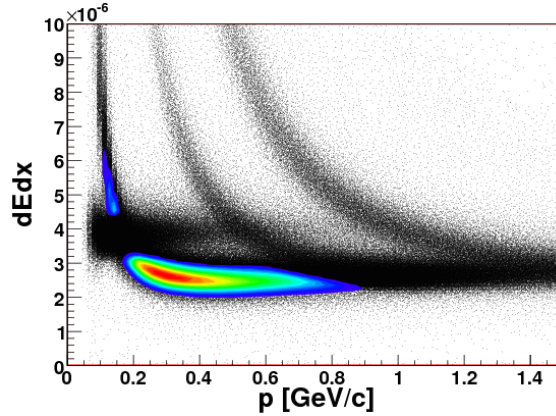
Figure 8.6: The distribution of the ionization energy loss of particle in the gas of the TPC detector versus its transverse momentum in $Au + Au$ collisions at $\sqrt{s_{NN}}$=19.6 GeV. Color band represent particles reconstructed as pions. See text for more details.

MeV/c. The lower momentum cut is about 120 MeV/c and it is imposed by the TPC acceptance and the magnetic field. Only tracks at midrapidity with $|y| < 0.5$ were used here. The above procedure of particle identification was used in both $p + p$ and $d + Au$ collisions at $\sqrt{s}$=200 GeV studied by the STAR Experiment.

8.3   Pair selection. Two-track effects

The analysis presented in this thesis was done for four bins in k_T ($k_T = \frac{1}{2}\left(p_{T,1} + p_{T,2}\right)$) within a range of $[0.15, 0.60]$ GeV/c. The bins are: $[0.15, 0.25]$, $[0.25, 0.35]$, $[0.35, 0.45]$, $[0.45, 0.60]$ GeV/c.

It is particularly important when studying correlations of particles at close relative velocities to account for possible two track effects like splitting (one particle reconstructed as two tracks) and merging (two particles reconstructed as one track). The experimental procedure to taken into account these effect is the same as previously used by STAR experiment and described in details in [67].

108
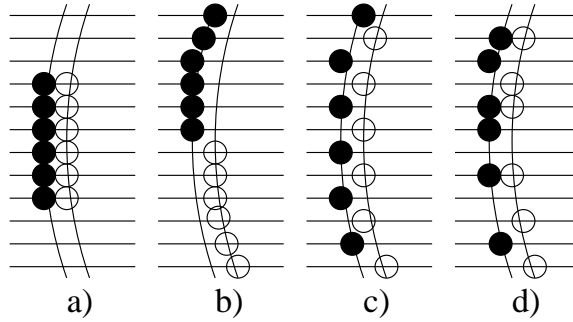
Figure 8.7: Four examples of possible distribution of the same number of hits in two tracks. Closed circles are hits belonging to one track and open circles to the other one. a) SL = 0.5 (two tracks - no splitting) b) SL = 1 (possible split track) c) SL = 1 (possible split track) d) SL = 0.08 (likely two tracks). Figure taken from [67]

Split tracks cause an increase of the number of pairs at low $\vec{q}$. To account for this unwanted effect we use information from TPC and compare the location of hits belonging to each track from the pair along the pad-rows in the TPC detector. A quantity called Splitting Level (SL) is assign to each pair in order to estimate the probability of having a split track. The SL is calculated according to the following formula

$$SL = \frac{\sum_i S_i}{N_{hits,1} + N_{hits,2}} \quad \text{where} \tag{8.1}$$

$$S_i = \begin{cases} +1 & - \text{ one track leaves a hit on a pad} - \text{row} \\ 0 & - \text{ neither track leaves a hit on a pad} - \text{row} \\ -1 & - \text{ both tracks leave hits on a pad} - \text{row} \end{cases}$$

where index i stands for the pad-row number and $N_{hits,1}$ and $N_{hits,2}$ are the number of hits associated to the first and the second track respectively.

Figure 8.7 shows four different configuration of hits and corresponding values of SL. Clearly, if there is no splitting (there are two real tracks) SL=0.5. If all hits belong to one track then SL=1.0. The maximum value of SL that guarantees that most of the split tracks are accounted was obtained by plotting the 1D correlation

function for different values of the upper limit of SL (see Fig. 8.8). Figure 8.9 shows
the correlation function plotted vs SL. The enhancement of pairs observed above
SL¿0.6 is due the splitting tracks. Thus, based on Fig. 8.8 and 8.9 the upper limit on
SL was chosen to be 0.6. Both effects can affect the shape of the correlation function
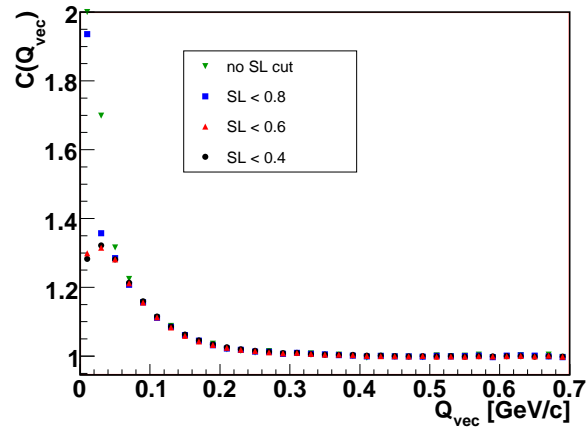
Figure 8.8: $C(Q_{vec})$ correlation functions from $p + p$ collisions at $\sqrt{s}$=200 GeV, in
$k_T = [0.15, 0.60]$ GeV/c for different ranges of splitting level (SL). See text for more
details.
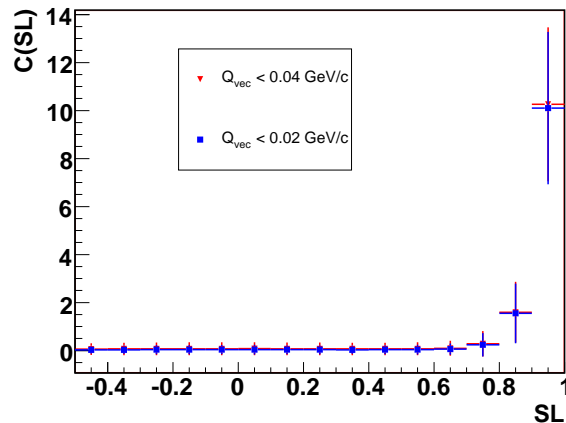
Figure 8.9: Correlation function $p + p$ collisions at $\sqrt{s}$=200 GeV, in $k_T = [0.15, 0.25]$
GeV/c plotted versus the splitting level (SL). See text for more details.
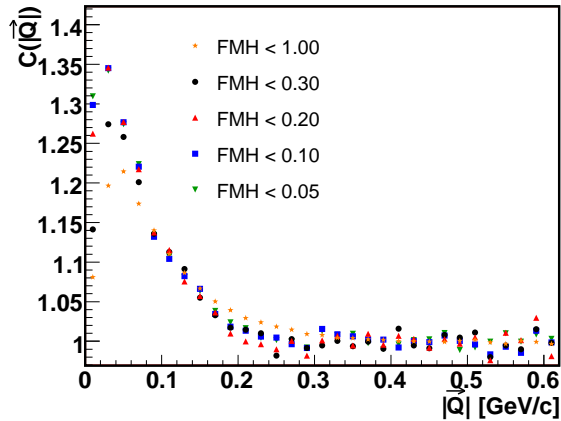
Figure 8.10: 1D correlation function for different values of the maximum fraction of merged hits allowed for a pair to be accepted in the analysis.

at very low $|\vec{q}| < 30$ MeV/c regardless the colliding system. However, their effects on the extracted sizes can be different due to the fact that the width of the correlation function is inversely proportional to the size of the emitting source. Therefore, it is expected that the low-q effects will be less important in $p + p$ collisions due to the fact that their correlation functions are wider than in $Au + Au$ collisions. This expectation has been confirmed and the effect of splitting and merging on the results presented here was found to be very small.

After taken care of the split tracks we should also do the same with the merging tracks. The effect of reconstructing two particles as one track has an opposite effect to splitting and causes the decrease of the number of pairs at low $\vec{q}$. To get rid of this effect we require that pairs from both numerator and denominator of the correlation functions have the fraction of merged hits (FMH) not larger than 10% (see Fig. 8.10). Simulations of the TPC detector were used to determined which hits are merged. It happens when the probability of separating two hits in TPC detector is smaller than 90%.

8.4 Consistency checks

In this section we present the consistency checks we did to verify possible sources of uncertainties that can affect the shape of the correlation function from $p + p$ and $d + Au$ collisions at $\sqrt{s_{NN}}$=200 GeV.

8.4.1 p+p collisions at $\sqrt{s}$=200 GeV
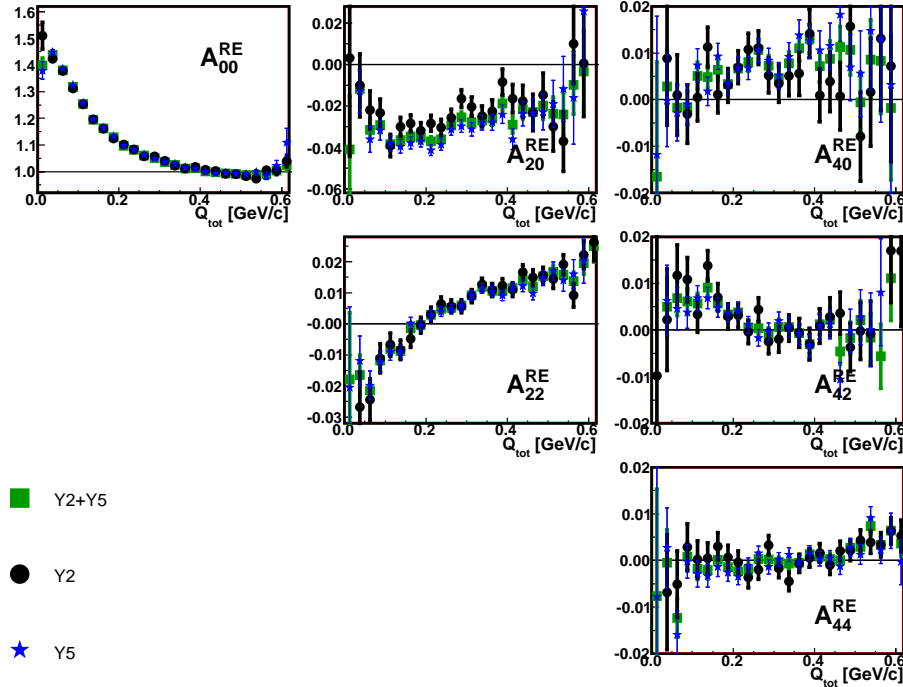
Figure 8.11: Correlation functions from $p + p$ collisions at $\sqrt{s}$=200 GeV for $k_T = [0.15, 0.60]$ GeV/c for two data sets coming from two runs of $p + p$ collisions at RHIC.

The data from $p + p$ collisions used in this thesis comes from two $p + p$ runs at the Relativistic Heavy Ion Collider from which one took place in 2002 and the other one and 2005. Figure 8.11 shows the comparison of the correlation function for

$p + p$ collisions coming from two runs. Based on the fact that no difference is observed we merged both data sets to increase the statistics and analysed them together.

We combined correlation functions for positive and negative pions together in all analyses presented in this paper. However, before we did it we verified that results from positive and negative pion correlations are consistent within the statistical error bars. An example of a comparison of the correlation function for both charged pions is presented on Fig. 8.12.
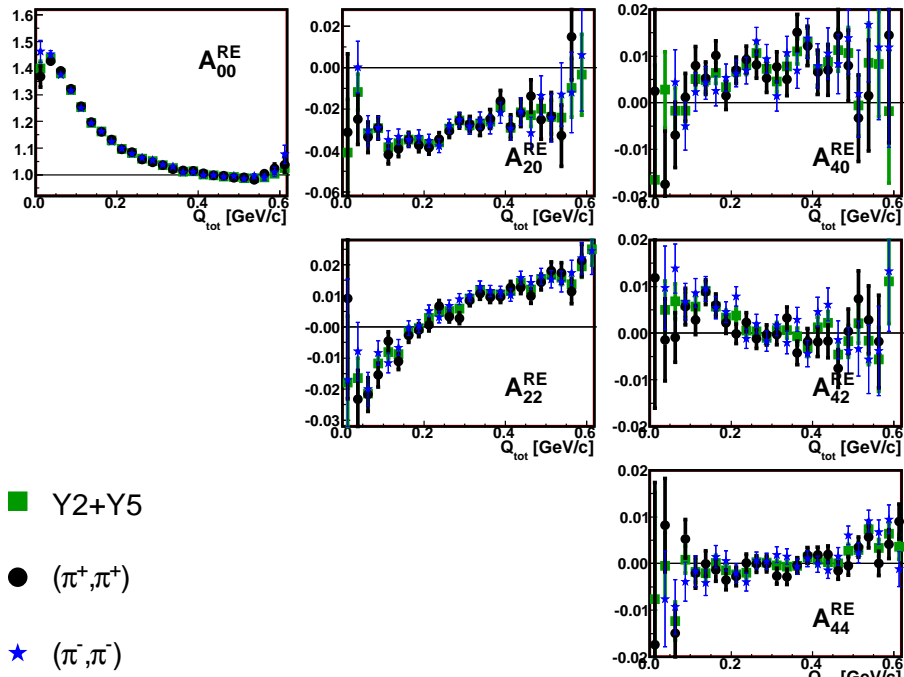
Figure 8.12: (π^+, π^+) and (π^-, π^-) correlation functions from $p + p$ collisions at $\sqrt{s}$=200 GeV for $k_T = [0.15, 0.60]$ GeV/c.

It is possible that a different sign and strength of the magnetic field within the TPC detector can produce some unphysical effects in the registered data. Figure 8.13

shows that there is no difference between the shape of correlation functions for two sets of the magnetic fields.
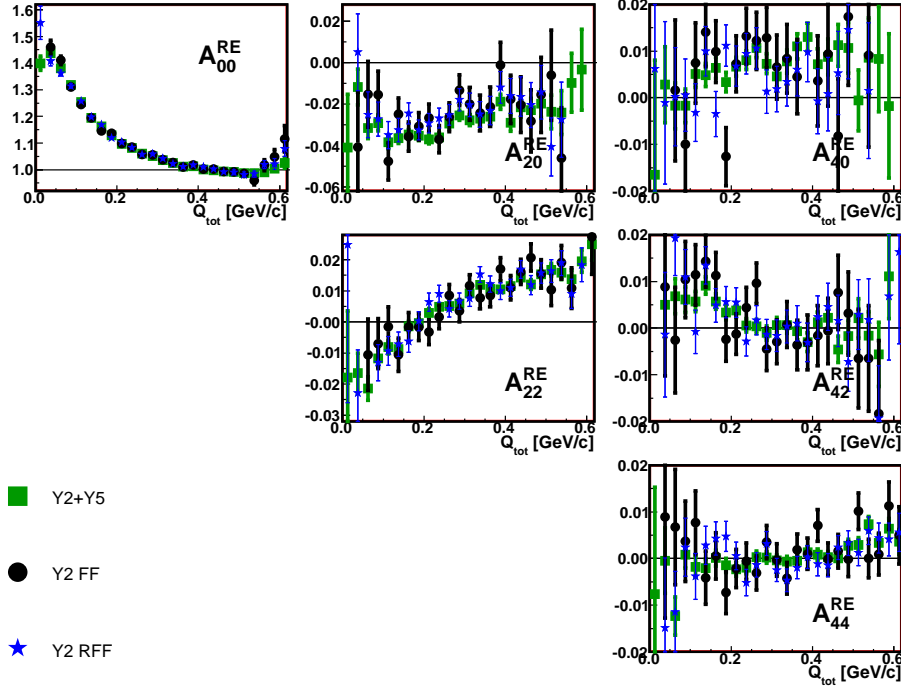
Figure 8.13: Correlation functions from $p + p$ collisions at $\sqrt{s}$=200 GeV for k_T = $[0.15, 0.60]$ GeV/c for two configurations of the magnetic field within TPC.

8.4.2 $d + Au$ collisions at $\sqrt{s_{NN}}$=200 GeV

We performed similar studies as described in previous Section also in $d + Au$ collisions at 200 GeV. Figure 8.14 shows correlation functions for positive and negative pions separately. The dependence of the correlation function on the magnetic field within the TPC detector is presented on Fig. 8.15. Since the quality of the track reconstruction depends also on the number of hits associated with a track we studied the shape of the correlation function for tracks with at least 10 and 15 hits. Results
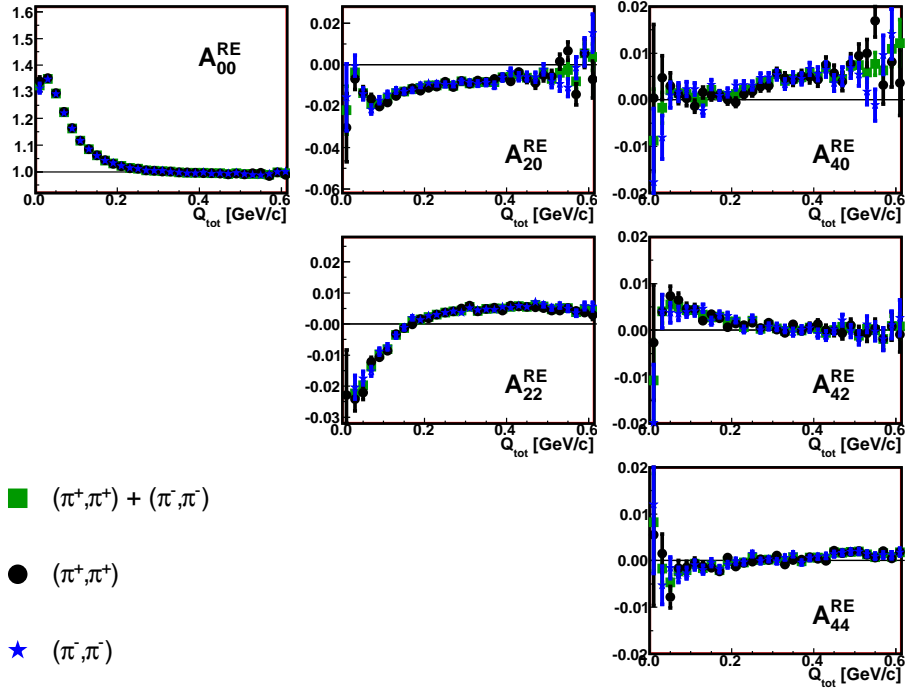
114

Figure 8.14: (π^+, π^+) and (π^-, π^-) correlation functions from minimum bias $d + Au$ collisions at $\sqrt{s_{NN}}$=200 GeV for $k_T = [0.15, 0.60]$ GeV/c.

shown on Fig. 8.16 clearly demonstrate no strong dependence of the shape of the correlation function on the number of hits. When constructing the denominator of the correlation function we should try to mix events as similar as possible. One of the criteria of similarity between events is the multiplicity. Figure 8.17 shows correlation functions for the case when mixing has been done in few multiplicity bins and when such selection has not been made.

.
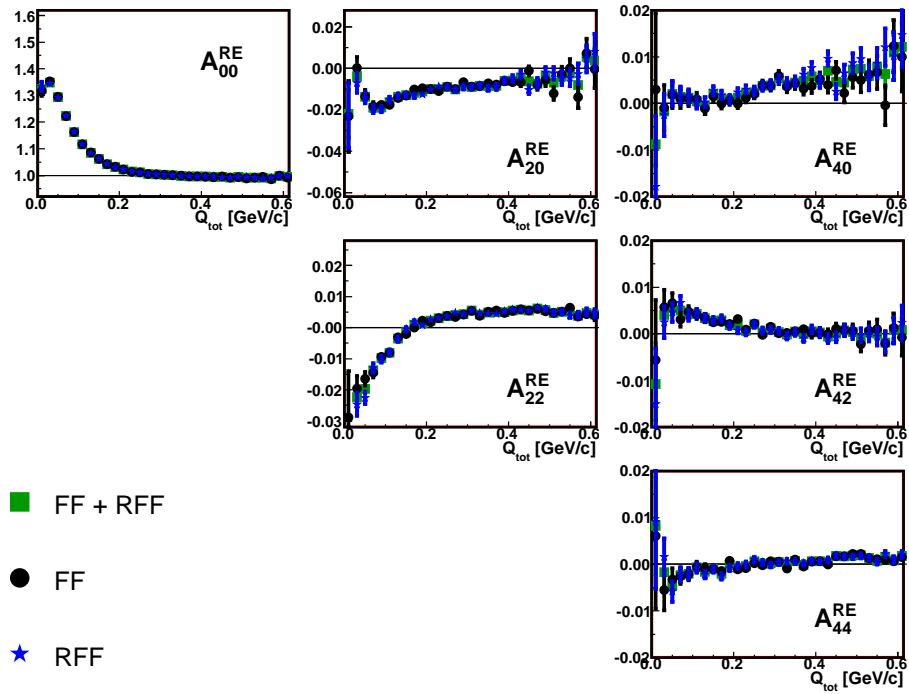
Figure 8.15: Correlation functions from minimum bias $d + Au$ collisions at $\sqrt{s_{NN}}$=200 GeV for $k_T = [0.15, 0.60]$ GeV/c for two sets of magnetic field within TPC.
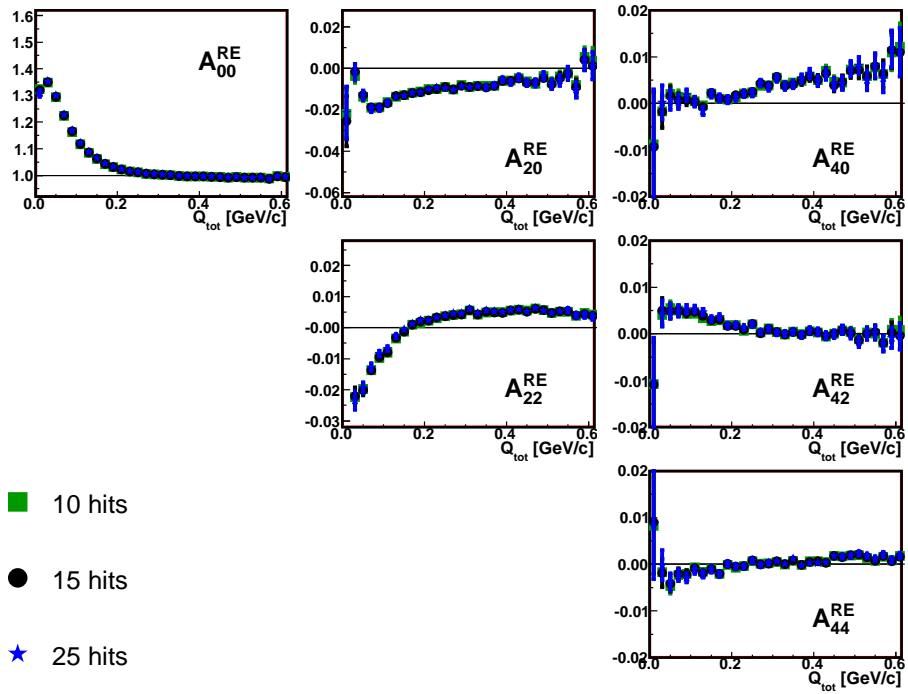
Figure 8.16: Correlation functions from minimum bias $d + Au$ collisions at $\sqrt{s_{NN}}$=200 GeV for $k_T = [0.15, 0.60]$ GeV/c for two values of the lowest number of hits per track.
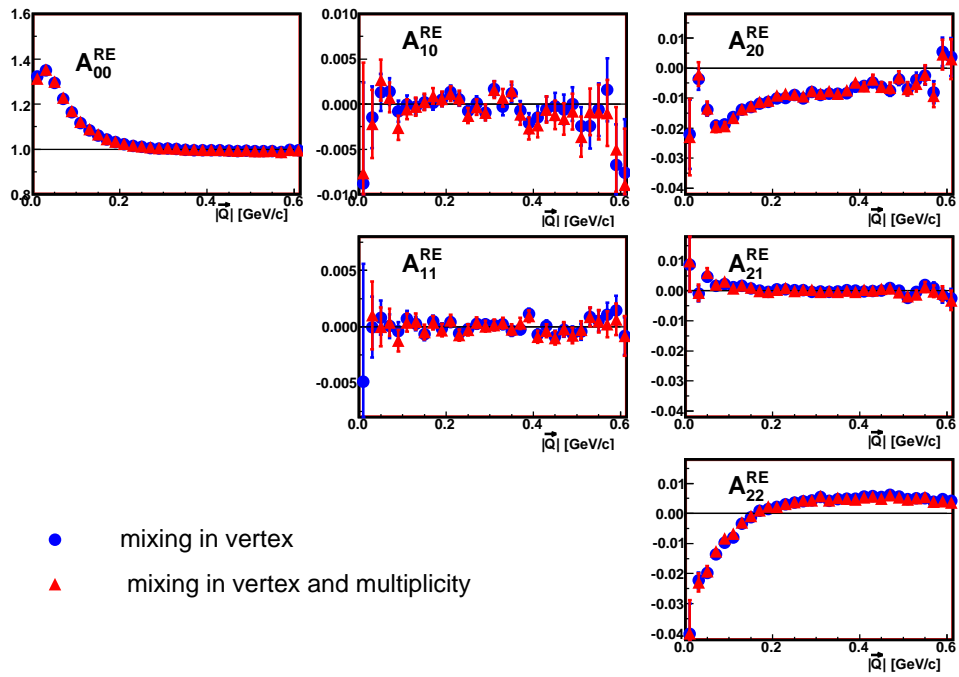
Figure 8.17: Correlation functions from minimum bias $d + Au$ collisions at $\sqrt{s_{NN}}$=200 GeV for $k_T = [0.15, 0.60]$ GeV/c where different binning in the mixing technique was used.

CHAPTER 9

EXPERIMENTAL RESULTS

In this chapter we present results from $p + p$ and $d + Au$ collisions at $\sqrt{s_{NN}}$=200 GeV and $Au + Au$ collisions at $\sqrt{s_{NN}}$=19.6 GeV registered by the STAR experiment at RHIC.

9.1 $p + p$ collisions at $\sqrt{s}{=}200$ GeV

9.1.1 The transverse mass dependence of 3D HBT radii

As a parameterization of the femtoscopic correlations we used Eq. 4.11. Additionally, we used different formulas to describe the non-femtoscopic correlations as discussed in Sec. 4.2. Results from various fits have been presented on Fig. 9.1 where pion HBT radii are plotted versus the transverse mass. Red stars represent the case where only femtoscopic correlations were fit (so-called "standard fit") and other possible correlations have been neglected. Violet circles show HBT results where Eq. 4.13 ("$\delta - Q$ fit") was used to parameterize non-femtoscopic part of the correlation functions. Non-femtoscopic correlations have been accounted for in two other formulas: Eq. 4.14 was used for orange triangles ("$\zeta - \beta$ fit") and Eq. 4.15 for black stars ("EM-CIC fit"). Results shown as orange triangles and black stars have been shifted around the correct values of $\langle m_T \rangle$ to improve visibility.

All results from Fig. 9.1 can be found in Tables 9.1- 9.4.   Figures 9.6, 9.7, 9.8, 9.9

k_T [GeV/c]	R_O [fm]	R_S [fm]	R_L [fm]	λ
$[0.15, 0.25]$	0.84 ± 0.02	0.89 ± 0.01	1.53 ± 0.02	0.422 ± 0.004
$[0.25, 0.35]$	0.81 ± 0.02	0.88 ± 0.01	1.45 ± 0.02	0.422 ± 0.005
$[0.35, 0.45]$	0.71 ± 0.02	0.82 ± 0.02	1.31 ± 0.02	0.433 ± 0.007
$[0.45, 0.60]$	0.68 ± 0.02	0.68 ± 0.01	1.05 ± 0.02	0.515 ± 0.009

Table 9.1: Fit results from a fit to data from $p + p$ collisions at $\sqrt{s}{=}$ 200 GeV using Eq. 4.11 to parameterize the femtoscopic correlations ("standard fit").

show spherical harmonic decomposition of the experimental correlation function for different k_T bins. Different lines represent different formulas used in the fit. Just for

fit parameter	k_T [GeV/c]			
	$[0.15, 0.25]$	$[0.25, 0.35]$	$[0.35, 0.45]$	$[0.45, 0.60]$
R_O [fm]	1.30 ± 0.03	1.21 ± 0.03	1.10 ± 0.03	0.93 ± 0.03
R_S [fm]	1.05 ± 0.03	1.05 ± 0.03	0.94 ± 0.03	0.82 ± 0.03
R_L [fm]	1.92 ± 0.05	1.67 ± 0.05	1.37 ± 0.05	1.17 ± 0.05
λ	0.295 ± 0.004	0.381 ± 0.005	0.433 ± 0.007	0.480 ± 0.009
δ_O	0.003 ± 0.003	0.020 ± 0.006	0.046 ± 0.006	0.041 ± 0.009
δ_S	-0.168 ± 0.005	-0.143 ± 0.005	-0.090 ± 0.006	-0.048 ± 0.010
δ_L	-0.233 ± 0.008	-0.295 ± 0.008	-0.228 ± 0.009	-0.147 ± 0.011

Table 9.2: Fit results from a fit to data from $p + p$ collisions at $\sqrt{s}$= 200 GeV using Eq. 4.11 to parameterize the femtoscopic correlations and Eq. 4.13 for nonfemtoscopic correlations ("$\delta - q$ fit").

k_T [GeV/c]	$[0.15, 0.25]$	$[0.25, 0.35]$	$[0.35, 0.45]$	$[0.45, 0.60]$
R_O [fm]	1.24 ± 0.04	1.14 ± 0.05	1.02 ± 0.04	0.89 ± 0.04
R_S [fm]	0.92 ± 0.03	0.89 ± 0.04	0.81 ± 0.05	0.71 ± 0.05
R_L [fm]	1.71 ± 0.04	1.37 ± 0.08	1.20 ± 0.07	1.09 ± 0.06
λ	0.392 ± 0.008	0.378 ± 0.006	0.434 ± 0.008	0.492 ± 0.009
ζ	0.017 ± 0.002	0.020 ± 0.004	0.018 ± 0.003	0.012 ± 0.003
β	-0.012 ± 0.002	-0.029 ± 0.003	-0.029 ± 0.004	-0.030 ± 0.004

Table 9.3: Fit results from a fit to data from $p + p$ collisions at $\sqrt{s}$= 200 GeV using Eq. 4.11 to parameterize the femtoscopic correlations and Eq. 4.14 for nonfemtoscopic correlations ("$\zeta - \beta$ fit").

k_T [GeV/c]	R_O [fm]	R_S [fm]	R_L [fm]	λ
$[0.15, 0.25]$	1.06 ± 0.03	1.00 ± 0.04	1.38 ± 0.05	0.665 ± 0.007
$[0.25, 0.35]$	0.96 ± 0.02	0.95 ± 0.03	1.21 ± 0.03	0.588 ± 0.006
$[0.35, 0.45]$	0.89 ± 0.02	0.88 ± 0.02	1.08 ± 0.04	0.579 ± 0.009
$[0.45, 0.60]$	0.78 ± 0.04	0.79 ± 0.02	0.94 ± 0.03	0.671 ± 0.028

Table 9.4: Fit results from a fit to data from $p + p$ collisions at $\sqrt{s}$= 200 GeV using Eq. 4.11 to parameterize the femtoscopic correlations and Eq. 4.15 for nonfemtoscopic correlations ("EMCIC fit").
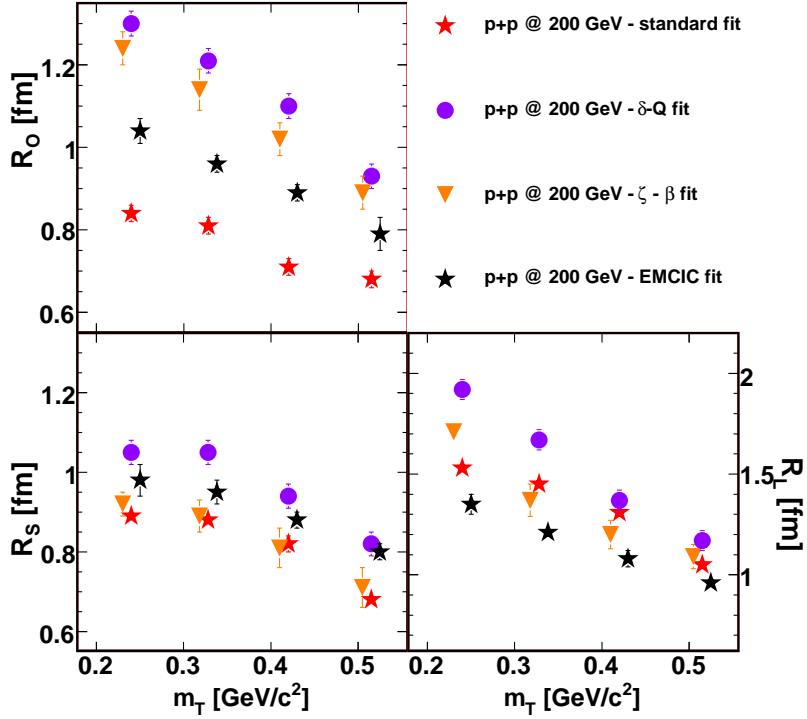
Figure 9.1: The m_T-dependence of HBT radii from $p + p$ collisions at $\sqrt{s}$=200 GeV for different parameterizations of the non-femtoscopic correlations used in the fit procedure. See text for more details. Results from $\delta - q$ and $\zeta - \beta$ fits have been shifted around the correct values of $\langle m_T \rangle$ to improve the visibility.

a comparison, Figs. 9.2- 9.5 shows the cartesian projections of the same correlation function as shown on Figs. 9.6- 9.9 (see Sec. 5 for more details).

Clearly none of the parameterization perfectly fits the experimental correlation function. The fact that they do not fit the low-Q part of the correlation function is probably due to the non-Gausianess of the source. This issue is not discussed in this paper further.

As discussed in Sec. 4.2, the two parameterizations of the non-femtoscopic correlations Eq. 4.13 and Eq. 4.14 are purely phenomenological and do not originate from
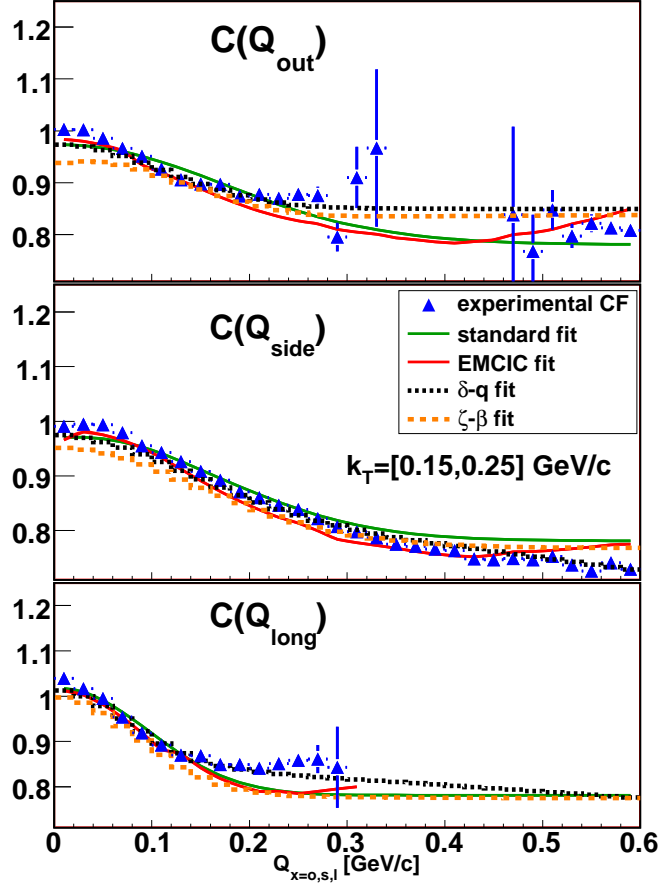
Figure 9.2: The one-dimensional cartesian projections of the 3D correlation function from $p + p$ collisions at $\sqrt{s}$=200 GeV, for $k_T = [0.15, 0.25]$ GeV/c. Different curves represent various parameterizations of non-femtoscopic correlations used in the fit and described in details in Sec. 4.2.

any known physical effect. So even though they often describe the shape of the correlation function better than Eq. 4.15, we should keep in mind that the last formula is based on the physics effect that is the energy and momentum conservation projected on the two-particle phase-space. Additionally, since we expect that the kinematic parameters like $\langle p_T^2 \rangle$, $\langle p_z^2 \rangle$, $\langle E^2 \rangle$ and $\langle E \rangle$ as well as N from Eq. 4.15 should be the same for different k_T bins we fit them simultaneously to the correlation functions for three k_T bins (Figs. 9.7, 9.8, 9.9). We obtained the following values of the EMCIC

parameters from the fit

$$M_1 = 0.43 \pm 0.07 \ (\text{GeV/c})^{-2}$$

$$M_2 = 0.22 \pm 0.06 \ (\text{GeV/c})^{-2}$$

$$M_3 = 1.51 \pm 0.12 \ \text{GeV}^{-2}$$

$$M_4 = 1.02 \pm 0.09 \ \text{GeV}^{-1}$$
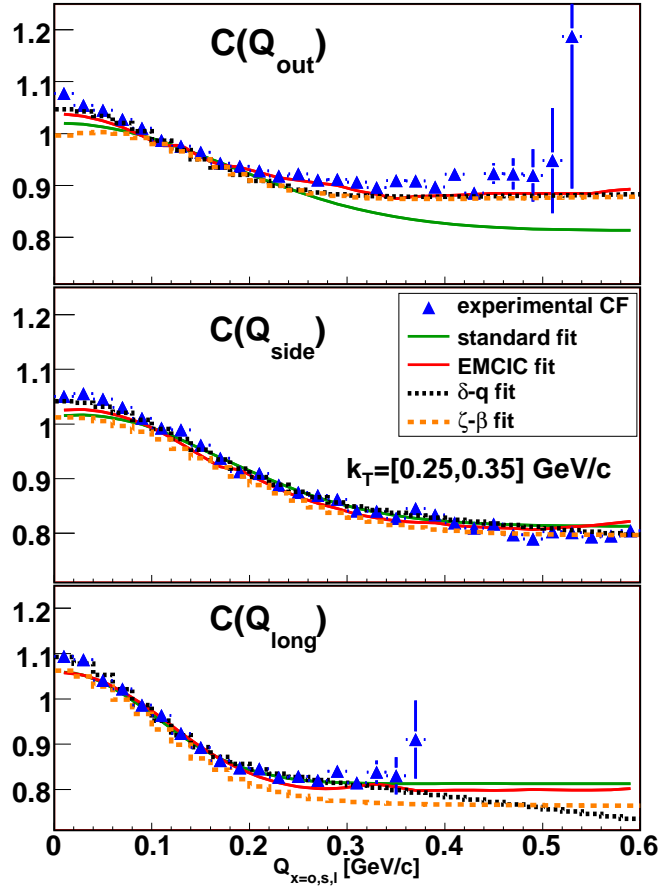
Figure 9.3: The one-dimensional cartesian projections of the 3D correlation function from $p + p$ collisions at $\sqrt{s}$=200 GeV, for $k_T = [0.25, 0.35]$ GeV/c. Different curves represent various parameterizations of non-femtoscopic correlations used in the fit and described in details in Sec. 4.2.
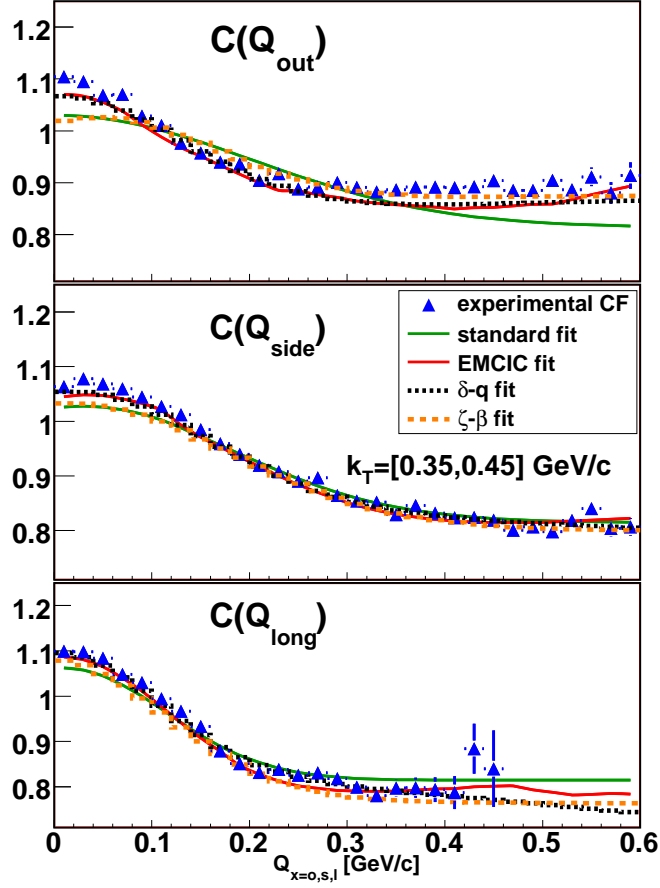
Figure 9.4: The one-dimensional cartesian projections of the 3D correlation function from $p + p$ collisions at $\sqrt{s}$=200 GeV, for $k_T = [0.35, 0.45]$ GeV/c. Different curves represent various parameterizations of non-femtoscopic correlations used in the fit and described in details in Sec. 4.2.

If we assume use Eqs. 4.18 and 4.19 and assume that the effective mass is equal a

mass of pion then the physical parameters obtained from $M_1 - M_4$ have the following

values:

$$N = 14.3 \pm 4.7$$

$$\langle p_T^2 \rangle = 0.17 \pm 0.06 \ (\mathrm{GeV/c})^2$$

$$\langle p_z^2 \rangle = 0.32 \pm 0.13 \ (\mathrm{GeV/c})^2$$

$$\langle E^2 \rangle = 0.51 \pm 0.11 \ \mathrm{GeV}^2$$

$$\langle E \rangle = 0.68 \pm 0.08 \ \mathrm{GeV}$$
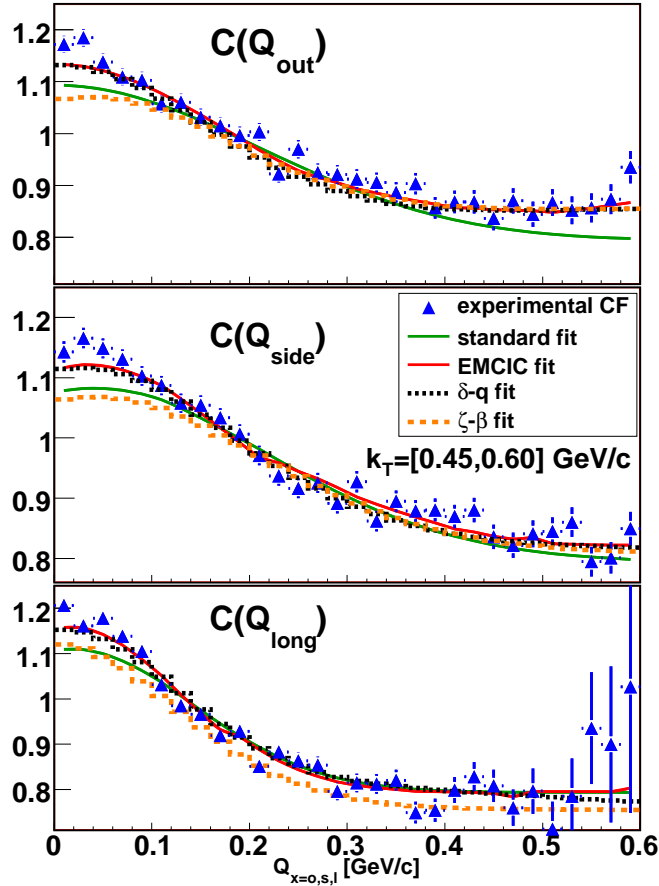
Figure 9.5: The one-dimensional cartesian projections of the 3D correlation function from $p + p$ collisions at $\sqrt{s}$=200 GeV, for $k_T = [0.45, 0.60]$ GeV/c. Different curves represent various parameterizations of non-femtoscopic correlations used in the fit and described in details in Sec. 4.2.
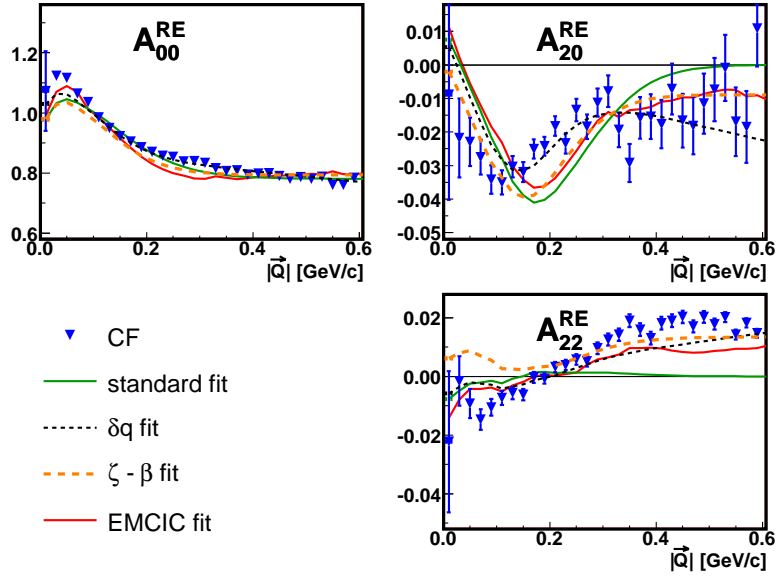
Figure 9.6: The first three non-vanished moments of the spherical harmonic decomposition of the correlation function from $p + p$ collisions at $\sqrt{s}$=200 GeV, for $k_T = [0.15, 0.25]$ GeV/c. Different curves represent various parameterizations of non-femtoscopic correlations used in the fit and described in details in Sec. 4.2.

The dependence of the physical parameters on the effective mass used in their calculations can be found in Appendix K.1. Clearly, the parameterization does not describe the correlation functions perfectly. However it catches the characteristics of the non-femtoscopic effect leaving some room for other physics effects that can also affect the correlation function and that the EMCIC formula does not account for. It is also worth to mention that in this case the effective number of additional parameters (besides femtoscopic parameters from Eq. 4.11) used to fit four correlation functions is 4 for "EMCIC fit". At the same time, one set of non-femtoscopic parameters from Eqs. 4.13 and 4.14 cannot describe the shape of the correlation functions for four different k_T bins so "$\delta - Q$ fit"(Eq. 4.13) gives additional 12 fit parameters and "$\zeta - \beta$ fit"(Eq. 4.14) introduces 8 new parameters.
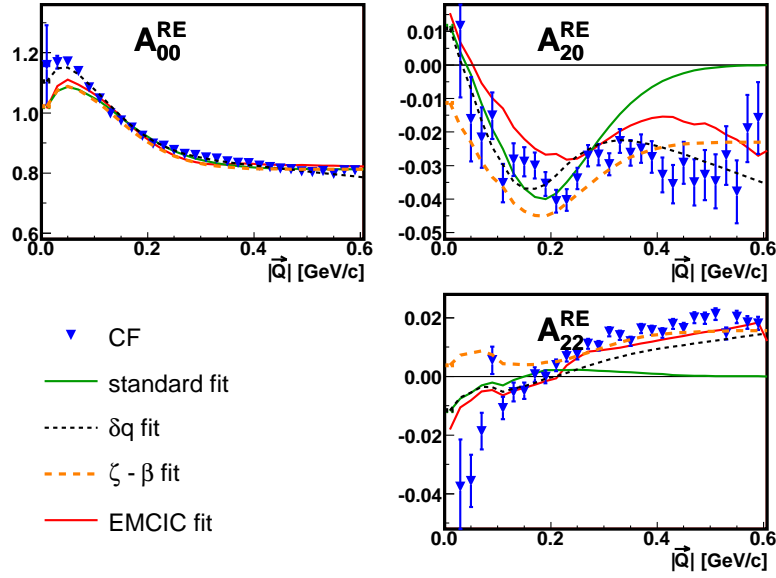
Figure 9.7: The first three non-vanished moments of the spherical harmonic decomposition of the correlation function from $p + p$ collisions at $\sqrt{s}$=200 GeV, for $k_T = [0.25, 0.35]$ GeV/c. Different curves represent various parameterizations of non-femtoscopic correlations used in the fit and described in details in Sec. 4.2.

9.1.2 Transverse mass and multiplicity dependence of 1D femtoscopic radii

Naturally, the 3D HBT radii carry more information about the homogeneity region than 1D radius. However, since most of the results from previous experiments from elementary particle collisions are in fact 1D radii we decided to do such analysis mostly for the sake of the comparison with previously presented results. Figure 9.10 shows the transverse mass dependence of the HBT radii when Eq. 4.6 was used to describe the femtoscopic part of the correlation function. Similarly like in Sec. 9.1.1 we used three different parameterizations of the non-femtoscopic correlations. Red stars represent the case when these additional correlations have been neglected, and Eq. 4.12 was used for green stars. Black star data points represent fit results where

128
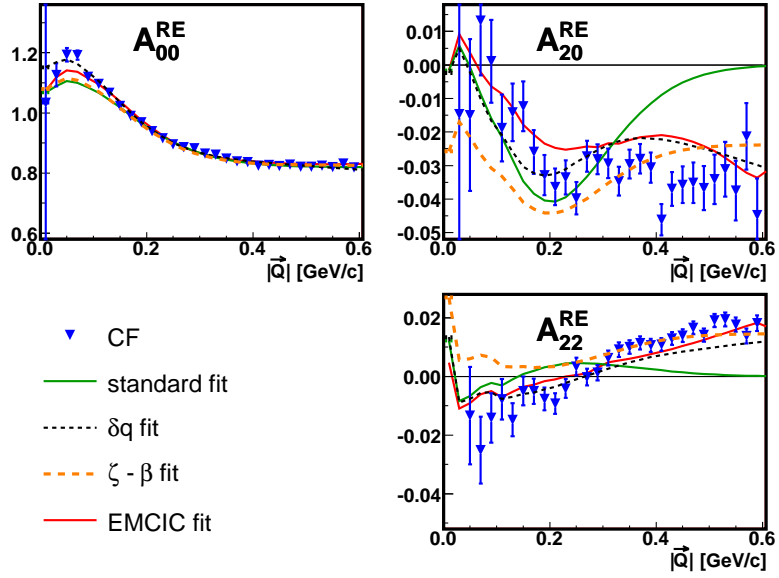
Figure 9.8: The first three non-vanished moments of the spherical harmonic decomposition of the correlation function from $p + p$ collisions at $\sqrt{s}$=200 GeV, for $k_T = [0.35, 0.45]$ GeV/c. Different curves represent various parameterizations of non-femtoscopic correlations used in the fit and described in details in Sec. 4.2.

Eq. 4.15 was used to fit non-femtoscopic correlations. However, parameters $M_1 - M_4$ where not fitted to one-dimensional correlation function but were taken from the fit to 3D correlation function (see Sec. 9.1.1 for more details). Even though different treatments of the non-femtoscopic correlations give different magnitude of R_{inv} the m_T dependence is seen in all results. Results from Fig. 9.10 are tabulated in Tables 9.5-9.7.

With the current statistics from $p + p$ collisions we were able to divide the data sample on two multiplicity bins and study k_T integrated correlation function ($k_T = [0.15, 0.60]$ GeV/c). Figure 9.11 shows correlation functions for two multiplicity ranges. Results from a fit using Eq. 4.6 are presented on Fig. 9.12. Figure 9.13 shows results using Eq. 4.7 and Eq.4.8. Since, as discussed in Sec. 9.1.1, the radius
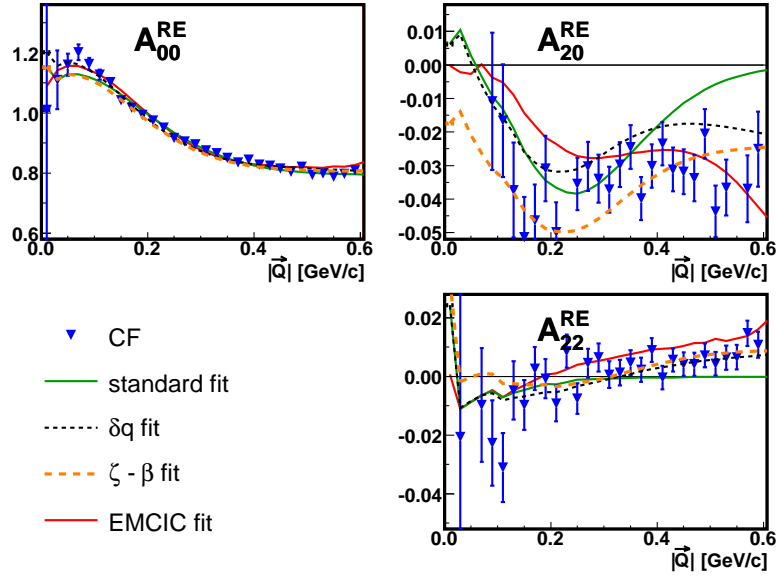
Figure 9.9: The first three non-vanished moments of the spherical harmonic decomposition of the correlation function from $p + p$ collisions at $\sqrt{s}$=200 GeV, for $k_T = [0.45, 0.60]$ GeV/c. Different curves represent various parameterizations of non-femtoscopic correlations used in the fit and described in details in Sec. 4.2.
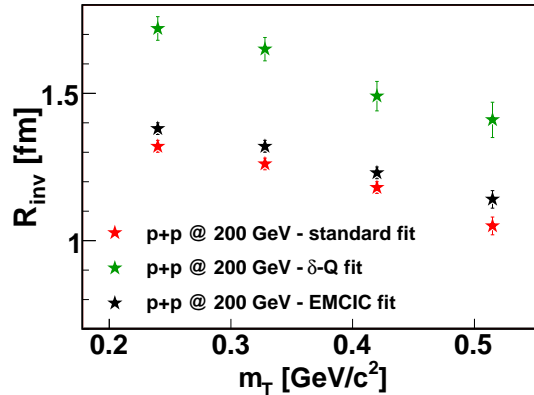
Figure 9.10: The m_T-dependence of R_{inv} from $p + p$ collisions at $\sqrt{s}$=200 GeV for different parameterizations of the non-femtoscopic correlations used in the fit procedure. See text for more details.

k_T [GeV/c]	R_{inv} [fm]	λ
$[0.15, 0.25]$	1.32 ± 0.02	0.345 ± 0.005
$[0.25, 0.35]$	1.26 ± 0.02	0.357 ± 0.007
$[0.35, 0.45]$	1.18 ± 0.02	0.348 ± 0.008
$[0.45, 0.60]$	1.05 ± 0.03	0.413 ± 0.012

Table 9.5: Fit results from a fit to 1D correlation function from $p + p$ collisions at $\sqrt{s}$= 200 GeV using Eq. 4.6 to parameterize the femtoscopic correlations ("standard fit").

k_T [GeV/c]	R_{inv} [fm]	λ	δQ_{inv}
$[0.15, 0.25]$	1.72 ± 0.04	0.285 ± 0.007	0.237 ± 0.007
$[0.25, 0.35]$	1.65 ± 0.04	0.339 ± 0.009	0.163 ± 0.008
$[0.35, 0.45]$	1.49 ± 0.05	0.308 ± 0.011	0.180 ± 0.015
$[0.45, 0.60]$	1.41 ± 0.06	0.338 ± 0.016	0.228 ± 0.017

Table 9.6: Fit results from a fit to 1D correlation function from $p + p$ collisions at $\sqrt{s}$= 200 GeV using Eq. 4.6 to parameterize the femtoscopic correlations and Eq. 4.12 for nonfemtoscopic correlations ($\delta - q$ fit").

k_T [GeV/c]	R_{inv} [fm]	λ
$[0.15, 0.25]$	1.38 ± 0.03	0.347 ± 0.005
$[0.25, 0.35]$	1.32 ± 0.03	0.354 ± 0.006
$[0.35, 0.45]$	1.23 ± 0.04	0.349 ± 0.009
$[0.45, 0.60]$	1.14 ± 0.05	0.411 ± 0.013

Table 9.7: Fit results from a fit to 1D correlation function from $p + p$ collisions at $\sqrt{s}$= 200 GeV using Eq. 4.6 to parameterize the femtoscopic correlations and Eq. 4.15 for nonfemtoscopic correlations (EMCIC fit").

obtained from the second formula is expected to be approximately twice larger than

method	fit parameter	$\langle dN_{ch}/d\eta\rangle$		
		4.25 (min-bias)	3.47	8.75
standard fit	R_{inv}	1.21 ± 0.01	1.09 ± 0.02	1.34 ± 0.02
	λ	0.353 ± 0.003	0.347 ± 0.04	0.356 ± 0.03
$\delta - q$ fit	R_{inv}	1.61 ± 0.01	1.50 ± 0.03	1.76 ± 0.03
	λ	0.312 ± 0.003	0.275 ± 0.005	0.322 ± 0.007
	δQ_{inv}	-0.191 ± 0.003	-0.242 ± 0.005	-0.194 ± 0.006
EMCIC fit	R_{inv}	1.32 ± 0.02	1.22 ± 0.03	1.46 ± 0.02
	λ	0.481 ± 0.003	0.485 ± 0.003	0.504 ± 0.004
Eq. 4.7	R_G	1.00 ± 0.01	0.91 ± 0.01	1.07 ± 0.01
	λ	0.407 ± 0.004	0.390 ± 0.004	0.370 ± 0.006
Eq. 4.8	R_B	1.83 ± 0.01	1.69 ± 0.01	1.93 ± 0.01
	λ	0.364 ± 0.003	0.352 ± 0.004	0.332 ± 0.004

Table 9.8: Multiplicity dependence of fit results to 1D correlation function from $p + p$ collisions at $\sqrt{s}= 200$ GeV for different fit parameterizations.
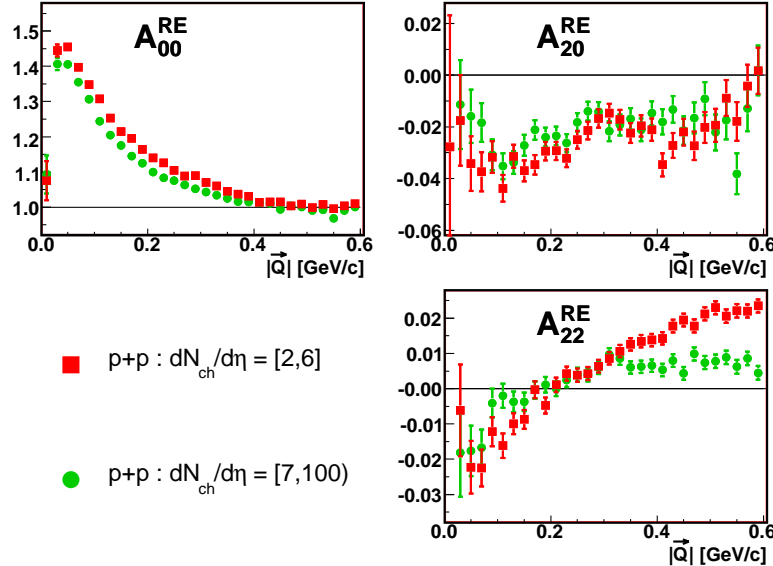
Figure 9.11: The first three non-vanished moments of the spherical harmonic decomposition of the correlation function from $p + p$ collisions at $\sqrt{s}=200$ GeV, for $k_T = [0.15, 0.60]$ GeV/c and for two event multiplicity ranges.
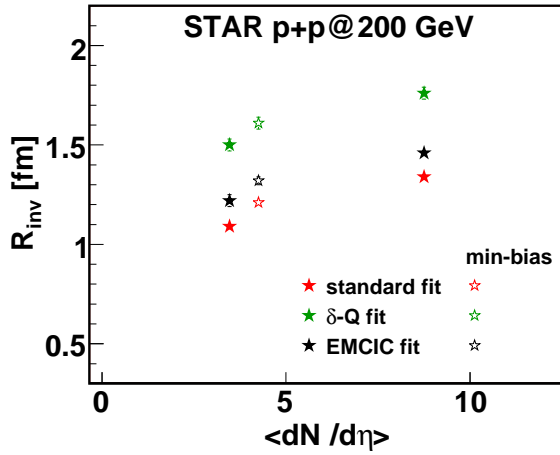
Figure 9.12: The multiplicity dependence of R_{inv} from $p+p$ collisions at $\sqrt{s}$=200 GeV for different parameterizations of the non-femtoscopic correlations. The particles within the range of $k_T = [0.15, 0.60]$ GeV/c were used in the analysis.

the radius from the first formula we divided the first radius by a factor of 2 for a comparison. As presented on Figs. 9.12- 9.13 the pion HBT radii increase with increasing multiplicity. Results shown on these figures can be found in Table 9.8.
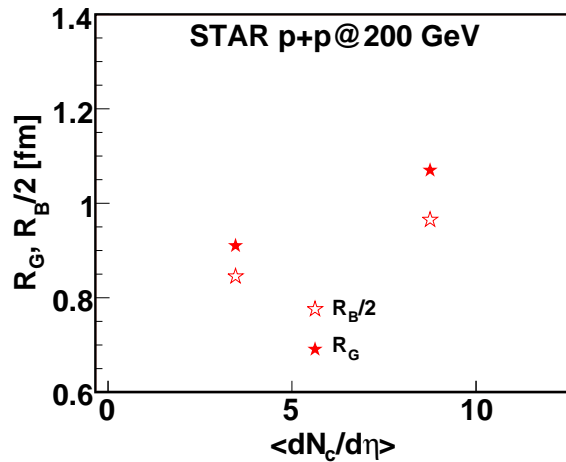
Figure 9.13: The multiplicity dependence of R_G and R_B from $p+p$ collisions at $\sqrt{s}$=200 GeV. The particles within the range of $k_T = [0.15, 0.60]$ GeV/c were used in the analysis.

133

9.1.3 Systematic errors

All results from various fits to the correlation functions from $p + p$ collisions at $\sqrt{s_{NN}}$=200 GeV that we presented so far included statistical error only. Here we would like to discuss the possible sources of systematic errors and estimate their magnitudes.

Two track effects like splitting (one particle reconstructed as two tracks) and merging (two particles reconstructed as one track) that were discussed in Sec. 8 can affect the shape of the correlation function at low $|\vec{q}|$ (< 30 MeV/c) regardless the colliding system. However, these effects have negligible impact on the femtoscopic sizes extracted from the fit to the correlation function from $p + p$ collisions because of the width of the femtoscopic effect that is about an order of magnitude larger. Additionally, the first few bins of the correlation functions have larger error bars due to the lower statistics of pairs at low-$|\vec{q}|$. Therefore, due to these reasons, the fit is not much sensitive to the first bins of the correlation functions.

The other possible source of systematic errors on fit parameters is the coulomb radius used in the fit using Eq. 4.11. In studies presented in this section we used $R_{coul} = 1$ fm. To study the R_{coul} dependence of fit parameters we repeated fits using Eq. 4.11 within a fit range $|\vec{q}| = [0, 0.60]$ GeV/c for few values of R_{coul}. Results are summarized in Table 9.9. As seen, the effect of using different values R_{coul} in a fit formula is of order of statistical errors.

The effect that dominates the systematic errors is the dependence of fit parameters on the fit range. Tables 9.10- 9.13 present the dependence of the femtoscopic parameters on the fit range and list the systematic errors.

R_{coul}	k_T [GeV/c]			
[fm]	$[0.15, 0.25]$	$[0.25, 0.35]$	$[0.35, 0.45]$	$[0.45, 0.60]$
R_O [fm]				
0.5	0.85 ± 0.02	0.83 ± 0.02	0.71 ± 0.02	0.68 ± 0.02
1.0	0.84 ± 0.02	0.81 ± 0.02	0.71 ± 0.02	0.67 ± 0.02
1.5	0.84 ± 0.02	0.81 ± 0.02	0.70 ± 0.02	0.68 ± 0.02
2.0	0.83 ± 0.02	0.80 ± 0.02	0.69 ± 0.02	0.69 ± 0.02
systematic	$+0.01$	$+0.02$	$+0.00$	$+0.01$
errors	-0.01	-0.01	-0.02	-0.01
R_S [fm]				
0.5	0.90 ± 0.01	0.90 ± 0.01	0.82 ± 0.02	0.68 ± 0.01
1.0	0.89 ± 0.01	0.88 ± 0.01	0.82 ± 0.02	0.68 ± 0.01
1.5	0.88 ± 0.01	0.88 ± 0.01	0.81 ± 0.02	0.68 ± 0.01
2.0	0.88 ± 0.01	0.87 ± 0.01	0.80 ± 0.02	0.67 ± 0.01
systematic	$+0.01$	$+0.02$	$+0.00$	$+0.00$
errors	-0.01	-0.01	-0.02	-0.01
R_L [fm]				
0.5	1.53 ± 0.02	1.44 ± 0.02	1.32 ± 0.02	1.06 ± 0.02
1.0	1.53 ± 0.02	1.45 ± 0.02	1.31 ± 0.02	1.05 ± 0.02
1.5	1.52 ± 0.02	1.46 ± 0.02	1.31 ± 0.02	1.06 ± 0.02
2.0	1.51 ± 0.02	1.47 ± 0.02	1.20 ± 0.02	1.05 ± 0.02
systematic	$+0.00$	$+0.01$	$+0.01$	$+0.01$
errors	-0.02	-0.02	-0.02	-0.00
λ				
0.5	0.422 ± 0.004	0.422 ± 0.005	0.437 ± 0.007	0.518 ± 0.009
1.0	0.422 ± 0.004	0.422 ± 0.005	0.433 ± 0.007	0.515 ± 0.009
1.5	0.422 ± 0.004	0.422 ± 0.005	0.424 ± 0.007	0.511 ± 0.009
2.0	0.422 ± 0.004	0.422 ± 0.005	0.426 ± 0.007	0.508 ± 0.009
systematic	$+0.002$	$+0.001$	$+0.004$	$+0.003$
errors	-0.008	-0.009	-0.009	-0.007

Table 9.9: The coulomb radius dependence of fit parameters. Coulomb radius used in the fit procedure using Eq. 4.11 given in the first column. The fit range used in these fits was $|\vec{q}| = [0, 0.60]$ GeV/c.

R_O [fm]				
fit range	k_T [GeV/c]			
[GeV/c]	$[0.15, 0.25]$	$[0.25, 0.35]$	$[0.35, 0.45]$	$[0.45, 0.60]$
0.40	0.92 ± 0.02	0.87 ± 0.02	0.78 ± 0.02	0.73 ± 0.02
0.44	0.89 ± 0.02	0.87 ± 0.02	0.76 ± 0.02	0.71 ± 0.02
0.48	0.87 ± 0.02	0.85 ± 0.02	0.73 ± 0.02	0.70 ± 0.02
0.52	0.86 ± 0.02	0.84 ± 0.02	0.72 ± 0.02	0.68 ± 0.02
0.56	0.84 ± 0.02	0.82 ± 0.02	0.71 ± 0.02	0.67 ± 0.02
0.60	0.84 ± 0.02	0.81 ± 0.02	0.71 ± 0.02	0.68 ± 0.02
0.64	0.84 ± 0.02	0.80 ± 0.02	0.69 ± 0.02	0.67 ± 0.02
systematic	$+0.09$	$+0.06$	$+0.07$	$+0.05$
errors	-0.00	-0.01	-0.02	-0.01

Table 9.10: Fit range dependence of the fit parameter R_O. The fit was performed within a range of $|\vec{q}| = [0, X]$ GeV/c where X is given in the first column.

In our studies we found that systematic errors due to the fit range, particle identification, two-track effects and the coulomb radius are estimated to be about 10%, similar to previous studies [67].

R_S [fm]				
fit range	k_T [GeV/c]			
[GeV/c]	$[0.15, 0.25]$	$[0.25, 0.35]$	$[0.35, 0.45]$	$[0.45, 0.60]$
0.40	0.97 ± 0.01	0.94 ± 0.01	0.87 ± 0.02	0.74 ± 0.01
0.44	0.97 ± 0.01	0.94 ± 0.01	0.86 ± 0.02	0.73 ± 0.01
0.48	0.95 ± 0.01	0.93 ± 0.01	0.84 ± 0.02	0.70 ± 0.01
0.52	0.92 ± 0.01	0.91 ± 0.01	0.83 ± 0.02	0.70 ± 0.01
0.56	0.89 ± 0.01	0.88 ± 0.01	0.82 ± 0.02	0.69 ± 0.01
0.60	0.89 ± 0.01	0.88 ± 0.01	0.82 ± 0.02	0.68 ± 0.01
0.64	0.88 ± 0.01	0.86 ± 0.01	0.81 ± 0.02	0.08 ± 0.01
systematic	$+0.09$	$+0.06$	$+0.05$	$+0.06$
errors	-0.01	-0.02	-0.01	-0.00

Table 9.11: Fit range dependence of the fit parameter R_S. The fit was performed within a range of $|\vec{q}| = [0, X]$ GeV/c where X is given in the first column.

R_L [fm]				
fit range	k_T [GeV/c]			
[GeV/c]	$[0.15, 0.25]$	$[0.25, 0.35]$	$[0.35, 0.45]$	$[0.45, 0.60]$
0.40	1.64 ± 0.02	1.53 ± 0.02	1.33 ± 0.02	1.14 ± 0.02
0.44	1.63 ± 0.02	1.52 ± 0.02	1.32 ± 0.02	1.14 ± 0.02
0.48	1.58 ± 0.02	1.52 ± 0.02	1.32 ± 0.02	1.11 ± 0.02
0.52	1.56 ± 0.02	1.47 ± 0.02	1.30 ± 0.02	1.09 ± 0.02
0.56	1.52 ± 0.02	1.46 ± 0.02	1.31 ± 0.02	1.06 ± 0.02
0.60	1.53 ± 0.02	1.45 ± 0.02	1.31 ± 0.02	1.05 ± 0.02
0.64	1.52 ± 0.00	1.42 ± 0.02	1.30 ± 0.02	1.02 ± 0.02
systematic	$+0.12$	$+0.08$	$+0.02$	$+0.09$
errors	-0.01	-0.03	-0.01	-0.03

Table 9.12: Fit range dependence of the fit parameter R_L. The fit was performed within a range of $|\vec{q}| = [0, X]$ GeV/c where X is given in the first column.

λ				
fit range	k_T [GeV/c]			
[GeV/c]	$[0.15, 0.25]$	$[0.25, 0.35]$	$[0.35, 0.45]$	$[0.45, 0.60]$
0.40	0.433 ± 0.005	0.449 ± 0.005	0.440 ± 0.007	0.542 ± 0.009
0.44	0.432 ± 0.005	0.442 ± 0.005	0.438 ± 0.007	0.538 ± 0.009
0.48	0.428 ± 0.005	0.437 ± 0.005	0.437 ± 0.008	0.527 ± 0.009
0.52	0.426 ± 0.004	0.428 ± 0.005	0.434 ± 0.007	0.521 ± 0.009
0.56	0.425 ± 0.004	0.425 ± 0.005	0.433 ± 0.007	0.518 ± 0.009
0.60	0.422 ± 0.004	0.422 ± 0.005	0.433 ± 0.007	0.515 ± 0.009
0.64	0.420 ± 0.004	0.421 ± 0.005	0.429 ± 0.008	0.516 ± 0.009
systematic	$+0.011$	$+0.025$	$+0.007$	$+0.027$
errors	-0.002	-0.001	-0.004	-0.000

Table 9.13: Fit range dependence of the fit parameter λ. The fit was performed within a range of $|\vec{q}| = [0, X]$ GeV/c where X is given in the first column.

9.2 $d + Au$ collisions at $\sqrt{s_{NN}}$=200 GeV

It is interesting to study $d + Au$ collisions at RHIC because they provide a bridge between elementary particle collisions and heavy ion collisions and thus can potentially help to understand the physics behind these collisions. In this section we present results from $d + Au$ collisions at $\sqrt{s_{NN}}$=200 GeV at RHIC for three centralities. We also show results from $p + Au$ collisions that were extracted from peripheral $d + Au$ collisions (see Sec. 8.1 for more details) and compare all results to data from $p + p$ collisions discussed in Sec.9.1.

9.2.1 Non-femtoscopic correlations
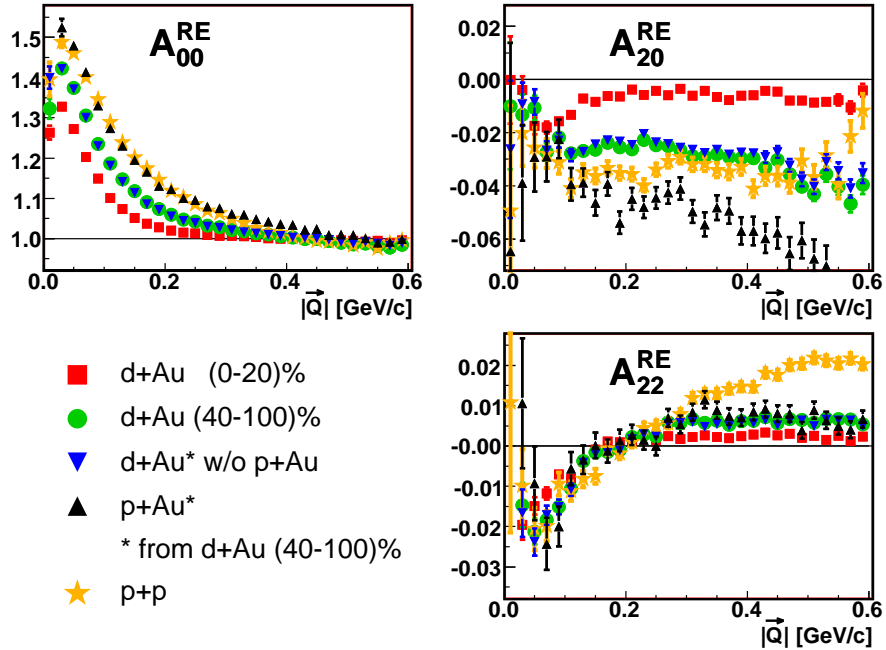
Figure 9.14: The first three non-vanished moments of the spherical harmonic decomposition of the correlation function from $d + Au$, $p + Au$ collisions at $\sqrt{s_{NN}}$=200 GeV and $p + p$ collisions at $\sqrt{s}$=200 GeV, for $k_T = [0.15, 0.60]$ GeV/c.

Non-femtoscopic correlations play important role in elementary particle collisions and become less important with an increase of the system size. As we discussed in Chapter 6, non-femtoscopic correlations can be neglected for large multiplicities like in central $Au + Au$ collisions at $\sqrt{s_{NN}}$=200 GeV at RHIC however they still have to be accounted for when studying correlations in $d + Au$ collisions, although their magnitude is smaller than in $p + p$ collisions. Figure 9.14 shows the first three non-vanished moments of the spherical harmonic decomposition of the k_T-integrated ($k_T = [0.15, 0.60] \; GeV/c$) correlation functions for three centralities of $d + Au$ collisions, $p + Au$ collisions extracted from peripheral $d + Au$ collisions, peripheral $d + Au$ collisions after removing $p + Au$ collisions as well as from $p + p$ collisions. All collisions at $\sqrt{s_{NN}}$=200 GeV.

9.2.2 Centrality and transverse mass dependence of HBT radii

Similarly as in femtoscopic analysis in $p + p$ collisions (Sec. 9.1 we used Eq. 4.11 as a parameterization of the femtoscopic correlations as well as we used different formulas to describe the non-femtoscopic correlations as discussed in Sec. 4.2. Results from various fits to four k_T bins and three centralities are presented on Fig. 9.15where pion HBT radii are plotted versus the transverse mass. Blue triangles, green squares and red stars represent the case where only femtoscopic correlations were fit (so-called "standard fit") while other possible correlations have been neglected. Open black stars, open blue squares and open red triangles show HBT results where Eq. 4.13 ("$\delta-q$ fit") was used to parameterize non-femtoscopic part of the correlation functions. Non-femtoscopic correlations have been also accounted for in formula expressed by Eq. 4.15 for open red stars, open green squares and open blue triangles ("EMCIC fit").
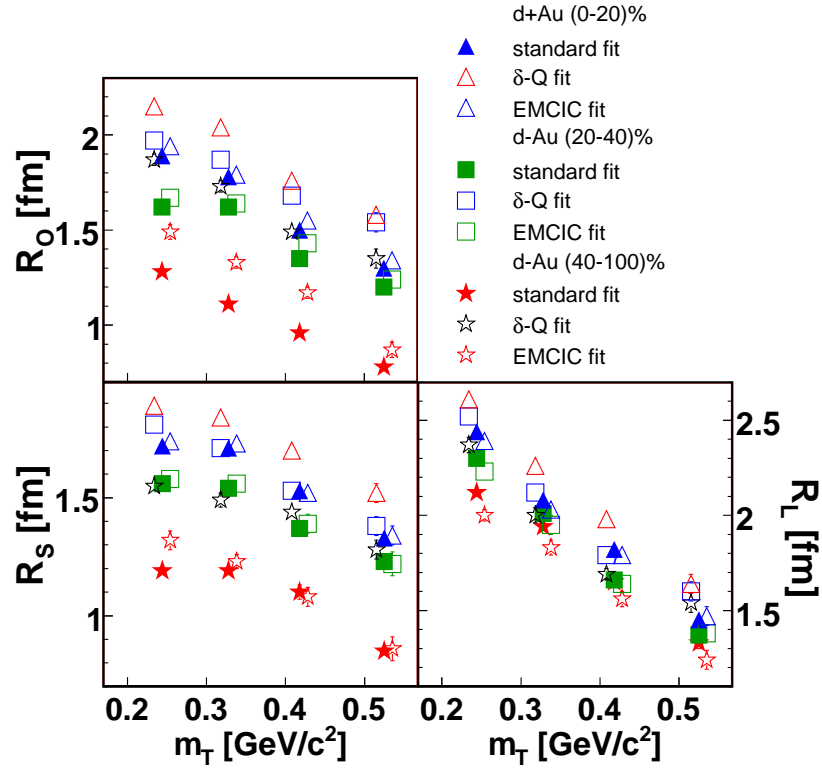
Figure 9.15: The m_T dependence of HBT radii for three centralities from $d + Au$ collisions obtained from various parameterizations of non-femtoscopic correlations. See text and Sec. 4.2 for more details.

Results from "$\delta - q$ fit" and "EMCIC fit" have been shifted around the correct values of $\langle m_T \rangle$ to improve visibility. All results from Fig. 9.15 can be found in Tables 9.14, 9.15 and 9.16. The correlation functions for three different centralities and four k_T bins are plotted together with fit formulas on Figs. 9.16-9.18.

As shown on Figures 9.16- 9.18 none of the parameterization perfectly fits the experimental correlation functions. We observed similar issue with various fits to correlation functions from $p + p$ collisions (Sec. 9.1). Similarly to $p + p$ collisions, the fact that the low-$|\vec{q}|$ part of the correction function is not perfectly describe by any of the parameterizations suggests that it is due to the non-Gausianess of the
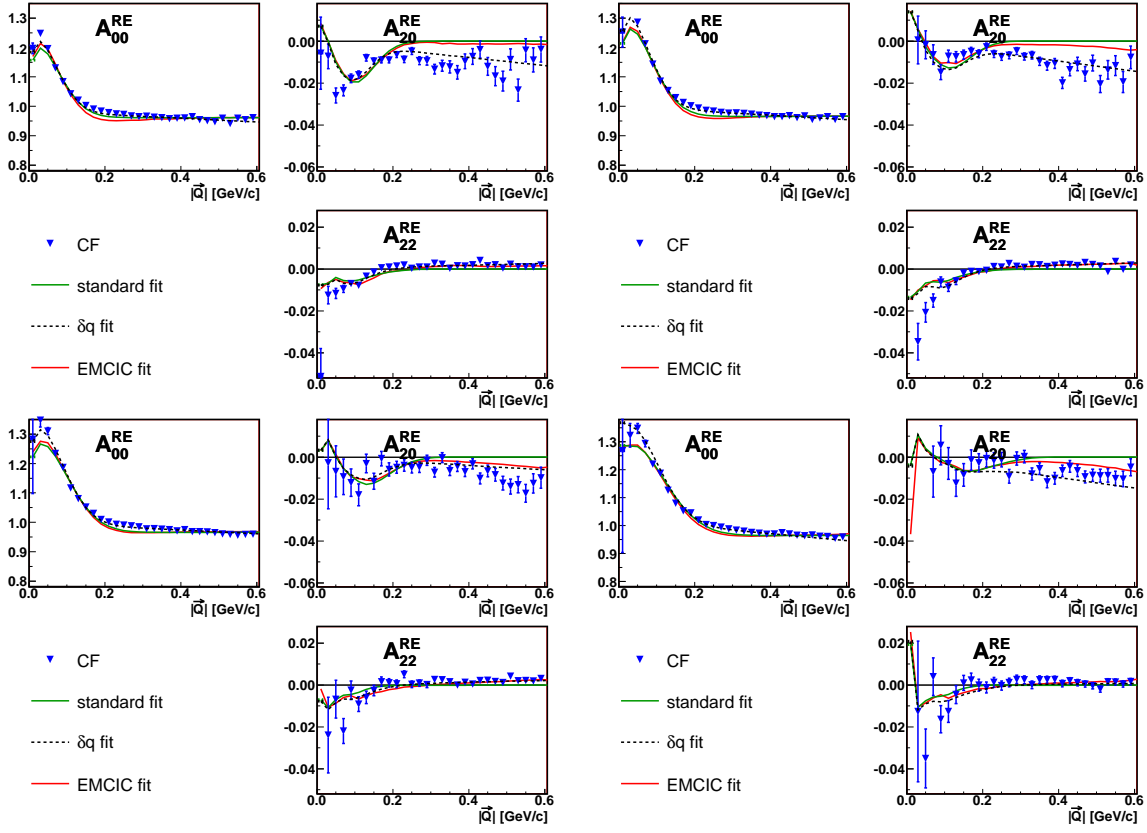
Figure 9.16: The first three non-vanished moments of the spherical harmonic decomposition of the correlation functions from central $d + Au$ collisions ([0-20]%) at $\sqrt{s_{NN}}$=200 GeV, for four k_T bins ([0.15, 0.25] GeV/c, [0.25, 0.35] GeV/c, [0.35, 0.45] GeV/c, [0.45, 0.60] GeV/c). Different curves represent various parameterizations of non-femtoscopic correlations used in the fit and described in details in Sec. 4.2

source, a well-known effect present in elementary particle collisions up to heavy ion collisions [67].

As discussed in Sec. 4.2, the parameterization of the non-femtoscopic correlations given by Eq. 4.13 is purely phenomenological and is not based on any known physical effect. Thus, even though it often describes the shape of the correlation function better than Eq. 4.15, we should keep in mind that the EMCIC formula (Eq. 4.15) is based on the physics effect that is the phase-space limit due to energy and momentum
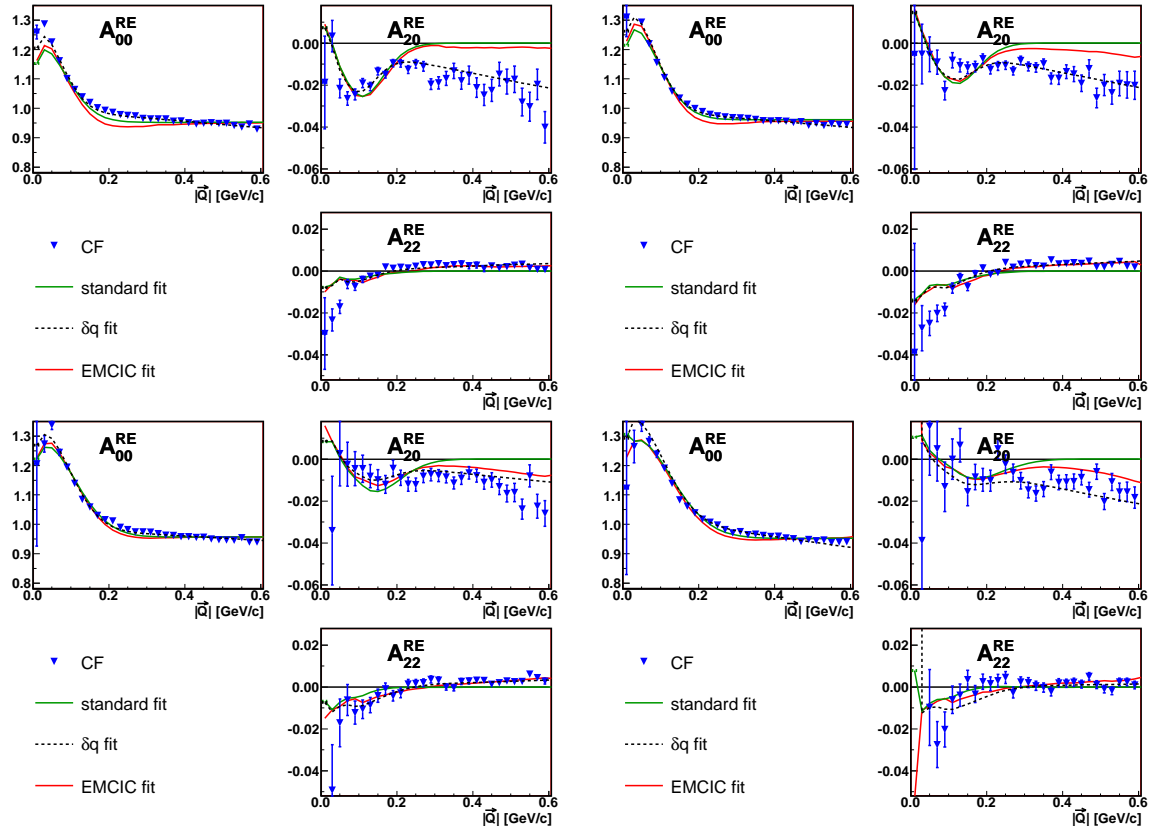
Figure 9.17: The first three non-vanished moments of the spherical harmonic decomposition of the correlation functions from mid-central $d + Au$ collisions ([20-40]%) at $\sqrt{s_{NN}}$=200 GeV, for four k_T bins ([0.15, 0.25] GeV/c, [0.25, 0.35] GeV/c, [0.35, 0.45] GeV/c, [0.45, 0.60] GeV/c). Different curves represent various parameterizations of non-femtoscopic correlations used in the fit and described in details in Sec. 4.2

conservation. Additionally, since we expect that the kinematic parameters like $\langle p_T^2 \rangle$, $\langle p_z^2 \rangle$, $\langle E^2 \rangle$ and $\langle E \rangle$ as well as N from Eq. 4.15 should be the same for different k_T bins we fit them simultaneously to the correlation functions for three k_T bins (Figs. 9.7, 9.8, 9.9) to A_{00} and A_{22} moments. The EMCIC formula was derived for a symmetric system so it is natural to expect that it may not describe part of the non-femtoscopic correlations in asymmetric collisions like $d + Au$. Since, A_{20} moment is sensitive to this asymmetry we did not include it in the fit. The values of the EMCIC

143
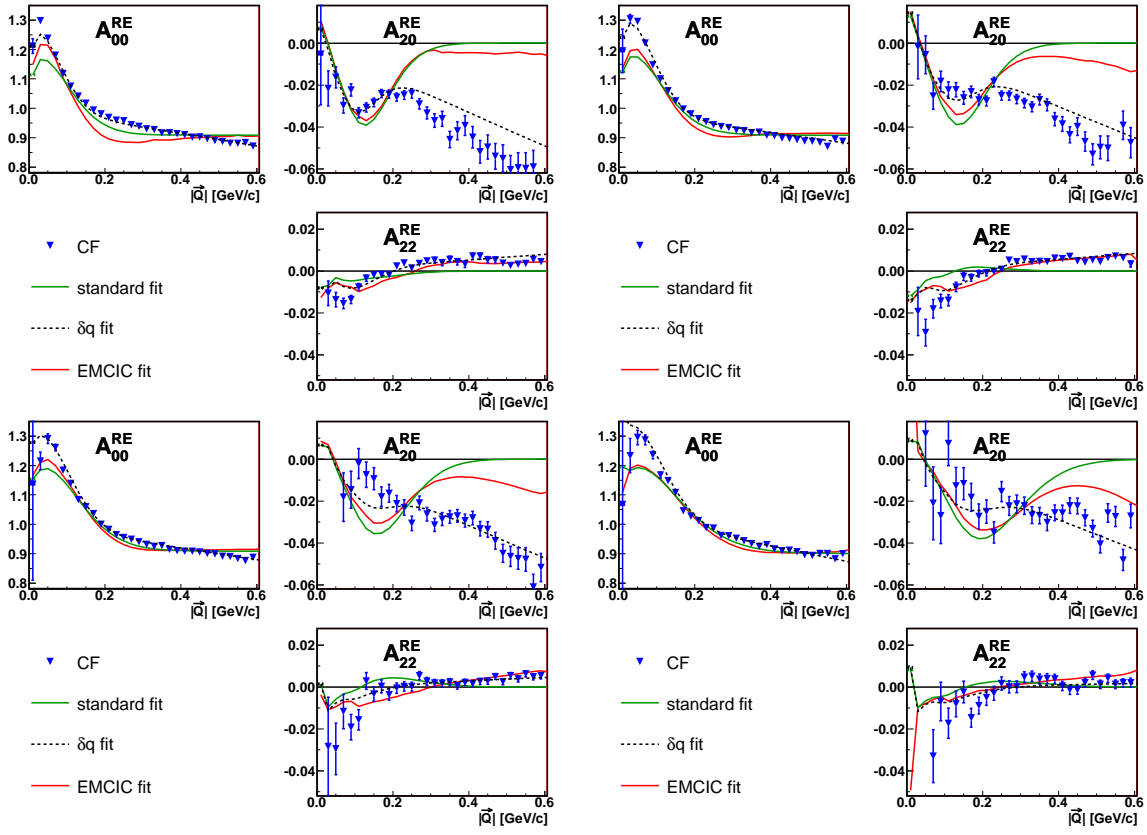
Figure 9.18: The first three non-vanished moments of the spherical harmonic decomposition of the correlation functions from peripheral $d + Au$ collisions ([40-100]%) at $\sqrt{s_{NN}}$=200 GeV, for four k_T bins ([0.15, 0.25] GeV/c, [0.25, 0.35] GeV/c, [0.35, 0.45] GeV/c, [0.45, 0.60] GeV/c). Different curves represent various parameterizations of non-femtoscopic correlations used in the fit and described in details in Sec. 4.2

parameters from the fit using Eq. 4.15 to three centralities in $d + Au$ collisions are presented in Table 9.17. This table also includes values of physical quantities that can be extracted from fit parameters under assumption that effective mass using in Eq. 4.18 is equal to pion mass. Appendix K.1 shows how physical parameters depend on the effective mass used in the calculations.

k_T [GeV/c]	R_O [fm]	R_S [fm]	R_L [fm]	λ
$d + Au$ [0 − 20]%				
[0.15, 0.25]	1.89 ± 0.03	1.72 ± 0.02	2.44 ± 0.02	0.338 ± 0.004
[0.25, 0.35]	1.78 ± 0.02	1.71 ± 0.03	2.08 ± 0.03	0.420 ± 0.009
[0.35, 0.45]	1.50 ± 0.03	1.53 ± 0.03	1.82 ± 0.03	0.415 ± 0.008
[0.45, 0.60]	1.30 ± 0.02	1.33 ± 0.03	1.45 ± 0.03	0.430 ± 0.010
$d + Au$ [20 − 40]%				
[0.15, 0.25]	1.62 ± 0.02	1.56 ± 0.02	2.30 ± 0.03	0.349 ± 0.005
[0.25, 0.35]	1.62 ± 0.03	1.54 ± 0.02	2.01 ± 0.03	0.429 ± 0.007
[0.35, 0.45]	1.35 ± 0.03	1.37 ± 0.03	1.66 ± 0.04	0.421 ± 0.010
[0.45, 0.60]	1.20 ± 0.03	1.23 ± 0.03	1.37 ± 0.03	0.447 ± 0.011
$d + Au$ [40 − 100]%				
[0.15, 0.25]	1.28 ± 0.02	1.19 ± 0.01	2.12 ± 0.02	0.372 ± 0.004
[0.25, 0.35]	1.11 ± 0.02	1.19 ± 0.02	1.94 ± 0.02	0.386 ± 0.006
[0.35, 0.45]	0.96 ± 0.02	1.10 ± 0.03	1.65 ± 0.03	0.395 ± 0.009
[0.45, 0.60]	0.78 ± 0.02	0.85 ± 0.02	1.33 ± 0.03	0.399 ± 0.009

Table 9.14: Fit results from a fit to data from $d + Au$ collisions at $\sqrt{s_{NN}}$=200 GeV using Eq. 4.11 to parameterize the femtoscopic correlations ("standard fit").

It is important to notice that even though different parameterizations of non-femtoscopic correlations change the values of femtoscopic parameters obtained from the fit, the m_T dependence of HBT radii from $d + Au$ collisions holds.

9.2.3 Separating $p + Au$ collisions from $d + Au$ collisions

As discussed in Sec. 8.1 the STAR experiment has tools to separate $p + Au$ collisions from the most peripheral $d + Au$ collisions. Thus, we did a separate study of correlations in $p + Au$ collisions and also in $d + Au$ collisions after removing $p + Au$ events. However, due to the method of extracting $p + Au$ collisions, we are biased towards "peripheral" $p + Au$ collisions (low multiplicity events). Also, even though we were able to separate $p + Au$ collisions our remaining $d + Au$ data sample still includes $n + Au$ collisions that we are technically not able to distinguish from $d + Au$ events.

Figure 9.19 shows the comparisons of the HBT radii obtained from $p + Au$ collisions (Table 9.18) with previously shown results from $d + Au$ and $p + p$ collisions using Eq. 4.11 to fit femtoscopic correlations and neglecting non-femtoscopic correlations. Interestingly, we see that R_O and R_S radii obtained from $p + Au$ collisions are smaller
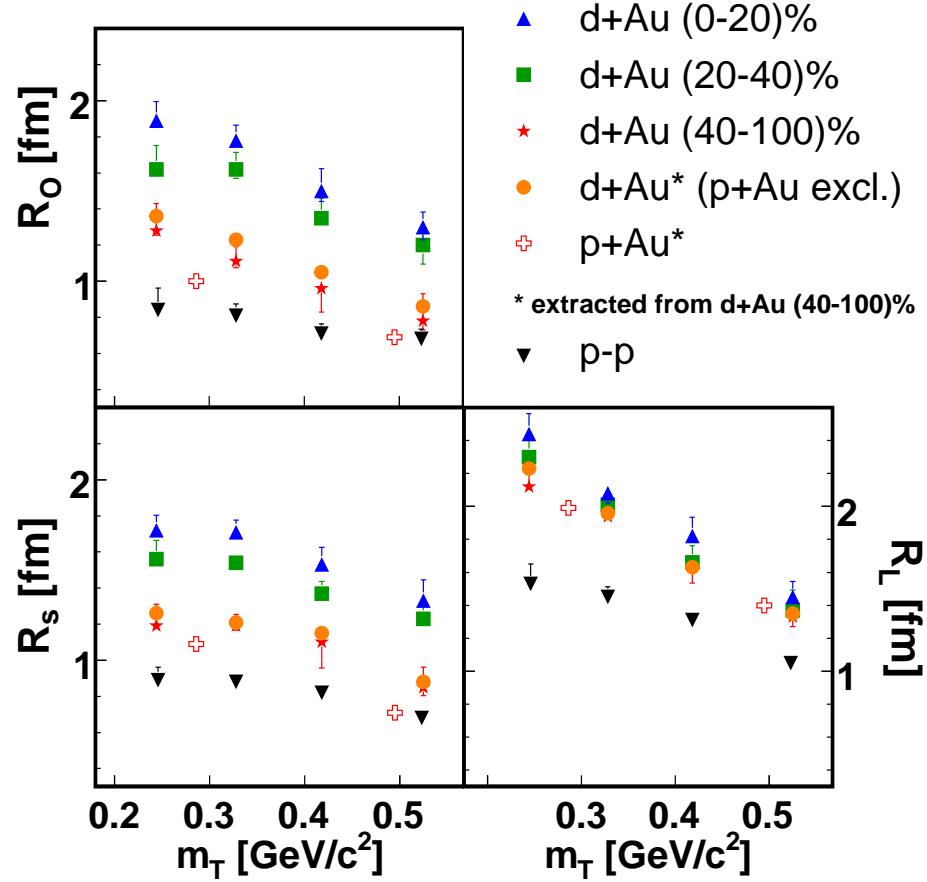
Figure 9.19: The m_T dependence of HBT radii for three centralities from $d + Au$ collisions, $p + Au$ and $p + p$ collisions at $\sqrt{s}$=200 GeV.

than the one from $d + Au$ collisions while not much difference is seen for R_L. Additionally, the values of R_O and R_S are comparable to results from $p + p$ collisions

(Section 9.1) suggesting that the geometrical size of the homogeneity region is sensitive to the smaller nuclei participating in the collisions.

Table 9.15: Fit results from a fit to data from $d + Au$ collisions at $\sqrt{s_{NN}}$= 200 GeV using Eq. 4.11 to parameterize the femtoscopic correlations and Eq. 4.13 for nonfemtoscopic correlations ("$\delta - q$ fit").

k_T [GeV/c]	R_O [fm]	R_S [fm]	R_L [fm]	λ	δ_O	δ_S	δ_L
				$d + Au\ [0 - 20]\%$			
$[0.15, 0.25]$	2.15 ± 0.03	1.89 ± 0.02	2.61 ± 0.04	0.339 ± 0.005	-0.0059 ± 0.0016	0.0334 ± 0.0019	-0.0894 ± 0.0034
$[0.25, 0.35]$	2.04 ± 0.03	1.84 ± 0.03	2.26 ± 0.03	0.423 ± 0.008	-0.0072 ± 0.0019	-0.0361 ± 0.0018	-0.1063 ± 0.0033
$[0.35, 0.45]$	1.76 ± 0.03	1.70 ± 0.03	1.98 ± 0.04	0.432 ± 0.012	-0.0204 ± 0.0027	-0.0417 ± 0.0027	-0.0658 ± 0.0039
$[0.45, 0.60]$	1.58 ± 0.04	1.52 ± 0.04	1.64 ± 0.05	0.441 ± 0.014	-0.0479 ± 0.0035	-0.0557 ± 0.0034	-0.1359 ± 0.0042
				$d + Au\ [20 - 40]\%$			
$[0.15, 0.25]$	1.97 ± 0.03	1.81 ± 0.03	2.52 ± 0.04	0.344 ± 0.005	-0.0120 ± 0.0020	-0.0485 ± 0.0025	-0.1573 ± 0.0042
$[0.25, 0.35]$	1.87 ± 0.03	1.71 ± 0.03	2.12 ± 0.04	0.431 ± 0.009	-0.0056 ± 0.0024	-0.0533 ± 0.0023	-0.1545 ± 0.0039
$[0.35, 0.45]$	1.68 ± 0.02	1.53 ± 0.03	1.79 ± 0.02	0.431 ± 0.008	-0.0109 ± 0.0035	-0.0448 ± 0.0034	-0.0923 ± 0.0050
$[0.45, 0.60]$	1.54 ± 0.05	1.38 ± 0.04	1.60 ± 0.05	0.423 ± 0.017	-0.0688 ± 0.0043	-0.0832 ± 0.0042	-0.1975 ± 0.0051
				$d + Au\ [40 - 100]\%$			
$[0.15, 0.25]$	1.87 ± 0.03	1.55 ± 0.02	2.37 ± 0.04	0.354 ± 0.005	-0.0019 ± 0.0029	-0.0815 ± 0.0030	-0.3387 ± 0.0048
$[0.25, 0.35]$	1.73 ± 0.03	1.49 ± 0.03	2.00 ± 0.04	0.417 ± 0.008	0.0139 ± 0.0031	-0.0714 ± 0.0028	-0.3036 ± 0.0046
$[0.35, 0.45]$	1.49 ± 0.02	1.44 ± 0.02	1.69 ± 0.03	0.412 ± 0.009	-0.0144 ± 0.0037	-0.0602 ± 0.0039	-0.3224 ± 0.0053
$[0.45, 0.60]$	1.35 ± 0.05	1.28 ± 0.04	1.54 ± 0.05	0.401 ± 0.015	-0.0747 ± 0.0046	-0.0915 ± 0.0047	-0.3339 ± 0.0057

k_T [GeV/c]	R_O [fm]	R_S [fm]	R_L [fm]	λ
$d + Au$ [0 − 20]%				
[0.15, 0.25]	1.94 ± 0.02	1.74 ± 0.01	2.39 ± 0.02	0.397 ± 0.006
[0.25, 0.35]	1.79 ± 0.02	1.73 ± 0.02	2.03 ± 0.02	0.462 ± 0.007
[0.35, 0.45]	1.55 ± 0.02	1.52 ± 0.03	1.79 ± 0.03	0.453 ± 0.012
[0.45, 0.60]	1.34 ± 0.02	1.34 ± 0.02	1.47 ± 0.03	0.462 ± 0.011
$d + Au$ [20 − 40]%				
[0.15, 0.25]	1.67 ± 0.03	1.58 ± 0.03	2.23 ± 0.02	0.425 ± 0.006
[0.25, 0.35]	1.64 ± 0.04	1.56 ± 0.03	1.95 ± 0.05	0.514 ± 0.006
[0.35, 0.45]	1.43 ± 0.03	1.39 ± 0.04	1.64 ± 0.03	0.476 ± 0.009
[0.45, 0.60]	1.24 ± 0.04	1.22 ± 0.05	1.38 ± 0.04	0.489 ± 0.009
$d + Au$ [40 − 100]%				
[0.15, 0.25]	1.49 ± 0.04	1.32 ± 0.04	2.00 ± 0.03	0.556 ± 0.008
[0.25, 0.35]	1.33 ± 0.03	1.23 ± 0.03	1.83 ± 0.04	0.487 ± 0.009
[0.35, 0.45]	1.17 ± 0.03	1.08 ± 0.04	1.56 ± 0.04	0.486 ± 0.011
[0.45, 0.60]	0.87 ± 0.04	0.86 ± 0.05	1.24 ± 0.05	0.475 ± 0.012

Table 9.16: Fit results from a fit to data from $d + Au$ collisions at $\sqrt{s_{NN}}$= 200 GeV using Eq. 4.11 to parameterize the femtoscopic correlations and Eq. 4.15 for nonfemtoscopic correlations ("EMCIC fit").

		d + Au			p + p
		[0-20]%	[20-40]%	[40-100]%	
fit parameters	M_1 $[(GeV/c)^{-2}]$	0.072	0.11	0.22	0.43
	M_2 $[(GeV/c)^{-2}]$	0.037	0.06	0.10	0.22
	M_3 $[GeV^{-2}]$	0.24	0.37	0.67	1.51
	M_4 $[GeV^{-1}]$	0.17	0.25	0.46	1.02
physical quantities	N	76.3	52.8	28.9	14.3
	$\langle p_T^2 \rangle$ $[(GeV/c)^2]$	0.18	0.17	0.16	0.17
	$\langle p_z^2 \rangle$ $[(GeV/c)^2]$	0.36	0.32	0.35	0.32
	$\langle E^2 \rangle$ $[GeV^2]$	0.56	0.51	0.53	0.51
	$\langle E \rangle$ $[GeV]$	0.71	0.68	0.69	0.68

Table 9.17: Fit parameters (M_1-M_4 from 4.15) for three centralities from $d + Au$ collisions at $\sqrt{s_{NN}}$=200 GeV and $p + p$ collisions at $\sqrt{s}$=200 GeV (Section 9.1) and corresponding physical quantities obtained from these parameters assuming pion mass. See Appendix K.2 for more details.

k_T [GeV/c]	R_O [fm]	R_S [fm]	R_L [fm]	λ
$[0.15, 0.25]$	1.36 ± 0.02	1.26 ± 0.02	2.23 ± 0.02	0.372 ± 0.004
$[0.25, 0.35]$	1.23 ± 0.02	1.21 ± 0.02	1.96 ± 0.02	0.401 ± 0.006
$[0.35, 0.45]$	1.05 ± 0.02	1.15 ± 0.02	1.63 ± 0.03	0.414 ± 0.010
$[0.45, 0.60]$	0.86 ± 0.02	0.88 ± 0.02	1.35 ± 0.03	0.410 ± 0.011

Table 9.18: Fit results from a fit to 3D correlation function from peripheral $d + Au$ collisions (40-100)% after removing $p + Au$ collisions.

k_T [GeV/c]	R_O [fm]	R_S [fm]	R_L [fm]	λ
$[0.15, 0.35]$	1.00 ± 0.03	1.09 ± 0.02	1.99 ± 0.03	0.369 ± 0.008
$[0.35, 0.60]$	0.69 ± 0.02	0.71 ± 0.02	1.40 ± 0.04	0.357 ± 0.010

Table 9.19: Fit results from a fit to 3D correlation function from peripheral $p + Au$ collisions extracted from peripheral $d + Au$ collisions (40-100)%.

9.3 $Au + Au$ collisions at $\sqrt{s_{NN}}$=19.6 GeV

In this section, we present a femtoscopic analysis of two-pion correlations measured in Au+Au collisions at $\sqrt{s_{NN}} = 19.6$ GeV by the STAR experiment at RHIC. The main motivation of doing this study was that the HBT radii from Gaussian fits to the correlation functions from $Au + Au$ collisions at $\sqrt{s_{NN}}$=19.6 GeV may be directly compared to existing data over a wide range of energies. In particular, we compare them to similar measurements at the CERN SPS. It is the first time that we can do such a comparison of femtoscopic results between experiments from RHIC and SPS.

9.3.1 Results

In Figure 9.20 is plotted the correlation function for charged pions at low transverse momentum. Projections of the fits to the correlation function with Equation 4.11, weighted according to the mixed-pair background are also plotted. In our analysis we used data from the most central [0-10%] $Au + Au$ collisions and fit the correlation function for four bins in k_T. Results are presented in Table 9.20 and plotted on Figs. 9.21 and 9.22.

k_T [GeV/c]	$\langle m_T \rangle$ [GeV/c]	R_O [fm]	R_S [fm]	R_L [fm]	λ
$[0.15, 0.25]$	0.240	4.84 ± 0.44	4.94 ± 0.42	5.87 ± 0.49	0.43 ± 0.07
$[0.25, 0.35]$	0.328	4.97 ± 0.27	4.71 ± 0.24	4.99 ± 0.27	0.53 ± 0.04
$[0.35, 0.45]$	0.420	4.46 ± 0.28	4.26 ± 0.26	4.10 ± 0.29	0.60 ± 0.07
$[0.45, 0.60]$	0.522	3.37 ± 0.36	3.76 ± 0.31	3.35 ± 0.37	0.45 ± 0.07

Table 9.20: Fit results from a fit to data from [0-10%] $Au + Au$ collisions at $\sqrt{s}$= 19.6 GeV using Eq. 4.11 to parameterize the femtoscopic correlations.
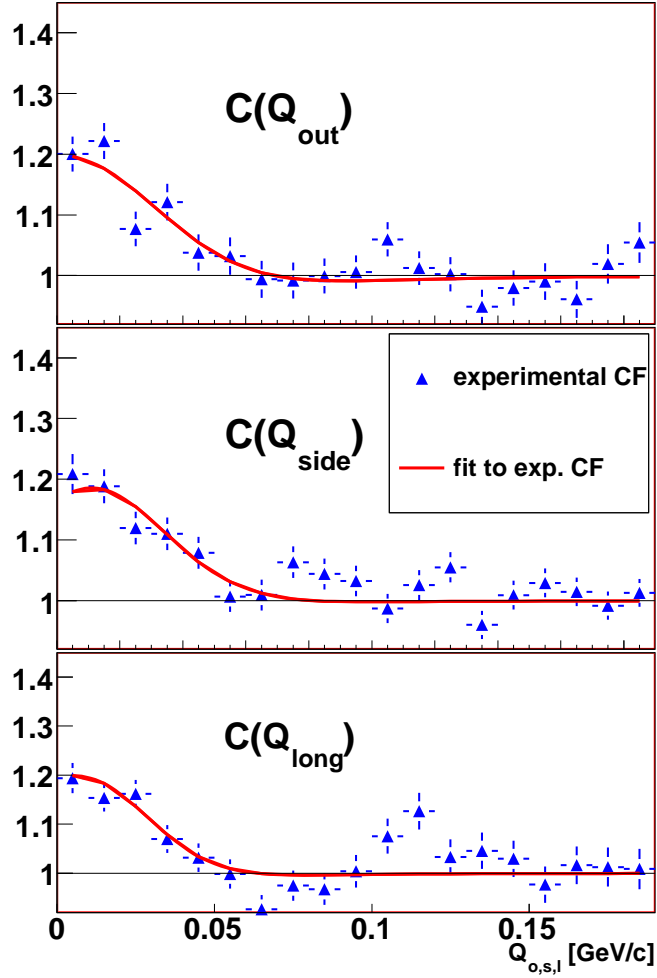
Figure 9.20: Projections of the three-dimensional correlation function onto the q_o, q_s and q_l axes. To project onto a given q-component, the others are integrated over the range **0-35 MeV/c**. Data shown is for charged pions from central collisions measured at midrapidity and with transverse pair momentum $k_T = [0.15 - 0.25]$ GeV/c. Projections of the three-dimensional fit with Equation 4.11 are shown as solid lines.

Gaussian femtoscopic radii have been measured for pions emitted from central Au (Pb) collisions over two orders of magnitude in $\sqrt{s_{NN}}$. Our results at $\sqrt{s_{NN}} =$ 19.6 GeV fall in the (logarithmic) center of this range, and are shown in the context of the world dataset in Figure 9.21.
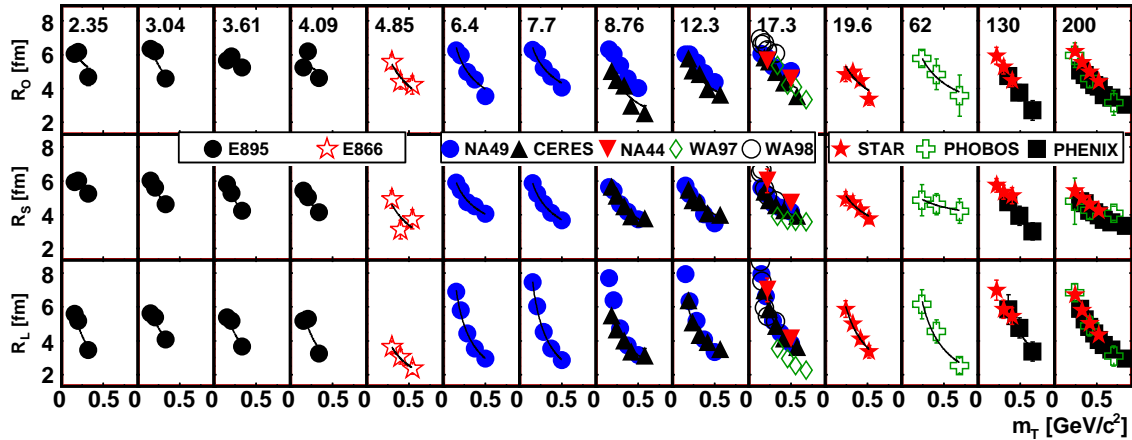
Figure 9.21: Femtoscopic radii from midrapidity pion correlations from central collisions of Au or Pb, plotted versus the transverse mass m_T, for 14 different values of collision energy, $\sqrt{s_{NN}}$ (indicated in each panel).

A direct comparison with STAR's measurement of Au+Au collisions at $\sqrt{s_{NN}} = 19.6$ GeV and Pb+Pb results at $\sqrt{s_{NN}} = 17.3$ GeV is justified because the difference in the energy of the collisions is less than 10%. This comparison is shown in Figure 9.22. The STAR results are consistent with those from CERES [109] and slightly less consistent with NA49 results [110] especially at the last m_T bin for R_O.

Figure 9.21 makes clear that the most discriminating comparison with SPS results would come from a STAR measurement at $\sqrt{s_{NN}} = 8.7$ GeV. This is also true for a confirmation of "kinks" and "horns" reported at the SPS. Such comparisons will take place during the future low-energy program at RHIC. However, it is also clear from

We quantify this point by characterizing the m_T-dependence of the femtoscopic radius R_μ by fitting the curves in Figure 9.21 with the form $R_\mu = R_{\mu,0}/m_T^{\alpha_\mu}$. This functional form is motivated by idealized hydrodynamical calculations [111], in which $\alpha = 0.5$. It is, however, probably less justified, physically, for the R_o than the other

154
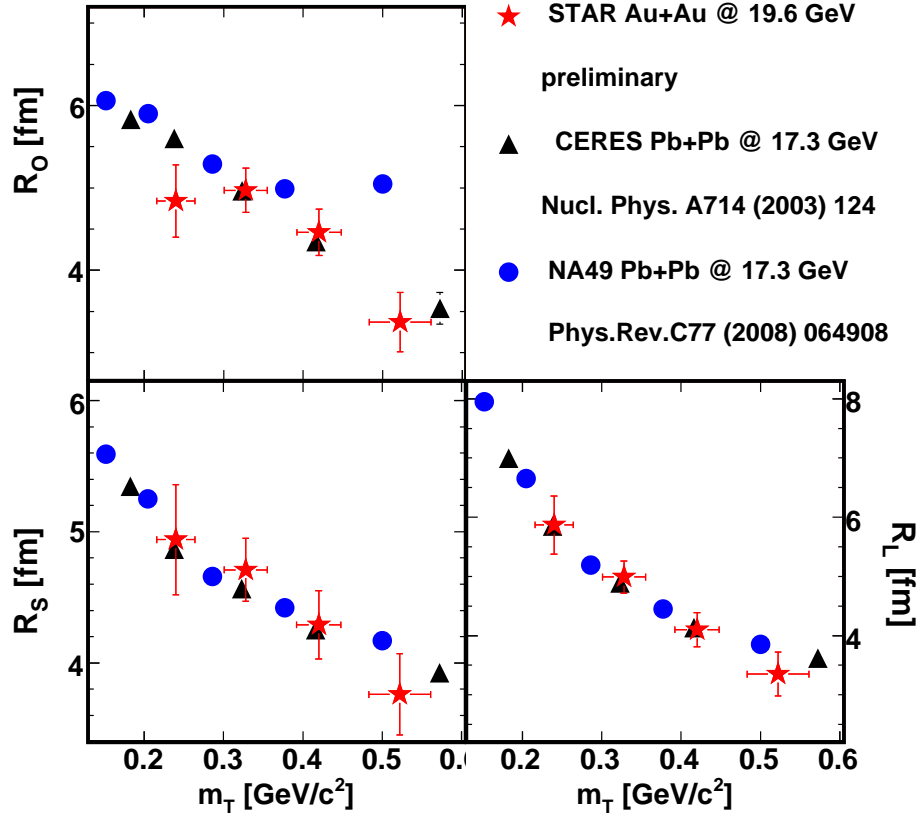
Figure 9.22: Femtoscopic radii measured by the STAR experiment at RHIC (red stars) are compared with those reported by CERES (green squares) and NA49 (black circles) at the SPS. See text for details.

radii, due to the admixture of space and time in R_o; we use the form here for simplicity and only as a numerical indication of the strength of the m_T-dependence. These fits are indicated by smooth curves in Figure 9.21.

The excitation function of this strength, α_μ, is shown in Figure 9.23. The systematic trend of the discrepancy, while somewhat ameliorated at the highest SPS energy, nevertheless persists there, and the new STAR data disfavors α_o much below 0.5 at energies $\sqrt{s_{NN}} \sim 20$ GeV.
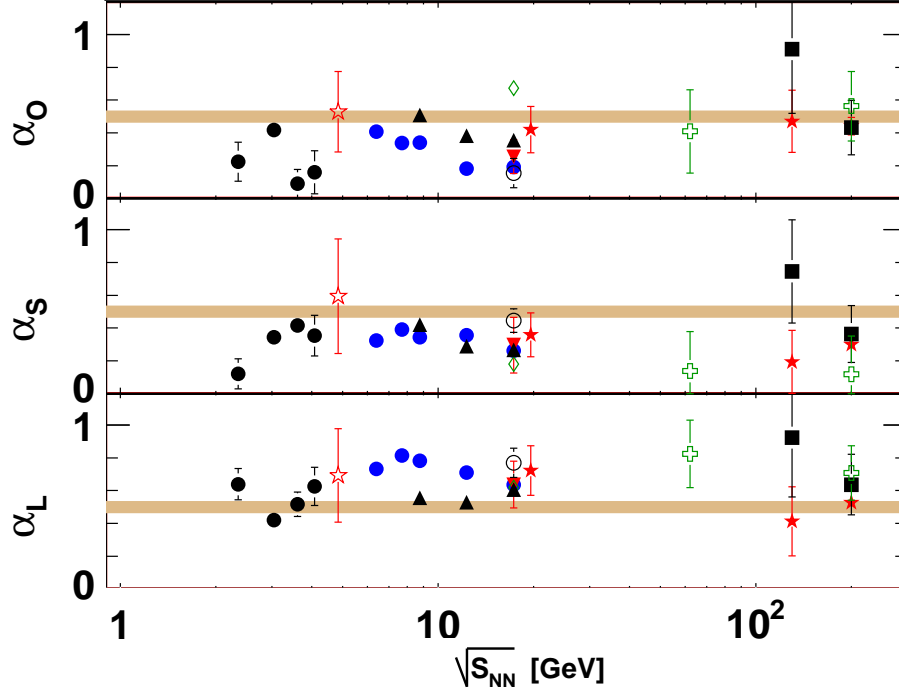
Figure 9.23: The strength of the m_T-dependence of the femtoscopic radii for central collisions is shown as a function of collision energy. See text for details. A yellow band, centered at $\alpha = 0.5$ is motivated by an idealized hydrodynamical model [111], and is only shown for reference.

Femtoscopic results from low energy $Au + Au$ collisions at RHIC also allow us to fill the gap in the HBT excitation function between AGS/SPS and RHIC results. Figure 9.24 shows the dependence of HBT radii from central heavy ion collisions on the energy of the collisions.

9.3.2   Blast-wave fit to spectra and HBT results

In Section 3 we discussed the results from $Au + Au$ collisions at $\sqrt{s_{NN}}$=200 GeV where we mentioned that femtoscopic results together with various momentum observables like single-particle distribution and v_2 show a very good agreement with

156
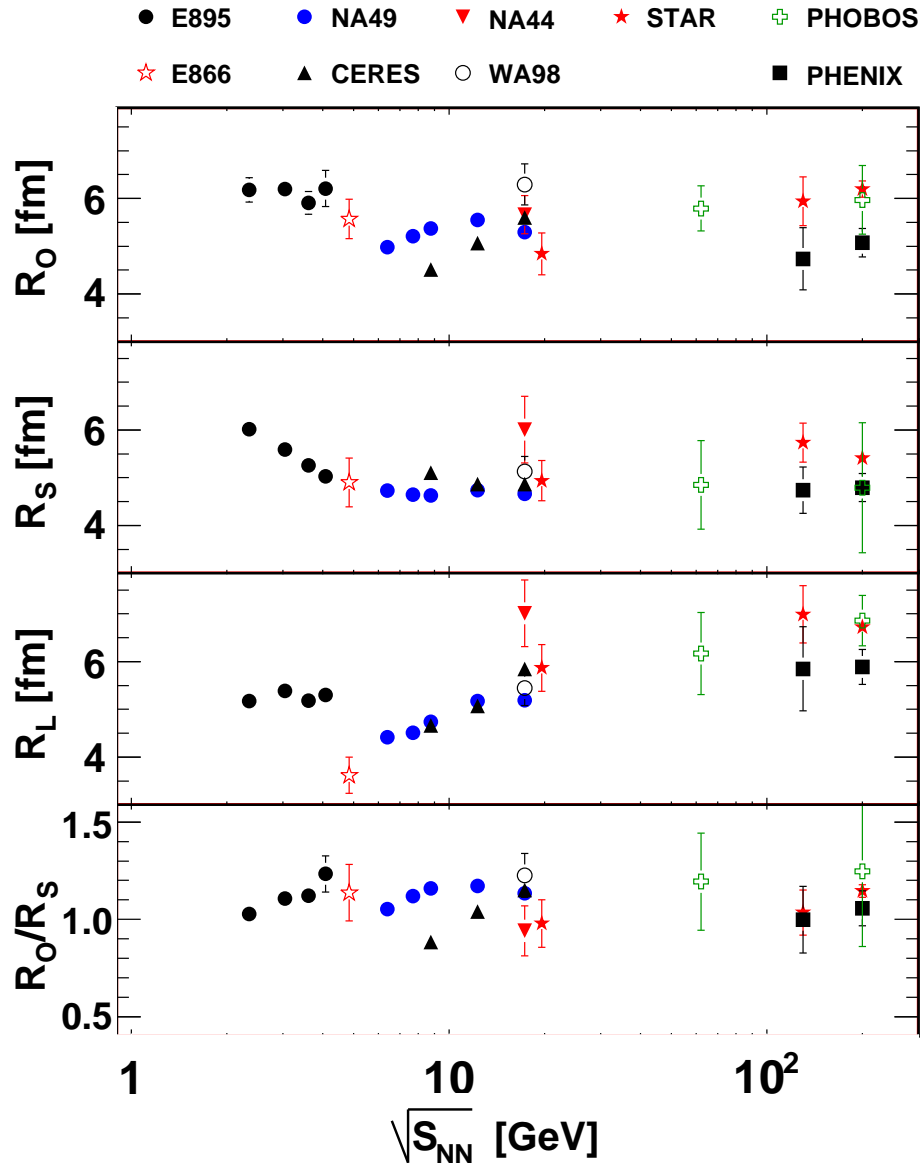
Figure 9.24: Excitation function for data from heavy ion collisions.

hydrodynamic models supporting a strong collectivity in heavy ion collisions at top RHIC energies. In this section, we are going to use a hydro-inspired blast-wave model [7] and fit results from $Au + Au$ collisions at $\sqrt{s_{NN}}$=19.6 GeV, an order of magnitude lower energy and verify whether these results are consistent with flow scenario.

157
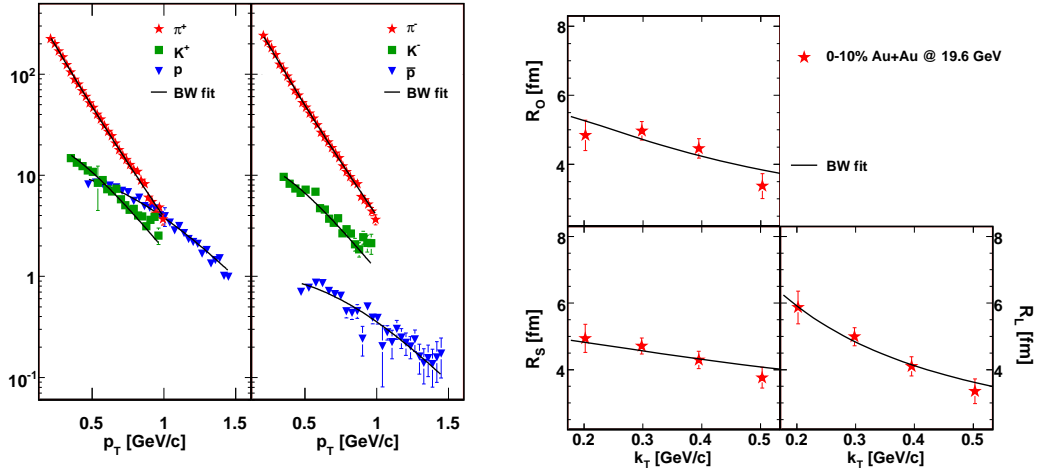
Figure 9.25: Particle spectra (left panel) and HBT results (right panel) from [0-10%] $Au + Au$ collisions at $\sqrt{s_{NN}}$=19.6 GeV. Lines represent results from a fit using the blast-wave model [7].

Results of the blast-wave fit to both spectra [112] for pions, kaons and protons and pion femtoscopic radii are presented in Table 9.21. Figure 9.25 shows experimental data used in this fit and lines representing the blast-wave curves obtained from the fit to experimental data.

parameter	fit value
T [MeV]	106 ± 2
β [c]	0.49 ± 0.02
R [fm]	11.1 ± 0.5
τ [fm/c]	7.3 ± 0.7
Δt [fm/c]	1.7 ± 0.7

Table 9.21: Results from blast-wave fit to spectra and HBT from [0-10%] $Au + Au$ collisions at $\sqrt{s_{NN}}$=19.6 GeV in STAR.

158

Clearly, the results show significant radial flow in low energy $Au + Au$ collisions although a little bit less than in $Au + Au$ collisions at $\sqrt{s_{NN}}$=200 GeV. A detailed comparison of fit results from blast-wave model to $Au + Au$ results at $\sqrt{s_{NN}}$=19.6 GeV presented in this chapter with previously published results from higher energies [67] is shown on Fig. 9.26.

This figure demonstrates that all results from the blast-wave fit show a smooth dependence on the total number of particles.

9.3.3 More on the time scale

We showed on Fig. 9.26 the dependence of evolution time (τ) obtained from the blast-wave fit on the event multiplicity. An alternative way of calculating the evolution time of the system was suggested by Sinyukov *et al.* [113, 12] who provided the following formula that can be fitted to the transverse mass dependence of R_L radius.

$$R_L(m_T) = \tau \sqrt{\frac{T}{m_T} \frac{K_2 \left(\frac{m_T}{T} \right)}{K_1 \left(\frac{m_T}{T} \right)}}, \tag{9.1}$$

where, T is the kinetic freeze-out temperature and K_1 and K_2 are modified Bessel functions. We should mention that this formula does assume zero flow and zero proper time ($\Delta \tau = 0$). If these two effects are included in calculations the final results do not differ by more than 15%.

Figure 9.27 shows the STAR results and fit curve using Eq. 9.1.

Now, we can compare the evolution time of the system obtained from the blast-wave model and analytic formula given by Eq. 9.1. Figure 9.28 shows such a comparison. Clearly, both approaches give very similar results within error bars.
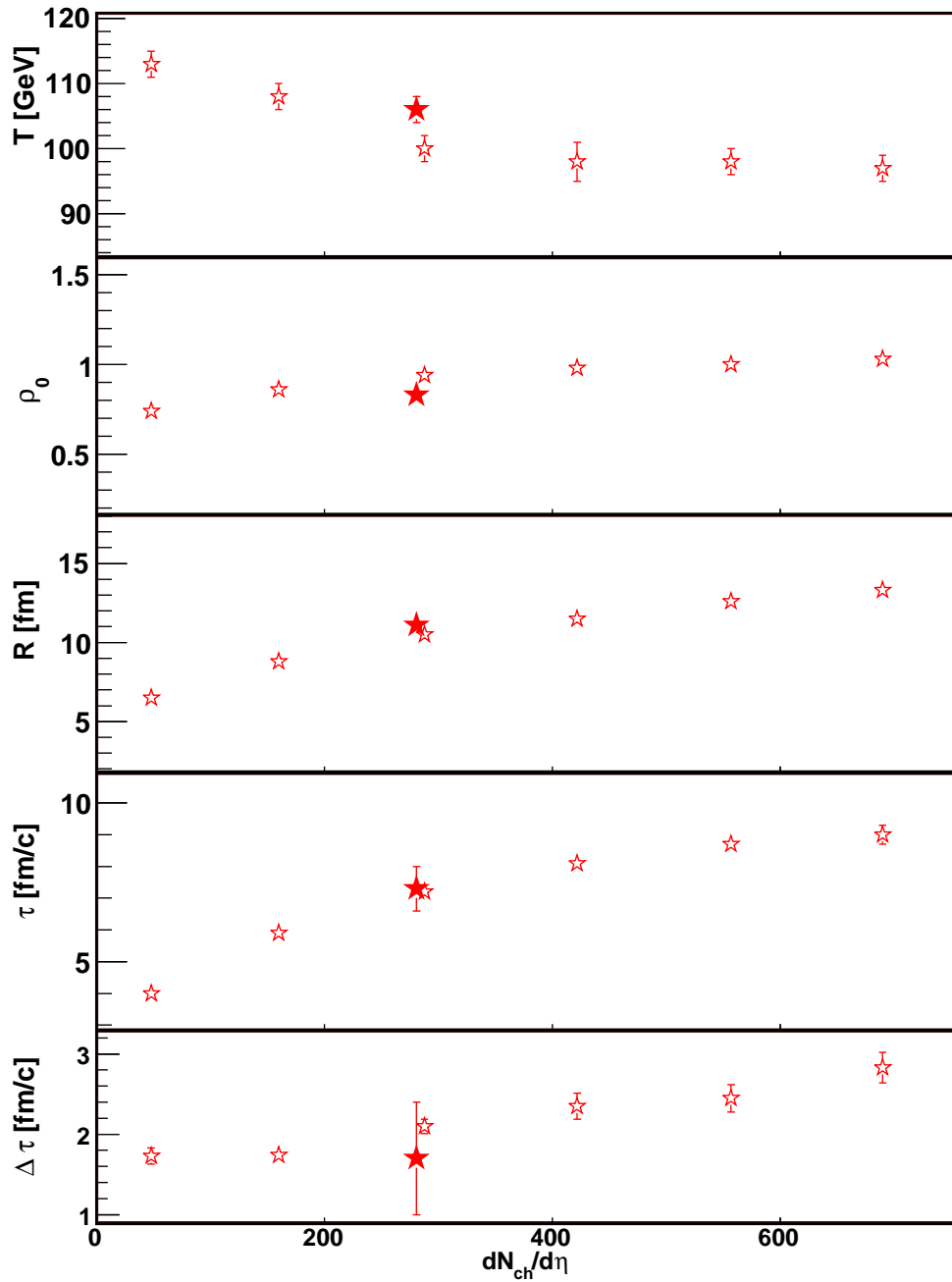
Figure 9.26: Comparison of the blast-wave fit results from $Au + Au$ collisions at $\sqrt{s_{NN}}$=19.6 GeV and $\sqrt{s_{NN}}$=200 GeV plotted versus the number of charged particles per unit of pseudorapidity.
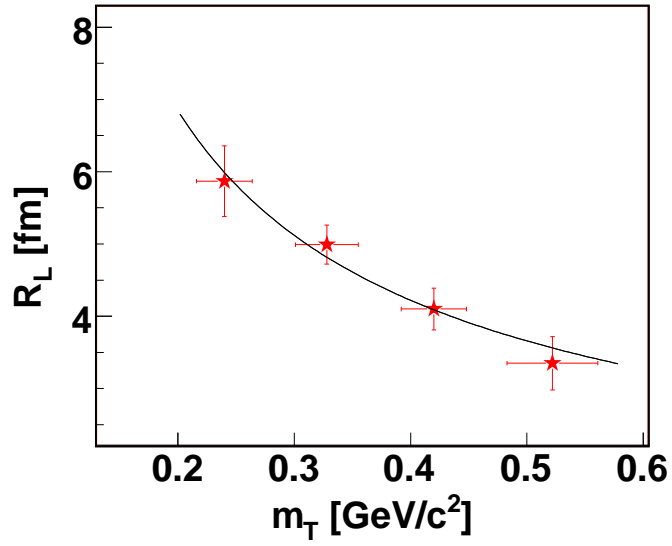
Figure 9.27: Fit to the m_T dependence of R_L from [0-10%] $Au + Au$ collisions at $\sqrt{s_{NN}}$=19.6 GeV using Eq. 9.1.
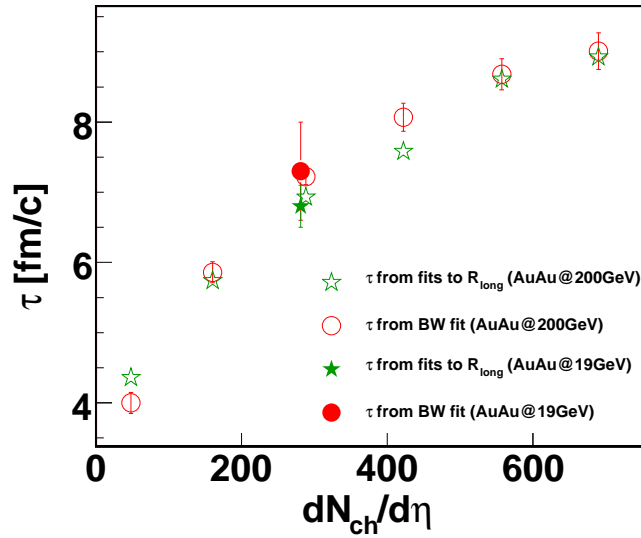
Figure 9.28: System evolution time vs multiplicity obtained from fits using blast-wave model [7] and Eq. 9.1. Data from $Au + Au$ collisions at $\sqrt{s_{NN}}$=200 GeV taken from [67].

161

CHAPTER 10

BIG SYSTEM VS SMALL SYSTEM: SURPRISING SCALINGS

The STAR experiment gives us a unique opportunity to compare physics from big systems like $Au + Au$ collisions and a small system like $p + p$ collisions in the same experiment, at the same energies, with the same detector acceptance, analysis technique and even the same software. In this chapter we compare the femtoscopic results from large systems, including $Au + Au$, $Cu + Cu$ and $d + Au$ collisions from STAR, with results from $p + p$ collisions. We also compare the multiplicity dependence of HBT radii from heavy ion collisions and $p + p$ collisions from RHIC with experiments from SPS and AGS facilities.

10.1 m_T dependence

In Sec. 9.1.1 we showed that the HBT radii from $p + p$ collisions at STAR decrease with increasing transverse mass. Similar effect is observed in many heavy ion collision data, including STAR data from $Au + Au$ collisions at 200 GeV [67] and it was attributed to flow [7] (see Sec. 3.1). Figure 10.1 shows the ratio of the three dimensional radii in Au+Au collisions to p+p radii obtained from various parameterizations (see Sec. 9.1.1 for more details) plotted versus the transverse mass of a pair (m_T). The

ratios presented on this figure look flat indicating very similar slope of the transverse

mass dependence of the HBT radii. Interestingly, the same scaling is observed for
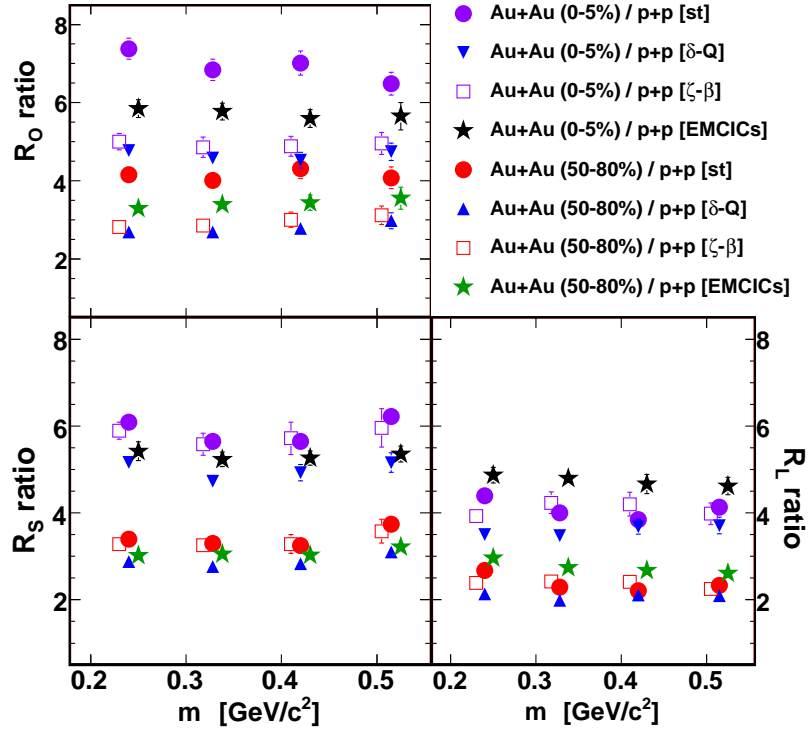
Figure 10.1: The ratio of the HBT radii from $Au + Au$ collisions [67] to results from $p + p$ collisions plotted versus the transverse mass.

data from $Cu + Cu$ [114] and $d + Au$ (Sec. 9.2) collisions at $\sqrt{s_{NN}}$=200 GeV as

shown on Fig. 10.2. It is rather surprising observation especially that it is expected

that different origins drive the transverse mass dependences of the femtoscopic radii

in heavy ion collisions (e.g. $Au + Au$) and $p + p$ collisions. If we assume that these

expectations are correct, the data show that we cannot distinguish different physics

behind $p + p$ and $Au + Au$ collisions when studding pion femtoscopy.
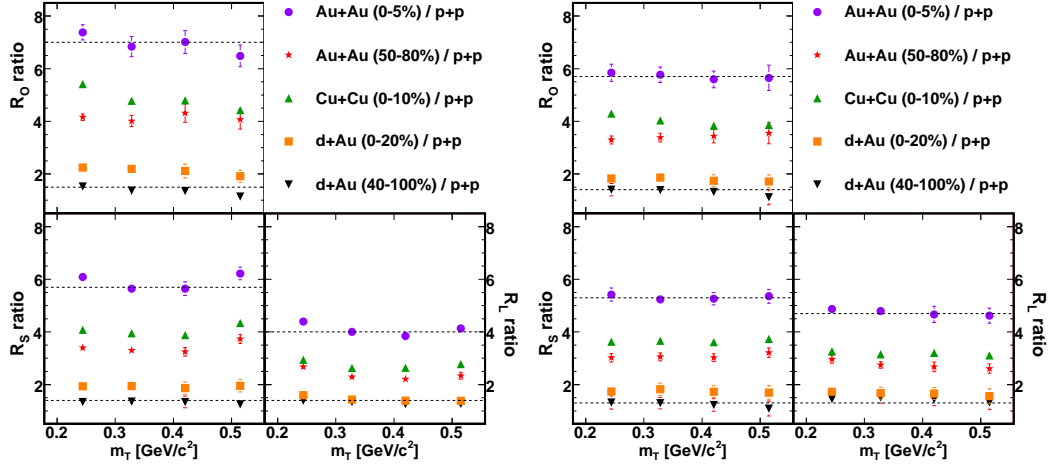
Figure 10.2: The ratio of the HBT radii from $Au + Au$ collisions [67], $Cu + Cu$ collisions [114], $d + Au$ collisions (see Sec. 9.2) to results from $p + p$ collisions at the same energy of the collisions 200 GeV plotted versus the transverse mass. Left side figure includes results from $p + p$ and $d + Au$ collisions obtained from the "standard fit" and the right side figure shows results from the "EMCIC fit". See Sections 9.1 and 9.2 for more details.

10.2 Multiplicity scaling

The dependence of the femtoscopic radii on $(dN_{ch}/d\eta)^{1/3}$ (dN_{ch} - number of charged particles at midrapidity) for different colliding systems and at different energies of the collisions is presented in Fig. 10.3. The main reason we are interested in studying such a relation is its connection to the final state geometry through the particle density at freeze-out. Results from $p + p$ (Sec.9.1), $d + Au$ (Sec. 9.2), $Cu + Cu$ [114] and $Au + Au$ collisions [67] from the STAR experiment for $\langle k_T \rangle = 0.2$ GeV/c are combined on the left panel of Fig. 10.3. The right panel also shows STAR results but for different average value of the k_T. Additionally, results from with AGS/SPS/RHIC experiments [26] are plotted for a comparison. It is stunning that the geometric radii (R_{side} and R_{long}) show a smooth increase with increase of the

multiplicity over a wide range of energies. Although it is not shown here, we checked

that this observation is present for all k_T bins studied by STAR. Results presented
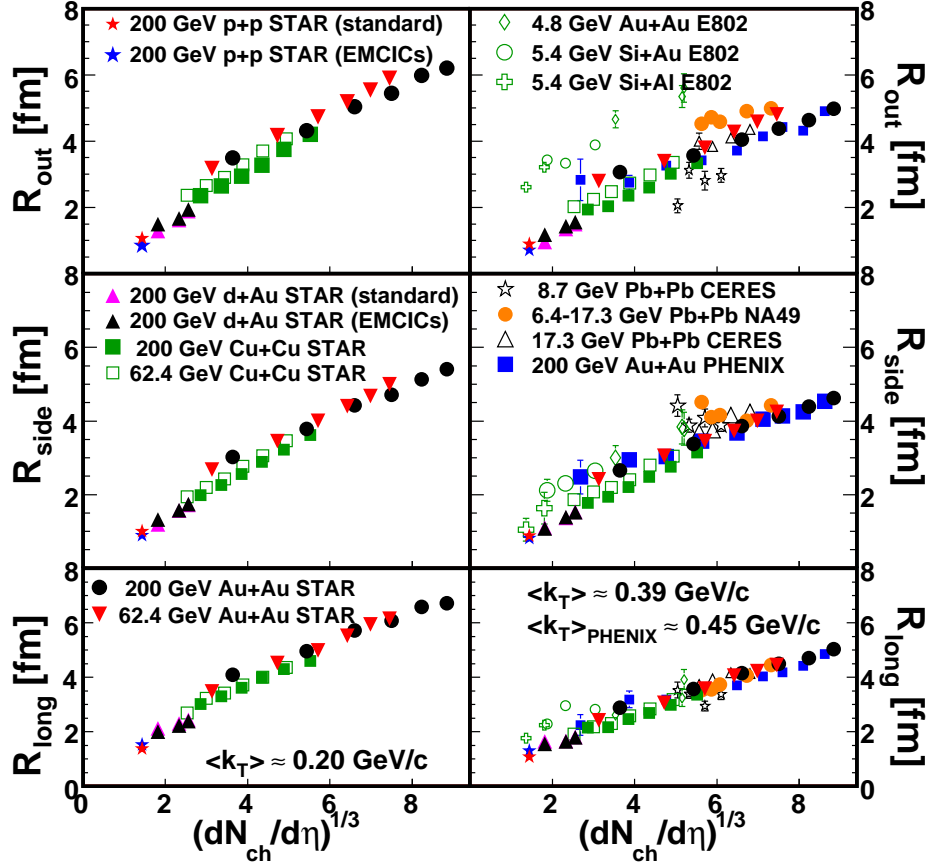
Figure 10.3: The multiplicity dependence of the HBT radii from $p + p$, $Cu + Cu$ and $Au + Au$ [67] collisions from STAR compared with results from other experiments [26].

on Fig. 10.3 clearly demonstrate that the multiplicity is a scaling variable that drives

geometric the femtoscopic radii at midrapidity. We do not expect this scaling to hold

for R_O because it mixes both the space and time information so it is not a purely

geometrical quantity. We believe that because of the presence of the finite intercepts

of the linear scaling [26, 115], the results presented here do not support the scenario that the freeze-out occurs at the constant particle density [116].

So far we verified this scaling at midrapidity only and we expect a dependence of this scaling on rapidity [116, 117, 118] It would be interesting to go to these larger rapidities to verify if and/or where this "universal scaling" breaks down.

An interesting results of our studies is that we can predict the size of the source without any knowledge about the collision (like total energy of the collisions, impact parameter, N_{part}, colliding nuclei etc.) and the only thing we need is the the multiplicity [116, 117, 118]. Such a scaling is expected to be observed in all systems that are meson dominated but will more likely be violated low energy collisions that are dominated by baryons [117, 26, 119].

10.3   System expansion

Having data from $p + p$ collisions up to $Au + Au$ collisions at the same energy ($\sqrt{s_{NN}}$=200 GeV) at RHIC we can study the system expansion. We can do it in a model-dependent approach by comparing the final system size to its initial size. Figure 10.4 presents such a relation relationship between initial and final geometry. The final size of the source was estimated by R_S at low $k_T \approx 0.2$ GeV/c [7]. The initial RMS of the overlapping region was estimated with a Glauber calculation. The initial size of the $p + p$ collisions was taken from an e^- scattering [120]. As seen, the system created in the most central $Au + Au$ collisions expands by a factor of two while the system in $p + p$ collisions shows none or a little expansion. Results from $d + Au$ and $Cu + Cu$ collisions are between these two extreme cases. However, we would like to
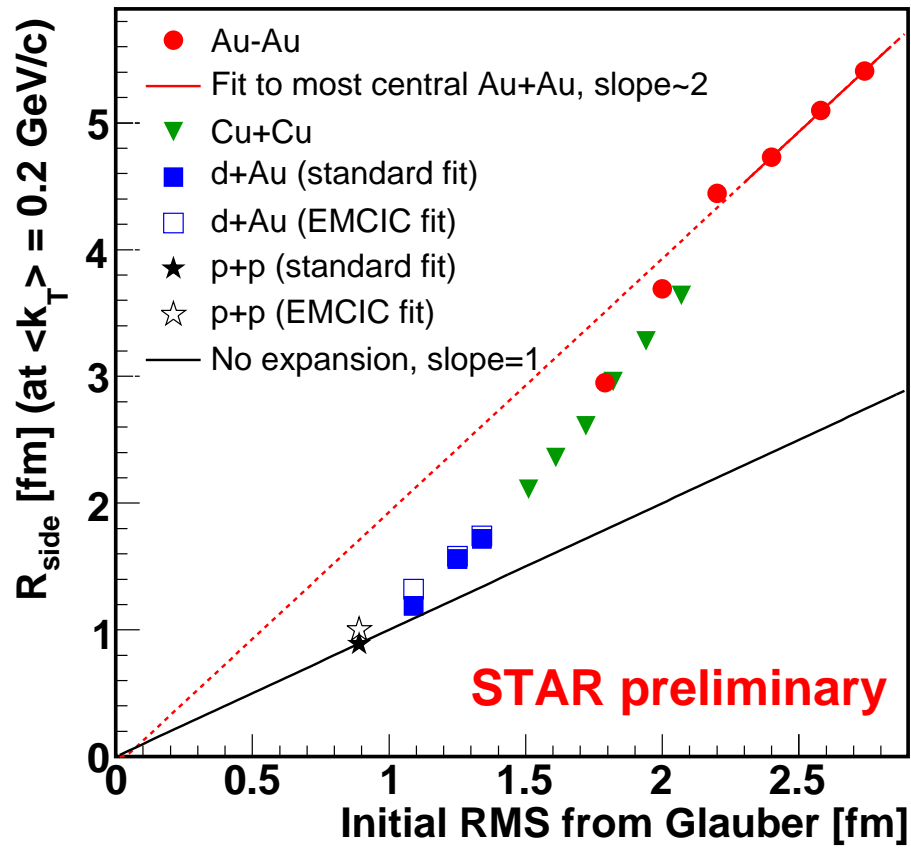
Figure 10.4: Final size of the source vs. initial radii calculated from Glauber model. STAR Au+Au data from [67].

stress that these results do not imply that small systems (from $p + p$ collisions) are less explosive than the large systems (from $Au + Au$ collisions) as shown in Sec. 10.1.

CHAPTER 11

PION FEMTOSCOPY IN SMALL SYSTEMS: WORLD SYSTEMATICS

In Section 3 we presented two scalings of HBT radii seen in heavy ion collisions. Here, we will focus on results from elementary particle collisions and look whether they show any scalings. To do that, we collected data from many experiments that published femtoscopic results from elementary particle collisions we put STAR results from $p + p$ collisions (Section 9.1) and put them in the context of the world systematics. The material presented in this chapter was published in [20].

11.1 Multiplicity dependence

Figure 11.1 shows a collection of results from a number of experiments, including the STAR experiment, studying $p + p$, $p + \bar{p}$, $e^+ + e^-$ and even $\alpha - \alpha$ collisions plotted versus the number of charged particles per unit of pseudorapidity. Upper panel shows the R_{inv}. Since $R_B \approx 2R_G$ we were able to plot both radii together on the lower panel by dividing R_B by a factor of 2. As seen, all results plotted on this figure show the increase of the femtoscopic size with increasing multiplicity of charged particles for each experiment separately. So even though the radii show multiplicity
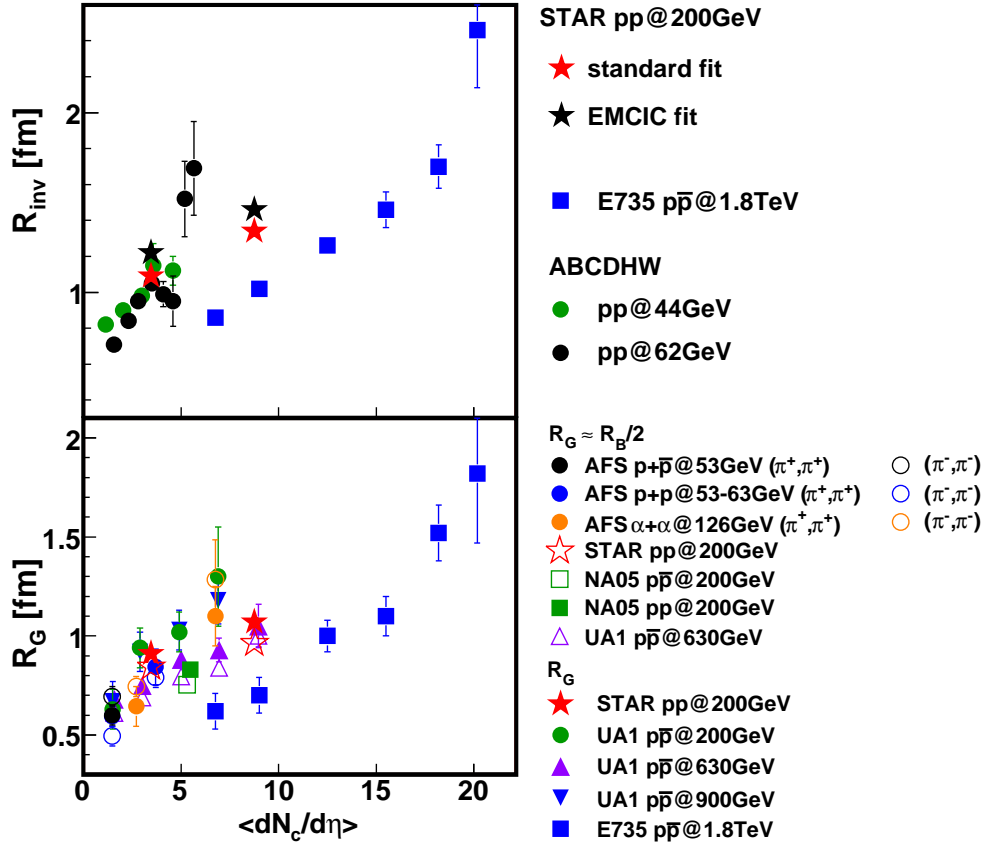
Figure 11.1: The multiplicity dependence of the pion HBT radii. Compilation of results from various experiments. Only data from collisions at $\sqrt{s} > 40\ GeV$ presented. STAR preliminary results (see Sec. 9.1) shown together with results from the following experiments E735 [56], ABCDHW [92], UA1 [121], AFS [122], NA5 [123], NA27 [61].

dependence, one does not see an universal scaling as observed in heavy ion collisions (Figure 3.3).

However, we will argue here that such a universal scaling is not expected to be seen in available experimental data not because it does not exists but because there are number of reasons why we can not do apple-to-apple comparison of results from various experiments. Bellow, we will briefly discuss three of them. Firstly, one should not expect similar results just because experiments do not use the same parameterizations
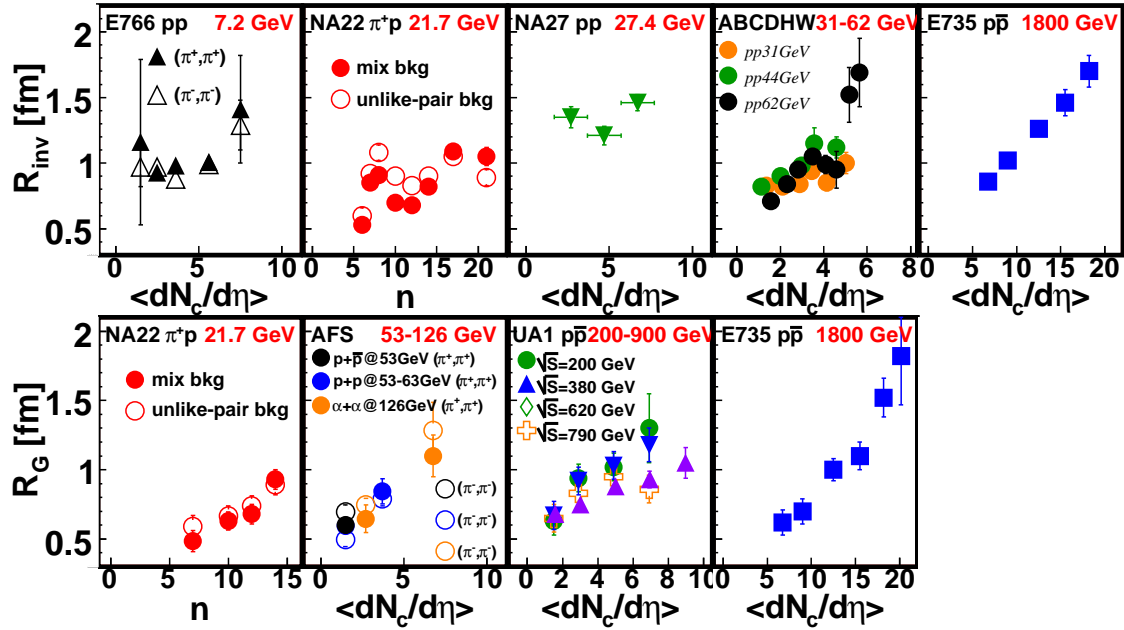
Figure 11.2: The multiplicity dependence of the pion HBT radii plotted separately for each experiment. STAR preliminary results (see Sec. 9.1) shown together with results from the following experiments: E735 [56], ABCDHW [92], UA1 [121], AFS [122], NA05 [123], E766 [54], NA22 [124], NA27 [61], H1 [125].

to obtain the femtoscopic sizes from the fit to experimental correlation functions. For example, when extracting R_{inv} presented on upper panel of Figure 11.1 experiments do not just use Equation 4.6 but often they multiply this formula by some ad-hoc terms that usually have either linear or quadratic dependence on q_{inv} as an attempt to parameterize non-femtoscopic correlations. As a results, various fits to the same correlation function will certainly give different results. The second reason is that the HBT radii depend not just multiplicity but also on $<p_T>$ of particles of interest or in general, on kinematic region that the data was taken from. We will discuss the transverse mass/momentum dependence of femtoscopic sizes bellow. The last issue is related to the extraction of the number of charged particles from various experiments.

Often, experiments do not provide this number directly but instead they do it on may other ways. One of them is to report the number of all particles per unit rapidity. In such case we assumed that charged particles are 2/3 of the total multiplicity. Also it happens that experiments provide the number of charged particles per some range of pseudorapidity. Then, we assumed that the pseudorapidity distribution is flat so we simply rescaled the value of observed charged particles to get their average number per unit of rapidity. Additionally, there is some unknown bias between experiments in the method of extracting the number of (charged) particles. So in general, one would have to include systematic errors on the number of charged particles obtained by various experiments but since we just look for trends in multiplicity dependence of HBT radii.

11.2 The transverse mass/momentum dependence

In Section 3 we showed that femtoscopic results from heavy ion collisions at RHIC decrease with increasing transverse mass of the particles. Here, we will look whether similar scaling is seen in small systems. Left panel of Figure 11.3 shows 1D pion HBT radii plotted versus transverse momentum. Data come from NA22, NA27 and E735 experiments. A clear anti-correlation between the femtoscopic size and transverse momentum looks very similar to what has been observed at RHIC in $p + p$ collisions as well as heavy ion collisions, as shown on Figure 3.2. To get more information about the directional dependence of the homogeneity region one should look at the data from 3D femtoscopic analysis. The collection of such results is presented on Figure 11.3. Similarly as in Section 11.1 results from different experiments presented on Figure 11.3 cannot be compared to each other in most cases because of two main
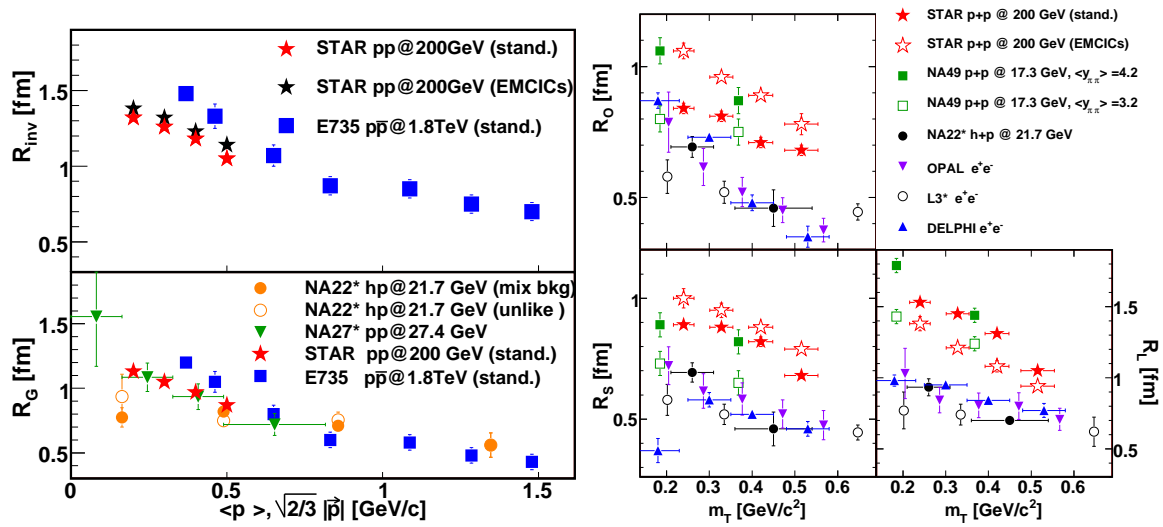
Figure 11.3: Left: The transverse mass dependence of R_{inv} from elementary particle collisions. Right: The transverse mass dependence of the 3D HBT radii from elementary particle collisions. STAR preliminary results (see Sec. 9.1) shown together with data from NA22 [51], NA49 preliminary [126], OPAL [52], L3 [60], DELPHI [127].

reasons. The average number of particles per unit of pseudorapidity is different in each experiment and as shown in Section11.1 the magnitude of the HBT radii depends on this value. Additionally, different variations of Eq. 4.11 were used to fit the experimental data when an extra ad-hoc term is added as an attempt to describe non-femtoscopic correlations.

11.3 Origin of the transverse mass dependence of HBT radii

11.3.1 Heisenberg uncertainty

The Heisenberg uncertainty principle was pointed by Alexander *et al.* [128] as a possible origin of the mass dependence of the HBT radii in $e^+ + e^-$ collisions. Authors argue that the dependence of the one-dimensional radius R_{inv} on the hadron mass obtained at LEP1 is consistent with the formula derived from the Heisenberg uncertainty principle

$$R_{inv}(m) = \frac{c\sqrt{\hbar \Delta t}}{\sqrt{m}}, \tag{11.1}$$

where Δt was chosen to be $10^{-24}s$ (0.3 fm).

However, one-dimensional radius provides limited information about the source that is in fact a three-dimensinal observable. Thus, to verify whether Heisenberg uncertainty principle can really explain the m_T dependence of HBT radii one should look at three (eventually two) dimensional radii. An example of such a dependence in DELPHI experiment can be found in [127] where Authors shows that all 3D femtoscopic radii are decreasing with m_T (for more discussion on the experimental results see Section 11). Alexander showed [129] that the Heisenberg uncertainty principle can also be applied to the longitudinal component of the radius r_z (sometimes noted as R_L) measured in LCMS frame using similar procedure as it was done for R_{inv}[128]. The final formula presented bellow gives the same dependence of the longitudinal femtoscopic size on m_T as in 1D case

$$R_L(m_T) \approx \frac{c\sqrt{\hbar \Delta t}}{\sqrt{m_T}}. \tag{11.2}$$

Left panel of Figure 11.4 shows DELPHI preliminary results [130]. Solid line represents the formula from Eq. 11.1 for $\Delta t = 2.1 \times 10^-24s$(0.63 fm) and dashed line
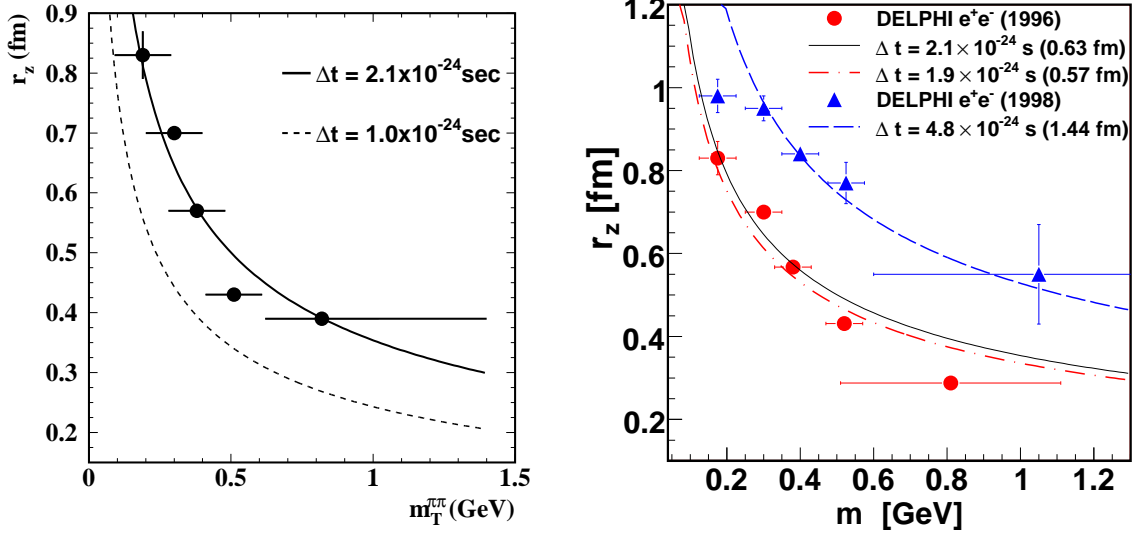
Figure 11.4: The m_T dependence of the longitudianl component of the HBT source size for pions; Left panel: Figure taken from [129]; Right panel: Red circles represent DELPHI data taken from [130]. Blue triangles show data points from [127]. See text for explanation of the curves.

$\Delta t = 1.0 \times 10^-24\ s$ which descibed the mass dependence of R_{inv} [128]. As seen, this figure shows a very good agreement between the experimental data and the theoretical curve. Howerver, we would like to make two points about this figure. Firstly, we believe that such a very good agreement is partially a result of a mistake that was made by the author. When presenting DELPHI preliminary results Alexander refers to [130]. However we found that there is a discrepancy between results presented in this paper and results plotted by Alexander. The main difference seems to be in the last point for $m_T = 0.81\ GeV$. The correct DELPHI data from [130] has been plotted on the right panel of Figure 11.4 represented by red inverse triangles. For comparision, we plotted the prediction from the Heisenberg uncertainty relations for $\Delta t = 2.1 \times 10^{-24}\ s$ represented by the solid black line that is the same curve plotted

on the left panel of Figure 11.4. We also performed a fit to the red triangles and found that the best Δt that described the DELPHI data is 1.9×10^{-24} s (dash-dotted green line). This is not a serious mistake however we found it should be mentioned here since the figure was copiously cited in many other articles.

The second point is about the DELPHI data themselves. While Alexander refers to results presented in 1996 and published as proceedings in 1997 [130] it should be also mentioned that the same experiment published,also as conference proceedings, newer results in 1999 and presented in 1998 [127] that are much different than the previous ones (see blue triangles on the right panel of Figure 11.4. Usually the experiment changes the results because of the mistake that was made in the previous analysis for because of the higher data statistics available so it seems reasonable to use the latest data available. Howerver, at the same time, we can only hypothesis which data is representative for the DELPHI experiment. The definite answer could be delivered by the DELPHI experiment by publishing the data as a regular publication that is a good scientific approach but unfortunatelly it has not been done yet.

Additionally, it is far from obvious that the Heisenberg uncertainty can also explain the m_T dependence of the transverse size (R_T and thus, R_O and R_S. As it was pointed out by Alexander [129], R_T mixes both the geometrical information as well as the emission time so it is not straightforward to apply undertainty relation for R_T.

11.4 Lund string model

String fragmentation can also generate the space-momentum correlations in small systems [131], thus the m_T dependence of the HBT radii. However, as brought up by

by Alexander [132], the mass dependence of the femtoscopic radii cannot be explained within a Lund string model.

11.5 Long-lived resonances

Long-lived resonances may also generate the space-momentum dependence of femtoscopic radii [133]. However, as discussed in [20], the resonances would affect the HBT radii from $p + p$ collisions differently than in $Au + Au$ collisions thus it would have to be a coincidence that the same m_T dependence is observed in both systems.

11.6 p-x correlations. Built-in assumption in the model

Białas *et al.* introduced a model [134] based on the proportionality between the four-momentum and the four-vector to describe the particle space-time position at freeze-out an was able to explain the data from $e^+ + e^-$ collisions.

11.7 Flow?

It is becoming increasingly common to explain the femtoscopic results from elementary particle collisions as originated from "flow" similarly as in heavy ion collisions [56, 51, 18, 135, 52]. We discuss this scenario in more details in the next chapter.

CHAPTER 12

EVIDENCE OF (RADIAL) FLOW IN $p + p$ COLLISIONS AT RHIC

In previous chapter, we presented world systematics on the HBT results in elementary collisions and discussed the possible physics effects that can cause the transverse mass dependence of the femtoscopic radii. One of them was the possibility of flow in small systems.

In Section 6.3.5 we discussed identified particle spectra in $p + p$ and $Au + Au$ collisions at $\sqrt{s_{NN}}$=200 GeV at RHIC and the effect of the phase-space constraints due to the energy and momentum correlations on the shape of the single particle distribution. In this chapter, we will focus on the physics behind the particle distribution and we will discuss what can we learn about the flow by looking into single particle spectra and two particle correlations at RHIC while the phase-space effects due to energy and momentum conservation are correctly taken into account.

12.1 Blast-Wave fits to spectra. Universal parent distribution

In this section we discuss the hydro-inspired blast-wave fits to the single particle spectra. Figure 12.1 shows the result of fits with a blast-wave model [7] to STAR spectra from $p + p$ and $Au + Au$ collisions at $\sqrt{s_{NN}}$=200 GeV at RHIC shown on
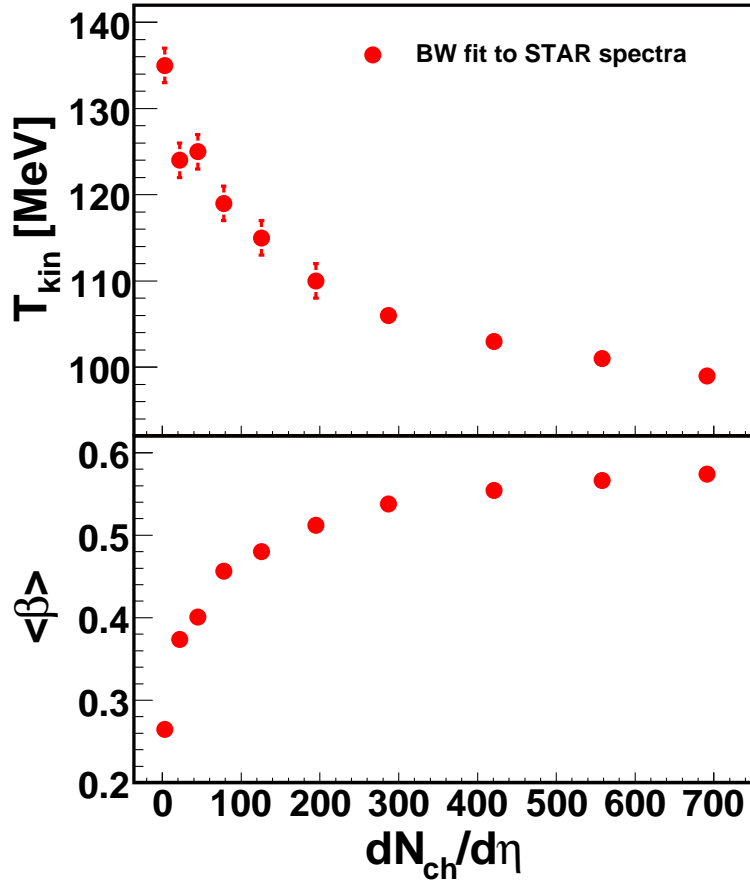
Figure 12.1: Circles show the temperature (top panel) and flow (bottom panel) parameters of a Blast-wave model [7] fit to the STAR spectra of Figure 6.5, as a function of the event multiplicity.

Fig. 6.5. They indicate a kinetic freeze-out temperature of about 100 MeV and average collective flow velocity about 0.6c for the most central collisions. For lower multiplicity collisions, the freeze-out temperature appears to grow to $\sim$ 130 MeV and the flow velocity decreases to $\sim$ 0.25c. The STAR collaboration, using a slightly different implementation of a blast-wave model, reported essentially identical values [80]. These results are often used as a proof of none (or a little) flow in $p + p$ collisions comparing to $Au + Au$ collisions at RHIC.

However, as we discussed in Chapter 6, the energy and momentum conservation can have a significant effect on the spectra in small systems like $p + p$. Moreover, we showed that if we assume that the parent distribution in $p + p$ and $Au + Au$ collisions is identical (see Sec. 6.3.2 for more details), we were able to fit the ratio of the spectra from $Au + Au$ and $p + p$ collisions leaving only a little room for other physics.

But since, the previously published STAR data suggested much less [80] flow in $p + p$ collisions than in heavy ion collisions we are going to see how EMCICs affect these parameters. In Figure 12.3, the p_T distributions for $p + p$ collisions and the six lowest multiplicity selections on $Au + Au$ collisions are shown. Blast-wave fits to the measured spectra, resulting in the parameters shown by red triangles in Figure 12.2 are shown as curves. On the linear scale of the Figure, some deviations between the fit and data, particularly at the lowest p_T for the light particle, is seen. This has been observed previously in Blast-wave fits, and may be due to resonances [136, 7]. Nevertheless, the fits to measured data are reasonable overall, and for simplicity, we do not exclude these bins.

Also shown in Figure 12.3 are the "EMCIC corrected" spectra, as discussed above. As already seen in Figure 6.7, these differ from the measured spectra mostly for low multiplicity collisions and for the heavier emitted particles. Blast-wave fits to these spectra are also shown. Especially for the very lowest multiplicity collisions, these fits are less satisfactory than those to the measured spectra; the "parent distributions" extracted via our approximate EMCIC correction procedure follow the Blast-wave shape only approximately. Much of the deviation is at $p_T \sim 0.9$ GeV/c for protons from the lowest multiplicity collisions (upper-right panels). This is the region around which the approximations used in deriving the EMCIC correction should start to
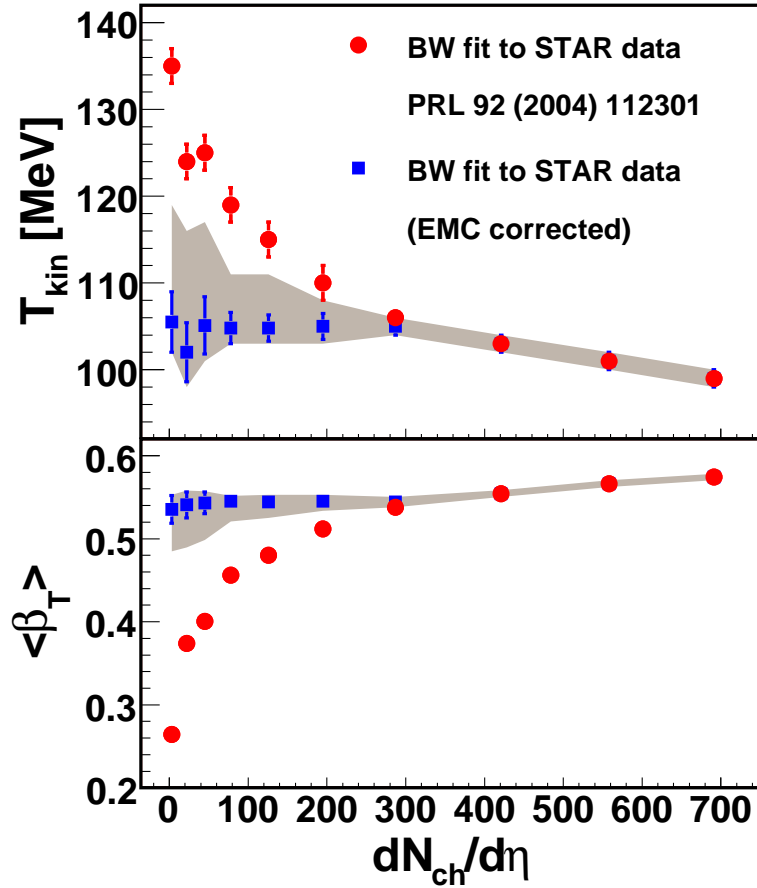
Figure 12.2: Circles show the temperature (top panel) and flow (bottom panel) parameters of a Blast-wave model [7] fit to the STAR spectra of Figure 6.5, as a function of the event multiplicity. Squares represent Blast-wave fit parameters to "EMCIC corrected spectra," and shaded region represents these results combined with systematic errors, as discussed in the text.

break down, as discussed in Appendix C. So, two fits are performed: one including all datapoints shown (blue squares in Figure 12.2), and the other excluding proton spectra points with $p_T > 0.8$ GeV/c. The resulting range of Blast-wave parameters is indicated by the shaded region in Figure 12.2. There, statistical errors on the fit parameters have been multiplied by $\sqrt{\chi^2/\text{d.o.f.}}$ (ranging from ~ 2 for spectra from $p + p$ collisions to ~ 1 for those from mid-peripheral and central $Au + Au$ collisions)
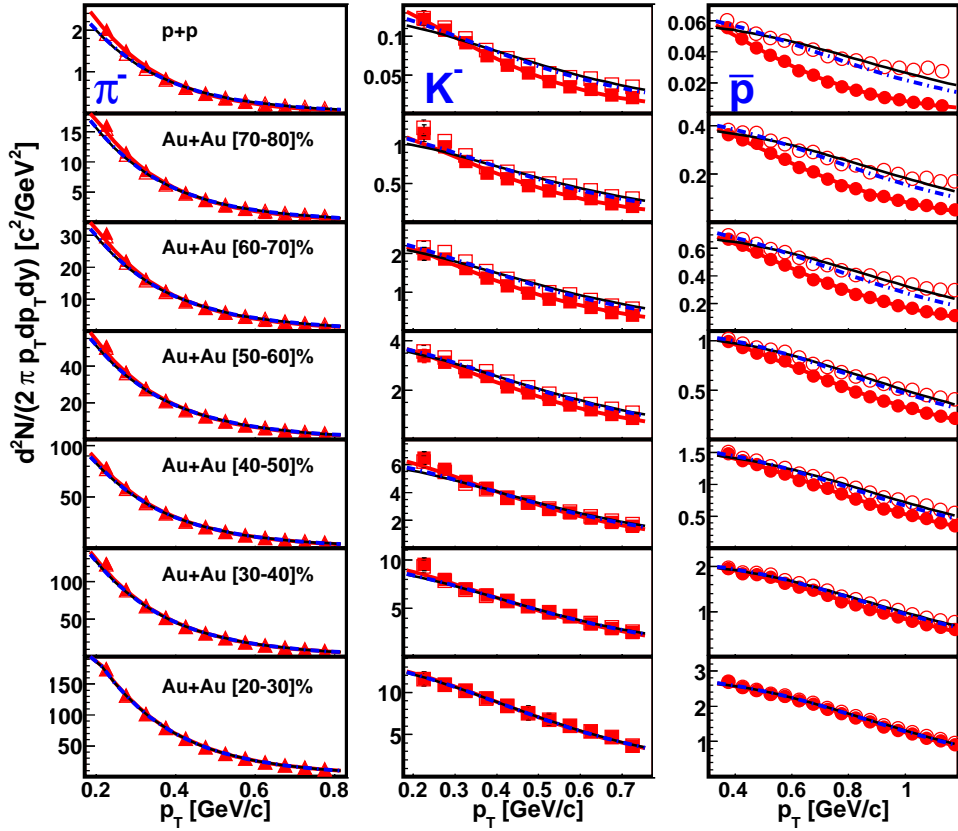
Figure 12.3: dN/dp_T^2 spectra for pions (left), kaons (center), and protons (right) are plotted on a linear scale, as a function of event multiplicity. Top panels show spectra for minimum-bias $p+p$ collisions, and the spectra for the six lowest multiplicity selections of $Au+Au$ collisions are shown in the lower panels. Filled symbols are the measured data, while open symbols are the "EMCIC corrected" distributions, discussed in the text. (For pions, these distributions overlap almost completely.) Blast-wave fits are indicated by the curves. For the "EMCIC corrected" spectra, two fits are performed, to estimate systematic errors. The solid line represents a fit to all datapoints, while the fit indicated by the dashed line ignores proton yields above $p_T = 0.8$ GeV/c.

and added to both ends of the range. Thus, the shaded region should represent a conservative estimate of blast-wave temperature and flow strengths to the parent distributions.

In particular, STAR [80] and others [7] have fitted the spectra with Blast-wave distributions, which ignore EMCIC effects. Based on these fits, they concluded that the difference in spectral shapes between high- and low-multiplicity collisions was due to much lower flow in the latter; c.f. Figure 12.1.

Recently, Tang et al. [137] arrived to the same conclusion, using a modified Blast-wave fit based on Tsallis statistics. This requires introduction of an extra parameter, q, intended to account for system fluctuation effects [138]. However, contrary to the claims in the Tang paper, the Tsallis distribution - with or without q - does *not* account for energy and momentum conservation [139]; EMCIC effects would need to be added on the top of the Tsallis statistics [139]. Therefore, conclusions about flow in low-multiplicity collisions based on these fits are suspect.

An independent measurement of flow would help clarify this issue. Two-particle femtoscopy ("HBT") is a sensitive probe of collective motion [26] and has been measured in $p + p$ collisions at RHIC [95]. Any scenario should be able to describe simultaneously both the spectral shapes and the m_T dependence of the femtoscopic scales. A study of this topic is underway.

12.2   Combined blast-wave fits to spectra and HBT results

In previous section, we argued that $p + p$ collisions show almost as much flow as $Au + Au$ collisions if the phase-space constraints due to energy and momentum correlations are taken into account. However, we made one crucial assumption that lead us to these results that was the universal parent distribution in both $p + p$ and heavy ion collisions. Thus, it would be more convincing if we were able to find

a measurement that could provide us the EMCIC parameters without making any assumption on the parent distribution and without using spectra at all.

In Section 6.5 we presented the formalism of the EMCIC effect on two-particle correlation function and we showed Section 9.1 that it nicely reproduces the non-femtoscopic part of the correlation function. The parameters that we got from the fit are the same parameters that show up in the formula on the EMCIC effect on the single-particle distribution. Thus, we can simply take the EMCIC parameters obtained from the fit to the correlation function and use them in Eq. 6.28 to obtained particle spectra "corrected on" the EMCIC effect.

Then, we can perform a Blast-Wave fit to STAR data but this time we do not have to limit ourselves to fitting spectra only but we can fit both spectra and pion HBT results (Sec. 9.1 simultaneously. Results of such a fit are presented on Figs. 12.4 and 12.5. First figure shows the "EMCIC-corrected" spectra for positive and negative pions and kaons, as well as protons and anti-protons from $p + p$ collision at $\sqrt{s}$=200 GeV from STAR and blast-wave fits and the second figure shows fit results to pion HBT radii from the same collisions.

The values of fit parameters from this blast-wave fit are presented in Table 12.1.

parameter	fit value
T [MeV]	109 ± 3
$\beta[c]$	0.45 ± 0.3
R [fm]	2.2 ± 0.05
τ [fm/c]	1.82 ± 0.07
Δt [fm/c]	0.29 ± 0.08

Table 12.1: Fit results from blast-wave fit to spectra and HBT from $p + p$ collisions at $\sqrt{s}$=200 GeV in STAR.
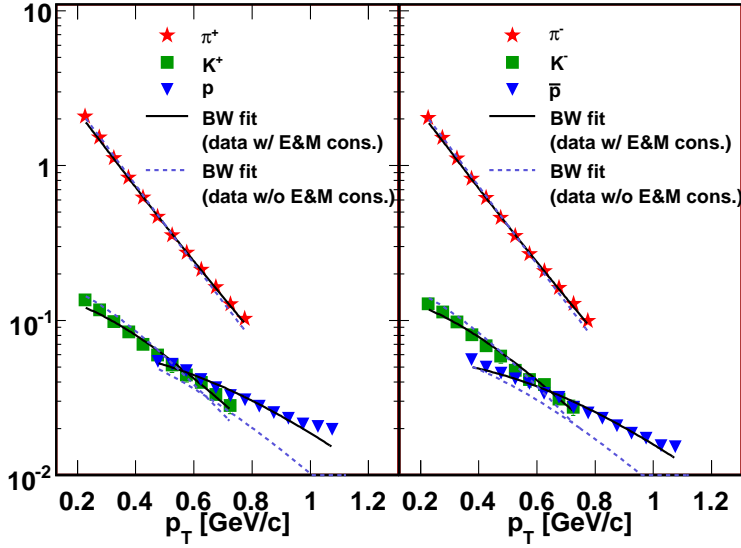
Figure 12.4: Blast-wave fit results to spectra for π^+, π^-, K^+, K^-, p and $\bar{p}$ from $p + p$ collisions at $\sqrt{s} = 200$ GeV at RHIC

12.3   Conclusions

Firstly, we showed that the radial flow obtained from the blast-wave fit to spectra from $p + p$ collisions is almost as large as observed in central $Au + Au$ collisions after including phase-space effects due to energy and momentum conservation in the single particle distribution and assuming universal parent distribution.

Secondly, being fully aware of possible controversy behind this assumption we presented an alternative approach to estimate the EMCIC effect that does not require any a-priori assumptions about the parent distribution. Then, we were able to perform a blast-wave fit to both spectra and femtoscopic results from $p + p$ collisions we proved again an existence of a strong radial flow in $p + p$ collisions although smaller by about 20$ than in central $Au + Au$ collisions at RHIC.
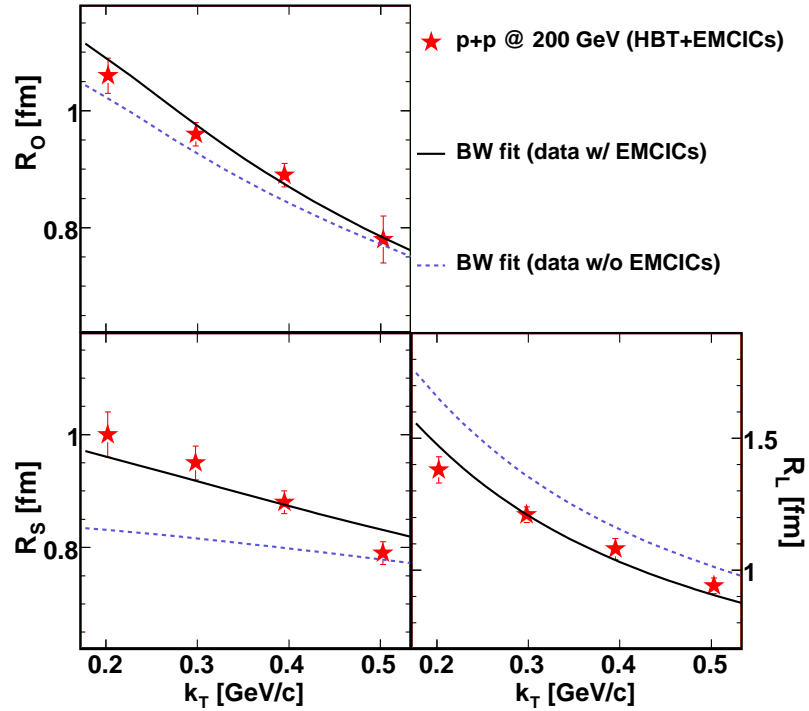
Figure 12.5: Blast-wave fit results to HBT radii from $p + p$ collisions at $\sqrt{s}$=200 GeV.

The fact that we used two independence approaches to take care of the phase-space constraint effect due to energy and momentum conservation and we ended up with the same conclusion that is a strong radial flow in $p + p$ (Fig. 12.6) magnifies the importance of results presented in this chapter.

It is still an open question whether elliptic flow can be seen in $p + p$ collisions and the analysis that could answer this question is very challenging since it involves measurement of the reaction plane in $p + p$ collisions. Probably it is more realistic to expect results from LHC experiments than RHIC due to the higher multiplicity $p + p$ collisions. It seems like it is rather a matter of time to verify the possible
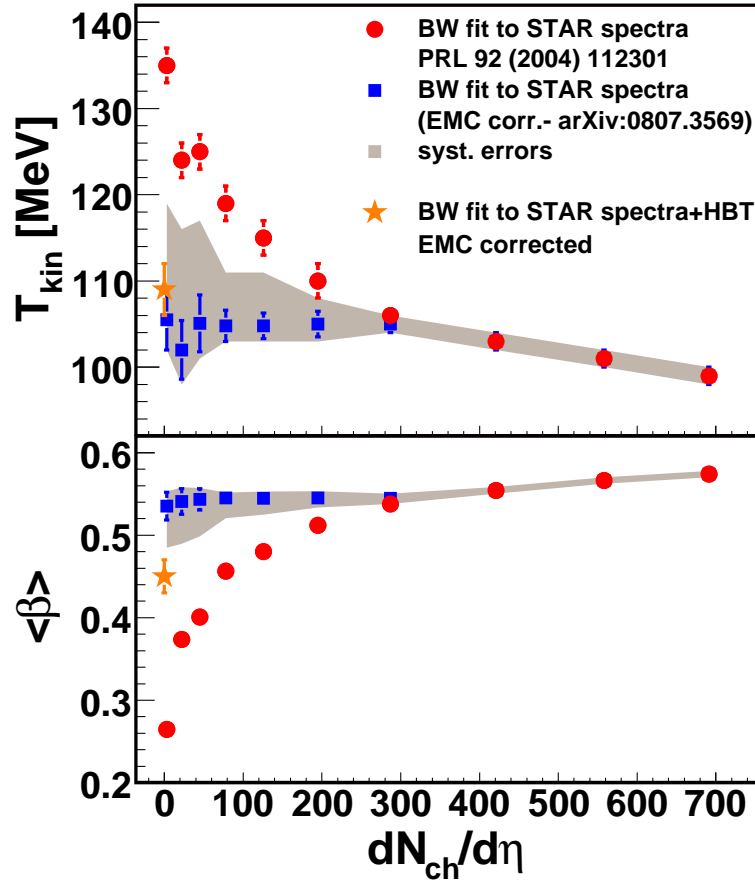
Figure 12.6: Results of the simultaneous blast-wave fit to both spectra and pion femtoscopic results from $p + p$ collisions (gold stars) where the EMCIC effect was estimated from the fit to the correlation function from $p + p$ collisions 9.1. See caption to Fig. 12.2 for explanation of the other data piloted on this figure.

existence of elliptic flow in small systems - something that theorists have been already thinking of [140].

CHAPTER 13

DISCUSSION AND SUMMARY

We presented STAR results from $Au + Au$ collisions at $\sqrt{s_{NN}}$=19.6 GeV that allowed us to make a direct comparison to results from two SPS experiments (CERES and NA49) at very similar energies for the first time. With these results we finally filled the gap in the energy dependence of femtoscopic radii between RHIC and previous facilities SPS and AGS that were providing heavy ion collisions at lower energies ($\sqrt{s_{NN}}$¡20 GeV). We also performed the hydro-inspired blast-wave fit to both particle spectra for charged particles and HBT radii from $Au + Au$ collisions at $\sqrt{s_{NN}}$=19.6 GeV. Then, we compared our results to previously published STAR results from $Au + Au$ collisions at $\sqrt{s_{NN}}$=200 GeV and found that all fit parameters (like T, $\langle \beta_T \rangle$, etc.) scale with the event multiplicity.

We have presented a formalism and analytic calculations of the effect of the phase-space constraints due to energy and momentum conservation on the single-particle distribution and many-body correlation functions. We have shown that the EMCIC effect can affect momentum observables in a non-trivial way and depends on the total number of particles and the kinematic scale of the system like $\langle p_T^2 \rangle$, $\langle p_z^2 \rangle$, $\langle E^2 \rangle$ and $\langle E \rangle$. We have also provided two alternative approaches on how to extract these parameters directly from the experimental data. The first one involves fits to a ratio

of spectra from heavy ion collisions and $p + p$ collisions from the STAR experiment under assumption of universal parent distribution. The second approach, involves fits to the two-particle correlation functions. We applied both approaches to the experimental data from the STAR experiment.

We have presented a systematic femtoscopic analysis of two-pion correlation functions from $p + p$, $d + Au$ and $Au + Au$ collisions at RHIC. In addition to femtoscopic correlations, the correlation functions show correlations due to energy and momentum conservation. Such effects have been observed previously in low-multiplicity measurements at Tevatron, SPS, and elsewhere. They have either been ignored, or treated with various semi-justified functional forms. We have used several such forms, as well as a recently-developed formalism to account for conservation-law-induced correlations. While the overall magnitude of the geometric scales ("HBT radii") vary with the method, the important systematics do not.

In particular, we observe a significant positive correlation between the one- and three-dimensional and the multiplicity of the collision. Negative correlations are observed between the radii and the pion transverse momentum. Qualitatively, similar multiplicity and momentum systematics have been observed previously in measurements of hadron and electron collisions at the $\mathrm{Sp\overline{p}S}$, Tevatron, ISR and LEP. However, the results from these experiments could not be directly compared to those from heavy ion collisions, due to differences in techniques, fitting methods, and acceptance.

Thus, our measurement in STAR has provided a unique possibility for an apples-to-apples comparison of femtoscopy in $p + p$ and $Au + Au$ collisions. This is crucial, since in the latter case, the p_T systematics have provided the most compelling evidence for collective flow in heavy ion collisions at RHIC. We have seen an identical p_T

scaling of the femtoscopic scales in $p + p$ as in $Au + Au$ collisions, independent of the fitting method employed. This raises the provocative possibility that proton collisions form a bulk collective system similar to– albeit smaller than– that created in heavy ion collisions. Indeed, simultaneously fitting the HBT radii and p_T spectra (after accounting for the same conservation law-induced effects as seen in the 2-particle correlations) with a blast-wave ansatz, indicates an emitting source with strong flow and low temperatures, as observed in $Au + Au$ collisions at RHIC.

Further study on the soft aspects of p+p collisions is warranted. The similarities observed could indicate a deep connection of the underlying bulk physics driving systems much larger than– and on the order of– the confinement scale. At the Large Hadron Collider, similar apples-to-apples comparisons will be possible, and the much higher energies available will render conservation law-driven effects less problematic.

APPENDIX A

ABBREVIATIONS

RHIC	Relativistic Heavy-Ion Collider
QGP	Quark Gluon Plasma
QCD	Quantum Chromodynamics
pQCD	Perturbative Quantum Chromodynamics
HBT	Hunbary-Brown-Twiss (interferometry)
TPC	Time Projection Chamber
FTPC	Forward Time Projection Chamber
TOF	Time of Flight
ZDC	Zero Degree Calorimeter

APPENDIX B

KINEMATIC VARIABLES

B.1 Event characteristics

$\sqrt{s_{NN}} = \sqrt{(E_1 + E_2)^2 - (p_1 + p_2)^2}$	energy of the collision in the center of mass frame index 1 and 2 stands for the colliding nuclei
N	total multiplicity
$dN_{ch}/d\eta$	number of charged particles per unit of rapidity

B.2 Related to a single particle

$p_T = \sqrt{p_x^2 + p_z^2}$	transverse momentum
$m_T = \sqrt{p_T^2 + m_0^2}$	transverse mass (m_0- mass of a particle)
$y = \frac{1}{2}ln\left(\frac{E+p_z}{E-p_z}\right) = tanh^{-1}\left(\frac{p_z}{E}\right)$	rapidity
$E = m_T cosh(y)$	energy
$p_z = m_T sinh(y)$	z-component of the momentum
$\eta = -lntan\left(\frac{\theta}{2}\right)$	pseudo-rapidity

$\vec{k_T} = \frac{1}{2}(\vec{p_1} + \vec{p_T})_T$	transverse momentum of the pair
$m_T = \sqrt{k_T^2 + m_0^2}$	transverse mass of the pair
$\vec{q} = \vec{p_1} - \vec{p_2}$	momentum difference of two particles

B.3 Related to two particles (a pair)

APPENDIX C

REGION OF APPLICABILITY FOR THE EMCIC FORMULA

The exact expression for the phase space integral of Eq. 6.24 was approximated by that in Eq. 6.25 through an appeal to the Central Limit Theorem. Discrepancies between the exact expression and the approximate Gaussian functional form will become more apparent in the tails of the distribution. For example, our approximate phase space suppression function never vanishes, thus permitting a tiny but finite probability for a particle to carry more energy than that of the entire system! In this Appendix, we perform simple numerical calculations with the GENBOD computer program [69], to estimate the range of quantitative reliability of Equation 6.25.

Given a total energy E_{tot}, multiplicity N and list of particle masses, GENBOD produces phasespace-weighted events of N 4-momenta by filling Lorentz-invariant phase space according to the Fermi distribution,

$$\tilde{f} \equiv 2E \frac{d^3N}{dp^3} = \frac{1}{2\pi p} \frac{dN}{dE} \propto e^{-E/\zeta}. \tag{C.1}$$

where ζ characterizes the slope of the energy distributions. Since it is $(1/p) \cdot dN/dE$ which is exponential and not $(1/p) \cdot dN/dE$, the inverse slope ζ should not be considered a "temperature," but only a parameter characterizing the parent distribution.
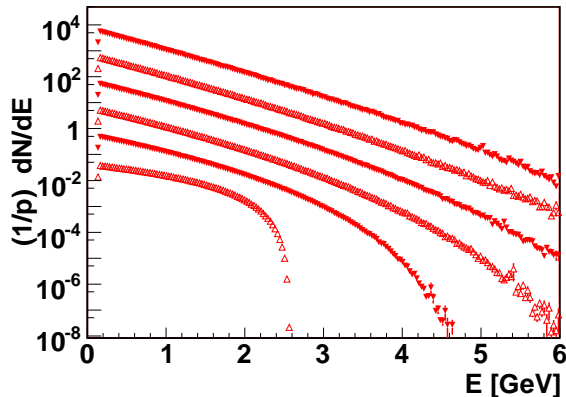
Figure C.1: $\frac{1}{p}\frac{dN}{dE}$ obtained from GENBOD events run for the same average energy ($\langle E \rangle_c = 1~GeV$) but different multiplicities: $N = 5, 10, 15, 20, 30, 40$ pions.

As a result, generated particles in an event are correlated only by energy and momentum conservation. Thus, EMCIC effects on the calculated single-particle spectrum, $\tilde{f}_c(p)$, are given precisely according to Equation 6.24.

To evaluate the region of validity of Equation 6.25, we use Eq. C.1 as a parent distribution, $\tilde{f}(p)$. Results of this exercise are presented on Figure C.1 which shows energy spectra from GENBOD events with the same average energy per particle $\langle E \rangle_c = E_{\text{tot}}/N = 1$ GeV, but different multiplicity N. As expected, in the limit of large N, $\tilde{f}_c(p) \to \tilde{f}(p)$, and it is clear that the plotted distribution is increasingly well-described by an exponential, as N increases.

It is appropriate here to point out why we wish to identify the parent distribution in the first place, rather than following the procedure outlined in Section 6.3.2. There, the parent distribution cancels when taking the ratio of two measured spectra $\tilde{f}_{c,1}/\tilde{f}_{c,2}$, using the postulate that the parent distributions $\tilde{f}_1$ and $\tilde{f}_2$ are identical. In contrast, the parent distributions for the different GENBOD spectra shown in Figure C.1 are

194
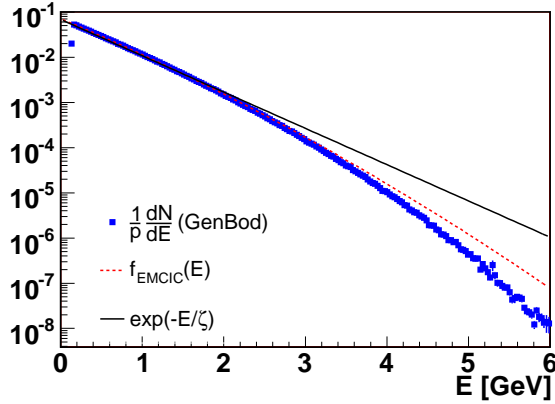
Figure C.2: Blue points are $\frac{1}{p}\frac{dN}{dE}$ obtained from GENBOD events run for $N = 20$, $\langle E \rangle = 1$ GeV. Black solid curve is an exponential, the assumed parent distribution; c.f. Equation C.1. Red dashed curve is the exponential times the EMCIC factor, as per Equation C.2.
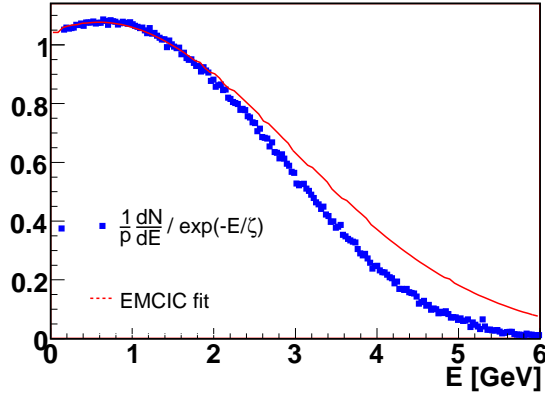
Figure C.3: Blue points are $\frac{1}{p}\frac{dN}{dE}$ obtained from GENBOD events run for $N = 20, \langle E \rangle = 1$ GeV, divided by $\exp\left(-E/\zeta\right)$; i.e. the blue points from Fig. C.2 divided by the black full curve from the same figure. Red dotted line is the EMCIC factor; i.e. the red dotted curve from Fig. C.2 divided by the black full curve from the same figure.

assuredly *not* the same. Those spectra came from event samples having the same $\langle E \rangle_c$ (c.f. Eq. 6.27), and thus *different* $\langle E \rangle$ (c.f. Eq. 6.26), implying different parents.

Having at hand a functional form for the GENBOD parent distribution, we may test our approximate formula for the phasespace modification factor, by fitting the calculated spectrum according to

$$\frac{dN_c}{dE} = A \cdot p \cdot e^{-E/\zeta} \quad \times$$

$$\left(\frac{N}{N-1}\right)^2 \exp\left[\left(-\frac{1}{2\left(N-1\right)}\right)\left(\frac{3p^2}{\langle p^2 \rangle}+ \right.\right.$$
$$\left.\left. +\frac{E^2}{\langle E^2 \rangle - \langle E \rangle^2} - \frac{2E\langle E \rangle}{\langle E^2 \rangle - \langle E \rangle^2} + \frac{\langle E \rangle^2}{\langle E^2 \rangle - \langle E \rangle^2}\right)\right],$$

(C.2)

where we used the fact that GENBOD generates particles isotropically so that $< p_x^2 >=< p_y^2 >=< p_z^2 >= \frac{1}{3} < p^2 >$. Since N is a known quantity, and $\langle E \rangle$, $\langle E^2 \rangle$ and $\langle p^2 \rangle$ may be directly calculated from ζ, the fit of Equation C.2 has only two parameters: the overall normalization A, which is unimportant to us, and ζ, which characterizes the parent distribution.

The results are shown in Figure C.2 and, for better detail, in Figure C.3. For the case here, which is typical of that in the data, we see that our approximation begins to break down for particle energies $E \gtrsim 2 \div 3\langle E \rangle$. Above this range, our approximation (e.g. Equation 6.29) should only be taken qualitatively.

APPENDIX D

EMCIC FACTORS FOR RAPIDITY- AND ANGLE-INTEGRATED P_T DISTRIBUTIONS

Equation 6.25 gives the EMCIC correction factor to the triple differential spectrum $\tilde{f}(p)$. Experimental measurements often report p_T distributions integrated over angle and a range of rapidity, i.e.

$$\tilde{f}_c(p_T) \equiv \frac{1}{4\pi \cdot y_{max}} \int_0^{2\pi} d\phi \int_{-y_{max}}^{y_{max}} dy \, \tilde{f}_c(p_x, p_y, p_z, E). \qquad (D.1)$$
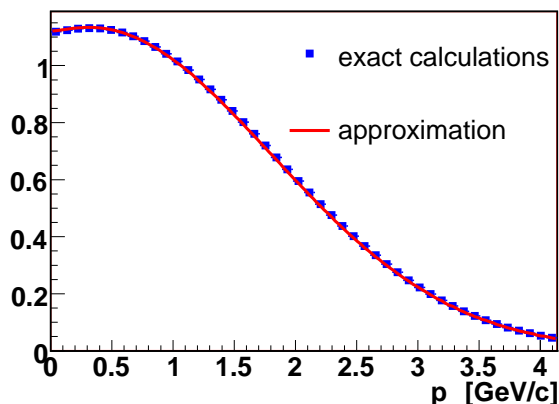
Figure D.1: EMCIC factor calculated using the numerical averaging of Equation D.2 and the approximation of Equation D.3.

In the absence of a triple-differential measurement, we consider azimuthally-symmetric distributions, and $\langle p_x^2 \rangle = \langle p_y^2 \rangle = \langle p_T^2 \rangle/2$. At midrapidity at RHIC, it

is reasonable also to assume a boost-invariant parent distribution. In this case, only part of the EMCIC factor remains in the rapidity integral:

$$
\tilde{f}_c\left(p_T\right) = \tilde{f}\left(p_T\right) \cdot \left(\frac{N}{N-1}\right)^2 \exp\left[\frac{-p_T^2}{(N-1)\langle p_T^2\rangle}\right] \times
$$
$$
\frac{1}{2y_{max}}\int_{-y_{max}}^{y_{max}} dy \exp\left[\frac{-1}{2(N-1)}\left(\frac{p_z^2}{\langle p_z^2\rangle}+\right.\right. \tag{D.2}
$$
$$
\left.\left.\frac{E^2}{\langle E^2\rangle-\langle E\rangle^2} - \frac{2E\langle E\rangle}{\langle E^2\rangle-\langle E\rangle^2} + \frac{\langle E\rangle^2}{\langle E^2\rangle-\langle E\rangle^2}\right)\right].
$$

To arrive at a closed form for our EMCIC factor, we approximate the average of the exponential with the exponential of the average, i.e.

$$
\tilde{f}_c\left(p_T\right) = \tilde{f}\left(p_T\right) \cdot \left(\frac{N}{N-1}\right)^2 \times
$$
$$
\exp\left[-\frac{1}{2(N-1)}\left(\frac{2p_T^2}{\langle p_T^2\rangle}+\frac{\overline{p_z^2}}{\langle p_z^2\rangle}\right.\right. \tag{D.3}
$$
$$
\left.\left.+\frac{\overline{E^2}}{\langle E^2\rangle-\langle E\rangle^2} - \frac{2\overline{E}\langle E\rangle}{\langle E^2\rangle-\langle E\rangle^2} + \frac{\langle E\rangle^2}{\langle E^2\rangle-\langle E\rangle^2}\right)\right].
$$

This expression is reproduced in Equation 6.28.

Here, the rapidity-averaged quantities are

$$
\overline{p_z^2} \equiv \frac{1}{2y_{max}}\int_{-y_{max}}^{y_{max}} p_z^2 dy = m_T^2\left(\frac{\sinh(2y_{max})}{4y_{max}}-\frac{1}{2}\right) \tag{D.4}
$$

$$
\overline{E^2} \equiv \frac{1}{2y_{max}}\int_{-y_{max}}^{y_{max}} E^2 dy = m_T^2\left(\frac{\sinh(2y_{max})}{4y_{max}}+\frac{1}{2}\right) \tag{D.5}
$$

$$
\overline{E} \equiv \frac{1}{2y_{max}}\int_{-y_{max}}^{y_{max}} E dy = m_T\frac{\sinh(y_{max})}{y_{max}}. \tag{D.6}
$$

The approximation used in going from Equation D.2 to D.3 is well-justified for typical numerical values used in this study. Figure D.1 shows a numerical integration of the EMCIC factor from Equation D.2 (labeled "exact") and Equation D.3 ("approximation") for values indicated in the Figure.

APPENDIX E

EMCIC EFFECTS ON V_2
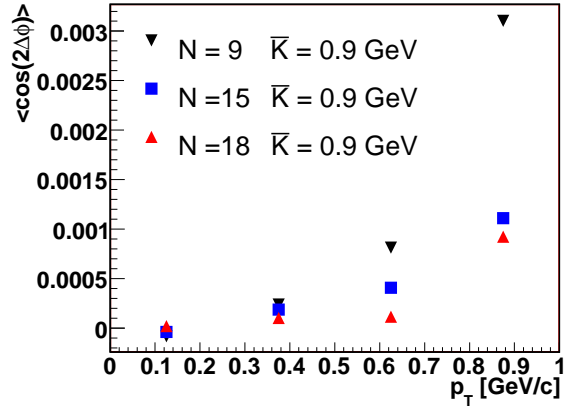
Figure E.1: $v_2(p_T)$ for different event multiplicities. See text for details.

Since EMCICs can produce a structure in the correlation function even in the absence of femtoscopic correlations, it is worthwhile to check analytically and then confirm with simulations whether v_2– a common measure of collective elliptic flow [5]– may be affected by EMCICs.

When calculating flow from two-particle correlations we have the following relations

$$\int \cos\left(m\Delta\phi\right)\cos\left(n\Delta\phi\right)d\Delta\phi = \delta_{m,n}\pi,\tag{E.1}$$

where for v_2, $n = 2$.

This means that in the absence of flow all EMCIC terms vanish except for the ones that exhibit $\cos(2\Delta\phi)$ dependence of $\Delta\phi$. For example in the first order expansion of EMCICs (see Eq. 6.22) there is a term $\vec{p}_{T,1}\vec{p}_{T,1} \sim \cos(\Delta\phi)$. This term gives no contribution to v_2, nor do any other terms from $1/N$ expansion. The first term that gives a non-zero contribution to v_2 (means, goes like $\cos(2\Delta\phi)$) is the second order expansion term in $\vec{p}_T$ that is proportional to $\left(\vec{p}_{T,1}\vec{p}_{T,1}\right)^2 \sim \cos^2(\Delta\phi) \sim \cos(2\Delta\phi)$. This term (as well as a few other terms in higher-order $1/N$ expansion) will give a non-zero contribution to v_2. In our GENBOD simulations we do not have a flow so we can study the magnitude of the EMCIC effects on v_2 measurements. Such results are presented on Figure E.1 where we plot v_2 vs p_T for three different event multiplicities while the free kinetic energy per particle is fixed ($\bar{K} = 0.9\ GeV$).

As seen, the magnitude of a non-flow contribution to v_2 from EMCICs is getting smaller with increasing multiplicity and even for low-multiplicity events the magnitude is of order of a few per-mile for large p_T. From this dependence we can predict that this effect will be so small in heavy ion collisions that it can be simply neglected.

APPENDIX F

SYMMETRY CONSIDERATIONS

The spherical harmonic decomposition representation, in which three-dimensional correlation functions are represented by several one-dimensional moments, $A_{l,m}$, efficiently condenses the shape information. A much *greater* increase in efficiency comes, however, with the realization that many $A_{l,m}$'s must vanish by symmetry, depending on the cuts and conditions of the analysis. Besides reducing information by significant factors, this realization also provides diagnostic power– non-physical artifacts often appear in $A_{l,m}$'s which do not vanish when they should. Digging out such effects in the traditional three-dimensional Cartesian representation can be quite difficult.

In the most general case, the 3-D correlation function may have any shape, with no symmetry constraints. In this case, none of the $A_{l,m}$'s need vanish. Usually, however, an analysis is less than fully general, and symmetry consequences then arise.

In particular, we will consider four common conditions used in practice:

[1] One measures correlations between identical particles

[2] The measurement covers a symmetric rapidity region about y=0 and the collision is between identical ions (e.g. Au+Au rather than Au+Si)

[3] The measurement is integrated over reaction-plane angle

201

[4] The measurement might be correlated with the *second*-order reaction-plane, but the first-order reaction-plane is not known. In other words, the direction of the impact parameter is known at best only modulo π.

Our strategy begins by identifying transformations in relative momentum $\vec{q}$ under which the measured correlation must be invariant. As an example, since the overall sign of $\vec{q}$ is meaningless when discussing pairs of identical particles (condition [A]), $C(q_o, q_o, q_l) = C(-q_o, -q_o, -q_l)$, or, in spherical coordinates, $C(Q, \cos\theta, \phi) = C(Q, -\cos\theta, \phi - \pi)$.

We then use a symmetry of the spherical harmonics, here $Y_{l,m}(\cos\theta, \phi) = (-1)^l Y_{l,m}(-\cos\theta, \phi+\pi)$ to find

$$
\begin{aligned}
A_{l,m}(Q) &\equiv \frac{1}{4\pi} \int_0^{2\pi} d\phi \int_{-1}^1 d\cos\theta\, C(Q, \cos\theta, \phi) Y_{l,m}(\cos\theta, \phi) \\
&= \frac{1}{4\pi} \int_0^{2\pi} d\phi \int_{-1}^1 d\cos\theta\, C(Q, -\cos\theta, \phi-\pi) Y_{l,m}(\cos\theta, \phi) \\
&= \frac{1}{4\pi} \int_{-\pi}^{\pi} d\phi \int_1^{-1} (-d\cos\theta) C(Q, \cos\theta, \phi) Y_{l,m}(-\cos\theta, \phi+\pi) \\
&= \frac{1}{4\pi} \int_0^{2\pi} d\phi \int_{-1}^1 d\cos\theta\, C(Q, \cos\theta, \phi)(-1)^l Y_{l,m}(\cos\theta, \phi)) \\
&= (-1)^l A_{l,m}(Q).
\end{aligned}
\tag{F.1}
$$

Thus, all odd-l moments $A_{l,m}$ must vanish, for correlations between identical particles.

The same type of reasoning is used below, in identifying symmetry constraints for various combinations of analysis conditions.

F.1 $\vec{q}$ transformations and $Y_{l,m}$ response

Table F.1 lists all combinations in which one or more of the components of $\vec{q}$ can change sign. For later reference, the transformations are numbered $0\ldots 7$, according

#	transformation	$Y_{l,m}$consequence
0	$(q_o, q_s, q_l) \rightarrow (+q_o, +q_s, +q_l)$	$Y_{l,m} \rightarrow Y_{l,m}$
1	$(q_o, q_s, q_l) \rightarrow (+q_o, +q_s, -q_l)$	$Y_{l,m} \rightarrow (-1)^{l+m} Y_{l,m}$
2	$(q_o, q_s, q_l) \rightarrow (+q_o, -q_s, +q_l)$	$Y_{l,m} \rightarrow Y_{l,m}{}^*$
3	$(q_o, q_s, q_l) \rightarrow (+q_o, -q_s, -q_l)$	$Y_{l,m} \rightarrow (-1)^{l+m} Y_{l,m}{}^*$
4	$(q_o, q_s, q_l) \rightarrow (-q_o, +q_s, +q_l)$	$Y_{l,m} \rightarrow (-1)^{m} Y_{l,m}{}^*$
5	$(q_o, q_s, q_l) \rightarrow (-q_o, +q_s, -q_l)$	$Y_{l,m} \rightarrow (-1)^{l} Y_{l,m}{}^*$
6	$(q_o, q_s, q_l) \rightarrow (-q_o, -q_s, +q_l)$	$Y_{l,m} \rightarrow (-1)^{m} Y_{l,m}$
7	$(q_o, q_s, q_l) \rightarrow (-q_o, -q_s, -q_l)$	$Y_{l,m} \rightarrow (-1)^{l} Y_{l,m}$

Table F.1: The possible transformations (numbered in the left column) in which the signs of $\vec{q}$ components flip, and the effect of the transformation on the $Y_{l,m}$'s.

to a binary scheme. The effect of the transformation on the spherical harmonics appears in the last column of the Table.

Transformation (0), of course, is the trivial identity transformation, under which any correlation function is invariant, and which imposes no symmetry constraint. We include it in the Table only for completeness, and do not discuss it further.

F.2 Restrictions, invariants, and consequences on $A_{l,m}$'s

Under which of the transformations in Table F.1 does the correlation function remain invariant? Since identical-particle correlations are more common than correlations between non-identical particles, there will be a greater familiarity with the symmetries of the former. Thus, we begin with this more familiar case and then discuss non-identical particle correlations.

F.2.1 Correlations between identical particles

To systematically identify those transformations in Table F.1 which leave a correlation function invariant, it helps to have a concrete functional form to discuss. For

Anal. Conditions				$C(\vec{q})$ invariances							which $A_{l,m}$'s vanish
[A]	[B]	[C]	[D]	1	2	3	4	5	6	7	
$\checkmark$										$\checkmark$	l odd
$\checkmark$	$\checkmark$									$\checkmark$	l odd
$\checkmark$		$\checkmark$	$(\checkmark)$		$\checkmark$		$\checkmark$			$\checkmark$	Re$[A_{l,m}]$: l odd Im$[A_{l,m}]$: $\forall l, m$
$\checkmark$	$\checkmark$	$\checkmark$	$(\checkmark)$	$\checkmark$	$\checkmark$	$\checkmark$	$\checkmark$	$\checkmark$	$\checkmark$	$\checkmark$	Re$[A_{l,m}]$: l and/or m odd Im$[A_{l,m}]$: $\forall l, m$
$\checkmark$			$\checkmark$							$\checkmark$	l odd
$\checkmark$	$\checkmark$		$\checkmark$	$\checkmark$					$\checkmark$	$\checkmark$	l and/or m odd
											-
	$\checkmark$										-
		$\checkmark$	$(\checkmark)$		$\checkmark$						Im$[A_{l,m}]$: $\forall l, m$
	$\checkmark$	$\checkmark$	$(\checkmark)$	$\checkmark$	$\checkmark$	$\checkmark$					Re$[A_{l,m}]$: odd $(l+m)$ Im$[A_{l,m}]$: $\forall l, m$
			$\checkmark$								-
	$\checkmark$		$\checkmark$	$\checkmark$							odd $(l+m)$

Table F.2: Symmetry consequences of analysis conditions. The left four columns show various combinations of analysis cuts and conditions, identified [A]-[D] as discussed in the beginning of this Appendix. (Note that condition [C] implies condition [D]; this is indicated by the symbol $(\checkmark)$ in column [D].) The middle seven columns indicate the consequent invariance symmetries of the correlation function according to the numbering scheme of Table F.1. The right-most column indicates which, if any, spherical harmonic moments of the correlation function must vanish.

identical pions, the correlation function is often parameterized as a Gaussian with six "radius" parameters,

$$C(q_o, q_o, q_l) = 1 + \lambda \cdot \exp\left(-R_o^2 q_o^2 - R_s^2 q_s^2 - R_l^2 q_l^2 - \right. \tag{F.2}$$

$$\left. -2R_{os}^2 q_o q_s - 2R_{ol}^2 q_o q_l - 2R_{sl}^2 q_s q_l\right).$$

While measured correlation functions often have non-Gaussian features not captured by this parameterization, the form given in Equation F.2 contains the generic and most general symmetries of all correlation functions using identical particles. Thus,

we use this familiar example to focus the discussion. The six parameters of form F.2 describe an ellipsoid described by three axis lengths, and rotated by three Euler angles in $\vec{q}$-space. Measured examples are shown and discussed in [40].

Clearly, the form of Equation F.2 is invariant under transformation (7), as discussed earlier. Invariance under any transformations (1)-(6) requires that one or more of the "radius" parameters R_{ij}^2 vanish. In general, none of them do [40, 141], even when considering a region symmetric about midrapidity in a collision between identical ions (condition [B]) [7].

If the measurement is integrated over reaction plane angle, then the "side" direction has no relevant sign, $R_{os}^2 = R_{sl}^2 = 0$, and the correlation function is invariant under transformation (2). While R_{ol}^2 need not vanish [142], the correlation function is unchanged if q_o and q_l change sign together (transformation (5)).

Further constraining the measurement to a symmetric region about midrapidity implies also that R_{ol}^2 vanish, and the correlation function is then invariant under all transformations (0)-(7). This is the most common set of measurement conditions.

At high energies, it is common only to determine the second-order reaction plane. This corresponds to condition [D]. If the measurement is performed at midrapidity (condition [B]), then R_{os}^2 is the only non-vanishing cross-term radius, so the correlation function is invariant under transformation (1). Away from midrapidity, R_{ol}^2 need not vanish, so (7) is again the only remaining transformation leaving $C(\vec{q})$ invariant.

---

[7]At first, it seems surprising that, in the absence of reaction-plane assumptions, no additional symmetry constraint is imposed onto the correlation function by a symmetric selection about midrapidity– i.e. none of the "radius" parameters R_{ij}^2 are required to vanish. However, the selection does impose symmetry constraints at a "higher" level. In identical-particle correlations, for example, while R_{ol}^2 need not vanish at midrapidity for any given measured correlation function, symmetry demands a relationship between R_{ol}^2 measured in different correlation functions; in particular $R_{ol}^2(\phi_{K,\mathrm{RP}} + \pi) = -R_{ol}^2(\phi_{K,\mathrm{RP}})$, where $\phi_{K,\mathrm{RP}}$ is the angle between the total pair momentum and the reaction plane. Symmetries at this level are discussed in detail in [41].

F.2.2 Correlations between non-identical particles

Correlations between non-identical particles are no longer invariant under transformation (7), as they may depend on odd-power terms of the components of $\vec{q}$. In the case of femtoscopic correlations, the strengths of these odd powers probe asymmetries in the average emission point between the two particle species [97].

From a symmetry standpoint, the correlation function will be characterized by nine parameters, rather than the six "HBT radii" of Equation F.2. In the simple case that $C(q_o, q_o, q_l)$ would be Gaussian, these new parameters might represent the offset from the origin of the ellipsoid in $\vec{q}$-space.

In the absence of any cuts– or if only the midrapidity condition [B] is applied [7], all nine parameters may take any value, and there are no required invariances or symmetry constraints. If the reaction-plane is integrated over (condition [C]) then $C(q_o, q_o, q_l)$ may remain sensitive to the sign of q_o (reflecting, for example, a different average time of emission between the particles [97]) and q_l (reflecting the difference in emission point in the beam direction, for analyses away from midrapidity), but not q_s, since an angle-averaged physical source must be symmetric with respect to the beam axis.

Unlike the case in which it is the sole condition, if the midrapidity condition [B] is imposed *together* with condition [C], then it does have an effect. In particular, a dependence on the sign of q_l vanishes.

If condition [C] is relaxed to condition [D] (i.e. the analysis is sensitive to the second-order reaction plane), then the sign of q_s may matter. This is because the sign of q_o always affects correlations between non-identical particles and, as in identical

206

particle correlations in which R_{os}^2 may be finite, so the sign of $q_o q_s$ may separately matter. Thus, imposition of [D] alone implies no symmetry constraints.

APPENDIX G

FINITE BINNING EFFECTS

Equation 4.4 defines the harmonic moments in terms of a continuous correlation function. Most experimentally-measured correlation functions are constructed via histograms with discrete, finite bins. For decomposition into spherical harmonics, a natural choice would be to use bins in Q, $\cos\theta$ and ϕ (c.f. Eq. 5.1). Here, we will find an approximate expression, analogous to Equation 4.4, for the harmonic moments in terms of the discretized correlation function.

We denote the fixed bin sizes in the angular coordinates as $\Delta_{\cos\theta}$ and Δ_ϕ. Binning in Q is unimportant here, since Q is carried as an explicit argument in both C and $A_{l,m}$. The binned correlation function (denoted with superscript Δ) is related to the

continuous one as

$$
\begin{aligned}
&C^{\Delta}\left(Q, \cos\theta_i, \phi_i\right) \\
&= \frac{1}{\Delta_\phi \Delta_{\cos\theta}} \int_{\phi_i-\Delta_\phi/2}^{\phi_i+\Delta_\phi/2} d\phi \int_{\cos\theta_i-\Delta\cos\theta/2}^{\cos\theta_i+\Delta\cos\theta/2} d(\cos\theta) C\left(Q, \cos\theta, \phi\right) \\
&= \frac{\sqrt{4\pi}}{\Delta_\phi \Delta_{\cos\theta}} \sum_{l'=0}^{\infty} \sum_{m'=-l'}^{+l'} A_{l',m'}(Q) \times \\
&\quad \int_{\phi_i-\Delta_\phi/2}^{\phi_i+\Delta_\phi/2} d\phi \int_{\cos\theta_i-\Delta_{\cos\theta}/2}^{\cos\theta_i+\Delta_{\cos\theta}/2} d(\cos\theta) Y_{l',m'}^*\left(\cos\theta, \phi\right) \\
&= \sqrt{4\pi} \sum_{l'=0}^{\infty} \sum_{m'=-l'}^{+l'} A_{l',m'}(Q) \cdot F_{l',m'}(\Delta_\phi, \Delta_{\cos\theta}, \cos\theta_i) \times \\
&\quad Y_{l',m'}^*\left(\cos\theta_i, \phi_i\right).
\end{aligned}
\tag{G.1}
$$

Here,

$$
F_{l',m'}(\Delta_\phi, \Delta_{\cos\theta}, \cos\theta_i) = \frac{\sin(m\Delta_\phi/2)}{m\Delta_\phi/2} \times \tag{G.2}
$$
$$
\frac{1}{\Delta_{\cos\theta} P_{l',m'}(\cos\theta_i)} \int_{\cos\theta_i-\Delta_{\cos\theta}/2}^{\cos\theta_i+\Delta_{\cos\theta}/2} d(\cos\theta) P_{l',m'}(\cos\theta)
$$

is the term which includes the finite binning effects.

Assuming that $A_{l,m}$'s vanish for l, m greater than the sampling Nyquist frequency, by the sampling theorem [143, 144], the $A_{l,m}$'s are completely determined by C^{Δ}. In fact, if $F_{l,m}$ were independent of $\cos\theta_i$, then we would have

$$
\begin{aligned}
A_{l,m}(Q) =& \frac{\Delta_\phi \Delta_{\cos\theta}}{F_{l,m}\left(\Delta_{\cos\theta}, \Delta_\phi\right)\sqrt{4\pi}} \times \\
& \sum_{\text{bins } i} C^{\Delta}\left(Q, \cos\theta_i, \phi_i\right) Y_{l,m}\left(\cos\theta_i, \phi_i\right),
\end{aligned}
$$

where the summation is over all bins of $\cos\theta$ and ϕ, for a given Q.

However, $F_{l,m}$ does depend on $\cos\theta_i$, so the above equation does not strictly hold. Nevertheless, we find, numerically, that an excellent approximation is

$$
A_{l,m}(Q) \approx \frac{\Delta_\phi \Delta_{\cos\theta}}{\sqrt{4\pi}} \sum_{\text{bins } i} \frac{C^{\Delta}\left(Q, \cos\theta_i, \phi_i\right) Y_{l,m}\left(\cos\theta_i, \phi_i\right)}{F_{l,m}\left(\Delta_{\cos\theta}, \Delta_\phi, \cos\theta_i\right)}. \tag{G.3}
$$

For any given measurement, one may check the validity of this approximation by plugging the result of Equation G.3 into the expression on the last line of Equation G.1. To the extent that it returns the measured correlation function C^{Δ}, the $A_{l,m}$'s returned by Equation G.3 are correctly extracted. If there are deviations, the correct $A_{l,m}$'s can be found by iterative techniques.

Other methods to remove binning effects have also been proposed [145].

APPENDIX H

WHEN CAN WE DROP THE P_Z-DEPENDENT TERMS WHEN FITTING SPECTRA USING EMCIC FORMULA?

In Section 6.3.1 we presented analytic formula, given by Eq. 6.28, to account for the EMCIC effect in a single particle distribution. Then, when discussing fits to the spectra at small rapidities in Sec. 6.3.3, we argued that we can drop a term from Eq. 6.28 that depends on p_z because it is very small comparing to other terms. Below, we prove above statement.

The proof is straightforward. We plot numerators of the terms from Eq. 6.28 versus the transverse mass for a given range of rapidity to compare their magnitudes. These are the quantities we plot on Fig. H.1.

$$\overline{p_z^2} \equiv \frac{1}{2y_{max}} \int_{-y_{max}}^{y_{max}} p_z^2 dy = m_T^2 \left(\frac{\sinh(2y_{max})}{4y_{max}} - \frac{1}{2} \right) \tag{H.1}$$

$$\overline{E^2} \equiv \frac{1}{2y_{max}} \int_{-y_{max}}^{y_{max}} E^2 dy = m_T^2 \left(\frac{\sinh(2y_{max})}{4y_{max}} + \frac{1}{2} \right) \tag{H.2}$$

$$\overline{E} \equiv \frac{1}{2y_{max}} \int_{-y_{max}}^{y_{max}} E dy = m_T \frac{\sinh(y_{max})}{y_{max}}, \tag{H.3}$$

where $m_T = \sqrt{p_T^2 + m_*^2}$ and rapidity of particles used in the calculations is within the range $y < |y_{max}|$. The values of y_{max} are given in a legend to Fig. H.1.
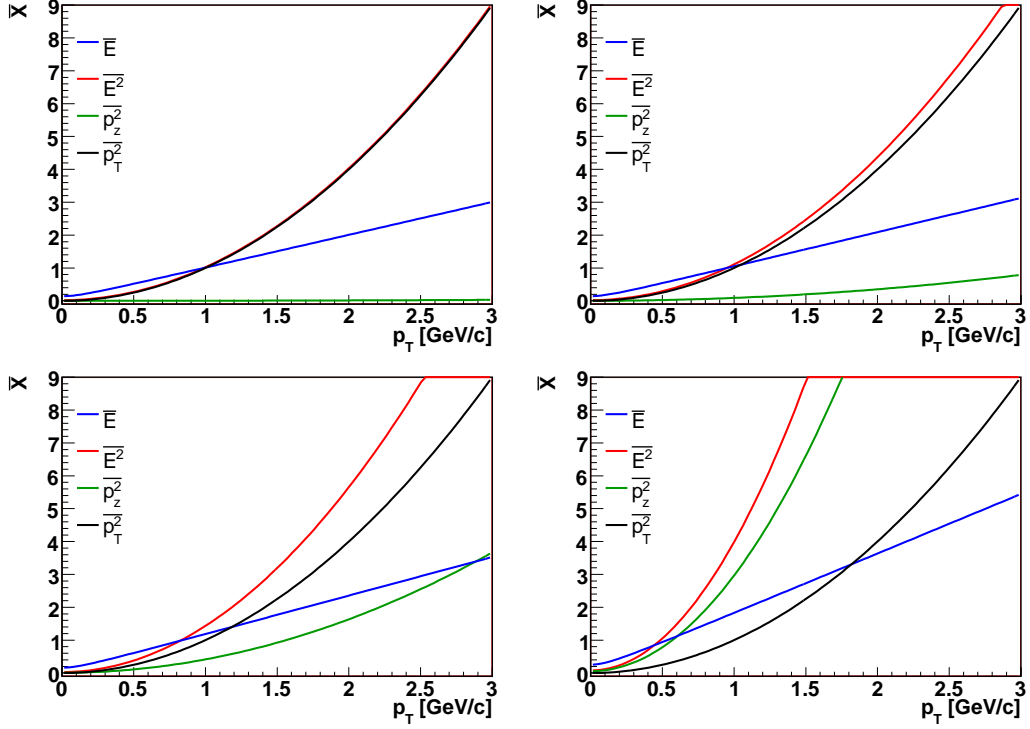
Figure H.1: Terms from Eqs. H.1- H.3 plotted vs the transverse momentum. The values of y_{max} are as follows: upper-left panel - $y_{max} = 0.1$, upper-right panel - $y_{max} = 0.5$, lower-left panel - $y_{max} = 1.0$ and lower-right panel - $y_{max} = 2.0$.

Clearly, $\overline{p_z^2}$ is smaller than any other terms by about two-order of magnitude for $y_{max} = 0.1$ and an order of magnitude for $y_{max} = 0.5$. It should not be ignored for higher rapidities. Additionally, the p_z term from Eq. 6.28 is getting even smaller because of the fact that $\langle p_z^2 \rangle > \langle p_T^2 \rangle$ in heavy ion collisions at RHIC.

APPENDIX I

ANALYTICAL METHOD OF FINDING EMCIC PARAMETERS DIRECTLY FROM THE CORRELATION FUNCTION

In this Appendix, we present a method of calculating EMCIC parameters directly from the correlation function.

We can write the formula for two-particle correlation function decomposed into the spherical harmonics (Section 5) if there is no other physics in the system but the momentum and energy conservation.

$$A_{l,m}(Q) = \delta_{l,0} \cdot \left(1 - M_4^2/M_3\right) - M_1 \cdot A_{l,m}^{p_T}(Q) \tag{I.1}$$

$$-M_2 \cdot A_{l,m}^{p_z}(Q) - M_3 \cdot A_{l,m}^{(E \cdot E)}(Q) + M_4 \cdot A_{l,m}^{(E+E)}(Q) \,.$$

where

$$A_{l,m}^{p_z}(Q) \equiv \sum_{\text{bins}\,i} \overline{\{p_{1,z} \cdot p_{2,z}\}}(Q, \cos\theta_i, \phi_i) \cdot Y_{l,m}(\cos\theta_i, \phi_i) \,,$$

$$A_{l,m}^{p_T}(Q) \equiv \sum_{\text{bins}\,i} \overline{\{p_{1,T} \cdot p_{2,T}\}}(Q, \cos\theta_i, \phi_i) \cdot Y_{l,m}(\cos\theta_i, \phi_i) \,,$$

$$A_{l,m}^{(E \cdot E)}(Q) \equiv \sum_{\text{bins}\,i} \overline{\{E_1 \cdot E_2\}}(Q, \cos\theta_i, \phi_i) \cdot Y_{l,m}(\cos\theta_i, \phi_i) \,,$$

$$A_{l,m}^{(E+E)}(Q) \equiv \sum_{\text{bins}\,i} \overline{\{E_1 + E_2\}}(Q, \cos\theta_i, \phi_i) \cdot Y_{l,m}(\cos\theta_i, \phi_i) \,. \tag{I.2}$$

There are four EMCIC parameters $M_{i=1,\ldots,4}$ in Eq. I.1 so to find them we need four independent equations that are (preferably) linear in M_i. Only equation for

$(l, m) = (0, 0)$ is not linear in M_i but we can choose any other equation for $l > 0$ to find M_i, e.g.

$$\begin{cases} A_{2,0} = -M_1 A_{2,0}^{p_T} - M_2 A_{2,0}^{p_z} - M_3 A_{2,0}^{(E\cdot E)} - M_4 A_{2,0}^{(E+E)} \\ A_{2,2} = -M_1 A_{2,2}^{p_T} - M_2 A_{2,2}^{p_z} - M_3 A_{2,2}^{(E\cdot E)} - M_4 A_{2,2}^{(E+E)} \\ A_{4,0} = -M_1 A_{4,0}^{p_T} - M_2 A_{4,0}^{p_z} - M_3 A_{4,0}^{(E\cdot E)} - M_4 A_{4,0}^{(E+E)} \\ A_{4,2} = -M_1 A_{4,2}^{p_T} - M_2 A_{4,2}^{p_z} - M_3 A_{4,2}^{(E\cdot E)} - M_4 A_{4,2}^{(E+E)} \end{cases} \tag{I.3}$$

then the problem reduces to solving the following equation

$$\mathbb{B} \begin{pmatrix} M_1 \\ M_2 \\ M_3 \\ M_4 \end{pmatrix} = \begin{pmatrix} A_{2,0} \\ A_{2,2} \\ A_{4,0} \\ A_{4,2} \end{pmatrix} \tag{I.4}$$

where

$$\mathbb{B} = \begin{pmatrix} -A_{2,0}^{p_T} - A_{2,0}^{p_z} - A_{2,0}^{(E\cdot E)} + A_{2,0}^{(E+E)} \\ -A_{2,2}^{p_T} - A_{2,2}^{p_z} - A_{2,2}^{(E\cdot E)} + A_{2,2}^{(E+E)} \\ -A_{4,0}^{p_T} - A_{4,0}^{p_z} - A_{4,0}^{(E\cdot E)} + A_{4,0}^{(E+E)} \\ -A_{4,2}^{p_T} - A_{4,2}^{p_z} - A_{4,2}^{(E\cdot E)} + A_{4,2}^{(E+E)} \end{pmatrix} \tag{I.5}$$

$$\begin{pmatrix} M_1 \\ M_2 \\ M_3 \\ M_4 \end{pmatrix} = \mathbb{B}^{-1} \begin{pmatrix} A_{2,0} \\ A_{2,2} \\ A_{4,0} \\ A_{4,2} \end{pmatrix} \tag{I.6}$$

The advantage of writing Eq. I.3 in a matrix form (Eq. I.4) is that we can calculate the determinant of the matrix $\mathbb{B}$. If it is very close to zero, it will indicate that it is hard to determine the values of M_i uniquely. However, in such a case, we can use another value of Q. Also, to get a feeling about "the best" value of Q we can plot $det\mathbb{B}$ as a function of Q. Unfortunately, this approach cannot be used if there are additional correlations (like femtoscopic ones) because the formula on the correlation function is more complicated and we cannot easily decompose the correlation function into spherical harmonics and end up with linear equations in M_i.

APPENDIX J

THE EFFECT OF THE PHASE-SPACE CONSTRAINTS DUE THE ENERGY AND MOMENTUM CONSERVATION ON TWO PARTICLE CORRELATION FUNCTION PROJECTED ONTO $(\Delta Y, \Delta \phi)$.

J.1 The motivation and formalism.

The two-particle correlations can provide an insight into the dynamics of the system and thus they are widely used in elementary physics, high energy and heavy ion physics communities to study various effects for different particle types and in different kinematic regions. In this appendix we focus on the projections of the two particle correlation functions onto $(\Delta y, \Delta \phi)$ for small systems. Such correlations have been studied both in $p + p$ [146, 147] and heavy ions (e.g. [148]) and attempt to describe the shape of the correlation function in terms of different components that are supposed to originate from different physics effects (like e.g. soft and hard processes). Here, we do not intend to discuss the conclusions presented in above papers but instead, we want to understand the effect of the phase-space constraints due to the energy and momentum conservation laws on the shape of the two-particle correlation function projected onto $(\Delta y, \Delta \phi)$. In other words, we want to study the shape of the correlation function when there is no other physics in the system except for the energy and momentum conservations.

As derived in Section 6.5, the two particle correlation function due to conservation laws only can be written as

$$C(p_1, p_2) \equiv \quad \frac{\tilde{f}_c(p_1, p_2)}{\tilde{f}_c(p_1)\,\tilde{f}_c(p_2)} = \frac{\left(\frac{N}{N-2}\right)^2}{\left(\frac{N}{N-1}\right)^4} \times$$
$$\frac{\exp\left[\frac{-1}{2(N-2)}\left\{\sum_{\mu=1}^{3}\left(\frac{\left(\sum_{i=1}^{2}p_{i,\mu}^2\right)^2}{\langle p_\mu^2\rangle}\right) + \frac{\left(\sum_{1}^{2}(E_i-\langle E\rangle)\right)^2}{\langle E^2\rangle-\langle E\rangle^2}\right\}\right]}{\exp\left[\frac{-1}{2(N-1)}\sum_{i=1}^{2}\left\{\sum_{\mu=1}^{3}\frac{p_{i,\mu}^2}{\langle p_\mu^2\rangle} + \frac{(E_i-\langle E\rangle)^2}{\langle E^2\rangle-\langle E\rangle^2}\right\}\right]} \tag{J.1}$$

Later, depending on the purpose of the study, this correlation function can be e.g. projected on the $(\Delta y, \Delta\phi)$.

J.2 Simulations

We used the Monte-Carlo technique to do simulations to to construct the correlation function described by Eq. J.1. The transverse momentum of each particle is generated according to the thermal distribution $f(p_T) \sim e^{-p_T/T}$, where T is a parameter. In these studies we used two values of T: 200 and 800 MeV. The rapidity distribution is assumed to be flat in a range of $[-1, 1]$ and is independent on the particle type as well as p_T. Then, E and p_z are calculated according to the following formulas: $p_z = m_T sinh(y)$ and $E = m_T cosh(y)$ where $m_T = \sqrt{p_T^2 + m_0^2}$. Since we only have to know the relative angular angle between two particles we decided to simulate only $\Delta\phi$ and we assumed it to be a flat distribution. We also assumed that all particles are of the same type (have the same mass). Since the Eq. J.1 requires a knowledge of the number of particles and the kinematic scale of the system, we used the following parameters in our simulations: $N = 13.6$, $< p_T^2 >= 0.171\ (GeV/c)^2$, $< p_z^2 >= 0.335\ (GeV/c)^2$, $< E^2 >= 0.505\ (GeV)^2$, $< E >= 0.676\ GeV$.

We could use two equivalent methods to obtain the three dimensional correlation function. The first method is to create separate histograms for the numerator and

denominator from Eq. J.1, filled them in simulations, and divide by each other to obtain the correlation function. The second method is to create two histograms and fill one of them with a weight equal to the correlation function from Eq. 4.15 and other one with a weight equal to 1. By doing a ratio of these two histograms we obtain the 3D correlation function. However, these two methods are not equivalent in case of the 2D correlation function. In that case only the first method can be used and that is exactly what we did in the following analyses.

J.3 Results

The results of simulations for events including pions that are emitted according to the thermal distribution with $T = 200 \; MeV$ are presented on Fig. J.1. Only particles with transverse momentum $p_T = [0.0, 2.0] \; GeV/c$ were used in this case. The upper-left plot, labeled "All terms" represents the correlation function according to Eq. J.1. The upper-right plot, labeled "p_T term" represents only these terms from Eq. J.1 that depend on p_T only. Two lower plots show p_z- and E-dependent terms from the same equation. As expected, the "'p_T term" distribution depend on $\Delta\phi$ only while "p_z term" distribution depends on Δy only. The "E term" depends mostly on the Δy and weakly on $\Delta\phi$.

Figure J.2 shows similar results as Fig. J.1 except for different temperature used in the simulations : $T = 800 \; MeV$.

Figures J.3 and J.4 present results from simulations as presented on Figs. J.1 and J.2 respectively but for different p_T range, $p_T = [0.8, 2.0] \; GeV/c$.

Additionally, Figures J.5- J.8 show the same results are Figs. J.1- J.4 except that all particles are assumed to be protons. These figures represent rather unrealistic cases

although the purpose of this study is to show the importance of the particle mass on the effect of the phase-space constraints due to energy and momentum conservations on two-particle correlation function projected onto $(\Delta\phi, \Delta y)$.

Figure J.1: The effect of the phase-space constraints due to energy and momentum conservation on two-particle correlation function (Eq. J.1) projected on $(\Delta y, \Delta\phi)$. Label "All Terms" means that all terms from the right side of Eq. J.1 are included in the correlation function. Similarly, "Pt Term" means that only terms from Eq.J.1 that depend on p_T were used, etc. All particles are assumed to be pions and the transverse momentum of each particle is generated from the thermal distribution assuming $T = 200\ GeV$. The range of the particle transverse momentum used in this analysis is $p_T = [0.0, 2.0]\ GeV/c$.

J.4 Femtoscopic correlations

When studying two-particle correlations projected onto $(\Delta\phi, \Delta y)$ it is unavoidable to deal with the femtoscopic correlations that certainly give a signal that is on the top of the correlations due to limited phase-space discussed above and other possible physics like e.g. so-called mini-jets as well as e.g. detector effects like particle misidentification (not discussed here).

In this section we consider only Bose-Einstein correlations between identical pions that should be dominant in pion-rich collisions although probably understanding other femtoscopic correlations is not less important when studying non-identified particle correlations as done by the STAR experiment (e.g. [146, 147, 148]).

To simulate Bose-Einstein correlations we generated pions similarly as described in Section J.2 and distributed them according to the weight

$$w(p_1, p_2, R_{inv}) = 1 + \lambda cos(Q_{inv} * r_{12}) \tag{J.2}$$

where $Q_{inv} = \sqrt{(E_1 - E2)^2 - (p_1 - p_2)^2}$ and r_{12} is the relative position of the pair and have a Gaussian distribution, with mean value equal to zero and $\sigma = \sqrt{2}R_{inv}$ and R_{inv} is the size of the system in one dimension. R_{inv} and λ are the input parameters in our simulations. As an outcome, we get a correlation effect that can be parameterized as $C(Q_{inv} = 1 + \lambda e^{-Q_{inv}^2 R_{inv}^2}$.

Results of our simulations are presented below. Figure J.9 shows Bose-Einstein effect projected onto $(\Delta\phi, \Delta y)$ when $R_{inv} = 0.6\ fm$ and $\lambda = 1.0$. The left-panel plots represent the case when pions were generated according to the thermal distribution with $T = 200\ MeV$ and the right panel plots when $T = 800\ MeV$. The difference

between upper and lower plots is the range of the transverse momentum used in the simulations. It's $[0.0, 2.0]$ GeV for upper plots and $[0.8, 2.0]$ GeV for lower plots.

Figure J.10 shows similar results as Fig. J.9 except for different size of the source used in the simulations that is $R_{inv} = 0.3$ fm.

J.5 Discussion

We showed that the phase-space distortion due to the energy and momentum conservation has a non-trivial effect on the shape of the two-particle correlation function projected onto $(\Delta\phi, \Delta y)$. Additionally, we demonstrated that the effect depends not only on the particle composition in events (through particle mass), but also on the range of phase-space that particles are taken from (like e.g. p_T, y) and even on the parent distribution. Clearly, the EMCIC effect has to be taken into account regardless the existence of other physics that can affect the shape of the correlation function. Not doing that can lead to misinterpretation of physics that drives the shape of the two-particle correlation function projected onto $(\Delta\phi, \Delta y)$.

Certainly, there are other physics effects that can affect the shape of the two-particle correlation function. Among them are the femtoscopic correlations. In this appendix, we showed that the Bose-Einstein effect projects non-trivially on the $(\Delta\phi, \Delta y)$ correlation function. Thus, it is of a great importance to deeply understand the effect of femtoscopic correlations especially that they mostly affect the correlation function at the same area of $(\Delta\phi, \Delta y)$ where some physicists expect a signal that is of different origin like mini-jets [146, 147, 148]. So far the experimentalists study the $(\Delta\phi, \Delta y)$ correlations for unidentified particles [146, 147, 148]. However in such a case, while it is expectable that in pion dominated events, the pion HBT correlations

should mostly contribute to the signal due to femtoscopic correlations one should not forget that other correlations like kaon-kaon correlations, non-identical correlations can also affect the shape of the correlation function in a way that is not easy to predict without proper simulations. It would certainly help to study the correlation of identified particles, both like- and unlikely charged since the femtoscopic correlations should change the shape of the correlation function differently in these cases. Additionally, since we know that the femtoscopic sizes change with the momentum and the multiplicity (e.g. [26]) it would be important to study the $(\Delta\phi, \Delta y)$ correlation function for different ranges of the particle momentum.

Only after careful treatment and understanding of the EMCIC effect and femtoscopic correlations and how these effects project onto $(\Delta\phi, \Delta y)$ correlations it becomes reasonable to look at other physics effects that can affect the shape of the correlation function.
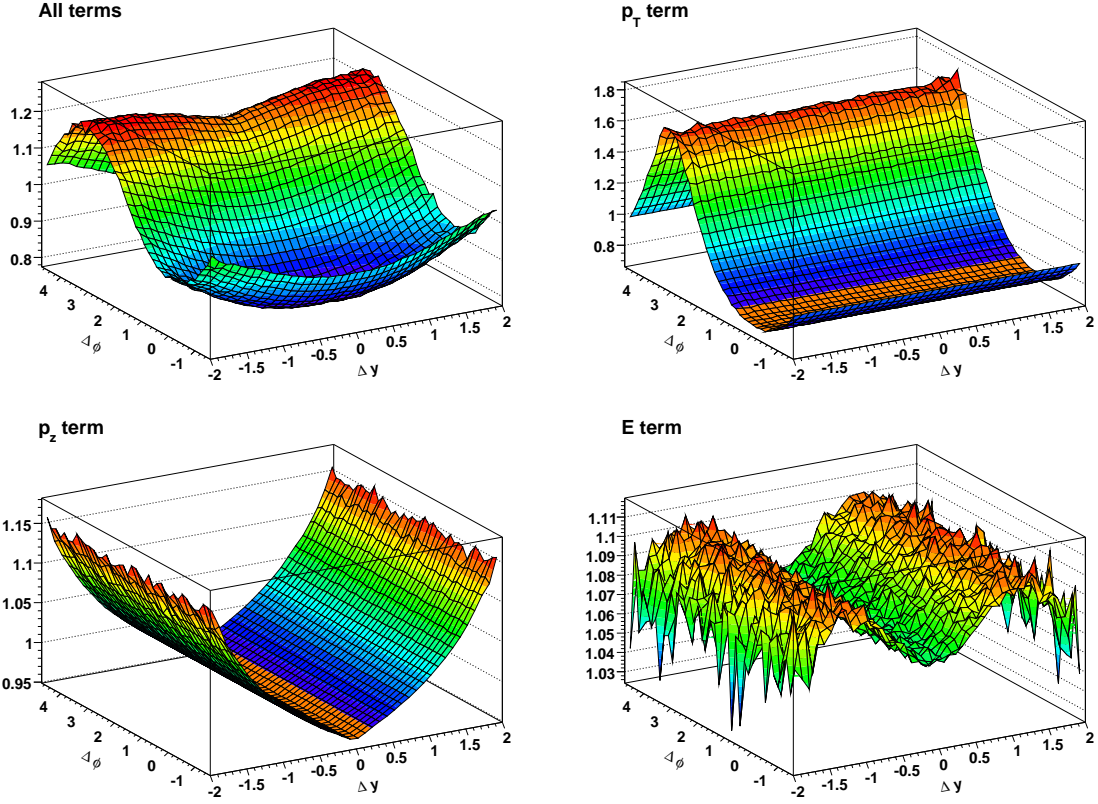
Figure J.2: The effect of the phase-space constraints due to energy and momentum conservation on two-particle correlation function (Eq. J.1) projected on $(\Delta y, \Delta \phi)$. Label "All Terms" means that all terms from the right side of Eq. J.1 are included in the correlation function. Similarly, "Pt Term" means that only terms from Eq.J.1 that depend on p_T were used, etc. All particles are assumed to be pions and the transverse momentum of each particle is generated from the thermal distribution assuming $T = 800 \; GeV$. The range of the particle transverse momentum used in this analysis is $p_T = [0.0, 2.0] \; GeV/c$.
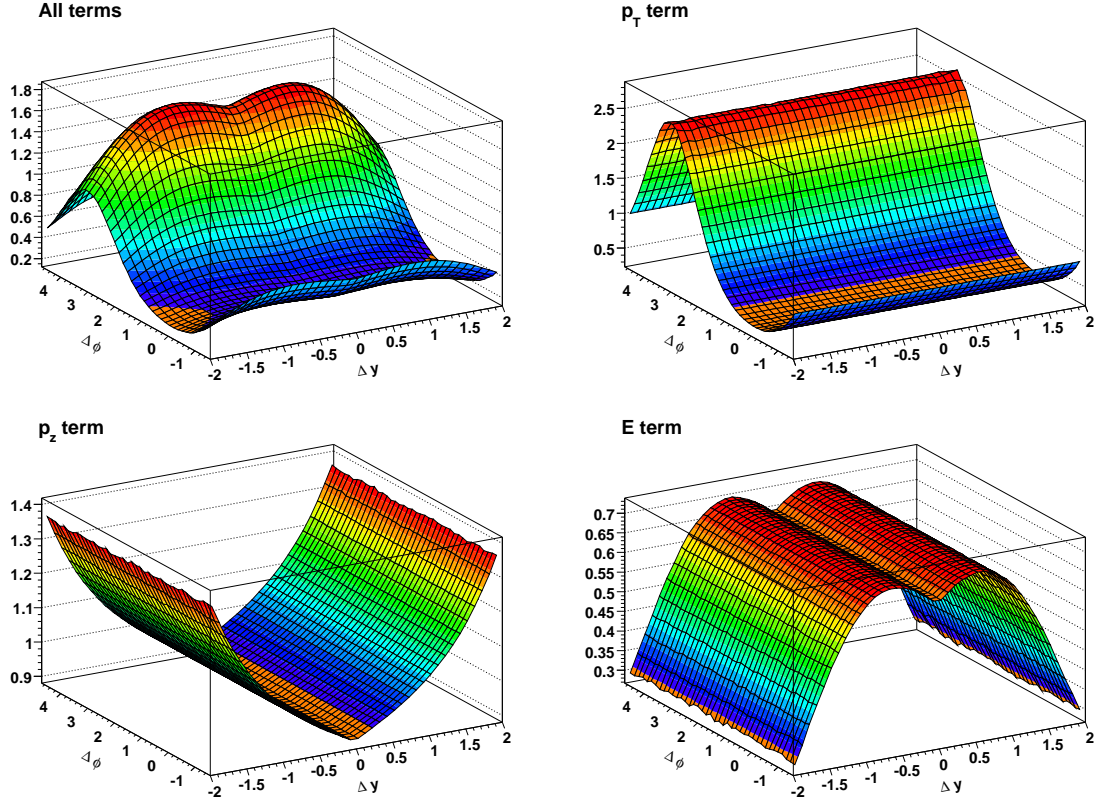
Figure J.3: The effect of the phase-space constraints due to energy and momentum conservation on two-particle correlation function (Eq. J.1) projected on $(\Delta y, \Delta\phi)$. Label "All Terms" means that all terms from the right side of Eq. J.1 are included in the correlation function. Similarly, "Pt Term" means that only terms from Eq.J.1 that depend on p_T were used, etc. All particles are assumed to be pions and the transverse momentum of each particle is generated from the thermal distribution assuming $T = 200\ GeV$. The range of the particle transverse momentum used in this analysis is $p_T = [0.8, 2.0]\ GeV/c$.
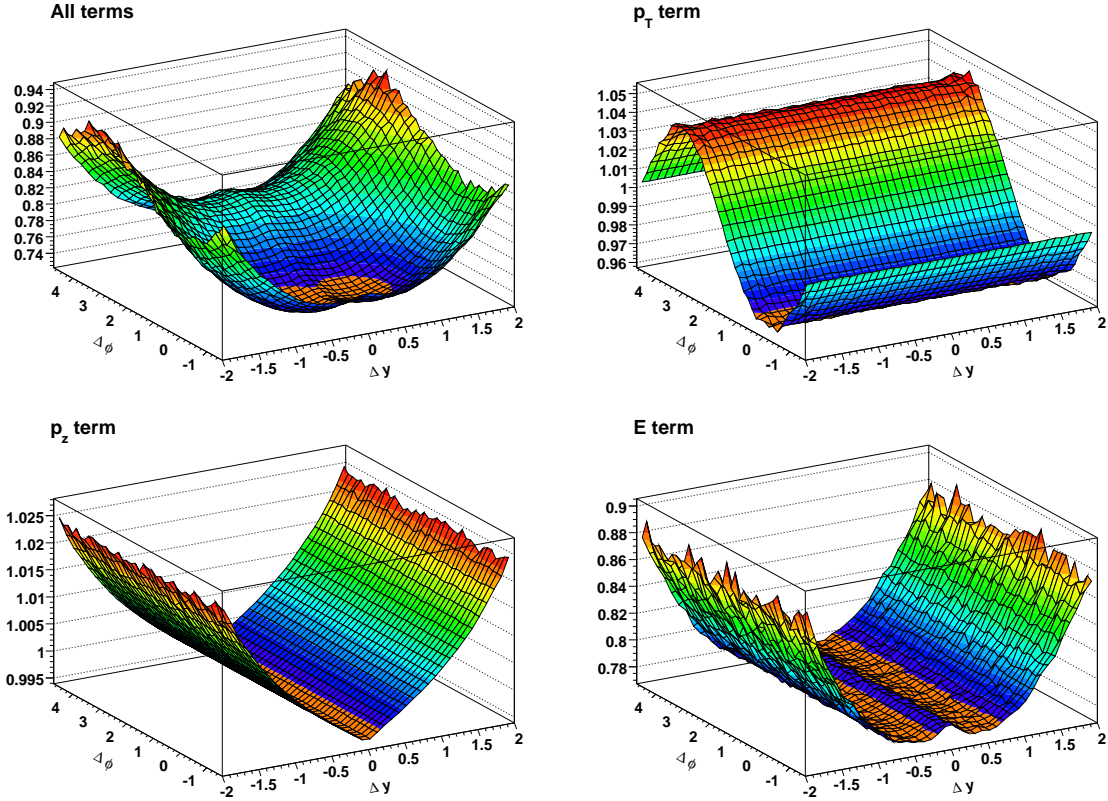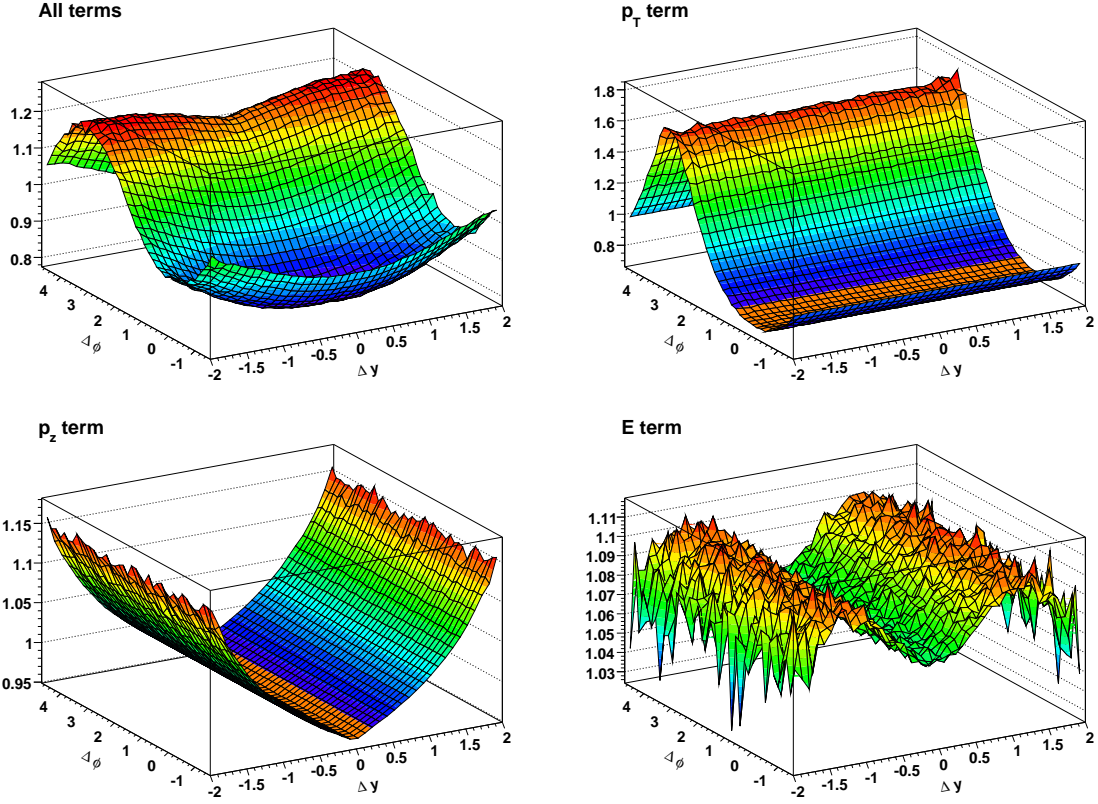
Figure J.4: The effect of the phase-space constraints due to energy and momentum conservation on two-particle correlation function (Eq. J.1) projected on $(\Delta y, \Delta \phi)$. Label "All Terms" means that all terms from the right side of Eq. J.1 are included in the correlation function. Similarly, "Pt Term" means that only terms from Eq.J.1 that depend on p_T were used, etc. All particles are assumed to be pions and the transverse momentum of each particle is generated from the thermal distribution assuming $T = 800 \ GeV$. The range of the particle transverse momentum used in this analysis is $p_T = [0.8, 2.0] \ GeV/c$.
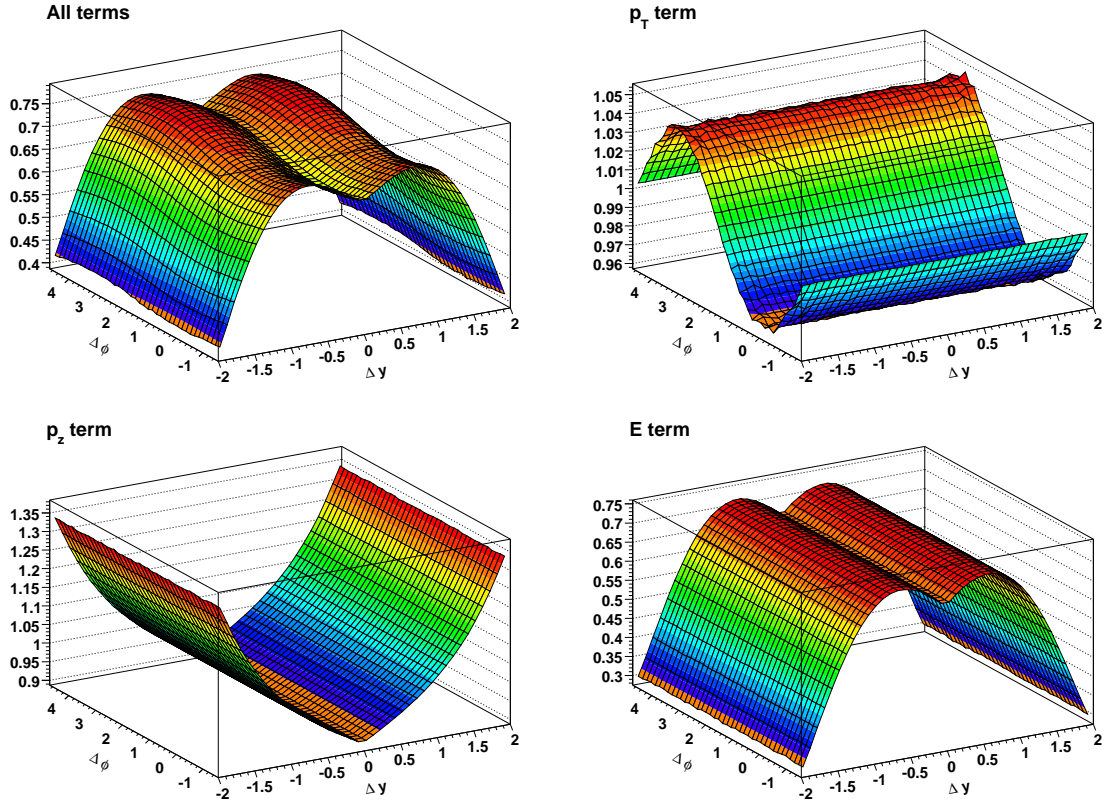
Figure J.5: The effect of the phase-space constraints due to energy and momentum conservation on two-particle correlation function (Eq. J.1) projected on $(\Delta y, \Delta \phi)$. Label "All Terms" means that all terms from the right side of Eq. J.1 are included in the correlation function. Similarly, "Pt Term" means that only terms from Eq.J.1 that depend on p_T were used, etc. All particles are assumed to be protons and the transverse momentum of each particle is generated from the thermal distribution assuming $T = 200 \, GeV$. The range of the particle transverse momentum used in this analysis is $p_T = [0.0, 2.0] \, GeV/c$.
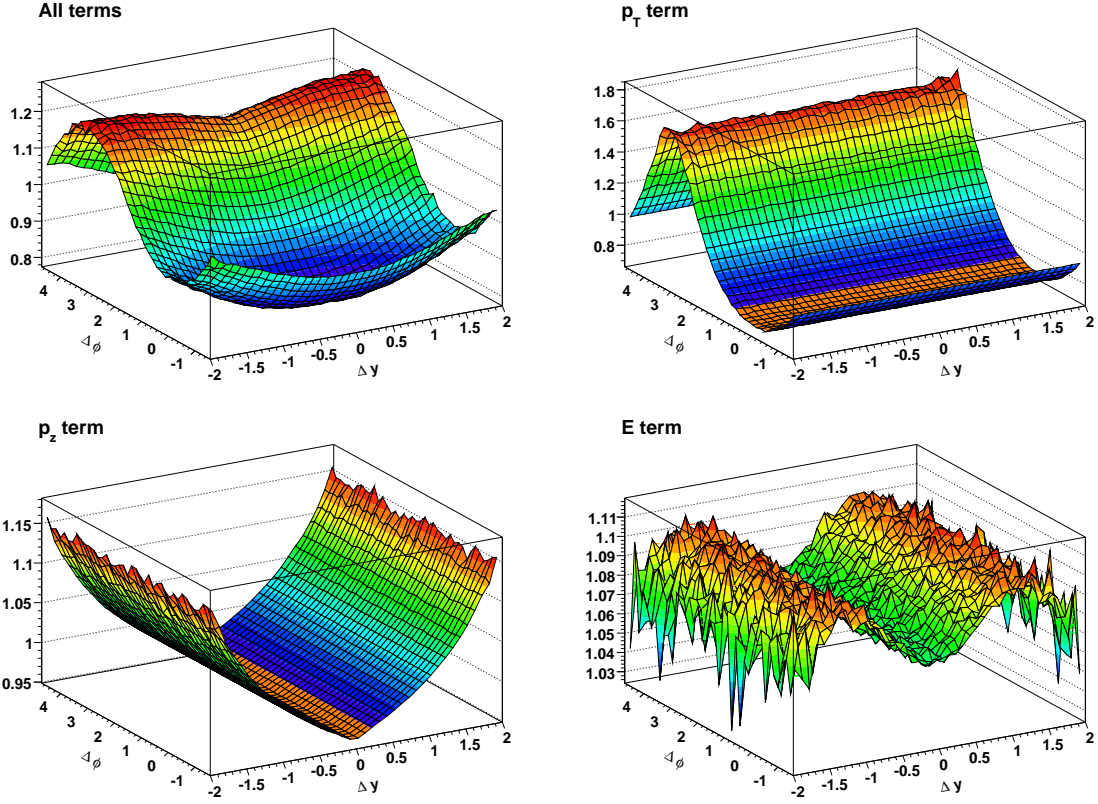
Figure J.6: The effect of the phase-space constraints due to energy and momentum conservation on two-particle correlation function (Eq. J.1) projected on $(\Delta y, \Delta \phi)$. Label "All Terms" means that all terms from the right side of Eq. J.1 are included in the correlation function. Similarly, "Pt Term" means that only terms from Eq. J.1 that depend on p_T were used, etc. All particles are assumed to be protons and the transverse momentum of each particle is generated from the thermal distribution assuming $T = 800 \ GeV$. The range of the particle transverse momentum used in this analysis is $p_T = [0.0, 2.0] \ GeV/c$.
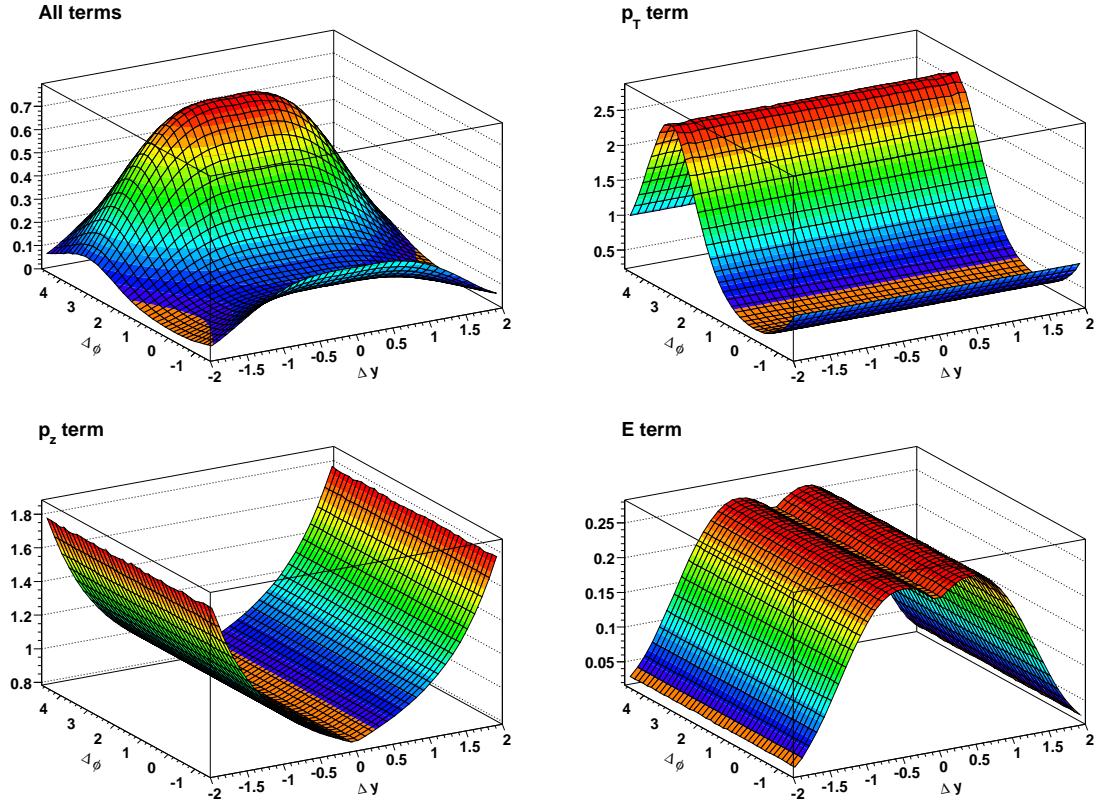
Figure J.7: The effect of the phase-space constraints due to energy and momentum conservation on two-particle correlation function (Eq. J.1) projected on $(\Delta y, \Delta \phi)$. Label "All Terms" means that all terms from the right side of Eq. J.1 are included in the correlation function. Similarly, "Pt Term" means that only terms from Eq.J.1 that depend on p_T were used, etc. All particles are assumed to be protons and the transverse momentum of each particle is generated from the thermal distribution assuming $T = 200\ GeV$. The range of the particle transverse momentum used in this analysis is $p_T = [0.8, 2.0]\ GeV/c$.
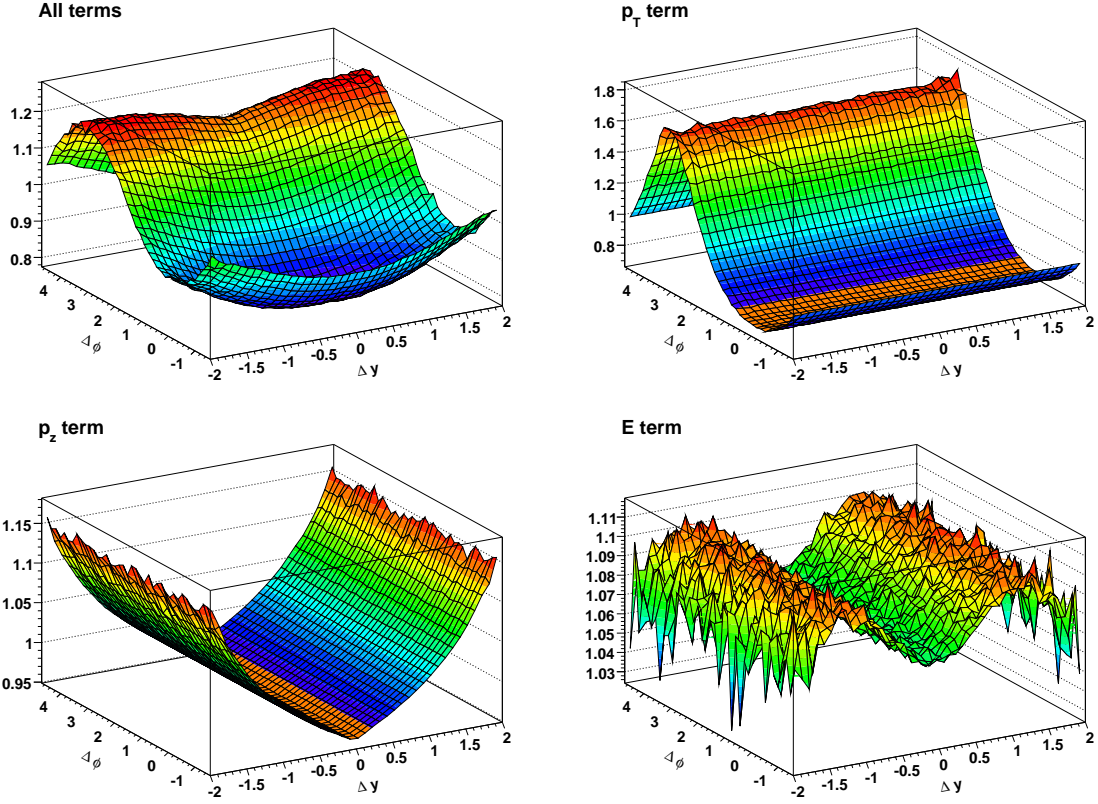
Figure J.8: The effect of the phase-space constraints due to energy and momentum conservation on two-particle correlation function (Eq. J.1) projected on $(\Delta y, \Delta\phi)$. Label "All Terms" means that all terms from the right side of Eq. J.1 are included in the correlation function. Similarly, "Pt Term" means that only terms from Eq.J.1 that depend on p_T were used, etc. All particles are assumed to be protons and the transverse momentum of each particle is generated from the thermal distribution assuming $T = 800\ GeV$. The range of the particle transverse momentum used in this analysis is $p_T = [0.8, 2.0]\ GeV/c$.
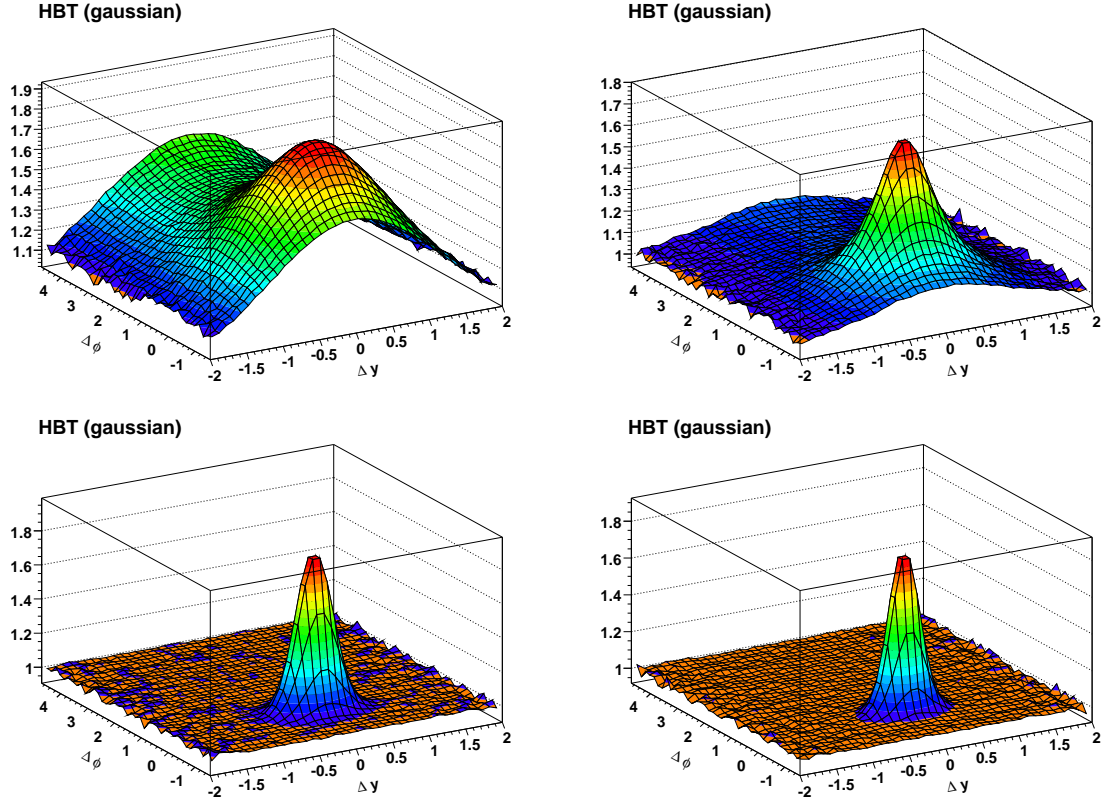
Figure J.9: Effect of HBT signal on a two-particle correlation function in the absence of any other correlations. The effect is parameterized by $C(Q_{inv}) = 1 + \lambda e^{-Q_{inv}^2 R_{inv}^2}$ where, $\lambda = 1.0$ and $R_{inv} = 0.6\ fm$. In simulations we assumed that all particles are pions and their transverse momenta are generated according to the thermal distribution, where $T = 200\ GeV$ for the left-panel plots and $T = 800\ GeV$ for the right-panel plots. The difference between both upper- and lower-panel plots is the p_T range of particles used in analysis, where $p_T = [0.0, 2.0]\ GeV/c$ and $p_T = [0.8, 2.0]\ GeV/c$, accordingly.
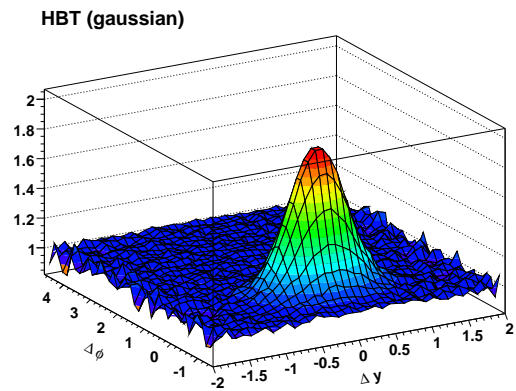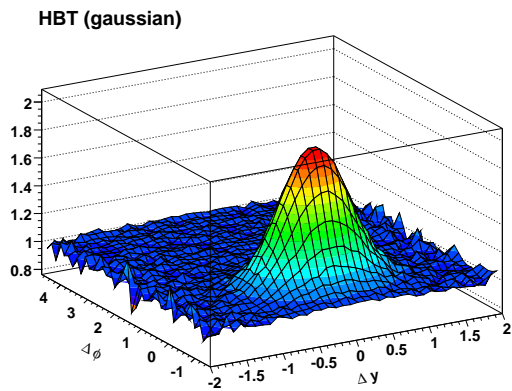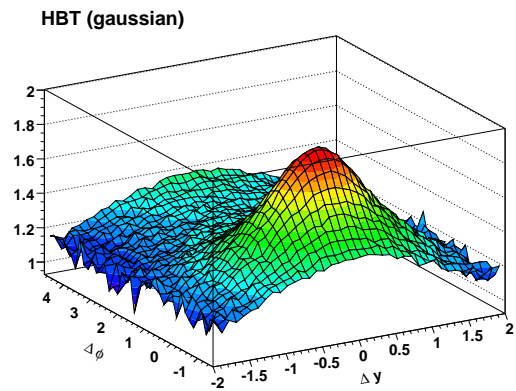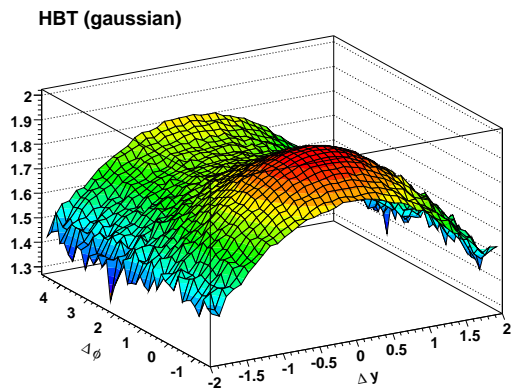
Figure J.10: Same as Fig. J.9 expect that $R_{inv} = 0.3 \ fm$.

APPENDIX K

OBTAINING PHYSICS QUANTITIES FROM FIT PARAMETERS TO NON-FEMTOSCOPIC PART OF THE CORRELATION FUNCTION

The formula for the non-femtoscopic correlations that acounts for the restricted phase-space that is available to a system with a finite number of particles that conserve energy and momentum [21] is given by

$$\Omega\left(p_1, p_2\right) = 1 - 2M_1 \cdot \overline{\left\{\vec{p}_{1,T} \cdot \vec{p}_{2,T}\right\}} - M_2 \cdot \overline{\left\{p_{1,z} \cdot p_{2,z}\right\}} \tag{K.1}$$
$$-M_3 \cdot \overline{\left\{E_1 \cdot E_2\right\}} + M_4 \cdot \overline{\left\{E_1 + E_2\right\}} - \frac{M_4^2}{M_3},$$

where

$$
\begin{aligned}
M_1 &\equiv \frac{1}{N\langle p_T^2 \rangle}, & M_2 &\equiv \frac{1}{N\langle p_z^2 \rangle} \\
M_3 &\equiv \frac{1}{N\left(\langle E^2 \rangle - \langle E \rangle^2\right)}, & M_4 &\equiv \frac{\langle E \rangle}{N\left(\langle E^2 \rangle - \langle E \rangle^2\right)}.
\end{aligned}
\tag{K.2}
$$

There are four fit parameters in Eq. K.1, $M_1 - M_4$ that are directly related to five physical quantities : N - the number of particles, $\langle p_T^2 \rangle, \langle p_z^2 \rangle$, $\langle E^2 \rangle, \langle E \rangle$) through Eq. K.2. If we assume that

$$\langle E^2 \rangle \approx \langle p_T^2 \rangle + \langle p_z^2 \rangle + m_*^2, \tag{K.3}$$

where m_* is the mass of a typical particle in the system (for a pion-dominated system, $m_* \approx m_\pi$), then we can express each physical parameters in terms of $M_1 - M_4$, e.g.

$$N \approx \frac{M_1^{-1} + M_2^{-1} - M_3^{-1}}{\left(\frac{M_4}{M_3}\right)^2 - m_*^2}. \tag{K.4}$$

Below we will present how physics parameters are changing when we change the effective mass - m_*.

K.1 $p + p$ collisions at $\sqrt{s}=200$ GeV

.

N	$\langle p_T^2 \rangle$ $[(GeV/c)^2]$	$\langle p_z^2 \rangle$ $[(GeV/c)^2]$	$\langle E^2 \rangle$ $[GeV^2]$	$\langle E \rangle$ $[GeV]$	m_* $[GeV/c]$
13.61 ± 4.36	0.171 ± 0.061	0.334 ± 0.141	0.505 ± 0.107	0.675 ± 0.080	0.0000
13.62 ± 4.37	0.171 ± 0.061	0.334 ± 0.141	0.505 ± 0.107	0.675 ± 0.080	0.0175
13.64 ± 4.38	0.170 ± 0.061	0.333 ± 0.140	0.505 ± 0.107	0.675 ± 0.080	0.0350
13.69 ± 4.40	0.170 ± 0.061	0.332 ± 0.140	0.505 ± 0.107	0.675 ± 0.080	0.0525
13.75 ± 4.44	0.169 ± 0.061	0.330 ± 0.140	0.504 ± 0.107	0.675 ± 0.080	0.0700
13.84 ± 4.48	0.168 ± 0.061	0.328 ± 0.139	0.504 ± 0.107	0.675 ± 0.080	0.0875
13.94 ± 4.53	0.167 ± 0.061	0.326 ± 0.138	0.504 ± 0.107	0.675 ± 0.080	0.1050
14.07 ± 4.60	0.165 ± 0.060	0.323 ± 0.137	0.503 ± 0.107	0.675 ± 0.080	0.1225
14.22 ± 4.67	0.164 ± 0.060	0.320 ± 0.137	0.503 ± 0.107	0.675 ± 0.080	0.1400
14.39 ± 4.76	0.162 ± 0.060	0.316 ± 0.135	0.502 ± 0.107	0.675 ± 0.080	0.1575
14.59 ± 4.87	0.159 ± 0.059	0.312 ± 0.134	0.502 ± 0.107	0.675 ± 0.080	0.1750
14.81 ± 4.99	0.157 ± 0.059	0.307 ± 0.133	0.501 ± 0.107	0.675 ± 0.080	0.1925
15.06 ± 5.12	0.154 ± 0.058	0.302 ± 0.132	0.500 ± 0.107	0.675 ± 0.080	0.2100
15.35 ± 5.28	0.152 ± 0.058	0.296 ± 0.130	0.499 ± 0.107	0.675 ± 0.080	0.2275
15.67 ± 5.46	0.148 ± 0.057	0.290 ± 0.128	0.499 ± 0.107	0.675 ± 0.080	0.2450
16.03 ± 5.67	0.145 ± 0.056	0.284 ± 0.127	0.498 ± 0.107	0.675 ± 0.080	0.2625
16.43 ± 5.90	0.142 ± 0.056	0.277 ± 0.125	0.497 ± 0.107	0.675 ± 0.080	0.2800
16.88 ± 6.18	0.138 ± 0.055	0.269 ± 0.123	0.496 ± 0.107	0.675 ± 0.080	0.2975
17.39 ± 6.49	0.134 ± 0.054	0.261 ± 0.121	0.494 ± 0.107	0.675 ± 0.080	0.3150
17.96 ± 6.85	0.130 ± 0.054	0.253 ± 0.119	0.493 ± 0.107	0.675 ± 0.080	0.3325
18.60 ± 7.27	0.125 ± 0.053	0.244 ± 0.116	0.492 ± 0.107	0.675 ± 0.080	0.3500
19.33 ± 7.76	0.120 ± 0.052	0.235 ± 0.114	0.491 ± 0.107	0.675 ± 0.080	0.3675
20.15 ± 8.34	0.115 ± 0.051	0.226 ± 0.112	0.489 ± 0.108	0.675 ± 0.080	0.3850
21.10 ± 9.04	0.110 ± 0.051	0.215 ± 0.109	0.488 ± 0.108	0.675 ± 0.080	0.4025
22.18 ± 9.87	0.105 ± 0.050	0.205 ± 0.107	0.486 ± 0.108	0.675 ± 0.080	0.4200

Table K.1: Physical quantities extracted from the EMCIC fit parameters to correlation functions from $p + p$ collisions ($M_1 = 0.43 \pm 0.07$ $(GeV/c)^{-2}$,
$M_2 = 0.22 \pm 0.06$ $(GeV/c)^{-2}$, $M_3 = 1.51 \pm 0.12$ GeV^{-2}, $M_4 = 1.02 \pm 0.09$ GeV^{-1}
from Eq. 4.15) for different values of the effective mass.

K.2 $d + Au$ collisions at $\sqrt{s_{NN}}$=200 GeV

.

N	$\langle p_T^2 \rangle$ $[(GeV/c)^2]$	$\langle p_z^2 \rangle$ $[(GeV/c)^2]$	$\langle E^2 \rangle$ $[GeV^2]$	$\langle E \rangle$ $[GeV]$	m_* $[GeV/c]$
27.69	0.164	0.361	0.525	0.687	0.0000
27.71	0.164	0.361	0.525	0.687	0.0175
27.76	0.164	0.360	0.525	0.687	0.0350
27.85	0.163	0.359	0.525	0.687	0.0525
27.98	0.162	0.357	0.525	0.687	0.0700
28.15	0.161	0.355	0.524	0.687	0.0875
28.35	0.160	0.353	0.524	0.687	0.1050
28.60	0.159	0.350	0.524	0.687	0.1225
28.89	0.157	0.346	0.523	0.687	0.1400
29.23	0.156	0.342	0.522	0.687	0.1575
29.62	0.153	0.338	0.522	0.687	0.1750
30.05	0.151	0.333	0.521	0.687	0.1925
30.55	0.149	0.327	0.520	0.687	0.2100
31.11	0.146	0.321	0.519	0.687	0.2275
31.73	0.143	0.315	0.518	0.687	0.2450
32.43	0.140	0.308	0.517	0.687	0.2625
33.22	0.137	0.301	0.516	0.687	0.2800
34.09	0.133	0.293	0.515	0.687	0.2975
35.07	0.130	0.285	0.514	0.687	0.3150
36.18	0.126	0.276	0.513	0.687	0.3325
37.41	0.121	0.267	0.511	0.687	0.3500
38.81	0.117	0.258	0.510	0.687	0.3675
40.39	0.113	0.248	0.508	0.687	0.3850
42.19	0.108	0.237	0.507	0.687	0.4025
44.25	0.103	0.226	0.505	0.687	0.4200

Table K.2: Physical quantities extracted from the EMCIC fit parameters to correlation functions from $d + Au$ [40-100]% collisions ($M_1 = 0.22$ $(GeV/c)^{-2}$, $M_2 = 0.10$ $(GeV/c)^{-2}$, $M_3 = 0.67$ GeV^{-2}, $M_4 = 0.46$ GeV^{-1} from Eq. 4.15) for different values of the effective mass.

N	$\langle p_T^2 \rangle$ [$(GeV/c)^2$]	$\langle p_z^2 \rangle$ [$(GeV/c)^2$]	$\langle E^2 \rangle$ [GeV^2]	$\langle E \rangle$ [GeV]	m_* [GeV/c]
50.50	0.180	0.330	0.510	0.676	0.0000
50.53	0.180	0.330	0.510	0.676	0.0175
50.64	0.180	0.329	0.510	0.676	0.0350
50.81	0.179	0.328	0.510	0.676	0.0525
51.05	0.178	0.326	0.509	0.676	0.0700
51.36	0.177	0.325	0.509	0.676	0.0875
51.75	0.176	0.322	0.509	0.676	0.1050
52.22	0.174	0.319	0.508	0.676	0.1225
52.76	0.172	0.316	0.508	0.676	0.1400
53.40	0.170	0.312	0.507	0.676	0.1575
54.13	0.168	0.308	0.506	0.676	0.1750
54.96	0.165	0.303	0.506	0.676	0.1925
55.90	0.163	0.298	0.505	0.676	0.2100
56.96	0.160	0.293	0.504	0.676	0.2275
58.14	0.156	0.287	0.503	0.676	0.2450
59.48	0.153	0.280	0.502	0.676	0.2625
60.97	0.149	0.273	0.501	0.676	0.2800
62.64	0.145	0.266	0.500	0.676	0.2975
64.52	0.141	0.258	0.498	0.676	0.3150
66.64	0.136	0.250	0.497	0.676	0.3325
69.02	0.132	0.241	0.496	0.676	0.3500
71.71	0.127	0.232	0.494	0.676	0.3675
74.78	0.122	0.223	0.493	0.676	0.3850
78.28	0.116	0.213	0.491	0.676	0.4025
82.30	0.110	0.203	0.489	0.676	0.4200

Table K.3: Physical quantities extracted from the EMCIC fit parameters to correlation functions from $d + Au$ [20-40]% collisions ($M_1 = 0.11$ $(GeV/c)^{-2}$, $M_2 = 0.06$ $(GeV/c)^{-2}$, $M_3 = 0.37$ GeV^{-2}, $M_4 = 0.25$ GeV^{-1} from Eq. 4.15) for different values of the effective mass.

N	$\langle p_T^2 \rangle$ $[(GeV/c)^2]$	$\langle p_z^2 \rangle$ $[(GeV/c)^2]$	$\langle E^2 \rangle$ $[GeV^2]$	$\langle E \rangle$ $[GeV]$	m_* $[GeV/c]$
73.24	0.190	0.369	0.559	0.708	0.0000
73.29	0.190	0.369	0.559	0.708	0.0175
73.42	0.189	0.368	0.558	0.708	0.0350
73.65	0.189	0.367	0.558	0.708	0.0525
73.97	0.188	0.365	0.558	0.708	0.0700
74.38	0.187	0.363	0.558	0.708	0.0875
74.89	0.185	0.361	0.557	0.708	0.1050
75.50	0.184	0.358	0.557	0.708	0.1225
76.22	0.182	0.355	0.556	0.708	0.1400
77.05	0.180	0.351	0.556	0.708	0.1575
78.01	0.178	0.346	0.555	0.708	0.1750
79.09	0.176	0.342	0.554	0.708	0.1925
80.30	0.173	0.337	0.554	0.708	0.2100
81.67	0.170	0.331	0.553	0.708	0.2275
83.20	0.167	0.325	0.552	0.708	0.2450
84.90	0.164	0.318	0.551	0.708	0.2625
86.81	0.160	0.311	0.550	0.708	0.2800
88.93	0.156	0.304	0.549	0.708	0.2975
91.30	0.152	0.296	0.547	0.708	0.3150
93.94	0.148	0.288	0.546	0.708	0.3325
96.90	0.143	0.279	0.545	0.708	0.3500
100.22	0.139	0.270	0.543	0.708	0.3675
103.96	0.134	0.260	0.542	0.708	0.3850
108.17	0.128	0.250	0.540	0.708	0.4025
112.96	0.123	0.239	0.539	0.708	0.4200

Table K.4: Physical quantities extracted from the EMCIC fit parameters to correlation functions from $d + Au$ [0-20]% collisions ($M_1 = 0.072$ $(GeV/c)^{-2}$, $M_2 = 0.037$ $(GeV/c)^{-2}$, $M_3 = 0.24$ GeV^{-2}, $M_4 = 0.17$ GeV^{-1} from Eq. 4.15) for different values of the effective mass.

APPENDIX L

EXPERIMENTAL CORRELATION FUNCTIONS FROM $p + p$ AND $d + Au$ COLLISIONS AT $\sqrt{s_{NN}}$=200 GEV IN THE PAIR REST FRAME
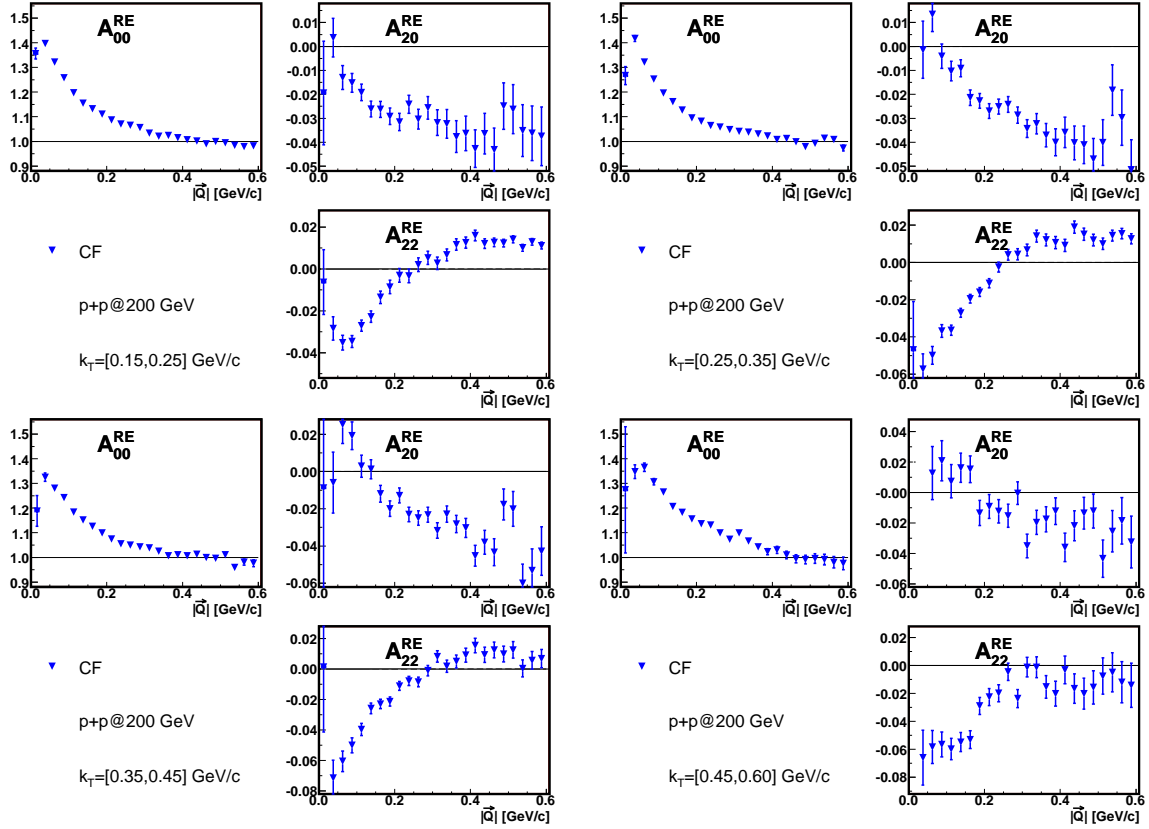
Figure L.1: The first three non-vanished moments of the spherical harmonic decomposition of the correlation functions from $p + p$ collisions at $\sqrt{s}$=200 GeV measured in the pair-rest frame.
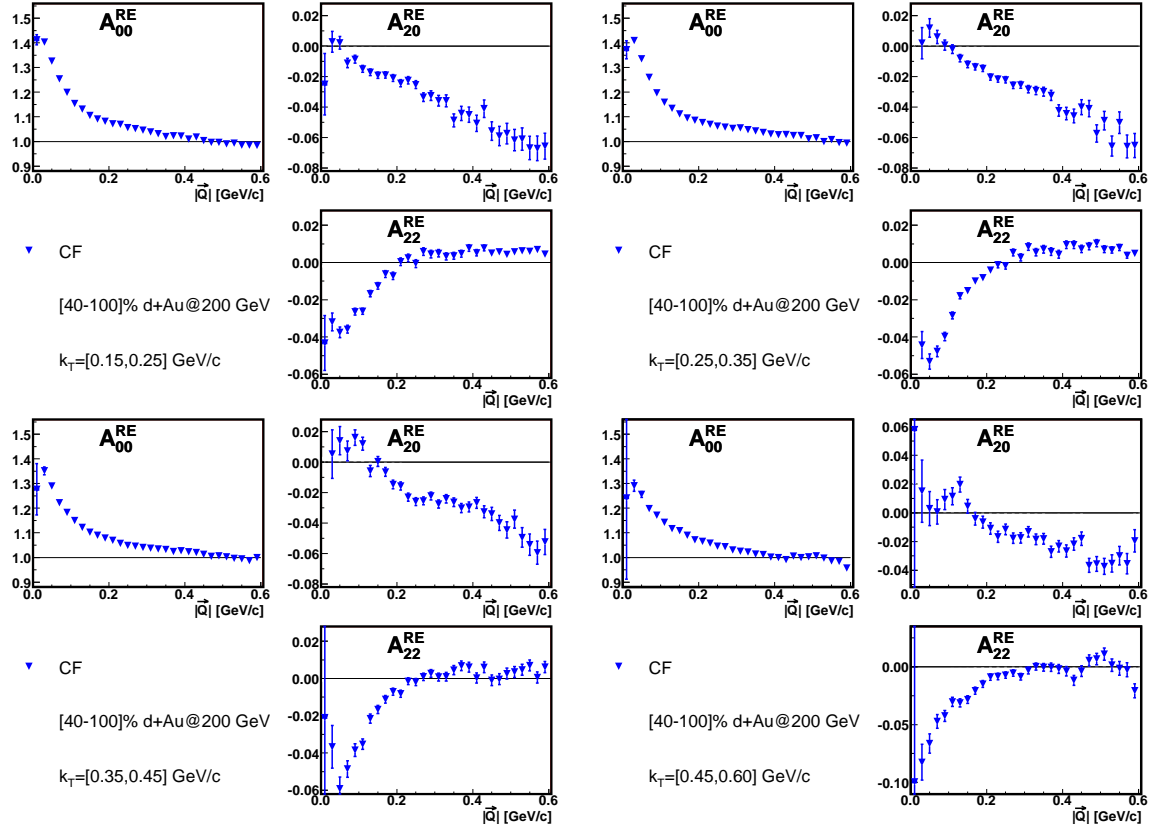
Figure L.2: The first three non-vanished moments of the spherical harmonic decomposition of the correlation functions from peripheral $d + Au$ collisions ([40-100]%) at $\sqrt{s_{NN}}$=200 GeV measured in the pair-rest frame.
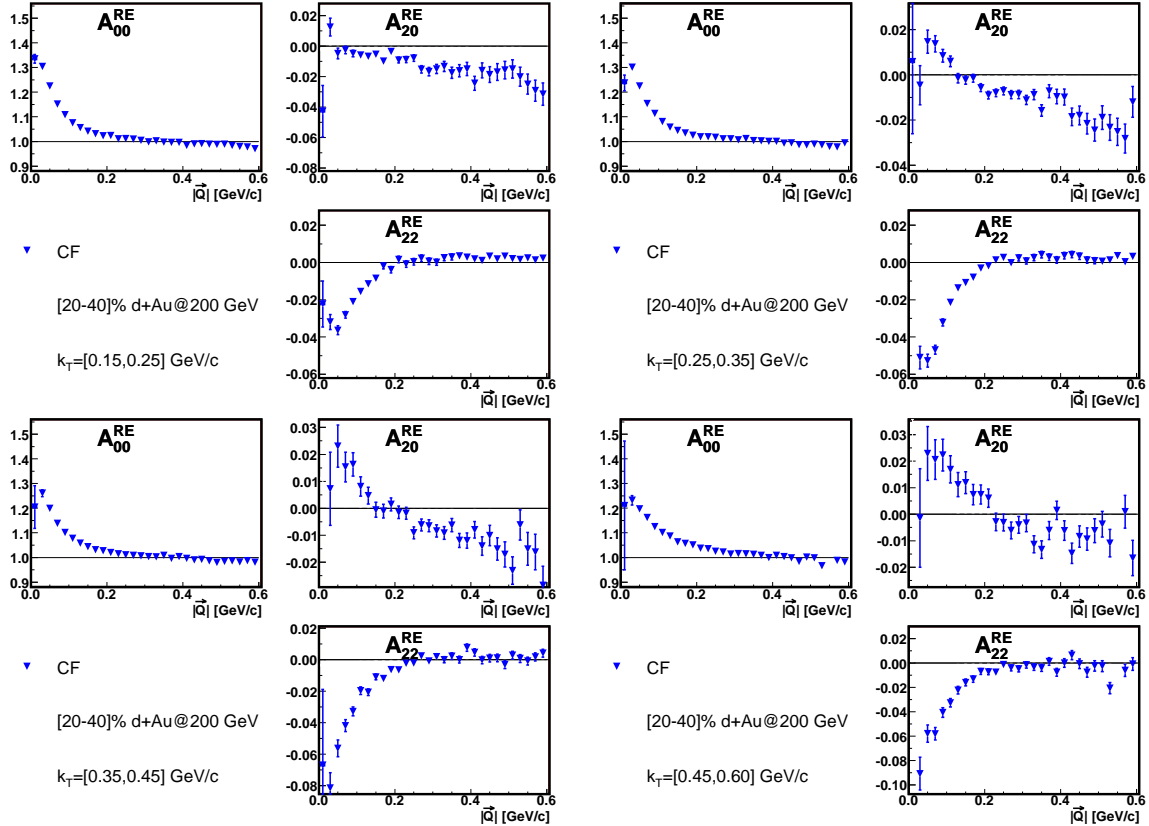
Figure L.3: The first three non-vanished moments of the spherical harmonic decomposition of the correlation functions from mid-central $d + Au$ collisions ([20-40]%) at $\sqrt{s_{NN}}$=200 GeV measured in the pair-rest frame.
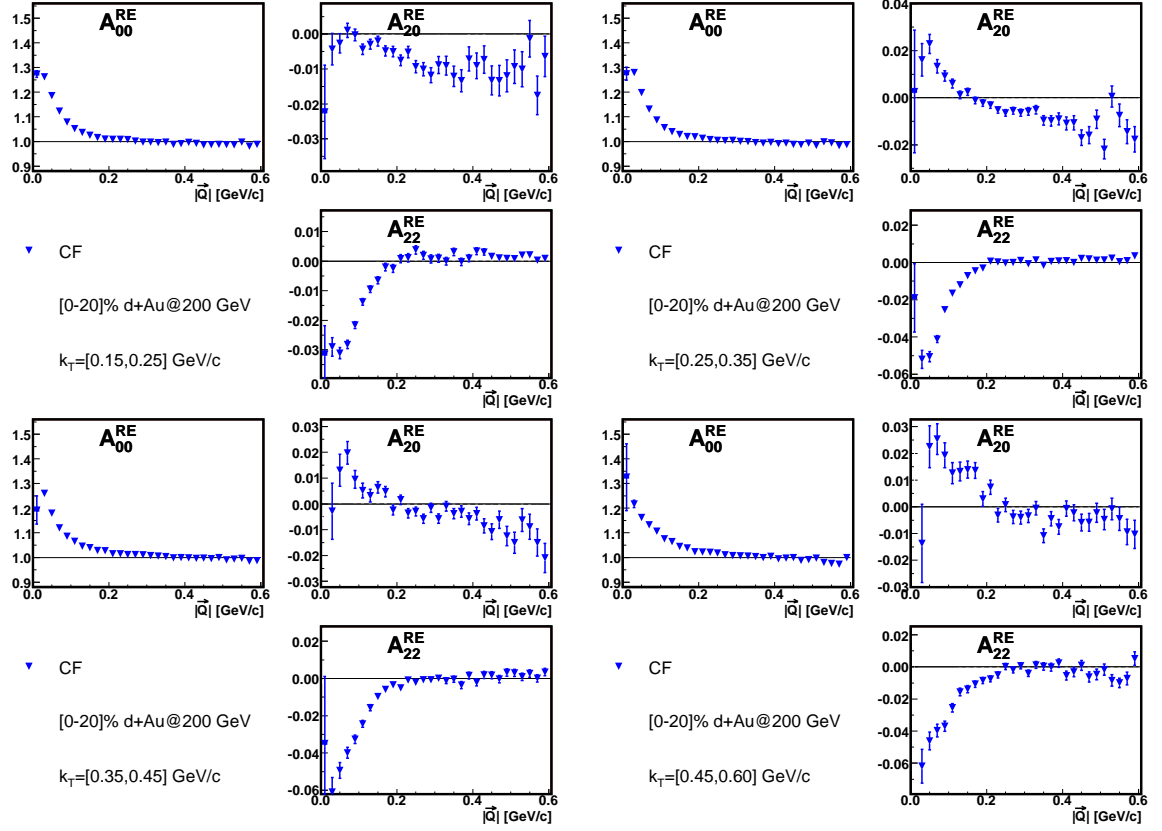
Figure L.4: The first three non-vanished moments of the spherical harmonic decomposition of the correlation functions from central $d + Au$ collisions ([0-20]%) at $\sqrt{s_{NN}}$=200 GeV measured in the pair-rest frame.

APPENDIX M

WHY CANNOT WE USE NON-IDENTICAL PION PAIRS AS A REFERENCE TO THE CORRELATION FUNCTION FOR IDENTICAL PION PAIRS?

In Section 4.3.2 we discussed the possibility of using non-identical pion pairs to create the reference distribution for identical pions. The motivation of this procedure is that all possible non-femtoscopic correlations should cancel out as well as the Coulomb effect and only the effect of quantum statistics should be left. However, we also mentioned that there is one major obstacle in this approach that is an effect of resonance production on non-identical pion correlations. Pions coming from resonance decays are not a big problem when studying identical pion correlations since they do not change the strength of the correlation effect for identical pions only the chaoticity parameter (λ in Eqs.4.6). However, the situation is more complicated when studying non-identical pion pairs since they can influence the shape of the correlation functions in a non-trivial way [21]. The effect and the location of each resonance at $|\vec{q}|$ depends on the mass of the resonance, its width and the decay channel. The procedure of removing resonance peaks from the range of Q in a fit is not always simple and introduces an additional systematic error to the extracted results.
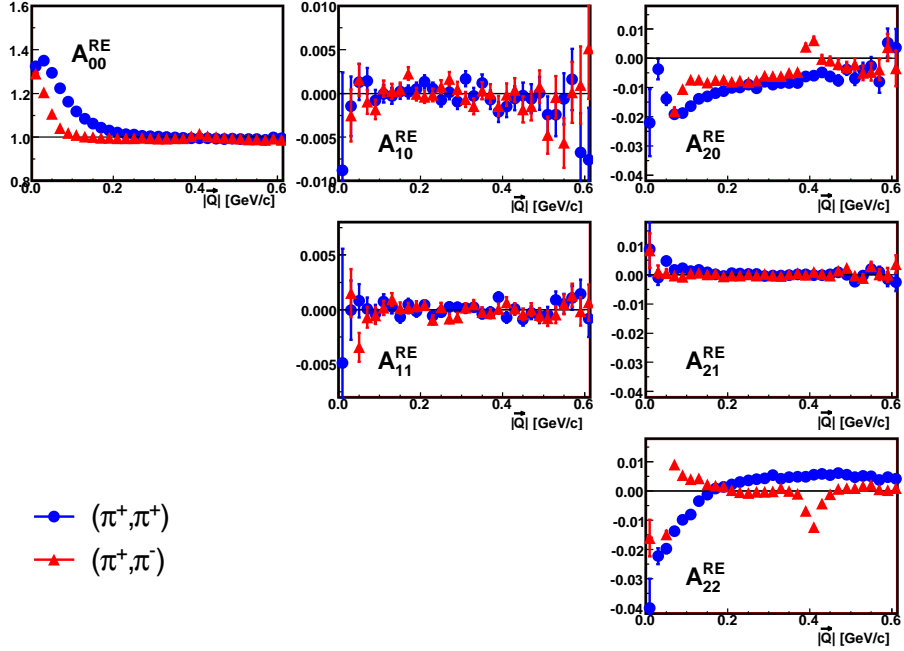
Figure M.1: Correlation functions from minimum bias $d + Au$ collisions at $\sqrt{s_{NN}}$=200 GeV for $k_T = [0.15, 0.60]$ GeV/c for identical and non-identical pions.

Figure M.1 shows the correlation functions for both identical and non-identical pion pars from min-bias $d + Au$ collisions at $\sqrt{s_{NN}}$=200 GeV. The non-femtoscopic correlations mostly affect the shape of the higher moments of the correlation functions ($A_{2,0}$ and $A_{2,2}$). Clearly, even though non-femtoscopic correlations are seen in both cases their magnitude and shape are not the same and the reason is that the correlation function from (π^+, π^-) correlations has additional structure due to resonance decays. Therefore, non-identical pion pairs should not be used as a reference distribution to identical pion correlations. This issue was also discussed in Sec. 6.6.1.

BIBLIOGRAPHY

[1] **STAR** Collaboration, J. Adams *et al.*, "Experimental and theoretical challenges in the search for the quark gluon plasma: The star collaboration's critical assessment of the evidence from rhic collisions," *Nucl. Phys.* **A757** (2005) 102–183, `nucl-ex/0501009`.

[2] **PHENIX** Collaboration, K. Adcox *et al.*, "Formation of dense partonic matter in relativistic nucleus nucleus collisions at rhic: Experimental evaluation by the phenix collaboration," *Nucl. Phys.* **A757** (2005) 184–283, `nucl-ex/0410003`.

[3] B. B. Back *et al.*, "The phobos perspective on discoveries at rhic," *Nucl. Phys.* **A757** (2005) 28–101, `nucl-ex/0410022`.

[4] **BRAHMS** Collaboration, I. Arsene *et al.*, "Quark gluon plasma and color glass condensate at rhic? the perspective from the brahms experiment," *Nucl. Phys.* **A757** (2005) 1–27, `nucl-ex/0410020`.

[5] J.-Y. Ollitrault, "Anisotropy as a signature of transverse collective flow," *Phys. Rev.* **D46** (1992) 229–245.

[6] P. Huovinen, P. F. Kolb, U. W. Heinz, P. V. Ruuskanen, and S. A. Voloshin, "Radial and elliptic flow at RHIC: further predictions," *Phys. Lett.* **B503** (2001) 58–64, `hep-ph/0101136`.

[7] F. Retiere and M. Lisa, "Observable implications of geometrical and dynamical aspects of freeze-out in heavy ion collisions," *Phys. Rev.* **C70** (2004) 044907, `nucl-th/0312024`.

[8] S. A. Voloshin, A. M. Poskanzer, and R. Snellings, "Collective phenomena in non-central nuclear collisions," `0809.2949`.

[9] S. Pratt, "Pion interferometry for exploding sources," *Phys. Rev. Lett.* **53** (1984) 1219–1221.

[10] R. Lednicky and V. L. Lyuboshits, "Final state interaction effect on correlations in narrow particles pairs,". In *Nantes 1990, Proceedings, Particle correlations and interferometry in nuclear collisions* 42-54.

244

[11] R. Lednicky, "Progress in correlation femtoscopy," `nucl-th/0212089`.

[12] S. V. Akkelin and Y. M. Sinyukov, "The HBT interferometry of expanding sources," *Phys. Lett.* **B356** (1995) 525–530.

[13] **STAR** Collaboration, J. Adams *et al.*, "Azimuthal anisotropy and correlations at large transverse momenta in p + p and Au + Au collisions at $\sqrt{s_{NN}}$= 200-GeV," *Phys. Rev. Lett.* **93** (2004) 252301, `nucl-ex/0407007`.

[14] **STAR** Collaboration, C. Adler *et al.*, "Disappearance of back-to-back high p(t) hadron correlations in central au + au collisions at $\sqrt{s_{NN}}$= 200-gev," *Phys. Rev. Lett.* **90** (2003) 082302, `nucl-ex/0210033`.

[15] **PHENIX** Collaboration, S. S. Adler *et al.*, "Suppressed pi0 production at large transverse momentum in central au + au collisions at $\sqrt{s_{NN}}$= 200-gev," *Phys. Rev. Lett.* **91** (2003) 072301, `nucl-ex/0304022`.

[16] **STAR** Collaboration, J. Adams *et al.*, "Transverse momentum and collision energy dependence of high p(t) hadron suppression in au + au collisions at ultrarelativistic energies," *Phys. Rev. Lett.* **91** (2003) 172302, `nucl-ex/0305015`.

[17] **STAR** Collaboration, J. Adams *et al.*, "Evidence from d + Au measurements for final-state suppression of high p(T) hadrons in Au + Au collisions at RHIC," *Phys. Rev. Lett.* **91** (2003) 072304, `nucl-ex/0306024`.

[18] W. Kittel, "Bose-Einstein correlations in Z fragmentation and other reactions," *Acta Phys. Polon.* **B32** (2001) 3927–3972, `hep-ph/0110088`.

[19] G. Alexander, "Bose-Einstein and Fermi-Dirac interferometry in particle physics," *Rept. Prog. Phys.* **66** (2003) 481–522, `hep-ph/0302130`.

[20] Z. Chajecki, "Femtoscopy in hadron and lepton collisions: World systematics," *Acta Phys. Polon.* **B40** (2009) 1119–1136, `0901.4078`.

[21] Z. Chajecki and M. Lisa, "Global Conservation Laws and Femtoscopy of Small Systems," *Phys. Rev.* **C78** (2008) 064903, `0803.0022`.

[22] Z. Chajecki and M. Lisa, "Conservation laws and the multiplicity evolution of spectra at energies available at the BNL Relativistic Heavy Ion Collider," *Phys. Rev.* **C79** (2009) 034908, `0807.3569`.

[23] R. Hanbury Brown and R. Q. Twiss, "A New type of interferometer for use in radio astronomy," *Phil. Mag.* **45** (1954) 663–682.

[24] G. Goldhaber, S. Goldhaber, W.-Y. Lee, and A. Pais, "Influence of Bose-Einstein statistics on the antiproton proton annihilation process," *Phys. Rev.* **120** (1960) 300–312.

[25] G. I. Kopylov and M. I. Podgoretsky, "Correlations of identical particles emitted by highly excited nuclei," *Sov. J. Nucl. Phys.* **15** (1972) 219–223.

[26] M. A. Lisa, S. Pratt, R. Soltz, and U. Wiedemann, "Femtoscopy in relativistic heavy ion collisions," *Ann. Rev. Nucl. Part. Sci.* **55** (2005) 357–402, `nucl-ex/0505014`.

[27] S. Pratt, "The Long Slow Death of the HBT Puzzle," *Acta Phys. Polon.* **B40** (2009) 1249–1256, `0812.4714`.

[28] S. Pratt, "Resolving the HBT Puzzle in Relativistic Heavy Ion Collision," `0811.3363`.

[29] U. W. Heinz and B. V. Jacak, "Two-particle correlations in relativistic heavy-ion collisions," *Ann. Rev. Nucl. Part. Sci.* **49** (1999) 529–579, `nucl-th/9902020`.

[30] U. A. Wiedemann and U. W. Heinz, "Particle interferometry for relativistic heavy-ion collisions," *Phys. Rept.* **319** (1999) 145–230, `nucl-th/9901094`.

[31] T. Csorgo, "Particle interferometry from 40-MeV to 40-TeV," *Heavy Ion Phys.* **15** (2002) 1–80, `hep-ph/0001233`.

[32] M. A. Lisa and S. Pratt, "Femtoscopically Probing the Freeze-out Configuration in Heavy Ion Collisions," `0811.1352`.

[33] Z. Chajecki, "Pion interferometry from p + p to Au + Au in STAR," *AIP Conf. Proc.* **828** (2006) 566–571, `nucl-ex/0511035`.

[34] **PHENIX** Collaboration, M. Heffner, "Two-particle interferometry of 200-GeV Au + Au collisions at PHENIX," *J. Phys.* **G30** (2004) S1043–S1047.

[35] **STAR** Collaboration, S. Bekele, "Charged and neutral kaon correlations in Au - Au collisions at s(NN) = 200-GeV using the solenoidal tracker at RHIC (STAR)," *J. Phys.* **G30** (2004) S229–S234.

[36] H. P. Gos, "Baryon - baryon correlations in Au + Au collisions at $\sqrt{s_{NN}}=$ 62-GeV and $\sqrt{s_{NN}}=$ 200-GeV, measured in the STAR experiment at RHIC," `nucl-ex/0610030`.

[37] P. Chaloupka, "Non-identical particle correlations at 62-GeV and 200-GeV at STAR," *Nucl. Phys.* **A774** (2006) 603, `nucl-ex/0510064`.

[38] **STAR** Collaboration, J. Adams *et al.*, "Pion kaon correlations in Au + Au collisions at $\sqrt{s_{NN}}=$ 130-GeV," *Phys. Rev. Lett.* **91** (2003) 262302, `nucl-ex/0307025`.

[39] S. A. Voloshin and W. E. Cleland, "Hbt Analysis of Anisotropic Transverse Flow," *Phys. Rev.* **C53** (1996) 896–900, `nucl-th/9509025`.

[40] **E895** Collaboration, M. A. Lisa *et al.*, "Azimuthal dependence of pion interferometry at the AGS," *Phys. Lett.* **B496** (2000) 1–8, `nucl-ex/0007022`.

[41] U. W. Heinz, A. Hummel, M. A. Lisa, and U. A. Wiedemann, "Symmetry constraints for the emission angle dependence of HBT radii," *Phys. Rev.* **C66** (2002) 044903, `nucl-th/0207003`.

[42] **STAR** Collaboration, J. Adams *et al.*, "Azimuthally sensitive HBT in Au + Au collisions at $\sqrt{s_{NN}}$= 200-GeV," *Phys. Rev. Lett.* **93** (2004) 012301, `nucl-ex/0312009`.

[43] P. F. Kolb and U. W. Heinz, "Hydrodynamic description of ultrarelativistic heavy-ion collisions," `nucl-th/0305084`.

[44] U. W. Heinz and P. F. Kolb, "Emission angle dependent pion interferometry at RHIC and beyond," *Phys. Lett.* **B542** (2002) 216–222, `hep-ph/0206278`.

[45] P. F. Kolb and U. W. Heinz, "Emission angle dependent HBT at RHIC and beyond," *Nucl. Phys.* **A715** (2003) 653–656, `nucl-th/0208047`.

[46] G. I. Kopylov, "Like particle correlations as a tool to study the multiple production mechanism," *Phys. Lett.* **B50** (1974) 472–474.

[47] G. Bertsch, M. Gong, and M. Tohyama, "Pion Interferometry in Ultrarelativistic Heavy Ion Collisions," *Phys. Rev.* **C37** (1988) 1896–1900.

[48] P. Danielewicz and S. Pratt, "Analysis of Low-Momentum Correlations with Cartesian Harmonics," *Phys. Lett.* **B618** (2005) 60–67, `nucl-th/0501003`.

[49] P. Danielewicz and S. Pratt, "Analyzing Correlation Functions with Tesseral and Cartesian Spherical Harmonics," *Phys. Rev.* **C75** (2007) 034907, `nucl-th/0612076`.

[50] P. Avery *et al.*, "Bose-Einstein correlations in e+ e- annihilations in the Upsilon region," *Phys. Rev.* **D32** (1985) 2294–2302.

[51] **EHS/NA22** Collaboration, N. M. Agababyan *et al.*, "Two- and three-dimensional analysis of Bose-Einstein correlations in pi+/K+ p interactions at 250-GeV/c," *Z. Phys.* **C71** (1996) 405–414.

[52] **OPAL** Collaboration, G. Abbiendi *et al.*, "Bose-Einstein study of position-momentum correlations of charged pions in hadronic Z0 decays," *Eur. Phys. J.* **C52** (2007) 787–803, `0708.1122`.

247

[53] **NA23** Collaboration, J. L. Bailly *et al.*, "Bose-Einstein Correlations for pions produced in p p COLLISIONS AT 360-GeV/c," *Z. Phys.* **C43** (1989) 341.

[54] **BNL-E766** Collaboration, J. Uribe *et al.*, "Pion pion correlations at low relative momentum produced in *pp* collisions at 27.5-GeV/c," *Phys. Rev.* **D49** (1994) 4373–4393.

[55] D. H. Boal, C. K. Gelbke, and B. K. Jennings, "Intensity interferometry in subatomic physics," *Rev. Mod. Phys.* **62** (1990) 553–602.

[56] T. Alexopoulos *et al.*, "A Study of source size in p anti-p collisions at $\sqrt{s}=$ 1.8-TeV using pion interferometry," *Phys. Rev.* **D48** (1993) 1931–1942.

[57] M. G. Bowler, "Coulomb corrections to Bose-Einstein correlations have been greatly exaggerated," *Phys. Lett.* **B270** (1991) 69–74.

[58] Y. Sinyukov, R. Lednicky, S. V. Akkelin, J. Pluta, and B. Erazmus, "Coulomb corrections for interferometry analysis of expanding hadron systems," *Phys. Lett.* **B432** (1998) 248–257.

[59] **ALEPH** Collaboration, D. Buskulic *et al.*, "Production of K0 and Lambda in hadronic Z decays," *Z. Phys.* **C64** (1994) 361–374.

[60] **L3** Collaboration, P. Achard *et al.*, "Bose-Einstein correlations of neutral and charged pions in hadronic *Z* decays," *Phys. Lett.* **B524** (2002) 55–64, hep-ex/0109036.

[61] **LEBC-EHS** Collaboration, M. Aguilar-Benitez *et al.*, "Bose-Einstein correlations in p p collisions at 400- GeV/c," *Z. Phys.* **C54** (1992) 21–32.

[62] **DELPHI** Collaboration, P. Abreu *et al.*, "Invariant mass dependence of particle correlations in hadronic final states from the decay of the Z0," *Z. Phys.* **C63** (1994) 17–28.

[63] **DELPHI** Collaboration, P. Abreu *et al.*, "Bose-Einstein correlations in the hadronic decays of the Z0," *Phys. Lett.* **B286** (1992) 201–210.

[64] **OPAL** Collaboration, G. Abbiendi *et al.*, "Transverse and longitudinal Bose-Einstein correlations in hadronic Z0 decays," *Eur. Phys. J.* **C16** (2000) 423–433, hep-ex/0002062.

[65] A. V. Stavinskiy *et al.*, "Some new aspects of femtoscopy at high energy," *Nukleonika* **49** (2004) S23–S25.

[66] S. Pratt, "Pion Interferometry of Quark-Gluon Plasma," *Phys. Rev.* **D33** (1986) 1314–1327.

[67] **STAR** Collaboration, J. Adams *et al.*, "Pion interferometry in Au + Au collisions at $\sqrt{s_{NN}}$= 200-GeV," *Phys. Rev.* **C71** (2005) 044906, `nucl-ex/0411036`.

[68] A. Kisiel and D. A. Brown, "Efficient and robust calculation of femtoscopic correlation functions in spherical harmonics directly from the raw pairs measured in heavy-ion collisions," `0901.3527`.

[69] F. James, "Monte-Carlo phase space,". CERN-68-15.

[70] H. Sorge, H. Stoecker, and W. Greiner, "RELATIVISTIC QUANTUM MOLECULAR DYNAMICS APPROACH TO NUCLEAR COLLISIONS AT ULTRARELATIVISTIC ENERGIES," *Nucl. Phys.* **A498** (1989) 567c–576c.

[71] M. Bleicher *et al.*, "Relativistic hadron hadron collisions in the ultra-relativistic quantum molecular dynamics model," *J. Phys.* **G25** (1999) 1859–1896, `hep-ph/9909407`.

[72] T. Sjostrand *et al.*, "High-energy-physics event generation with PYTHIA 6.1," *Comput. Phys. Commun.* **135** (2001) 238–259, `hep-ph/0010017`.

[73] R. Hagedorn, "Relativistic Kinematics,". *Relativistic Kinematics*, N.Y. Benjamin, 1963, 166pp.

[74] E. Fermi, "High-energy nuclear events," *Prog. Theor. Phys.* **5** (1950) 570–583.

[75] P. Danielewicz *et al.*, "Collective motion in nucleus-nucleus collisions at 800-mev/nucleon," *Phys. Rev.* **C38** (1988) 120–134.

[76] N. Borghini, P. M. Dinh, and J.-Y. Ollitrault, "Are flow measurements at sps reliable?," *Phys. Rev.* **C62** (2000) 034902, `nucl-th/0004026`.

[77] N. Borghini, "Multiparticle correlations from momentum conservation," *Eur. Phys. J.* **C30** (2003) 381–385, `hep-ph/0302139`.

[78] N. Borghini, "Momentum conservation and correlation analyses in heavy- ion collisions at ultrarelativistic energies," *Phys. Rev.* **C75** (2007) 021904, `nucl-th/0612093`.

[79] A. M. Poskanzer and S. A. Voloshin, "Methods for analyzing anisotropic flow in relativistic nuclear collisions," *Phys. Rev.* **C58** (1998) 1671–1678, `nucl-ex/9805001`.

[80] **STAR** Collaboration, J. Adams *et al.*, "Identified particle distributions in p p and au + au collisions at $\sqrt{s}$= 200-gev," *Phys. Rev. Lett.* **92** (2004) 112301, `nucl-ex/0310004`.

[81] R. Hagedorn, "A new derivation of the statistical theory of particle production with numerical results for p-p collisions at 25 gev," *Nuovo Cimento* **15** (1960) 434.

[82] **Antiproton Collaboration Experiment** Collaboration, W. Barkas *et al.*, "Antiproton-nucleon annihilation process," *Phys. Rev.* **105** (1957) 1037.

[83] F. Cerulus, "Consequences of a strong pi-pi interaction in the statistical theory of p-anti-p annihilation," *Nuovo Cimento* **14** (1959) 827.

[84] O. Chamberlain, G. Golbhaber, L. Janeau, T. Kalogeropoulos, E. Segrè, and R. Silberberg, "Antiproton-nucleon annihilation process. ii," *Phys. Rev.* **113** (1959) 1615.

[85] A. Tounsi and K. Redlich, "Strangeness enhancement and canonical suppression," `hep-ph/0111159`.

[86] O. Fochler *et al.*, "Canonical suppression in microscopic transport models," *Phys. Rev.* **C74** (2006) 034902, `nucl-th/0601062`.

[87] P. Huovinen and P. V. Ruuskanen, "Hydrodynamic models for heavy ion collisions," *Ann. Rev. Nucl. Part. Sci.* **56** (2006) 163–206, `nucl-th/0605008`.

[88] E. Schnedermann, J. Sollfrank, and U. W. Heinz, "Thermal phenomenology of hadrons from 200-a/gev s+s collisions," *Phys. Rev.* **C48** (1993) 2462–2475, `nucl-th/9307020`.

[89] **STAR** Collaboration, J. Adams *et al.*, "The multiplicity dependence of inclusive p(t) spectra from p p collisions at $\sqrt{s}$= 200-GeV," *Phys. Rev.* **D74** (2006) 032006, `nucl-ex/0606028`.

[90] **PHENIX** Collaboration, K. Adcox *et al.*, "Suppression of hadrons with large transverse momentum in central Au + Au collisions at $\sqrt{s}$(N N) = 130-GeV," *Phys. Rev. Lett.* **88** (2002) 022301, `nucl-ex/0109003`.

[91] T. Alexopoulos *et al.*, "MULTIPLICITY DEPENDENCE OF THE TRANSVERSE MOMENTUM SPECTRUM FOR CENTRALLY PRODUCED HADRONS IN ANTI-PROTON - PROTON COLLISIONS AT $\sqrt{s}$= 1.8-TeV," *Phys. Rev. Lett.* **60** (1988) 1622.

[92] **Ames-Bologna-CERN-Dortmund-Heidelberg-Warsaw** Collaboration, A. Breakstone *et al.*, "Multiplicity dependence of the average transverse momentum and of the particle source size in p+p interactions at $\sqrt{s}$= 62-GeV, 44-GeV AND 31-GeV," *Z. Phys.* **C33** (1987) 333.

[93] **UA1** Collaboration, G. Arnison *et al.*, "Transverse Momentum Spectra for Charged Particles at the CERN Proton anti-Proton Collider," *Phys. Lett.* **B118** (1982) 167.

[94] D. Brown and P. Danielewicz, "Imaging of sources in heavy-ion reactions," *Phys. Lett.* **B398** (1997) 252–258, `nucl-th/9701010`.

[95] **STAR** Collaboration, Z. Chajecki, "Identical particle correlations in STAR," *Nucl. Phys.* **A774** (2006) 599–602, `nucl-ex/0510014`.

[96] **ZEUS** Collaboration, S. Chekanov *et al.*, "Bose-Einstein correlations in one and two dimensions in deep inelastic scattering," *Phys. Lett.* **B583** (2004) 231–246, `hep-ex/0311030`.

[97] R. Lednicky, V. L. Lyuboshits, B. Erazmus, and D. Nouais, "How to measure which sort of particles was emitted earlier and which later," *Phys. Lett.* **B373** (1996) 30–34.

[98] **PHOBOS** Collaboration, B. B. Back *et al.*, "The PHOBOS detector at RHIC," *Nucl. Instrum. Meth.* **A499** (2003) 603–623.

[99] **PHENIX** Collaboration, K. Adcox *et al.*, "PHENIX detector overview," *Nucl. Instrum. Meth.* **A499** (2003) 469–479.

[100] **STAR** Collaboration, K. H. Ackermann *et al.*, "STAR detector overview," *Nucl. Instrum. Meth.* **A499** (2003) 624–632.

[101] **BRAHMS** Collaboration, M. Adamczyk *et al.*, "The BRAHMS experiment at RHIC," *Nucl. Instrum. Meth.* **A499** (2003) 437–468.

[102] I. Alekseev *et al.*, "Polarized proton collider at RHIC," *Nucl. Instrum. Meth.* **A499** (2003) 392–414.

[103] M. Harrison, T. Ludlam, and S. Ozaki, "RHIC project overview," *Nucl. Instrum. Meth.* **A499** (2003) 235–244.

[104] E. V. Shuryak, "Quark-Gluon Plasma and Hadronic Production of Leptons, Photons and Psions," *Phys. Lett.* **B78** (1978) 150.

[105] M. Anderson *et al.*, "The STAR time projection chamber: A unique tool for studying high multiplicity events at RHIC," *Nucl. Instrum. Meth.* **A499** (2003) 659–678, `nucl-ex/0301015`.

[106] K. H. Ackermann *et al.*, "The forward time projection chamber (FTPC) in STAR," *Nucl. Instrum. Meth.* **A499** (2003) 713–719, `nucl-ex/0211014`.

[107] **STAR** Collaboration, M. Beddo *et al.*, "The STAR barrel electromagnetic calorimeter," *Nucl. Instrum. Meth.* **A499** (2003) 725–739.

[108] **STAR** Collaboration, C. E. Allgower *et al.*, "The STAR endcap electromagnetic calorimeter," *Nucl. Instrum. Meth.* **A499** (2003) 740–750.

[109] **CERES** Collaboration, D. Adamova *et al.*, "Beam energy and centrality dependence of two-pion Bose- Einstein correlations at SPS energies," *Nucl. Phys.* **A714** (2003) 124–144, `nucl-ex/0207005`.

[110] **NA49** Collaboration, C. Alt *et al.*, "Bose-Einstein correlations of pion pairs in central Pb+Pb collisions at CERN SPS energies," *Phys. Rev.* **C77** (2008) 064908, `0709.4507`.

[111] T. Csorgo and B. Lorstad, "Bose-Einstein Correlations for Three-Dimensionally Expanding, Cylindrically Symmetric, Finite Systems," *Phys. Rev.* **C54** (1996) 1390–1403, `hep-ph/9509213`.

[112] **STAR** Collaboration, D. Cebra, "Charged hadron results from Au+Au at 19.6 GeV," `0903.4702`.

[113] A. N. Makhlin and Y. M. Sinyukov, "The hydrodynamics of hadron matter under a pion interferometric microscope," *Z. Phys.* **C39** (1988) 69.

[114] **STAR** Collaboration, B. I. Abelev *et al.*, "Pion Interferometry in Au+Au and Cu+Cu Collisions at RHIC," `0903.1296`.

[115] **PHENIX** Collaboration, S. S. Adler *et al.*, "Bose-Einstein correlations of charged pion pairs in Au + Au collisions at $\sqrt{s_{NN}}$= 200-GeV," *Phys. Rev. Lett.* **93** (2004) 152302, `nucl-ex/0401003`.

[116] T. Csorgo and L. P. Csernai, "Quark - gluon plasma freezeout from a supercooled state?," *Phys. Lett.* **B333** (1994) 494–499, `hep-ph/9406365`.

[117] R. Stock, "Pion interferometry in high-energy hadron and nuclear collisions: Radial expansion and freezeout," *Annalen Phys.* **48** (1991) 195–206.

[118] M. Lisa, "Femtoscopy in heavy ion collisions: Wherefore, whence, and whither?," *AIP Conf. Proc.* **828** (2006) 226–237, `nucl-ex/0512008`.

[119] **CERES** Collaboration, D. Adamova *et al.*, "Universal pion freeze-out in heavy-ion collisions," *Phys. Rev. Lett.* **90** (2003) 022301, `nucl-ex/0207008`.

[120] I. Sick, "Nucleon form factors at low q," *Eur. Phys. J.* **A24S1** (2005) 65–67.

[121] **UA1** Collaboration, C. Albajar *et al.*, "Bose-Einstein correlations in anti-p p interactions at $\sqrt{s}$= 0.2-TeV TO 0.9-TeV," *Phys. Lett.* **B226** (1989) 410.

[122] **Axial Field Spectrometer** Collaboration, T. Akesson *et al.*, "Bose-Einstein correlations in alpha alpha, p p and p anti- p interactions," *Phys. Lett.* **B129** (1983) 269.

[123] C. De Marzo *et al.*, "Measurement of the average transverse momentum and of the pion emission volume in proton-nucleus and anti-proton-nucleus reactions at 200 GeV," *Phys. Rev.* **D29** (1984) 363–367.

[124] **EHS-NA22** Collaboration, N. M. Agababyan *et al.*, "Influence of multiplicity and kinematical cuts on Bose- Einstein correlations in pi+ p interactions at 250-GeV/c," *Z. Phys.* **C59** (1993) 195–210.

[125] **H1** Collaboration, C. Adloff *et al.*, "Bose-Einstein correlations in deep inelastic e p scattering at HERA," *Z. Phys.* **C75** (1997) 437–451, `hep-ex/9705001`.

[126] **NA49** Collaboration, R. Ganz, "A systematic study of two particle correlations from NA49 at CERN SPS," *Nucl. Phys.* **A661** (1999) 448–451, `nucl-ex/9909003`.

[127] A. Smirnova, "Bose-einstein correlations at the z0 peak,". *Soft Multihadron Dynamics*, Hackensack, USA: World Scientific (1999) eds. N.G. Antoniou et al., pp.157-167.

[128] G. Alexander, I. Cohen, and E. Levin, "The dependence of the emission size on the hadron mass," *Phys. Lett.* **B452** (1999) 159–166, `hep-ph/9901341`.

[129] G. Alexander, "Mass and transverse mass effects on the hadron emitter size," *Phys. Lett.* **B506** (2001) 45–51, `hep-ph/0101319`.

[130] B. Lorstad and O. G. Smirnova, "Transverse mass dependence of Bose-Einstein correlation radii in e+ e- annihilation at the LEP energies,". Prepared for 7th International Workshop on Multiparticle Production: Correlations and Fluctuations, Nijmegen, Netherlands, 30 Jun - 6 July 1996.

[131] B. Andersson and W. Hofmann, "Bose-Einstein Correlations and Color Strings," *Phys. Lett.* **B169** (1986) 364.

[132] G. Alexander, "Open questions related to Bose-Einstein correlations in e+ e- -¿ hadrons," *Acta Phys. Polon.* **B35** (2004) 69–76, `hep-ph/0311114`.

[133] U. A. Wiedemann and U. W. Heinz, "Resonance contributions to HBT correlation radii," *Phys. Rev.* **C56** (1997) 3265–3286, `nucl-th/9611031`.

[134] A. Bialas, M. Kucharczyk, H. Palka, and K. Zalewski, "Mass dependence of HBT correlations in e+ e- annihilation," *Phys. Rev.* **D62** (2000) 114007, `hep-ph/0006290`.

[135] T. Csorgo, M. Csanad, B. Lorstad, and A. Ster, "Analysis of identified particle yields and Bose-Einstein (HBT) correlations in p + p collisions at RHIC," *Acta Phys. Hung.* **A24** (2005) 139–144, `hep-ph/0406042`.

[136] W. Broniowski and W. Florkowski, "Explanation of the RHIC p(T)-spectra in a thermal model with expansion," *Phys. Rev. Lett.* **87** (2001) 272302, `nucl-th/0106050`.

[137] Z. Tang *et al.*, "Spectra and radial flow at RHIC with Tsallis statistics in a Blast-Wave description," `0812.1609`.

[138] G. Wilk and Z. Wlodarczyk, "Power laws in elementary and heavy-ion collisions - A story of fluctuations and nonextensivity? -," `0810.2939`.

[139] G. Wilk *Private communication.*

[140] L. Frankfurt, M. Strikman, and C. Weiss, "Dijet production as a centrality trigger for *pp* collisions at CERN LHC," *Phys. Rev.* **D69** (2004) 114010, `hep-ph/0311231`.

[141] M. A. Lisa, U. W. Heinz, and U. A. Wiedemann, "Tilted pion sources from azimuthally sensitive HBT interferometry," *Phys. Lett.* **B489** (2000) 287–292, `nucl-th/0003022`.

[142] S. Chapman, P. Scotto, and U. W. Heinz, "A New cross term in the two particle HBT correlation function," *Phys. Rev. Lett.* **74** (1995) 4400–4403, `hep-ph/9408207`.

[143] C. E. Shannon, "Communication in the presence of noise," *Proc. Institute of Radio Engineers* **37** (1949) 10–21.

[144] A. J. Jerri, "The Shannon Sampling Theorem-Its Various Extensions and Applications: A Tutorial Review," *Proc. of IEEE* **65** (1977) 1565–1596.

[145] D. Brown *in preparation. Private comm.*

[146] **STAR** Collaboration, R. J. Porter and T. A. Trainor, "Correlations from *pp* collisions at $\sqrt{s}$ = 200- GeV," *J. Phys. Conf. Ser.* **27** (2005) 98–107, `hep-ph/0506172`.

[147] **STAR** Collaboration, R. J. Porter and T. A. Trainor, "Correlations in p p collisions," *PoS* **CFRNC2006** (2006) 004.

[148] **STAR** Collaboration, J. Adams *et al.*, "Minijet deformation and charge-independent angular correlations on momentum subspace (eta, phi) in Au-Au collisions at $\sqrt{s_{NN}}$= 130-GeV," *Phys. Rev.* **C73** (2006) 064907, `nucl-ex/0411003`.

254